MATHEMATICAL MODELING OF FIELD DRIVEN MEAN CURVATURE SURFACES

by

Derek E. Moulton

A dissertation submitted to the Faculty of the University of Delaware in partial fulfillment of the requirements for the degree of Doctor of Philosophy in Applied Mathematics

Spring 2008

MATHEMATICAL MODELING OF FIELD DRIVEN MEAN CURVATURE SURFACES

by

Derek E. Moulton

Approved: ______________________________

Peter Monk, Ph.D.
Chair of the Department of Mathematical Sciences

Approved: ______________________________

Tom Apple, Ph.D.
Dean of the College of Arts and Sciences

Approved: ______________________________

Carolyn A. Thoroughgood, Ph.D.
Vice Provost for Research and Graduate Studies

I certify that I have read this dissertation and that in my opinion it meets the academic and professional standard required by the University as a dissertation for the degree of Doctor of Philosophy.

Signed: ______________________________

John A. Pelesko, Ph.D.
Professor in charge of dissertation

I certify that I have read this dissertation and that in my opinion it meets the academic and professional standard required by the University as a dissertation for the degree of Doctor of Philosophy.

Signed: ______________________________

Richard J. Braun, Ph.D.
Member of dissertation committee

I certify that I have read this dissertation and that in my opinion it meets the academic and professional standard required by the University as a dissertation for the degree of Doctor of Philosophy.

Signed: ______________________________

John McCuan, Ph.D.
Member of dissertation committee

I certify that I have read this dissertation and that in my opinion it meets the academic and professional standard required by the University as a dissertation for the degree of Doctor of Philosophy.

Signed: ______________________________

Gilberto Schleiniger, Ph.D.
Member of dissertation committee

ACKNOWLEDGEMENTS

This dissertation is the culmination of a long and truly joyous journey, and I am grateful to many people for their help along the way. Some have directly contributed to the material that resides within these pages; others have made immeasurable contributions to the general happiness in my life. To begin, I must thank my advisor, Dr. John A. Pelesko. Since the first time I walked into his office over three years ago, it has been a unique pleasure working with him and learning from him. So much of my growth as a mathematician and a researcher is due to his guidance and support, and I am lucky to have had him as an advisor. A great deal of thanks goes to the rest of the faculty in the math department at the University of Delaware, for the knowledge I have gained through interactions in and out of the classroom. I am indebted to my committee members, Dr. Richard Braun, Dr. Gilberto Schleiniger, and Dr. John McCuan, for their helpful comments and for donating their time to this thesis.

Graduate school would not have been the great experience it was without my friends and fellow graduate students. In particular, thanks to Regan Beckham for his endless enthusiasm. He was always willing to lend his time and his thoughts to any endeavor or problem. And of course, to Pam and Kara, friends first and colleagues second, without whom I may have finished my degree a year earlier but would not have had nearly as much fun doing it. I don't know how I will survive Friday lunches without you around.

I would never have made it this far without my loving family - they have always been encouraging, and have even made occasional attempts to understand what it is that I do. Thanks to my Mom for instilling in me the confidence to be who I am, my Dad for showing me the beauty of solving puzzles, my brother Ben for being someone I could look up to, and my sister Lauren for always bringing a smile to my face. A special thanks to my wife Jeannie, the love of my life, whose support has been unwavering and who has kept my life the happy balance that it is. I cannot thank you enough just for being you.

TABLE OF CONTENTS

LIST OF FIGURES

LIST OF TABLES

ABSTRACT

This thesis investigates the interaction of static electric fields with surfaces of zero and constant mean curvature. Such systems have as their driving components surface tension and electrostatic forces. These forces are prominent on the micro- and nano scale, and understanding their interaction is of key importance in many applications, including micro- and nanoelectromechanical systems (MEMS and NEMS), self-assembly, nanolithography, and microfluidic processes.

Two particular systems are explored. Mathematical models are developed and subsequently studied through a combination of analysis, numerics, and experiment. One system involves a minimal surface catenoid membrane deflected by an axially symmetric electric field. A model is formulated via variational techniques to describe equilibrium shapes of the membrane. A detailed analysis of the general solution set is performed, with emphasis on stability and the effect of dimensionless parameters. Techniques utilized include perturbation theory, phase space analysis, methods from non-linear dynamics, and numerical branch tracing for bifurcation diagrams. Experimental analysis is performed using soap-film bridges and a high voltage power source. Experimental observations verify the validity of the theory in predicting membrane profile as well as stability boundaries. Different geometries are considered, as well as the variations of unequal boundary radii and the addition of a volume constraint. The general effect of the electric field is determined and the utility of an electric field in such systems examined.

The second system explored involves the dynamics of bubbles deflating through tubes and subjected to an applied electric field. The effect of added electrostatic pressure on a single bubble collapse is explored theoretically and experimentally. Differential equations describing the size of the bubble as a function of time are derived and analyzed. Systems of two bubbles connected via a common tube are then considered. Here, differences in surface tension and electrostatic forces between bubbles interact as bubbles compete for a fixed volume of air. The solution structure is fully characterized in the two bubble system for arbitrary surface tension and surface charge. Several examples are given to illustrate the drastic effect of parameters on system dynamics.

Chapter 1

INTRODUCTION

Anyone who has ever shuffled across a carpet and then touched a doorknob has experienced electrostatics. Anytime we watch drops of liquid form or bugs walking on water, we are watching surface tension at work. Both electrostatic and surface tension forces are extremely common in daily life, and yet both often go unnoticed. Most people's association ends with these small examples. For scientists, mathematicians, and engineers working on small scales, however, it is a different story; in the world of atoms, these forces are king.

Electrostatic forces, and more generally electromagnetic forces, have intrigued cultures since at least 600 B.C., when Greek philosophers created electric charge by rubbing fur on amber. It was not until the 18th century that researchers would begin to understand, control, and manipulate these forces. Contributions from such greats as Franklin, Gauss, Faraday, and Maxwell (among many others) paved the way for our current understanding, so that today, of the four basic forces, the electromagnetic force is the only one we fully understand [25]. Electrostatics is the branch of electromagnetism that deals with stationary electric charges. Since its inception, electrostatics has been utilized in a wide array of applications. The first electric generators were electrostatic, beginning with Otto von Geuricke's rotating sulphur ball in the late 1600's. The Leyden jar, introduced in 1745, served as the first capacitor. As understanding and control of electricity has continued to increase through the years, more and more devices and applications that utilize static electricity have mounted. Electrostatic forces have been used in such wide ranging areas as electrophotography [44], separation methods in mineral processing [38], color printers [2], and even agriculture [4]. Mathematically, the governing equations for electrostatics are taken from Maxwell's equations, with all time derivatives set to zero. In terms of electric potential, one must solve Poisson's equation in regions of charge distribution or Laplace's equation in regions of zero charge. These equations are extremely well studied, and a multitude of methods, both numerical and theoretical, have been developed for their treatment. Still, when coupled with other forces or when dealing with complex geometries, electrostatics can still be challenging and yield unexpected results.

Most pertinent to this thesis is the propensity of electrostatic forces to move things, a notion which has long been appreciated and has been exploited in many applications. In the modern era of micro- and nanotechnology, electrostatic forces are more pervasive than ever. Due to favorable scaling laws, electrostatic forces are dominant on the micro and nano scale [72]. Hence, while we would never consider, say, lifting a car with electrostatic forces, on small scales these forces provide one of the dominant means of actuation. As the technology to manipulate objects and build on small scales increases, it becomes increasingly important to understand exactly how these forces move things, what their limits are, and how they interact with other forces. Mathematical models that address such questions can be of tremendous value for industrial applications as well as in fundamental understanding.

Similar to electrostatic forces, surface tension forces are ever present in the macro world, but are rarely dominant. Again due to favorable scaling laws, this is not the case on the micro scale. Many phenomena that occur on small scales have surface tension as the driving force. Perhaps the best way to appreciate surface tension is to play with soap-film. Due to its thinness, gravity is negligible, and a soap-film assumes its shape as a consequence of surface tension. For this reason, soap-film has intrigued mathematicians for over a hundred years. The earliest notable investigation into the properties of soap-films was by Plateau in the 19th century [54]. Another notable contribution occurred around the turn of the 20th century in the work of C.V. Boys [11]. Much of the intrigue comes from the ability of soap-film to automatically solve a well-posed mathematical problem: "Given a boundary configuration, what is the spanning surface with the least surface area?" Physically, create a soap-film across a boundary configuration, and the film automatically assumes the surface with the smallest surface area, at least locally. The soap-film simply minimizes free energy, which is proportional to surface area. Such a surface is called a minimal surface. Mathematically, the problem is posed by the requirement that the mean curvature of the surface is everywhere zero. The mathematical formulation began to take shape in 1805, when Young introduced the concept of mean curvature [21].

A close relative to the minimal surface is the capillary surface. A capillary surface is a free interface that occurs when a liquid comes into contact with another liquid or a solid. Similar to the minimal surface, in the absence of external forces such as gravity, the capillary surface forms a shape driven by surface tension. The primary difference between a capillary surface and a minimal surface is that a capillary surface satisfies a volume constraint. Mathematically, a capillary surface in the absence of external forces has *constant* mean curvature. Of course, by this definition, a minimal surface is a capillary surface as well. However, it is traditionally understood that constant mean curvature and zero mean curvature are separate cases. In this thesis, we will use the term mean curvature surfaces to encompass both capillary and minimal surfaces.

Aside from their mathematical interest, mean curvature surfaces have great biological and industrial significance. In nature they are abundant. One need look no further than the building blocks of life – the structure of DNA – to find minimal surfaces [8]. They are found both in inorganic and organic structures [3]. They are of fundamental importance in fluid dynamics. From an engineering standpoint, mean curvature surfaces are utilized in multiple areas, including object detection in image analysis [13], forming glass surfaces [28], and the construction of microchannels [34]. A particular area of interest is in the field of self-assembly, where surface tension provides one of the primary driving forces [50].

As we have illustrated, both electrostatic forces and mean curvature surfaces have long been appreciated, exist in many physical phenomena, and are vital in a multitude of industrial applications. Systems which combine the effects of surface tension and electrostatic forces are potentially of great value, and indeed, many systems do just this. One example occurs in nanolithography. A relatively new technique for pattern formation on the submicrometer scale involves subjecting polymer films to strong electric fields, causing them to organize into a prescribed pattern [63]. There are many other systems which have both electrostatic and surface tension forces present; however, the notion of subjecting mean curvature surfaces to electric forces to exploit the tendencies of each remains unexplored in many potential applications. For example, in [68], Syms *et al.* describe a self-assembly technique in which a drop minimizing its surface area pulls components into place. The key idea behind this process is to exploit the tendency of a mean curvature surface to minimize free surface energy. The process is remarkably simple, yet rather slow as well. By combining the surface tension forces with electrostatic forces, there is potential to speed up the process as well as to achieve configurations otherwise unattainable. The success of this would be dependent upon having the proper balance between the two forces.

In this thesis, we explore several systems in which electrostatics and surface tension combine to provide the primary forces. Physically, we subject a mean curvature surface to an electric field and study the shape of the resulting interface. Mathematically, the mean curvature operator, arriving via the role of surface tension, is combined with terms describing the effect of the electric field. We designate such surfaces as Field Driven Mean Curvature (FDMC) Surfaces.

The first system we study consists of a catenoid bridge subjected to an axially symmetric electric field. Along with the trivial case of the plane, the catenoid is the only minimal surface of revolution, and is formed by rotating a catenary around its axis. Physically, a catenoid is created when a soap-film membrane is suspended between two parallel circular rings. This surface was discovered by Euler in 1744, although somewhat obscurely, and is often attributed instead to Meusnier in 1776 [40, 73]. Equations describing a catenoid can be written explicitly, and its properties are well-known. We subject this simple minimal surface to electrostatic forces by placing a fixed cylindrical electrode either inside or outside the catenoid and applying an electric potential difference between the catenoid and the electrode. The catenoid membrane is assumed to be perfectly conducting. Hence the membrane and the electrode form a capacitor, and a Coulomb attraction exists between the electrode, which is rigid and stationary, and the membrane, which is elastic. The shape of the membrane is determined by the combination of electrostatic and surface tension forces.

Motivation for this particular system comes from several areas. One is the theory of electrostatic actuation. This field found its start in the 1960's, when G.I. Taylor launched the field of electrohydrodynamics through a series of pioneering studies. Of special note is [70], where Taylor studied the electrostatic deflection of planar soap-films. While Taylor's intent was to shed light on the coalescence of raindrops in electrified clouds, the last fifty years have shown that Taylor's simple system is in fact of great technological importance. Today, researchers studying engineering technologies such as micro- and nanoelectromechanical systems (MEMS and NEMS) [51], self-assembly [31], and electrospinning [46] all point to Taylor's work as a seminal contribution to their fields.

Perhaps the most direct application of Taylor's soap-film study has been in the field of MEMS and NEMS. Here, researchers have developed a variety of devices such as grating light valves, micromirrors, comb drives, and micropumps, that operate based on the principle of electrostatic actuation explored by Taylor. All of these systems operate in essentially the same way: a voltage difference is applied between mechanical components of the system, this voltage difference induces a Coulomb force between the components, and, in turn, the components deform in the presence of this force. In the Taylor system, the mechanical components were a pair of planar soap-films. The first industrial application that operated under this principle was Nathanson's resonant gate transistor [43], an electrical tuning device famous for being the first MEMS device.

Present in the Taylor system and in all related engineering systems is an instability commonly known as the "pull-in instability." The origin of this instability lies in the competition of the elastic and electrostatic forces in these systems. Roughly speaking, as mechanical components are pulled together, the strength of the Coulomb force increases with the inverse of the square of their distance while the elastic restoring force increases linearly with their distance. At some point, the electrostatic force dominates, and the mechanical components snap together, or "pull-in."

The restrictive nature of this instability in the design of engineering systems has led to a host of mathematical models attempting to understand, characterize, and control such systems [22, 49, 51, 53]. In turn, the development of these models has been strongly influenced by typical features of MEMS and NEMS devices. The most important of these features is the small aspect ratio of most MEMS and NEMS systems. Since MEMS and NEMS technology is largely an outgrowth of planar fabrication technology developed for integrated circuits, most MEMS and NEMS are inherently planar. That is, they typically consist of large, flat, mechanical components separated by a small gap. This is reflected in mathematical models of such systems in two ways. First, the small gap allows for simplification of the equations governing the electric field – this is the well known parallel plate approximation. Second, the presence of small elastic deflections justifies the use of linear elasticity theory.

Recent developments, especially in the field of self-assembly, indicate that it is time to push the development of mathematical models of electrostatic actuation to a new level. Perhaps the clearest example of this need lies in the experimental work of Whitesides [31]. In attempting to develop new fabrication technologies for MEMS and NEMS, Whitesides placed drops of polydimethylsiloxane (PDMS) between two rigid plates. These droplets naturally form a "liquid bridge." By adjusting the gap between the plates and the relative orientation of the plates, a variety of structures can be formed. In the PDMS system, the polymer can be cross-linked, solidifying the liquid bridge and hence leading to the production of small components with a variety of shapes. In [31], Whitesides notes that a much greater range of shapes could be formed if the bridges were manipulated with an electric field. This brings us back to the problem of electrostatic actuation, but with a twist: linear elasticity is no longer appropriate, the electric field is no longer simple, and volume constraints may need to be taken into account.

Motivated by the Whitesides example, and as a first step in extending the theory of electrostatic actuation, we explore a catenoid bridge subjected to an electric field. It is useful to contrast the model developed here with typical models of electrostatic actuation. The governing equation that we will derive has the general form

$$Hu = f(u) \;, \tag{1.1}$$

where the function u gives the radial coordinate of a deflected surface of revolution. Here, H is the mean curvature operator, and the function $f(u)$ captures the Coulomb force due to the presence of the electric field. Typical models of electrostatic actuation have the general form

$$\Delta u = g(u) \;, \tag{1.2}$$

where again, u measures the deflection of some surface, and $g(u)$ captures the Coulomb force. Note that moving to a non-planar geometry implies that the mean curvature operator, H, cannot be linearized and replaced by the Laplacian as in Equation (1.2). Also note that $g(u)$ typically contains a simple inverse square non-linearity, while here we are forced to deal with a more complicated logarithmic non-linearity in $f(u)$.

The connection between electrostatic actuation and the theory of mean curvature surfaces is clear in view of Equation (1.1). When the electric field is turned off, the surface satisfies $Hu = 0$, i.e. it is a minimal surface. The term $f(u)$ arises due to the presence of the electric field; hence the designation Field Driven Mean Curvature Surface.

A second motivation for the catenoid bridge in an electric field system relates to liquid bridges. Generally speaking, we can define a liquid bridge as a liquid surface of fixed volume spanning the distance between two boundaries. This basic configuration is found frequently in daily life (a running faucet, for instance) and is of importance in many fluid mechanical systems, particularly in low or zero gravity conditions. Accordingly, a considerable amount of literature has been devoted to various aspects of liquid bridges. A liquid bridge acted upon only by surface tension will have constant mean curvature. When the volume constraint is dropped, the constant is zero and we return to the catenoid. The main properties of the catenoid have been known for hundreds of years – classical stability results were obtained experimentally by Plateau [54] and are found in many textbooks. Still, theoretical studies exploring various aspects of this system continue to surface. More precise stability results are found in [19, 81]. In the simple case of fixed contact rings of equal radii, a catenoid is stable with respect to axisymmetric perturbations if the ratio of the boundary ring radii to the bridge length is greater than approximately 0.7544. For fixed boundary rings, when the critical length corresponding to this stability boundary is reached, the bridge pinches off at the mid-plane between the rings and collapses. Multiple analyses of the shape change dynamics during this onset of instability have been performed [15, 17, 42, 61].

With the addition of a volume constraint, more interface shapes become possible. Even in the simplest configuration, consisting of parallel, circular contact boundaries, an explicit solution can be found only in special cases. Many investigations of stability properties have been carried out. In [14], stabilization of a liquid bridge is explored by balancing gravity and an axial flow. Lowry and Steen explore stability of axisymmetric bridges in terms of volume and pressure by plotting "preferred" bifurcation diagrams [36]. This presents an appealing approach to stability which stems from the work of Maddocks [37]. We discuss this idea and apply it to our system in Chapter 2. In [74] and [75], Vogel considers stability for fixed contact angles as a function of bridge volume. We return to some of his results in Chapter 4. These studies concern axisymmetric perturbations. Bifurcations corresponding to non-axisymmetric perturbations are explored in [65]. Variations on the bridge setup include the work of Meseguer and Perales [39], which considers the case of almost circular boundary disks, and that of Concus, Finn, and McCuan [16], which explores the effect of tilting the boundary plates so that they are no longer parallel.

Both of these variations disrupt the inherent symmetry in the system, make computations significantly more difficult, and can lead to unexpected behavior. In the latter study, for instance, it is found that except in special cases, tilting the plates leads to a discontinuous change in bridge shape.

The aforementioned studies provide a sample of the vast work in conjunction with liquid bridges. Note that electric fields are not present in any of the foregoing work. Multiple studies have been performed involving liquid bridges subjected to electric fields, however. Applications for liquid bridges in the presence of electric fields include the areas of mixing, electrostatic spraying, propulsion, and ink jet printers. The system we present in this thesis is closely related to previous studies, yet there are several key differences. Perhaps the biggest difference is in geometry. To the authors' knowledge, all previous work in electrified mean curvature bridges has involved applying axial electric fields. That is, the liquid bridge is formed between two parallel electrodes, so that the bridge essentially sits inside a capacitor. In the present study, the membrane forms the second part of the capacitor – a potential difference is applied between a cylindrical electrode and the film itself. This difference drastically alters the interaction of electrostatic and elastic forces – in our geometry, the electric field is directly "pulling" on the membrane.

The typical approach in electrified liquid bridge problems is to take Laplace's equation for the electrostatic potential, Navier Stokes equations for the fluid (i.e. the bridge), and a modified Young-Laplace equation relating interface shape to the pressure jump across the interface. Mathematically, this presents a complex system, and numerical methods become necessary. In [56], for instance, the system is solved using a finite element method. In [76], a more efficient means of solving the same basic system is presented by means of a boundary integral method. In [47] and [24], theoretical analyses are performed by considering cylindrical and nearly cylindrical bridges, where linear stability becomes applicable. In our system, on the other hand, we have a soap-film bridge rather than a liquid mass, and flow equations are unnecessary. Also, we exploit a small aspect ratio in order to solve for the electrostatic potential to first order. This results in governing equations for the interface which permit a theoretical analysis.

Another difference between our analysis and previous work concerns the effect of the electric field. In [24], [47], and [56], the main effect explored is stabilization of the bridge with the electric field. With our setup, we find that the field may be used to stabilize in one geometry, whereas in the other geometry the field serves instead to destabilize the bridge. This presents a new twist, and perhaps opens up new applications where bridge breakup is desired.

The catenoid bridge in an electric field is quite complex mathematically, and we devote three chapters to various aspects of this system. In Chapter 2, we investigate the geometry where a cylindrical electrode sits at a greater radius than the boundary rings of the catenoid. This geometry yields the most complexity, with high multiplicity of solutions and peculiar stability results. In Chapter 3, we consider the geometry where the cylindrical electrode sits inside the catenoid bridge. Analytically, in both of these chapters we explore equilibrium configurations of the interface, questions of stability, and dependence on parameters. In particular, we explore the main effects of the applied electric field and attempt to quantify the interplay between surface tension and electrostatic forces. We obtain the result that in the geometry of Chapter 2, the surface tension and electrostatic components can be balanced in a way that enables for the stabilization of long bridges. In the geometry of Chapter 3, we find just the opposite result, that the electric field serves to destabilize the bridge.

In Chapter 3, we combine an experimental investigation with the theoretical study. Experimentally, we seek to verify the stability limits derived in the theory, and also to test the predictability of the theory in regards to membrane shape.

Good agreement is found between theory and experiment. Similar experimental studies with liquid bridges in electric fields include the work of [12], [57], and [32]. These studies differ from the analysis in this thesis in that they all involve liquid bridges and, as stated before, axial electric fields. Note that the experiments in [12] were performed on a space shuttle to achieve a gravity free environment. In the experiments of [57] and [32], gravity is either accounted for in the model or made negligible through density matching or small experimental dimensions. A nice advantage of using soap-film is that gravity is negligible even in a macro sized experimental setup.

In Chapter 4, we explore two variations to the system. First, we consider the setup where the catenoid is formed between rings of unequal radii. This change removes the inherent symmetry about the mid-plane, and complicates the nature of solutions even in the absence of an electric field. We investigate the role of the ratio of ring radii in relation to critical parameter values and the location of bifurcations in the solution set. Following this, we consider the addition of a volume constraint. This is an important addition in that it takes the problem into the realm of *liquid* bridges, but it also adds a significant complication mathematically. Though our discussion of the volume constrained problem is brief, we do reach some counterintuitive conclusions regarding the stability of cylindrical bridges.

In Chapter 5 we explore a rather different system. We investigate a bubble which is attached to the end of a tube and under the influence of an electric field, and model the size of the bubble as a function of time as it deflates through the tube. The primary motivation for this system is that it is a dynamical FDMC surface. The catenoid system we explore in Chapters 2 - 4 involves a static mean curvature surface influenced by an electric field. The FDMC surface in Chapters 2 - 4 is difficult to describe analytically, but is facilitated by the static nature of the system. In Chapter 5, the FDMC surface is more easily described; however, the system is by nature dynamic, with the shape of the surface a function of time.

Minus the field, the deflating bubble scenario was discussed by Plateau [54] and Boys [11], and was investigated in detail by Grosse in 1967 [26]. Grosse treated the bubble as a perfect sphere, and modeled the radius as a function of time. An important component in the system, as noted by Grosse, is that the flow is entirely driven by surface tension. That is, the air flow is caused by surface tension "pushing" air out of the bubble. Mathematically, the flux of air through the tube is driven by a pressure difference Δp across the bubble equal to $2\gamma/R$, where γ is the surface tension and R the radius of the bubble. This is the Young-Laplace law. As pointed out by Grosse, this scenario is not limited to soap-bubbles, but is applicable to spheres of liquid as well. The primary difference with a sphere of liquid is that a collapse will take twice as long, since there is only one interfacial film for a liquid sphere in contrast to two layers for a soap-bubble. Hence an extra factor of 2 appears in the pressure difference when dealing with a soap-bubble.

Grosse's analysis was duplicated by Rämme in 1996 [55]. Rämme experimented with a bubble collapsing through a capillary tube, and used the predicted total collapse time to accurately determine the surface tension of the bubble. The idea of a collapsing bubble has been applied in studying the permeability of monolayers. In [10], a technique is described whereby the size of a bubble made of a particular soap-solution is measured against time as gas diffuses out. The rate at which the gas diffuses out is then used to determine monolayer permeability. This system is different than that explored by Grosse and Rämme in that the collapse is due to diffusion rather than air flow through a tube. However, the key ideas remain – a pressure difference proportional to surface tension and inversely proportional to the radius of the bubble drives air flow out of the bubble.

In his original study, Grosse also considers several interesting systems involving two bubbles or two spheres of liquid. In one setup, two bubbles sit on opposite ends of a connecting tube. Essentially, the bubbles must compete for a fixed volume. The result, which dates back to Plateau, is that the larger bubble grows at the expense of the smaller. Mathematically, this is easy to see. The pressure in each bubble is inversely proportional to the radius, which means that the smaller bubble is "pushing" its air out harder than the larger bubble. As we will demonstrate, this elementary idea is actually a key component in a number of phenomena, both industrial and biological. Wente [78] examined this problem for two and three bubble setups, analyzing equilibrium solutions and stability as a function of total volume. He studied the problem from the viewpoint of catastrophe theory, demonstrating the presence of a cusp catastrophe with the radii at the ends of the connecting tube serving as unfolding parameters.

Dynamics of a similar system were explored by Theisen *et al.* [71]. Their setup consists of two liquid spherical caps connected by a tube. The system is constrained to a finite volume, and the same steady state solutions exist as described by Wente. The important feature of the steady state solutions is that for large enough volume, the system exhibits bi-stability. Dynamics enter in by giving the system a finite amplitude "kick". In the inertia dominant regime, they find large looping oscillations between the two distant steady states given a large enough amplitude disturbance. Experimental results agree well with predictions. A potential application for this idea is in liquid micro-lens devices. In [35], for instance, an adaptive liquid lens is presented composed of the same setup as the Theisen group. Changes in relative surface tension of the two spherical caps is used to control drop curvature and hence focal length of the lens.

A more general application of the two spherical cap setup is the droplet-droplet switch. The idea is to exploit the bi-stability in the system to create a switch by toggling between stable states. If the system is within a basin of attraction, surface tension drives it to a stable state. Hence, one must only provide enough energy to leave one potential well, and allow stored energy to drive the system to an alternate state. In the droplet-droplet switch analyzed in [27], changes in total volume provide the "kick" necessary to toggle the system. Another approach is presented in [9], in which a liquid bridge is formed in a chamber between two liquid spherical caps. The shape of the bridge is controlled by adjusting the pressure in the chamber, and altering the bridge is used to mediate the droplet switch. This idea is particularly interesting in the context of this thesis, in that it combines the components of a liquid bridge (explored in Chapters 2 - 4) with the notion of interacting spherical drops (explored in Chapter 5) in a single device.

A closely related system is explored by Slobozhanin and Alexander in [64]. The setup they consider consists of two pendant drops suspended from a horizontal plate, connected by a liquid layer above the plate through which the two drops communicate. This is fundamentally the same as the spherical cap system when gravity is negligible. In their analysis Slobozhanin and Alexander also explore the effects of gravity as well as boundary hole radii inequality. Behind all of these systems is the same basic principle explored in Grosse's two bubble experiment: surface tension drives the system to equilibrium based on pressure differences related to the relative size of the drops.

Fundamentally similar systems are found in the theory of drop coalescence. The actual physics of two drops coalescing are quite different from the systems described above. For one, the "connecting bridge" for coalescing drops is the point where the two drops meet. Unlike the systems above, this bridge is part of the fluid itself and thus has a size that varies with time. From a fundamental standpoint, however, the process is very similar. The coalescence is driven by surface tension, and pressure differences are ascribed to curvature. Essentially, the larger drop "eats" the smaller drop in the same manner as seen in bubble experiments. Multiple studies have been conducted in this area, exploring various aspects of drop coalescence. A nice theoretical analysis is provided by Eggers *et al.* [20]. The focus of their analysis is the size of the connecting bridge as a function of time early in the coalescence and the shape of the meniscus that forms at the end of the bridge. A related experimental analysis is found in [80]. One interesting result of the Eggers group is that in the early stage of coalescence, a bubble forms at the meniscus of the connecting bridge. Locally, the shape of the drop near this area may be treated as a bubble connected to a thin neck. Hence, there may be subtle relations between drop coalescence and connected bubble/drop systems. Until recently, most applications for drop coalescence involved sintering, which is the merging of a powder by heating. A renewed interest involves microfluidic mixing. Droplet based microfluidic techniques involve the transport, mixing, and separating of fluids on an individual droplet control level. In [45], the effect of drop aspect ratio on drop coalescence is explored, and related to lab-on-a-chip applications. An interesting biological phenomenon in this area is the spore dispersal of mushrooms. As is explored in [41], the coalescence of two drops enables a certain type of mushroom spore to discharge from its location on the gills at 25,000 times the acceleration of gravity. This incredible acceleration is brought about entirely by the capillary force of a small liquid drop merging with a large drop.

In a related but different area, a significant amount of work has been done in the study of bubbles and drops whose shape is controlled by a combination of surface tension and electrostatic forces. The starting point is the work by Lord Rayleigh in 1882 [58]. Rayleigh analyzed axisymmetric perturbations of a charged, conducting spherical drop surrounded by a fluid insulator, and showed that the spherical shape becomes unstable with respect to a disturbance proportional to a Legendre polynomial of order 2 when the drop charge exceeds $8\pi\sqrt{\epsilon_0 R^3 \gamma}$, where ϵ_0 is the permittivity of the insulator, γ is surface tension, and R is the drop radius. This charge is known as the Rayleigh limit. In 1964, G.I. Taylor calculated equilibrium shapes beyond this limit by assuming that the drop deforms into a prolate spheroid [69]. Taylor was studying the disintegration of drops in strong electric fields, and was interested in the possible relation to the formation of thunderstorms. He performed calculations both for charged drops as well as drops in uniform electric fields. In regards to the latter, he deduced a stability limit in the strength of the applied field beyond which the drop is unstable and the famous Taylor cones form. This is known as the Taylor limit. Prior to this instability, and more pertinent to the present investigation is the following notion: a drop will not remain spherical in the presence of a uniform field, no matter how small, but can be approximated by a spheroid prolate in the direction of the field. Interestingly, in 1924, 40 years earlier, Wilson and Taylor (Taylor was just a graduate student at the time) performed an experimental investigation of soap-bubbles placed in a uniform electric field [79]. In Chapter 5 we use the same basic experimental setup to explore a collapsing bubble in an electric field.

Following the work of Taylor, several others have investigated equilibrium shapes and stability of drops influenced by electric fields. With respect to charged drops, Taylor had shown that the prolate family of spheroids appear as a subcritical branch bifurcating from the family of spheres at the Rayleigh limit. However, Taylor only considered positive deviations from a sphere. Negative deviations lead to oblate spheroids, which were analyzed and shown to be stable by Basaran and Scriven [5]. Pelekasis, Tsamopoulos, and Manolis [48] performed a similar analysis using a hybrid numerical method, reaffirming previous results and also uncovering information about new equilibrium families.

Several other analyses of note are due to Basaran and Scrivens. In [6], they place charged drops in an external electric field. Stability and drop shape are determined numerically via finite element analysis. Results agree well with experimental studies in [18] and [1]. In [7], pendant and sessile drops in an electric field are studied. Cases of fixed contact angle are considered as well as fixed contact line. An analysis by Song and Li [66] concerns liquid drops in electric fields, with multiple effects accounted for, including viscous flow within the drop as well as thermal effects which in turn cause variation in surface tension. This numerical study is performed by a mixed finite element and boundary element method. This list is certainly not exhaustive. Shape and stability questions of drops and bubbles in the presence of electric forces is of interest to researchers across multiple fields. These questions are not only of fundamental importance in physics and fluid dynamics, but have been found to be applicable in fields ranging from the study of thunderstorms to electrohydrodynamic atomization to ink-jet printers.

The studies we have mentioned in conjunction with Chapter 5 fall into two basic groups. In the first group, beginning with Grosse, are dynamical problems involving spherical bubble/drop capillary systems. In these systems, the main (and generally only) force acting on the system is surface tension, and dynamics come into play because the volume of the drop or bubble is not permanently fixed. Either the volume is able to escape, as in collapsing bubble systems, or the system is comprised of multiple drops/bubbles, in which case the volume can transfer between different states. In the second group, beginning with the work of Rayleigh, an external force is brought in with the addition of an electric field. In these systems, electric forces compete with surface tension (and perhaps other forces) to determine shape and stability. This greatly complicates knowledge of the shape. On the other hand, these systems are by nature static, in the sense that the drop/bubble is isolated, has a fixed volume, and does not communicate with other drops.

In Chapter 5, we investigate several systems which combine the elements from each of these two groups. Namely, we explore dynamical systems of drops/bubbles in which shape is determined by a combination of surface tension and electrostatic forces. To begin with, we explore Grosse's collapsing bubble problem in more detail, and develop a more precise model. We then add electrostatic forces by considering both collapsing charged bubbles and collapsing bubbles in electric fields, and explore the effect of the electric field. It is determined that in theory, charging a bubble can effectively stop the collapse before the bubble is fully deflated. With a uniform field, the general effect found is that the field serves to slow down the collapse. We then consider a connected two bubble system, but with the added effects of electrical surface charge and surface tension inequality. In studying this system, we uncover some interesting dynamical effects achieved through different combinations of surface tension, electric charge, and total volume.

The primary objective in Chapter 5 is to investigate a dynamical system involving an FDMC surface and to determine any effect and or potential advantages of the added field. By its nature, this poses a complex problem, with elements of fluid dynamics, electrostatics, and mean curvature surfaces. In many of the systems we study, a full treatment of the problem will not admit analytic solutions. Under several simplifying assumptions, however, the models we develop allow for a theoretical treatment. Along with theory, we perform several experimental studies. The experimental analysis serves to demonstrate the limitations due to the assumptions, but also confirms the validity of the theory in appropriate regimes.

Chapter 2

SOAP-FILM BRIDGE IN AN ELECTRIC FIELD – OUTER CYLINDER

2.1 Introduction

In this chapter we study a catenoid shaped soap-film bridge placed in an axially symmetric applied electric field. As discussed in Chapter 1, we consider two geometries for this system. The geometry in the present chapter involves a cylindrical electrode external to the bridge – this is the outer cylinder geometry. We begin in Section 2.2 by deriving the governing equations for the shape of the electrostatically deflected bridge. We take a variational approach to deriving the model. Having derived the governing differential equation, we next study the solution set. In Section 2.3 we take a dynamical systems approach by casting the problem into phase space and studying the nature of trajectories. In Section 2.4, we turn to perturbation methods and perform a detailed analysis of solutions in the special cases of small voltage and cylindrical bridges. In Section 2.5, we address stability, and also place the specific solutions of Section 2.4 in the framework of the general solution set. We conclude the chapter with an analysis of bifurcation diagrams.

2.2 Formulation of the model

In this section we present the governing equations for the behavior of the electrostatically actuated membrane. The system we study consists of two parallel rings of radius a with a thin elastic conducting membrane forming a bridge between

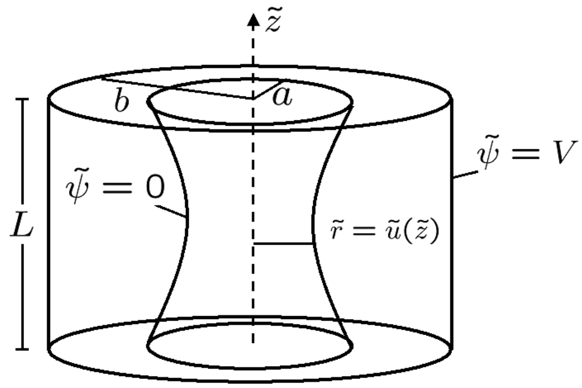

Figure 2.1: The basic setup for the problem.

the rings. We take the distance between the rings to be of length L. Surrounding the rings is a uniform cylinder of radius b with $b > a$. The top and bottom of the apparatus are left open, and there is no direct connection between the rings and the outer cylinder. The outer cylinder is connected to a battery while the inner rings are grounded, so that a potential difference is applied between the membrane and the outer cylinder. The outer cylinder has potential V and the membrane has zero potential. This geometry is sketched in Figure 2.1.

Under the above assumptions, we formulate the equilibrium equation for the shape of the membrane as an energy minimizer. The two main energies present in the system are electrostatic and elastic. We begin by formulating the equations governing the electric field. Denoting the electrostatic potential by $\tilde{\psi}$ and working in cylindrical coordinates, $\tilde{\psi}(\tilde{r}, \theta, \tilde{z})$ satisfies

$$\Delta\tilde{\psi} = 0 \tag{2.1}$$

$$\tilde{\psi}(b, \theta, \tilde{z}) = V \tag{2.2}$$

$$\tilde{\psi}(\tilde{u}(\tilde{z}), \theta, \tilde{z}) = 0 \; , \tag{2.3}$$

where $\tilde{r} = \tilde{u}(\tilde{z})$ is the radius of the membrane. Note that we are assuming axial symmetry so that the radius depends only on $\tilde{z}$; the membrane is a surface of revolution. Also note that we use tildes here to denote dimensional variables.

To simplify the problem, we introduce the non-dimensional variables

$$z = \frac{\tilde{z}}{L}, \quad r = \frac{\tilde{r}}{b-a}, \quad \psi = \frac{\tilde{\psi}}{V}, \quad u = \frac{\tilde{u}}{a} \; . \tag{2.4}$$

Here we have scaled the radius by the "gap size" $b - a$ between the inner and outer cylinders. Making these substitutions in Equations (2.1) – (2.3), we obtain

$$\frac{\partial^2 \psi}{\partial r^2} + \frac{1}{r}\frac{\partial \psi}{\partial r} + \epsilon^2 \frac{\partial^2 \psi}{\partial z^2} = 0 \tag{2.5}$$

$$\psi = 1 \quad \text{at} \quad r = \frac{b}{b-a} \tag{2.6}$$

$$\psi = 0, \quad \text{at } r = u(z)\frac{a}{b-a} \; . \tag{2.7}$$

Here,

$$\epsilon = \frac{b-a}{L}$$

is a dimensionless aspect ratio comparing the gap size between the rings and the outer cylinder to the length of the device. We assume $\epsilon^2 << 1$. With this assumption, ψ only has radial dependence to leading order. Equations (2.5) – (2.7) are then easily solved to yield

$$\psi = \frac{\ln r - \ln(\frac{au(z)}{b-a})}{\ln(\delta / u(z))} \tag{2.8}$$

where

$$\delta = \frac{b}{a}$$

is the ratio of the radii of the outer and inner cylinders.

The electrostatic field energy is given in dimensional form by

$$-\frac{\epsilon_0}{2}\int |\nabla\tilde{\psi}|^2 \tag{2.9}$$

where the integral is taken over the region between the outer cylinder and the membrane, and ϵ_0 is the permittivity of free space. Using the divergence theorem, and changing to dimensionless variables, this energy can be written as

$$-\pi\epsilon_0 V^2 L\frac{b}{b-a}\int\limits_{-1/2}^{1/2} \frac{\partial\psi}{\partial r}\Big|_{r=\frac{b}{b-a}}\,dz\ . \tag{2.10}$$

The integral (2.10) represents an integral over the outer cylinder. We have used the fact that $\psi = 1$ on the outer cylinder and that $\psi = 0$ on the membrane so that the integral over that portion of the boundary vanishes. Inserting ψ from Equation (2.8) into (2.10), the electric field energy becomes

$$-\pi\epsilon_0 V^2 L\int\limits_{-1/2}^{1/2}\left(\ln\frac{\delta}{u(z)}\right)^{-1}\,dz\ . \tag{2.11}$$

The elastic energy of the system is proportional to the change in surface area, and is given by

$$2\pi T L a\int\limits_{-1/2}^{1/2} u(z)\sqrt{1+\sigma^2 u'(z)^2}\,dz\ , \tag{2.12}$$

where

$$\sigma = \frac{a}{L}$$

is the ratio of the inner radius to the length, and T is the surface tension. (Note that we use primes to denote differentiation with respect to z.)

Taking the sum of these two energies and dividing by $2\pi TLa$, we obtain the dimensionless energy functional

$$\mathcal{E}[u] = \int_{-1/2}^{1/2} u\sqrt{1+\sigma^2 u'^2} - \frac{\lambda}{\ln(\delta/u)}\, dz \ , \tag{2.13}$$

where

$$\lambda = \frac{\epsilon_0 V^2}{2Ta}$$

is a dimensionless variable which characterizes the relative strengths of electrostatic and mechanical forces in the problem. We may think of λ as a control parameter related to the voltage. We minimize the energy $\mathcal{E}$ by taking a first variational derivative and obtain the following ODE for the shape of the membrane $u(z)$

$$\frac{1+\sigma^2 u'^2 - \sigma^2 u u''}{(1+\sigma^2 u'^2)^{3/2}} = \frac{\lambda}{u \ln^2(\delta/u)} \ . \tag{2.14}$$

To complete the system, we impose the boundary condition that the membrane be connected to the rings, expressed in dimensionless form as

$$u(1/2) = u(-1/2) = 1 \ . \tag{2.15}$$

Equations (2.14) – (2.15) govern the equilibrium shape of the deflected membrane. Note that the left hand side of Equation (2.14) is the mean curvature operator, while the right hand side contains the effect of the electric field. Our goal is to determine the solution set to this boundary value problem, to explore stability and multiplicity of solutions, and to understand the solution set in terms of the parameters λ, σ, and δ.

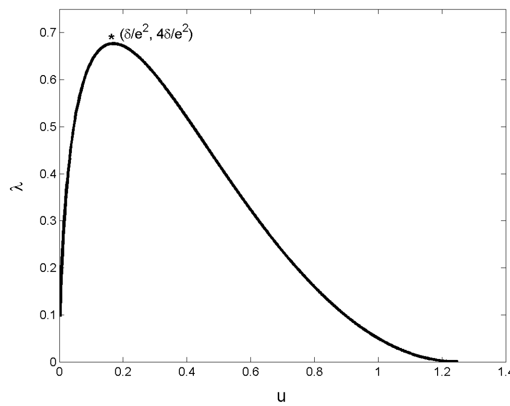

Figure 2.2: Curve of λ vs. u for which we have critical points in the phase plane. (Here, $\delta = 1.25$)

2.3 Phase plane analysis

We begin our analysis of (2.14) – (2.15) by considering the nature of trajectories in the phase plane. Rewriting the ODE (2.14) as a first order system, we have

$$\begin{aligned} u' &= v \\ v' &= \frac{1+\sigma^2 v^2}{\sigma^2 u} - \frac{\lambda(1+\sigma^2 v^2)^{3/2}}{\sigma^2 u^2 \ln^2(\delta/u)} \ . \end{aligned} \tag{2.16}$$

The critical points for this system are located at $v = 0$, and solutions of $u \ln^2(\delta/u) = \lambda$. In Figure 2.2, we plot the curve $\lambda = u \ln^2(\delta/u)$. For a given λ, there are 2 solutions, meaning that there are 2 critical points, which we denote $(u^*_{(1)}, 0)$ and $(u^*_{(2)}, 0)$, with $u^*_{(1)} < u^*_{(2)}$. We see from Figure 2.2 that these 2 critical points coalesce as λ is increased. This coalescence occurs at $u = \delta/e^2$, $\lambda = 4\delta/e^2$. If $\lambda > 4\delta/e^2$, there are no critical points for the system.

For $\lambda < 4\delta/e^2$, linear stability analysis shows that $(u^*_{(1)}, 0)$ is a saddle node, while $(u^*_{(2)}, 0)$ is a center. See Figure 2.3 for a sample phase portrait. Note that the system (2.16) is unaltered by the change of variables

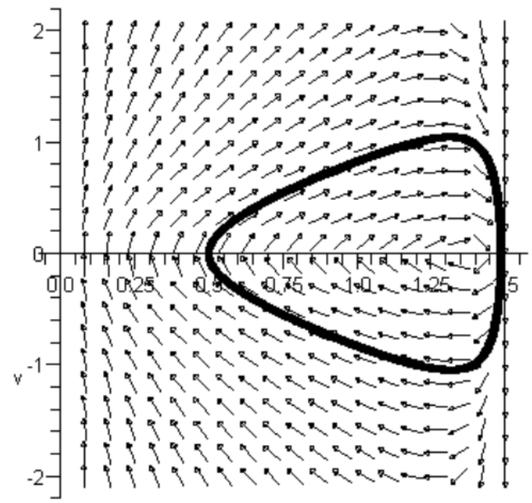

Figure 2.3: Sample phase plane plot in the u,v plane. There are 2 critical points: a saddle point located approx. at $(0.02, 0)$, and a center at approx. $(1.36, 0)$. A sample trajectory is included

$$v \mapsto -v, \quad z \mapsto -z \ .$$

This symmetry means that the trajectories in the lower half plane are the same as in the upper half but with the direction reversed, which is evident in Figure 2.3. This symmetry allows us to conclude that the right critical point is indeed a center [67].

Note that v' blows up at $u = 0$ and $u = \delta$. However, solutions to Equations (2.14) – (2.15) are entirely contained within $0 < u < \delta$. The case $u = 0$ corresponds to self-intersection of the membrane. The case $u = \delta$ corresponds to the membrane touching the outer cylinder. These are the physical bounds for the problem, so we restrict our attention to $u \in (0, \delta)$.

To further understand the structure of the phase portrait, we claim that there is a homoclinic orbit leaving and returning to the left critical point $(u^*_{(1)}, 0)$. To show this, we follow the trajectory that leaves the left critical point (saddle point) into the

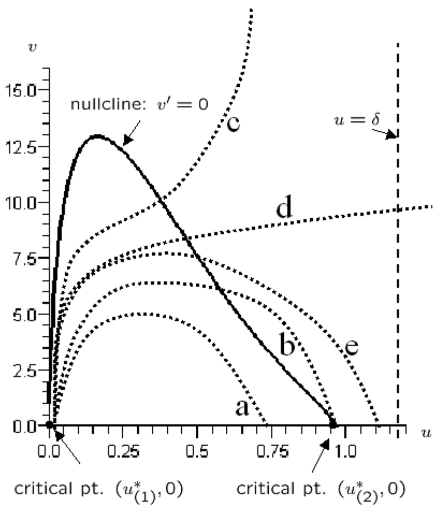

Figure 2.4: Nullcline curve and possible fates of the trajectory leaving the critical point $(u^*_{(1)}, 0)$.

upper half plane, and note that all we need to show is that this trajectory returns to the u-axis in finite time. If it does return to the axis, then due to the symmetry it will follow the mirrored path in the lower half plane, but in the opposite direction, returning to $(u^*_{(1)}, 0)$ as $z \to \infty$.

To prove that this is the case, consider Figure 2.4. Here, we have plotted the nullcline $v' = 0$. Note that $u' > 0$ in the upper half plane, and so all trajectories move monotonically to the right. Also, $v' > 0$ inside the nullcline, and $v' < 0$ outside the nullcline. (Due to symmetry, the nullcline will form a closed curve when combined with the lower half plane, and so when viewing Figure 2.4, "inside" means "under".) Since we are following the trajectory that leaves the critical point, it must originate inside the nullcline. In Figure 2.4, we display and label each possible path of this trajectory. We consider each of these paths in turn:

a) *The trajectory hits the axis to the left of the other critical point.* This cannot happen, because the nullcline intersects the right critical point, so for this to happen the trajectory would have to hit the axis inside the nullcline curve, which is impossible since $v' > 0$ in this region.

b) *The trajectory hits the other critical point.* Since the right critical point is a center, this cannot occur.

c) *The trajectory approaches a vertical asymptote.* The nullcline encloses a finite region where $v' > 0$, and so a trajectory cannot go up interminally. This path is also impossible.

d) *The trajectory approaches a horizontal asymptote.* This is not possible. As $u \to \delta$, $\frac{dv}{du} \to -\infty$, and so all trajectories turn down and hit the axis before they reach the vertical line $u = \delta$

e) *The trajectory hits the axis to the right of the right critical point, but before the line $u = \delta$.* This is the only remaining possibility, and the only logical outcome for the trajectory.

By means of this simple analysis, we have shown that a homoclinic orbit is present, enclosing the right critical point $(u^*_{(2)}, 0)$. The immediate impact of this is that it divides the phase plane into two regions. Inside the homoclinic orbit, all trajectories are periodic, circling the right critical point. Outside the orbit trajectories are non-periodic and approach $v = \pm\infty$. Trajectories outside the orbit are further divided by those that hit the u-axis to the right of the homoclinic orbit and those that hit the axis in between the left critical point and the v-axis.

Returning to the boundary value problem, recall the boundary conditions

$$u(1/2) = u(-1/2) = 1 \ .$$

To be a solution to the boundary value problem, a trajectory in the phase plane must start on the vertical line $u = 1$, and return to this line after a time of flight

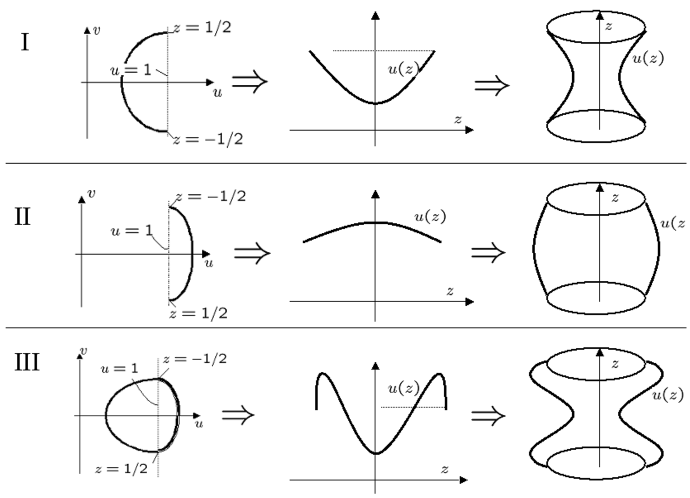

Figure 2.5: Depiction of solution trajectories in the phase plane and the resulting solution curves and membrane surfaces.

of 1. The trajectory may wrap around any number of times, which will dictate the shape of the solution. Figure 2.5 depicts some potential solution trajectories and the resultant membrane surfaces they define.

To begin, we consider solutions which are symmetric about the midplane $z = 0$. Under this symmetry assumption, we classify a solution as a trajectory that satisfies the following:

(1) it begins on the axis $v = 0$, and

(2) it ends on the line $u = 1$ after a time of flight of $1/2$.

An easy way to visualize solutions is to plot a meander for the boundary value problem. In this approach, we choose a starting point $u(0)$ with $v(0) = 0$, integrate the ODE from $z = 0$ to $z = 1/2$, and plot the resulting point $(u(1/2),\ v(1/2))$. In this manner, ranging through all starting points $u(0)$ inside the homoclinic orbit, we may plot a curve in the $(u(1/2),\ v(1/2))$ plane parameterized by $u(0)$. Every intersection with the line $u(1/2) = 1$ represents a solution to the boundary value

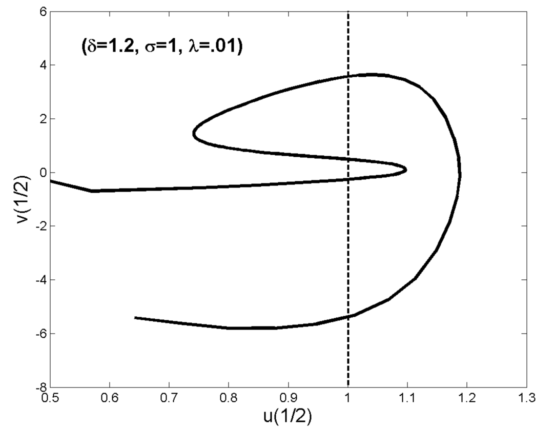

Figure 2.6: Meander plot in the $(u(1/2), v(1/2))$ plane.

problem. A sample meander plot is provided in Figure 2.6. To produce this, the integration was performed using ode23tb in Matlab. Alternatively, we may view the same curve in the $(u(0), u(1/2))$ plane, which enables us to see where on the phase plane a trajectory started. Here, a solution is found anywhere the curve crosses the horizontal line $u(1/2) = 1$. In Figure 2.7, this second view is plotted with the same parameter values as Figure 2.6. In each case, there are at least 4 solutions for the given parameters. However, the curves are not smooth toward the edges. For $u(0)$ close to zero and $u(0)$ close to δ, the ODE becomes unmanageably stiff due to large values of v' close to the singularities at zero and δ. Efforts to resolve the curve in these areas using alternative ode solvers in Matlab produced varying degrees of success, but a smooth curve for the full region could not be resolved.

Due to the difficulty in numerics, we now approach the problem by defining time of flight integrals for trajectories. This will enable us to resolve the "ends" of the meander curve and to further understand the general solution set. First, apply the Beltrami identity [77] to the energy functional Equation (2.13). The autonomous nature of the functional enables us to obtain the following first integral of Equation (2.14):

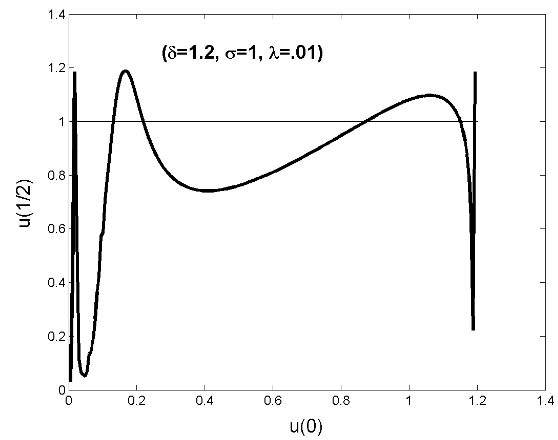

Figure 2.7: Alternative way to view the meander curve of Figure 2.6. Here we plot $u(1/2)$ versus $u(0)$. Intersections with the line $u(1/2) = 1$ represent solutions.

$$\frac{u}{\sqrt{1+\sigma^2 u'^2}} - \frac{\lambda}{\ln(\delta/u)} = E \; . \tag{2.17}$$

Here the constant E represents a conserved quantity in the system. Setting $z = 0$ and using $u'(0) = 0$, we find

$$E = u_0 - \frac{\lambda}{\ln(\delta/u_0)} \; , \tag{2.18}$$

where $u_0 = u(0)$. Solving Equation (2.17) for u', we have

$$u' = \frac{1}{\sigma}\left\{\left(\frac{u}{E + \frac{\lambda}{\ln(\delta/u)}}\right)^2 - 1\right\}^{1/2} \; . \tag{2.19}$$

Note that we have taken the positive square root. Due to the symmetry in the problem, this is an unimportant detail. Had we taken the negative, the following analysis would be identical except that the focus would be on the lower half of the phase plane.

Denote the right hand side of Equation (2.19) by $f(u; u_0)$. We may separate variables and obtain

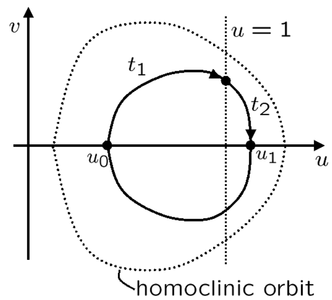

Figure 2.8: The values t_1 and t_2 for trajectories inside the homoclinic orbit.

$$z = \int_{u_0}^{u(z)} \frac{du}{f(u; u_0)} \ . \tag{2.20}$$

A solution must satisfy $u(1/2) = 1$, which would lead us to require

$$\int_{u_0}^{1} \frac{du}{f(u; u_0)} = 1/2 \ . \tag{2.21}$$

However, this is not sufficient, as we will not catch trajectories that "wrap around" in time of flight 1/2 before ending on the line $u = 1$, for in these cases the domain of the integrand is not well defined in the integral. See, for instance, Example III in Figure 2.5. Such a trajectory can only occur inside the homoclinic orbit, so for the time being we restrict our attention to this region.

We begin with trajectories for which $u_0 = u(0) < 1$. Consider Figure 2.8. In order to verify whether a trajectory inside the homoclinic orbit is a solution or not, all we need to know are the values t_1 and t_2, which represent the time it takes the trajectory to travel from the u-axis to the line $u = 1$ and the time it takes to go from this line back to the axis, respectively. In particular, if $t_1 = 1/2$, we have a simple monotonic solution (on the interval $[0, 1/2]$), as depicted in Example I of Figure 2.5, but this is certainly not the only possibility. If, for example, $t_1 + 2t_2 = 1/2$, this would solve the problem as well. In general, a solution will satisfy

$$\begin{gathered} (2k+1)t_1 + (2k)t_2 = 1/2 \\ \text{or} \\ (2k+1)t_1 + (2k+2)t_2 = 1/2, \quad k \in \mathbb{N}_0 \, . \end{gathered} \tag{2.22}$$

These combinations account for every possible way that a trajectory may begin on the line $v = 0$ with $u < 1$ and end on the line $u = 1$ after a time of flight of 1/2. The value of the non-negative integer k signifies the number of times the trajectory will circle around in the phase plane in time of flight 1/2, and thus the number of oscillations in the solution curve. The larger k is, the more oscillatory the solution. Hence, we will refer to k as describing the mode of the solution.

To find the values t_1 and t_2, we need the corresponding u value where the trajectory intersects the u-axis (see Figure 2.8). Denoting this by u_1, we see that u_1 must satisfy $f(u_1; u_0) = 0$, since $u' = f(u; u_0)$. This implies

$$u_1 = E + \frac{\lambda}{\ln(\delta/u_1)} \, ,$$

where E is defined by u_0. Referring to Equation (2.20), we find that

$$t_1(u_0) = \int_{u_0}^{1} \frac{du}{f(u; u_0)} \tag{2.23a}$$

$$t_2(u_0) = \int_{1}^{u_1} \frac{du}{f(u; u_0)} \, . \tag{2.23b}$$

Now consider trajectories that satisfy $u_0 = u(0) > 1$. These trajectories correspond to the same closed orbits just considered, but with starting point to the right of $u = 1$. In other words, we switch u_0 and u_1 in Figure 2.8. To find solutions of this type, we need merely interchange the roles of t_1 and t_2 in the above analysis. We keep the same values of u_0 and u_1, and determine t_1 and t_2 in the exact same way, but now the zero mode solution is $t_2 = 1/2$. In general, the solution criteria for these solutions is

$$\begin{gathered}(2k+1)t_2 + (2k)t_1 = 1/2 \\ \text{or} \\ (2k+1)t_2 + (2k+2)t_1 = 1/2, \quad k \in \mathbb{N}_0\ .\end{gathered} \tag{2.24}$$

These combinations account for every possible way that a trajectory may begin on the line $v = 0$ with $u > 1$ and end on the line $u = 1$ after a time of flight of $1/2$. Again, k may be viewed as representing the mode of the solution.

In principle, if we find the values t_1 and t_2 for all values of u_0, we may use the criteria of Equations (2.22) and (2.24) to determine the location and mode of all solutions as well as determine the total number of solutions for a given parameter set. However, the situation is complicated by the nature of the integrals for t_1 and t_2 given in Equations (2.23). The integrands are sufficiently complex to prevent direct integration. Further, we note that they are in fact improper integrals, as $f(u_0; u_0) = f(u_1; u_0) = 0$, and so the values of t_1 and t_2 are not always easily available numerically. Despite these difficulties, casting the problem in terms of the t_i will enable us to determine the structure of the solution set and to resolve the "ends" of the meander curve.

The main difficulties with the numerics in this problem occur towards the edges of the domain; i.e., when u is close to 0 or δ. For typical parameter values, the homoclinic orbit runs right through these regions. Consequently, the following difficulty arises. Due to proximity to the singularities, trajectories move tremendously quickly through these regions, so if u_0 is inside the homoclinic orbit but near the edge, then $t_1(u_0)$ and $t_2(u_0)$ can become very small. The trajectory that starts on

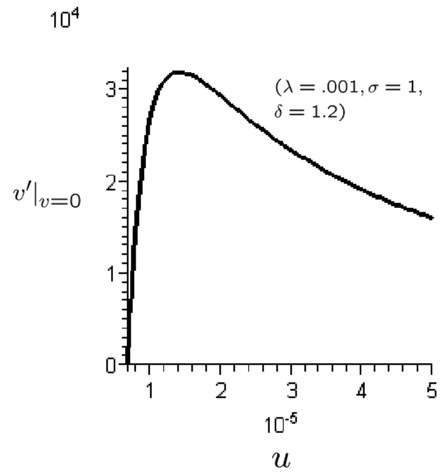

Figure 2.9: Plot of v' on the u-axis near the critical point $(u^*_{(1)}, 0)$ and edge of the homoclinic orbit.

the homoclinic orbit corresponds to the critical point $u^*_{(1)}$ where t_1 is infinite. So, as $u_0 \to u^*_{(1)}$, $t_1 \to \infty$. At the same time, the function $t_1(u_0)$ will take its minimum very close to $u^*_{(1)}$, since this will be the region where the trajectories move the fastest. This implies that there is a very rapid transition in the value of t_1 over an extremely small distance. To see this mathematically, we consider

$$h(u) := v'(z)\Big|_{v=0} = \frac{1}{\sigma^2 u} - \frac{\lambda}{\sigma^2 u^2 \ln^2(\delta/u)} \; . \tag{2.25}$$

In Figure 2.9, $h(u)$ is plotted for u very close to the critical point at $u^*_{(1)}$. Notice the scaling in Figure 2.9 – h increases on the order of 10^4 over a distance of 10^{-5} in the u direction. The u_0 value for which the curve is maximized yields the trajectory moving the "fastest" across the axis, yet is within $2 * 10^{-5}$ of the trajectory at $u^*_{(1)}$ that does not move at all.

In Figure 2.10, we return to the meander plot of Figure 2.6. Due to the behavior toward the edge of the homoclinic orbit just described, many solutions are potentially found in the "ends" of the meander which were not found numerically.

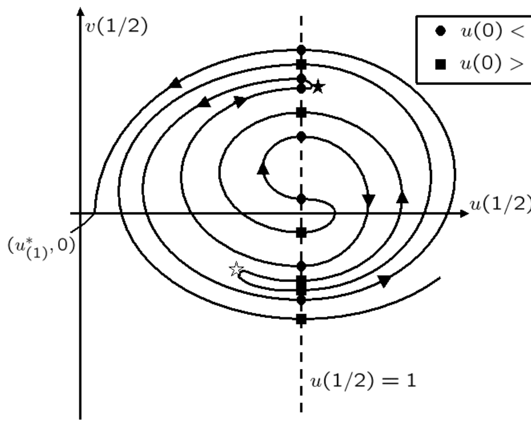

Figure 2.10: Cartoon depiction of the spiral meander inside the homoclinic orbit, with the scaling toward the edge of the homoclinic orbit blown up for clarity. Each intersection with the line $u(1/2) = 1$ represents a solution. The type of solution is indicated. The arrows indicate the direction of decreasing u_0.

Upon including these solutions, we find a rich spiral structure to the meander curve which was not seen earlier.

Figure 2.10 is a cartoon depiction of the spiral meander. To produce it, we have used the following facts:

- Inside the homoclinic orbit, u' and v' are continuously differentiable for all z, so the meander curve is continuous and non self-intersecting.

- The center of the spiral denotes the lowest mode solutions, and is easily resolved numerically.

The structure of this meander and the number of arms in the spiral is dependent upon the period of the different orbits. In terms of the functions t_1 and t_2, the period of the orbit starting at u_0 is

$$p(u_0) = 2(t_1(u_0) + t_2(u_0)) . \tag{2.26}$$

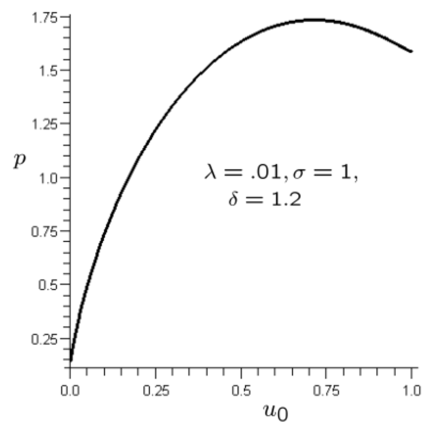

Figure 2.11: A sample plot of the period of the orbits as a function of the starting point u_0 on the u-axis

We must be careful with this definition. Depending on the location of the critical points, not all orbits will intersect the line $u = 1$, and the t_i are not defined for such trajectories. These regions are easily determined, however, so for the time being we only consider values of u_0 for which Equation (2.26) is valid.

In Figure 2.11, a sample plot of the function $p(u_0)$ is given for u_0 ranging from the left critical point $u^* \approx 0.00012$ to 1. Notice that the period is minimized to the left, which corresponds to the edge of the homoclinic orbit. The period actually approaches infinity as $u_0 \to u^*$, but this transition occurs over such a small range of u_0 that it is not visible in the graph. This transition can be understood in terms of the behavior of Equation (2.25) as seen in Figure 2.9.

Recall that the meander is produced by choosing a point $u_0 = u(0)$ on the u axis, following the trajectory forward for a time of flight of 1/2 and plotting the point where it ends. For a given trajectory, let N denote the number of times the trajectory intersects the line $u = 1$ in time of flight 1/2. In the center of the spiral, the period is maximized and N is minimized. Toward the edge of the homoclinic

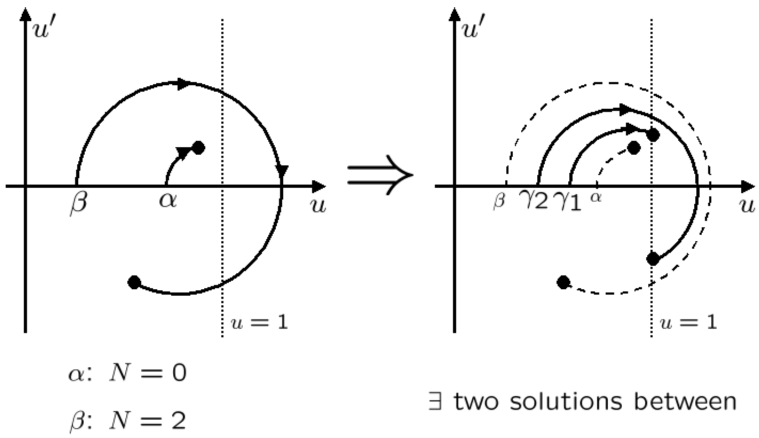

Figure 2.12: Illustration of how the structure of the meander depends on the values of N.

orbit, the fastest trajectories reside, so this is where the period is smallest and N is the largest. The difference in the periods of these two regions defines the structure of the spiral.

To see this, suppose that $N = N_1$ for a trajectory for which $u_0 = \alpha$, and $N = N_2 > N_1$ for a different trajectory for which $u_0 = \beta$, and that neither trajectory is a solution to the BVP. There must be a continuous transition as the parameter u_0 moves from α to β, meaning that there will be at least $N_2 - N_1$ trajectories between the trajectories at α and β which intersect the line $u = 1$ in time of flight $1/2$ and thus represent solutions to the BVP. Hence, as u_0 moves from α to β, the meander curve would wrap around and intersect the line $u(1/2) = 1$ a minimum of $N_2 - N_1$ times. This idea is illustrated in the simple case $N_1 = 0$, $N_2 = 2$ in Figure 2.12.

Once u_0 reaches the point for which the period is minimized and N is maximized, at N_{max} say, the meander curve will alternate from clockwise to counterclockwise, because at this point successive trajectories will not circle as far around in time of flight $1/2$. This point is denoted by a solid star in Figure 2.10. Then, as u_0 moves over the very small interval to the critical point $u^*_{(1)}$ where $N = 0$, a rapid transition must occur, with the meander curve quickly wrapping around to produce

N_{max} solutions before the curve intersects the axis at $(u^*_{(1)}, 0)$.

Similarly, as u_0 approaches the right side of the homoclinic orbit, the spiral wraps around until u_0 reaches the point where N is maximized (the hollow star in Figure 2.10), and then changes direction. Another way to consider this, however, is that the curve is in a sense "stuck" inside the spiral, and must turn around to work its way out. In this sense, we see the direct relationship between the number of solutions satisfying $u_0 < 1$ and those satisfying $u_0 > 1$.

It should be clear that much of this behavior is occurring over an extremely small range of u_0. Figure 2.10 is completely inaccurate as far as scaling is concerned, because the outer rings of the spiral are in fact so close to each other as to be indiscernible. These regions have been blown up in Figure 2.10 to clarify the nature of the curve and to allow for visualization of the general structure and behavior of the solution set.

2.3.1 Outside the homoclinic orbit

We now investigate the trajectories outside of the homoclinic orbit. As was mentioned, this region is comprised of non-periodic trajectories which approach $v = \pm\infty$, and so the only type of solution which can occur in this region is a "bulge" of the cylinder depicted in Example II of Figure 2.5. To find solutions in this region, we follow the same method as before. The difference is that since the trajectories are not periodic, there are no "wrap-around" possibilities. Further, the trajectories have vertical asymptotes, and so for a certain region, trajectories never reach the line $u = 1$. To see this, we first show that the trajectories are laterally bounded and must have a vertical asymptote in accordance with their monotonic behavior. This is seen easily by rewriting the identity in Equation (2.17) as

$$\frac{u}{\sqrt{1 + \sigma^2 u'^2}} = u_0 - \frac{\lambda}{\ln(\delta/u_0)} + \frac{\lambda}{\ln(\delta/u)} \, . \tag{2.27}$$

The left hand side of Equation (2.27) is strictly positive, so setting the right hand side greater than zero and solving for u, we find that

$$u > \delta \exp\left(\frac{-\lambda \ln(\delta/u_0)}{\lambda - u_0 \ln(\delta/u_0)}\right) . \tag{2.28}$$

Thus, each trajectory must stay to the right of a line that depends on the starting point u_0. This implies a vertical asymptote. If we can find the value of u_0 that has the line $u = 1$ as an asymptote, we will have found the edge of the region where potential solutions lie outside the homoclinic orbit. Let u_0^* denote this point. For the trajectory with initial conditions $u(0) = u_0^*$, $v(0) = 0$, it will hold that when $u \to 1$, the slope of the trajectory $\frac{dv}{du}$ should be infinite. From the phase plane equations, we may write

$$\frac{dv}{du} = \frac{v'}{u'} = \frac{1 + \sigma^2 v^2}{\sigma^2 u v} - \frac{\lambda(1 + \sigma^2 v^2)^{3/2}}{\sigma^2 u^2 v \ln(\delta/u)^2} . \tag{2.29}$$

In the Beltrami identity Equation (2.17), we set $u = 1$ and obtain the following relationship between the starting point u_0^* and the value of v at the line $u = 1$

$$1 + \sigma^2 v^2 = \frac{1}{H^2} , \tag{2.30}$$

where

$$H := u_0^* - \frac{\lambda}{\ln(\delta/u_0^*)} + \frac{\lambda}{\ln \delta} .$$

Setting $u = 1$ in Equation (2.29), and making use of Equation (2.30), we have after some manipulation

$$\left.\frac{dv}{du}\right|_{u=1} = \frac{H \ln^2 \delta - \lambda}{\sigma^2 v H^3 \ln^2 \delta} . \tag{2.31}$$

As we require this to be infinite, we must have $H = 0$, since $v = 0$ gives the undesired case of infinite slope on the u-axis. Hence the critical point u_0^* is the solution of

$$u_0^* = \frac{\lambda}{\ln(\delta/u_0^*)} - \frac{\lambda}{\ln\delta} \, . \tag{2.32}$$

Solving Equation (2.32) gives the starting point u_0^* whose trajectory asymptotically approaches the line $u = 1$. Any trajectory with starting point $u_0 > u_0^*$ will never reach the line $u = 1$, and so to find solutions outside of the homoclinic orbit, we need merely look at the function $t_2(u_0)$ where u_0 ranges from the right edge of the homoclinic orbit to the value u_0^*, such that if $t_2(u_0) = 1/2$, we have a solution. We return to this issue and explore the properties of t_2 in Section 2.5.1.

2.3.2 Non-symmetric formulation

Thus far, we have only considered solutions which are symmetric about the midplane $z = 0$. For these solutions, it was always the case that $u'(0) = 0$, and it was only necessary to consider half of the solution trajectories in the phase plane. In this section, we consider the problem more broadly and eliminate the requirement that solutions maintain this symmetry.

The main difference in terms of the phase plane is that we no longer take trajectories to start on the u-axis and follow them forward for a time of flight of 1/2. Now we take trajectories to start on the line $u = 1$, follow them forward for a time of flight of 1, and define a solution as any trajectory which ends on the line $u = 1$. An example is provided in Figure 2.13.

We may still define solutions in terms of the integrals $t_1(u_0)$ and $t_2(u_0)$, with the criteria for a solution as follows:

$$\begin{aligned} (2k)t_1 + (2k-2)t_2 &= 1 \\ (2k)t_1 + (2k)t_2 &= 1 \\ (2k-2)t_1 + (2k)t_2 &= 1, \quad k \in \mathbb{N} \, . \end{aligned} \tag{2.33}$$

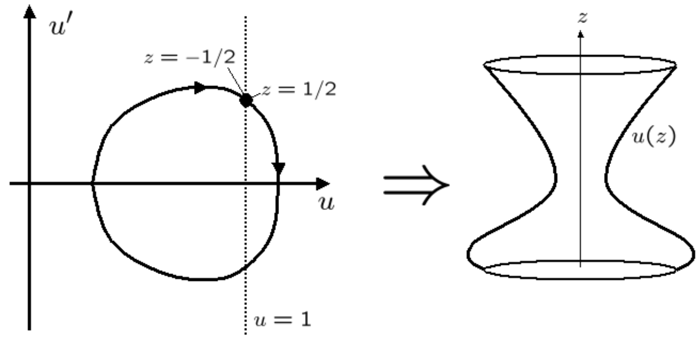

Figure 2.13: An example of a trajectory for a non-symmetric solution, and the corresponding membrane profile.

These combinations account for every possible way that a trajectory may start and end on the line $u = 1$. In considering these combinations and the potential for non-symmetric solutions, it is more convenient to consider the time of flight integrals not in terms of u_0, but in terms of the value of v at which the trajectory intersects the line $u = 1$. Refer to this as v_0. Numerically, we can visualize these solutions in a meander approach by marching along the line $u = 1$, following the trajectory forward for a time of flight of 1, and classifying solutions based on whether or not $u(1) = 1$.

Several things become apparent. First, we observe that a non-symmetric solution can only occur inside the homoclinic orbit, as such a solution would have to correspond to a periodic trajectory. Hence, in choosing different values of v_0, it is important to determine where the boundary of the homoclinic orbit is located. To do this, we use Equation (2.17) and the fact that the constant E is a conserved quantity along trajectories. Setting u equal to the left critical point $u^*_{(1)}$ determines $E = E^*$ along the homoclinic orbit. Solving for v and setting $u = 1$, we determine that the bounds for v_0 are given by

$$v = \pm\frac{1}{\sigma}\left\{\left(E^* + \frac{\lambda}{\ln\delta}\right)^{-2} - 1\right\}^{1/2} . \tag{2.34}$$

The next thing we observe is that non-symmetric solutions will always occur in pairs. In Equations (2.33), it is the second combination of the t_i which admits non-symmetric solutions – these correspond to trajectories which return to the same exact point in time of flight equal to 1. Hence a solution is found starting at the positive or negative value of v_0. For example, note that in Figure 2.13, starting at the negative intersection with $u = 1$ would have led to the same non-symmetric solution, just inverted vertically.

Finally, we observe that due to continuity, non-symmetric solutions will be found in between two symmetric solutions on the line $u = 1$. As v_0 gets closer to the edge of the homoclinic orbit, trajectories move faster (as was demonstrated earlier) and wrap farther around in time of flight one until the "fastest" trajectory is reached. Consider Figure 2.14. This cartoon depicts three trajectories which start in the bottom half plane on the line $u = 1$. The innermost trajectory reaches the line $u = 1$ in the top half plane in time of flight one. This is a symmetric solution. The outermost trajectory represents the next possible symmetric solution, in which the trajectory wraps around one and a half times before reaching $u = 1$ in the upper half plane. Due to continuity, there must be a non-symmetric solution between these two. Indeed, the middle trajectory wraps around exactly once in time of flight one, ending in the lower half plane. This solution is non-symmetric.

Figure 2.15 shows a meander plot, including non-symmetric solutions, inside the homoclinic orbit. Here, we have chosen starting points $u = 1$, $v = v_0$, integrated forward one, and plotted the resulting point in the $(u(1), v(1))$ plane. Solutions are represented by intersections with the line $u = 1$, and the curve is parameterized by v_0. As in the symmetric case, the curve becomes rough toward the edges of the homoclinic orbit. However, by the above observations, we can deduce that the

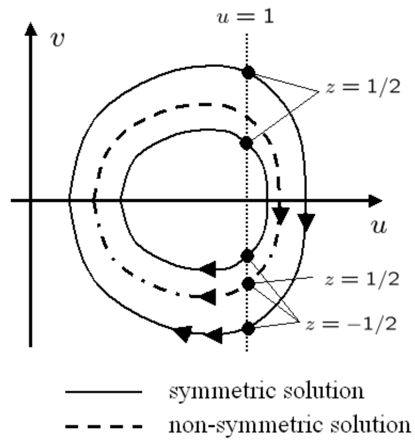

Figure 2.14: The structure of the phase plane, demonstrating that non-symmetric solutions are located in between symmetric solutions as we move along the line $u = 1$. The arrows indicate how many times the trajectories wrap around.

meander has the same spiral shape as in the symmetric case depicted in Figure 2.10. It is somewhat interesting that the structures would be the same when considering that the non-symmetric solutions were absent in the previous spiral meander.

2.3.3 Dependence of the solution set on parameters

In this section, we briefly consider how the solution set evolves as the parameters change. First, we consider the effect of λ. As $\lambda \to 0$, the critical points in the phase plane approach the singularities at 0 and δ. Hence, the trajectories at the edge of the homoclinic orbit move faster, the spiral meander gains more spirals, and there are more solutions. Increasing λ has just the opposite effect. By increasing λ enough, physically we expect that with enough voltage, all solutions should be lost. As was mentioned, when $\lambda \to 4\delta/e^2$, the two critical points bifurcate and the structure of the phase plane loses all complexity. Actually, the solution structure

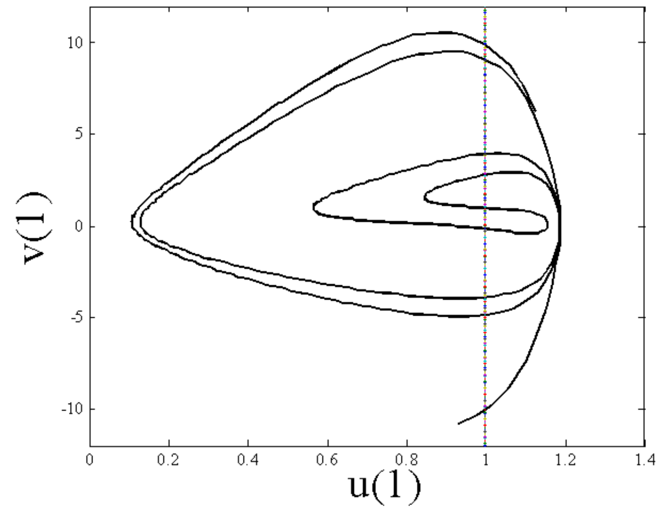

Figure 2.15: Meander plot inside the homoclinic orbit. Solutions are given by intersections with the line $u(1) = 1$.

becomes much simpler before λ reaches this value, because once the entire homoclinic orbit is to the left of the line $u = 1$, there can be no solutions inside this orbit.

We can find the exact voltage for which this will occur – we need merely find the voltage for which the right side of the homoclinic orbit hits the u-axis at $u = 1$. This can be expressed by the equation

$$f(1; u^*_{(1)}) = 0 \,, \tag{2.35}$$

where $f(u; u_0) = u'$ is defined by Equation (2.19) and $u^*_{(1)}$ is the left critical point. Since $u^*_{(1)}$ is a critical point, it satisfies $u^*_{(1)} \ln^2(\delta/u^*_{(1)}) = \lambda$, and so we may combine this with Equation (2.35) and solve for λ. We obtain as the critical voltage

$$\lambda = u^*_{(1)} \ln^2(\delta/u^*_{(1)}) \,, \tag{2.36}$$

where $u^*_{(1)}$ solves

$$u^*_{(1)} \ln^2(\delta/u^*_{(1)}) = \frac{(u^*_{(1)} - 1)\ln(\delta)\ln(\delta/u^*_{(1)})}{\ln(u^*_{(1)})} \; . \tag{2.37}$$

The effect of the parameter σ on the solution set can be seen by observing that the only influence of σ on the time of flight integrals is as a scalar multiplier. Thus, decreasing σ causes t_1 and t_2 to decrease, thereby gaining higher mode solutions at the cost of lower mode solutions. In other words, the solution criteria of Equations (2.22) and (2.24) will cease to be met for smaller integers k but will be be valid for higher integers. Just the opposite occurs when increasing σ.

We consider the effects and interplay of the parameters more rigorously in Section 2.5. First, we explore several particular solutions in the next section.

2.4 Special solutions

In this section, we investigate two special solutions, the catenoid that appears when there is zero voltage, and the cylindrical solution. We develop asymptotic schemes to explore perturbations from these solutions and to understand their dependence on the parameters.

2.4.1 Small voltage case

First, we examine the case of small voltage. Suppose there is zero voltage. Eliminating the electric field reduces the problem to that of a thin membrane bridging two parallel rings. Setting $\lambda = 0$ in Equation (2.14), $u(z)$ must have zero mean curvature; that is, the membrane should be a minimal surface. This problem has the well-known catenoid solution defined by

$$u(z) = \frac{\cosh(c_2 z)}{c_2 \sigma} \; , \tag{2.38}$$

where c_2 is a constant satisfying

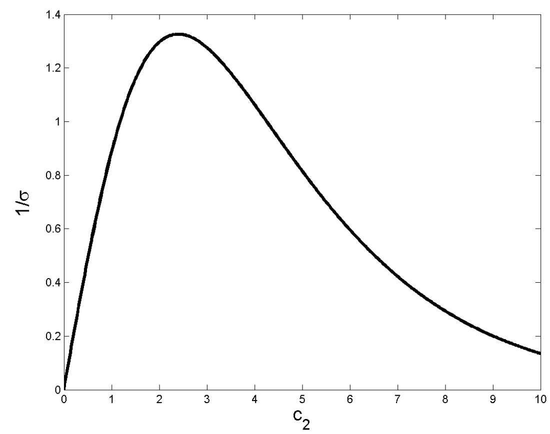

Figure 2.16: Plot of $1/\sigma = c_2/\cosh(c_2/2)$. Shows the c_2-σ pairs for which we have a catenoid solution

$$\sigma = \frac{\cosh(c_2/2)}{c_2} \,. \tag{2.39}$$

In Figure 2.16, we plot $1/\sigma$ as given by Equation (2.39). Observe that for certain values of $1/\sigma$, there are two possible values of c_2 and thus two catenoid solutions. The value on the left branch of the curve, corresponding to the smaller value of c_2, will be the stable catenoid solution while the other value corresponds to an unstable solution. There is a critical value of σ (or $1/\sigma$ when looking at Figure 2.16), beyond which there is no solution. The range for which a solution does exist is given approximately by $\sigma \geq .7545$. Denote this critical value $\sigma_{cr} \approx 0.7545$. The fact that the catenoid ceases to exist beyond this is tantamount to the observation that if you pull the two rings too far apart (i.e., increase the L in $\sigma = a/L$), you will reach a point where the membrane pinches off and disappears.

With the solutions of zero voltage in mind, we consider the case of small voltage, and look for perturbations from the catenoid solutions. To do this, we assume that $\lambda << 1$, and that $u(z)$ can be expanded as

$$u \sim u_0 + \lambda u_1 + \lambda^2 u_2 + \cdots \tag{2.40}$$

Before we proceed, recall that in deriving the energy functional, we used the small aspect ratio assumption

$$\epsilon^2 << 1, \quad \epsilon = \frac{b-a}{L} \tag{2.41}$$

in order to solve for the electric potential to leading order. In order for the current asymptotic analyis to be compatible with this, we must assume that $\epsilon^2 << \lambda$. In other words, in implicitly deriving the energy functional from a first order expansion in ϵ^2, we must clarify that the other parameters in the problem are bigger than ϵ^2. The parameter ϵ is related to σ and δ by

$$\epsilon = \sigma(\delta - 1) \Rightarrow \delta = 1 + \epsilon/\sigma \ . \tag{2.42}$$

Since $\sigma_{cr} \approx 0.7545$, we assume in general that $\sigma = O(1)$. Thus the comparison between ϵ and λ appears in the differential equation by comparing λ and δ. As we discuss in Section 2.4.2, the constant solution $u = 1$ solves the ODE for $\lambda = \ln^2 \delta$. In other words, when $\lambda = \ln^2 \delta$, the voltage is such that the membrane can deflect out to a cylindrical state. Our goal here is to capture perturbations from the catenoid, and so we need the voltage to be smaller than this cylindrical voltage. Thus, the current asymptotics are valid in the region

$$\epsilon^2 << \lambda < \ln^2 \delta = \ln^2(1 + \epsilon/\sigma) \ . \tag{2.43}$$

Under these assumptions, we now insert the expansion (2.40) into Equation (2.14) and collect like powers of λ. We obtain as a leading order solution the catenoid given by Equation (2.38), i.e.

$$u_0(z) = \frac{\cosh(c_2 z)}{c_2 \sigma} \ . \tag{2.44}$$

At $O(\lambda)$, we have

$$u_1'' - 2c_2 \tanh(c_2 z) u_1' + c_2^2 u_1 = \frac{-(1+\sigma^2 u_0^2)^{3/2}}{\sigma^2 u_0^2 \ln^2(\delta/u_0)} \tag{2.45}$$

along with boundary conditions

$$u_1(1/2) = u_1(-1/2) = 0 \; . \tag{2.46}$$

To analyze Equation (2.45), we consider the homogeneous problem. Upon making the substitution $y = \sinh(c_2 z)$ and letting $v(y) = u_1(z)$, Equation (2.45) (with zero right hand side) is transformed to

$$(1+y^2)v'' - yv' + v = 0 \; .$$

This equation is easily found to have solution

$$v(y) = Ay + B(\operatorname{arcsinh}(y)y - \sqrt{1+y^2})$$

or, undoing the substitution,

$$u_1(z) = A\sinh(c_2 z) + B(c_2 z \sinh(c_2 z) - \cosh(c_2 z)) \; , \tag{2.47}$$

where A and B are constants. Using the boundary conditions, we find that the homogeneous problem has a solution only if

$$\frac{c_2}{2} \sinh\left(\frac{c_2}{2}\right) - \cosh\left(\frac{c_2}{2}\right) = 0 \tag{2.48}$$

is satisfied. However, by considering the curve

$$\frac{1}{\sigma} = \frac{c_2}{\cosh(c_2/2)}$$

we observe that condition (2.48) is equivalent to the slope of the curve $1/\sigma$ equaling zero. In other words, the homogeneous problem only has a solution for the (c_2, σ)

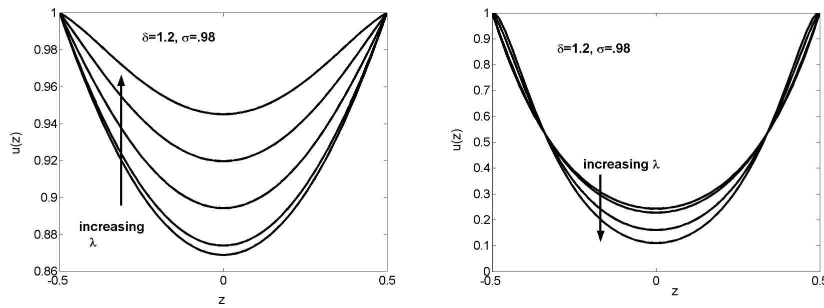

(a) (b)

Figure 2.17: Perturbations from the (a) stable and (b) unstable catenoids, and the effect of increasing λ.

pair at the critical value σ_{cr}. Thus, if $\sigma > \sigma_{cr}$, the non-homogeneous problem Equation (2.45) will have a solution $u_1(z)$. Actually, for such a σ, there are two solutions, as there are two valid c_2 values. We have a perturbation from the stable catenoid solution as well as a perturbation from the unstable catenoid. These solutions may by found using variation of parameters.

In Figure 2.17, we plot these solutions $u_0(z) + \lambda u_1(z)$ for the stable catenoid perturbation and unstable catenoid perturbation, respectively, for $\delta = 1.2$, $\sigma = 0.98$, and varying values of λ. The full membrane may be envisioned by rotating the curve about the z-axis. Observe the scaling in these plots – the stable catenoid perturbation is the shallower of the two curves.

For the stable catenoid perturbation, increasing λ causes the curve to move upward. Pysically, the membrane is deflecting outwards towards the outer cylinder as the voltage is increased. With the unstable catenoid perturbation, the opposite occurs, with the curve moving downwards as λ is increased. In problems of electrostatic deflection, it is typical that a stable solution deflects toward the source of the applied voltage while an unstable solution deflects in the opposite direction. See, for instance, [51].

If $\sigma = \sigma_{cr}$, the homogeneous problem will have a solution, which we denote u_1^h, and the criteria for there to be a solution to the $O(\lambda)$ problem is

$$\int_{-1/2}^{1/2} \frac{(1+\sigma^2 u_0'^2)^{3/2}}{u_0^2 \ln^2(\delta/u_0)} \cdot u_1^h \, dz = 0 \; . \tag{2.49}$$

However, it can be shown that u_1^h carries only one sign in the interval $[-1/2, 1/2]$, and so the integral cannot vanish. Thus, our asymptotic expansion fails when $\sigma = \sigma_{cr}$. To fix this, we need to modify our assumption on the ordering of the expansion. If we instead assume the expansion

$$u \sim u_0 + \lambda^{1/2} u_1 + \lambda u_2 + \cdots$$

we will arrive at the same first order solution, $u_0 = \cosh\left(c_2 z/(\sigma_{cr} c_2)\right)$. Here, there is only one value of c_2 and thus one u_0 solution, since $\sigma = \sigma_{cr}$. In this case, the $O(\lambda^{1/2})$ problem, i.e., the u_1 problem, is the same as the $O(\lambda)$ problem before, but now with zero right hand side. We define a new operator L as follows:

$$L[u] := u'' - 2c_2 \tanh(c_2 z) u' + c_2^2 u \; . \tag{2.50}$$

In terms of this operator, the $O(\lambda^{1/2})$ problem is

$$\begin{aligned} L[u_1] &= 0 \\ u_1(-1/2) = u_1(1/2) &= 0 \; . \end{aligned} \tag{2.51}$$

Since we are at the critical σ value, this problem has a solution, given by

$$u_1 = B \cdot \left(c_2 z \sinh(c_2 z) - \cosh(c_2 z)\right) \; .$$

The constant B is undetermined, as one boundary condition is automatically satisfied. To determine B, we go to $O(\lambda)$, which can be written

$$L[u_2] = -\frac{(1+\sigma^2 u_0'^2)^{3/2}}{\sigma^2 u_0^2 \ln^2(\delta/u_0)} + \frac{u_1'^2}{u_0} - \frac{u_1 u_1''}{u_0} \ . \tag{2.52}$$

Everything on the right hand side of Equation (2.52) is fixed except for the unknown constant B in u_1. Denote the right hand side as $G(B)$. The solvability condition for u_2 is

$$\int_{-1/2}^{1/2} G(B) u_2^h \, dz = 0 \ , \tag{2.53}$$

where u_2^h is the homogeneous solution to Equation (2.52). However, u_2^h will only differ by a constant factor from u_1, so we may replace Equation (2.53) with

$$\int_{-1/2}^{1/2} G(B) u_1 \, dz = 0 \ . \tag{2.54}$$

This gives us a condition for finding the value B that determines u_1. In fact, we may find this explicitly if we introduce the function

$$\hat{u} = c_2 z \sinh(c_2 z) - \cosh(c_2 z)$$

so that $u_1 = B\hat{u}$. Inserting this into Equation (2.54), we may solve to find

$$B^2 = \frac{\displaystyle\int_{-1/2}^{1/2} \frac{\hat{u}(1+\sigma_{cr}^2 u_0'^2)^{3/2}}{\sigma_{cr}^2 u_0^2 \ln^2(\delta/u_0)} \, dz}{\displaystyle\int_{-1/2}^{1/2} \frac{\hat{u}\hat{u}'^2 - \hat{u}^2 \hat{u}''}{u_0} \, dz} \ . \tag{2.55}$$

The right hand side of Equation (2.55) is completely determined for fixed δ, and is found to be positive. Accordingly, there are two possible values for B, and so two solutions at $\sigma = \sigma_{cr}$. This is not surprising. Recall that σ_{cr} defines the bifurcation length for the stable and unstable catenoids with zero voltage. By applying the electric field, we have added a force counter to the surface tension which is pulling the membrane in. We should expect that the membrane is able to be stabilized at lengths greater than occur without any applied voltage. In other words, with small voltage, we see that the bifurcation point will occur for a smaller value of σ, i.e., a greater length, than with no voltage.

When will the bifurcation occur? To answer this, we return to the expansion and again assume small voltage, but take $\sigma < \sigma_{cr}$, so that the length is greater than the critical zero voltage length. More precisely, we assume

$$\sigma^2 = \sigma_{cr}^2 - \gamma\lambda^\beta, \quad u \sim u_0 + \lambda^{1/2}u_1 + \lambda u_2 + \cdots \tag{2.56}$$

where $\gamma > 0$ and β are to be determined. We find once again that

$$u_0 = \frac{\cosh(c_2 z)}{\sigma_{cr} c_2}$$

is the zero voltage bifurcation catenoid. There are a couple of reasonable possibilities for the next order problem, depending on the value of β. If $\beta = 1/2$, the $O(\lambda^{1/2})$ problem may be written as

$$L[u_1] = \gamma \left(\frac{c_2^2}{\sigma_{cr}^2 u_0} \right) . \tag{2.57}$$

The requirement for u_1 to have a solution in this case is

$$\gamma \int_{-1/2}^{1/2} u_1^h \frac{c_2^2}{\sigma_{cr}^2 u_0}\, dz = 0 , \tag{2.58}$$

which can only be satisfied in the trivial case $\gamma = 0$, demonstrating that $\beta \neq 1/2$.

Instead, we try $\beta = 1$. In this case, we have $L[u_1] = 0$, implying as before that $u_1 = B\hat{u}$ where B is yet to be determined. At $O(\lambda)$, we find that

$$L[u_2] = -\frac{(1+\sigma_{cr}^2 u_0'^2)^{3/2}}{\sigma_{cr}^2 u_0^2 \ln^2(\delta/u_0)} - \frac{u_1 u_1''}{u_0} + \frac{u_1'^2}{u_0} - \gamma \left(\frac{u_0'^2 - u_0 u_0''}{\sigma_{cr}^2 u_0} \right) . \tag{2.59}$$

Noting that the right hand side of Equation (2.59) depends only on B and γ, we denote the right hand side by $G(B,\gamma)$. In this case, the orthogonality condition

$$\int_{-1/2}^{1/2} u_2^h G(B,\gamma)\, dz = 0 \tag{2.60}$$

gives us a relationship between B and γ, where again, u_2^h solves $L[u_2^h] = 0$. After some simplification, this relationship (2.60) may be expressed as

$$B^2 I_1 - I_2 = \gamma I_3 \ , \tag{2.61}$$

where the values $I_k,\ k = 1,2,3$ are explicitly defined by

$$I_1 = \int_{-1/2}^{1/2} \frac{\hat{u}\hat{u}'^2 - \hat{u}^2\hat{u}''}{u_0}\, dz \tag{2.62a}$$

$$I_2 = \int_{-1/2}^{1/2} \frac{\hat{u}(1+\sigma_{cr}^2 u_0'^2)^{3/2}}{\sigma_{cr}^2 u_0^2 \ln^2(\delta/u_0)}\, dz \tag{2.62b}$$

$$I_3 = \int_{-1/2}^{1/2} \frac{\hat{u}(u_0'^2 - u_0 u_0'')}{\sigma_{cr}^2 u_0}\, dz \ . \tag{2.62c}$$

Note that $I_1 \approx -10.248, \quad I_3 \approx 3.459$ are fixed values, while I_2 depends on δ, but will always be negative.

There are two ways to view Equation (2.61). Suppose that we have fixed the length of the device greater than the critical length of zero voltage, and have also fixed the voltage. Then we have fixed σ and λ, and so, recalling the relationship

$$\sigma^2 = \sigma_{cr}^2 - \gamma\lambda^\beta \ ,$$

we have a fixed value of γ (noting that $\beta = 1$). We may solve Equation (2.61) for B, again finding two possible solutions representing the perturbations from the stable and unstable catenoids.

However, this will only work if the term within the square root is positive when solving for B. Thus, the other way to view (2.61) is that it enables us to approximate the critical length at which the bifurcation between the two perturbed catenoids occurs. To be precise, suppose that $\lambda << 1$ and δ are fixed. From Equation (2.61) and in view of the signs of the integrals I_k in Equation (2.62), we must have

$$0 < \gamma \leq \frac{-I_2}{I_3} .$$

The bifurcation occurs when $\gamma = \frac{-I_2}{I_3}$, and so the critical value of σ is

$$\sigma^* = \left(\sigma_{cr}^2 + \frac{I_2 \lambda}{I_3}\right)^{1/2} . \tag{2.63}$$

For clarity, note that we use σ^* here to denote the critical length ratio when the voltage is on, whereas σ_{cr} is the well known critical length ratio of zero voltage.

2.4.2 Cylinder solution

In this section, we consider the constant solution $u = 1$. Observe from Equation (2.14) that this solution occurs for $\lambda = \ln^2 \delta$. Physically, this represents the membrane forming a cylindrical bridge. To investigate perturbations from the cylinder, let

$$\lambda = \ln^2 \delta + \nu, \quad u \sim 1 + \nu u_1 + \nu^2 u_2 + \ldots, \quad \nu << 1 \tag{2.64}$$

As before, we need to compare the size of ν with ϵ. Here, the requirement is simply that $\nu << \ln^2(1 + \epsilon/\sigma)$, which relates the fact that the perturbation should be smaller than the voltage we are perturbing from.

Inserting the expansion (2.64) into the ODE (2.14), we obtain the $O(\nu)$ problem

$$u_1'' + \mu^2 u_1 = -A$$
$$u_1(-1/2) = 0 \tag{2.65}$$
$$u_1(1/2) = 0\ ,$$

where

$$\mu^2 = \frac{2 - \ln\delta}{\sigma^2 \ln\delta}, \quad A = \frac{1}{\sigma^2 \ln^2\delta}\ .$$

Note that $\mu^2 > 0$ if $\delta < e^2$. In this case, the solution is found to be

$$u_1 = \frac{A}{\mu^2}\left(\frac{\cos(\mu z)}{\cos(\mu/2)} - 1\right)\ . \tag{2.66}$$

If $\delta = e^2$, we get parabolic solutions, and $\delta > e^2$ leads to hyperbolic solutions. However, based on our previous ordering arguments, $\delta < e^2$ is the physically relevant parameter range, and so we restrict our analysis to this set. Note that

$$0 < \mu < \pi \Rightarrow u_1(0) > 0$$
$$\pi < \mu < 3\pi \Rightarrow u_1(0) < 0 \tag{2.67}$$
$$3\pi < \mu < 5\pi \Rightarrow u_1(0) > 0,\ etc\ldots$$

Aside from determining the sign of $u(0)$, the value of μ can also be seen as defining the mode of solution, which is clear from the presence of the term $\cos(\mu z)$ in Equation (2.66). More importantly, note that the solution does not exist when $\mu = (2n+1)\pi$ for integers n. That is, the expansion fails for μ equal to any odd multiple of π. To fix this, we return to the expansion (2.64) under the assumption that $\mu = (2n+1)\pi$. We again take $\lambda = \ln^2\delta + \nu$, but now assume u to be of the form

$$u \sim 1 + \nu^{1/2} u_1 + \nu u_2 + \ldots , \quad 0 < \nu << 1$$

In this case, the $O(\nu^{1/2})$ problem that emerges can be written as

$$\begin{aligned} u_1'' + \mu^2 u_1 &= 0 \\ u_1(-1/2) = u_1(1/2) &= 0 \ , \end{aligned} \tag{2.68}$$

which has solution

$$u_1(z) = c_1 \cos(\mu z) + c_2 \sin(\mu z) \ . \tag{2.69}$$

The constant $c_2 = 0$ from the symmetry condition $u'(0) = 0$, and the boundary conditions are automatically satisfied by the assumption on μ. Thus,

$$u_1(z) = c_1 \cos(\mu z) \ , \tag{2.70}$$

where the constant c_1 is yet to be determined. To find the value of c_1, we go to the next order in the expansion. We obtain the following $O(\nu)$ problem

$$u_2'' + \mu^2 u_2 = -\frac{1}{\sigma^2 \ln^2 \delta} - \frac{3}{2} u_1'^2 + c_1^2 \mu^2 + \sigma^2 \mu^2 u_1'' u_1 + u_1^2 \left(\frac{1 - \ln \delta}{\sigma^2 \ln^2 \delta} \right) \ . \tag{2.71}$$

Noting that the right hand side of Equation (2.71) depends only on c_1, denote it by $G(c_1)$. The solvability condition for Equation (2.71) is

$$\int_{-1/2}^{1/2} u_2^h G(c_1) \, dz = 0 \ . \tag{2.72}$$

Since the homogeneous solution u_2^h only differs from u_1 by a constant, Equation (2.72) gives us a condition to find c_1. Plugging in $u_1(z) = c_1 \cos(\mu z)$, we may recast Equation (2.72) in the form

$$c_1^2 K_1 = K_2 \ , \tag{2.73}$$

where

$$K_1 = \int\limits_{-1/2}^{1/2} \left[\mu^2 \cos(\mu z) - \frac{3}{2}\mu^2 \sin^2(\mu z)\cos(\mu z) + \cos^3(\mu z)\left(\frac{3\ln\delta - \ln^2\delta - 3}{\sigma^2 \ln^2\delta}\right)\right] dz \tag{2.74a}$$

$$K_2 = \int\limits_{-1/2}^{1/2} \frac{\cos(\mu z)}{\sigma^2 \ln^2\delta} \, dz \ . \tag{2.74b}$$

These integrals may be solved to yield the simpler forms

$$K_1 = \begin{cases} \mu - \left(\dfrac{4}{3}\right) \dfrac{\ln^2\delta - 3\ln\delta + 3}{\sigma^2 \ln^2\delta\mu} & \text{if } n \text{ is even} \\ \\ -\mu + \left(\dfrac{4}{3}\right) \dfrac{\ln^2\delta - 3\ln\delta + 3}{\sigma^2 \ln^2\delta\mu} & \text{if } n \text{ is odd} \end{cases} \tag{2.75}$$

and

$$K_2 = \begin{cases} \dfrac{2}{\mu\sigma^2 \ln^2\delta} & \text{if } n \text{ is even} \\ \\ \dfrac{-2}{\mu\sigma^2 \ln^2\delta} & \text{if } n \text{ is odd .} \end{cases} \tag{2.76}$$

The signs of K_1 and K_2 are important, because in view of Equation (2.73), we will only have a solution if K_2/K_1 is positive. Clearly K_2 will be positive for n even, i.e., for the values $\mu = \pi, 5\pi, 9\pi, \ldots$, and will be negative for n odd, i.e., $\mu = 3\pi, 7\pi, \ldots$. To determine the sign of K_1, recall the relationship

$$\mu^2 = \frac{2 - \ln\delta}{\sigma^2 \ln\delta} \ .$$

Replacing the $1/\sigma^2$ term in K_1, and dealing only with the n even case for the moment, we may write

$$K_1 = \mu \left(1 - \left(\frac{4}{3} \right) \frac{\ln^2 \delta - 3 \ln \delta + 3}{2 \ln \delta - \ln^2 \delta} \right) . \tag{2.77}$$

We will show that K_1 takes only one sign in the interval $1 < \delta < e^2$. Setting $K_1 = 0$, we obtain

$$7 \ln^2 \delta - 18 \ln \delta + 12 = 0 . \tag{2.78}$$

It is easily verified that there are no real solutions to this quadratic in $\ln \delta$. Since K_1 is continuous for $\delta \in [1, e^2]$, it must be of only one sign. Further, $K_1(e) = -\mu/3 < 0$, and so $K_1 < 0$ for n even and $\delta \in [1, e^2]$. For n odd, K_1 is just the negative of the n even case, and so $K_1 > 0$ for n odd and $\delta \in [1, e^2]$.

Therefore, in view of Equation (2.73), our expansion has failed again in both the n even and n odd case. The reason is as follows: in the expansion, we assumed $\lambda = \ln^2 \delta + \nu$. In other words, under the assumption that $\nu > 0$, we took the voltage to be slightly greater than the cylinder voltage. If we instead take $\lambda = \ln^2 \delta - \nu$ in the expansion – that is, if we take the voltage slightly less than the critical voltage – we find that there is a solution. In this case, everything works out the same as in the above analysis, except that the sign of K_2 will change. Thus, $c_1 = \pm\sqrt{K_2/K_1}$ may be found to yield two symmetric solutions,

$$\begin{aligned} u^{(1)}(z) &= 1 + \nu^{1/2} \left(\frac{K_2}{K_1} \right)^{1/2} \cos(\mu z) + O(\nu) \\ u^{(2)}(z) &= 1 - \nu^{1/2} \left(\frac{K_2}{K_1} \right)^{1/2} \cos(\mu z) + O(\nu) . \end{aligned} \tag{2.79}$$

Increasing $\lambda \to \ln^2 \delta$ causes these two solutions to bifurcate, and so taking any $\lambda > \ln^2 \delta$ yields no solution.

2.5 Stability and special solutions in the general solution set

In this section, we examine the stability of the different solutions, and place the special solutions of Section 2.4 in the framework of the general solution set. The requirement for stability is that the second variation of the functional $\mathcal{E}[u]$ be greater than zero. Hence we define a solution as being stable if it is locally minimizes the energy. Physically, the surface will meet this criteria if it is stable subject to axially symmetric mechanical perturbations. As outlined in [23], the requirement that the second variation be greater than zero may be expressed in terms of conjugate points for a second order differential equation. In particular, we look at the solution $h(z)$ of the initial value problem

$$\begin{aligned} -\frac{d}{dz}(Ph') + Qh = 0 \\ h(-1/2) = 0 \\ h'(-1/2) = 1 \ , \end{aligned} \tag{2.80}$$

where

$$\begin{aligned} P =& \frac{\sigma^2 u}{2(1+\sigma^2 u'^2)^{3/2}} \\ Q =& \frac{1}{2}\left(\frac{\lambda(\ln(\delta/u)-2)}{u^2\ln^3(\delta/u)} - \frac{\sigma^2 u''}{(1+\sigma^2 u'^2)^{3/2}}\right) \ . \end{aligned} \tag{2.81}$$

If there are no points $c \in (-1/2, 1/2]$ such that $h(c) = 0$, then the functional $\mathcal{E}[u]$ given by Equation (2.13) has a weak minimum at the function $u(z)$. If such a c does exist, it is referred to as a conjugate point. Note that this approach is only valid if $P > 0$; however, this will be true for any solution since all solutions satisfy $u > 0$.

In general, the functions P and Q given in Equation (2.81) are too complicated to allow for an analytic solution of Equation (2.80). However, for the cylinder solution $u = 1$, these equations are greatly simplified, and an analysis is readily available. Indeed, in this case, Equation (2.80) becomes

$$
\begin{aligned}
h'' + \mu^2 h &= 0 \\
h(-1/2) &= 0 \\
h'(-1/2) &= 1 \ ,
\end{aligned}
\tag{2.82}
$$

where

$$
\mu^2 = \frac{2 - \ln\delta}{\sigma^2 \ln\delta} \tag{2.83}
$$

is the same parameter as in Section 2.4.2. Solving the system (2.82), it is easily seen that there are no conjugate points only if $\mu < \pi$. This means that the cylinder solution is stable only in the range $\mu < \pi$.

One impact of this result is that it enables us to use the electric field as a stabilizer for the cylindrical solution. Adding the electric field enables us to achieve stable cylindrical bridges at greater lengths by manipulating the relationship given by Equation (2.83).

Recall that $\sigma = a/L$, the ratio of the radius of the surface to length. Increasing the length is equivalent to decreasing σ, which in turn causes μ to increase. If we only increase the length, the cylinder solution will lose stability once $\mu > \pi$. If, however, we counter the increase in length by also increasing δ, we may keep $\mu < \pi$. In fact, by taking δ closer and closer to e^2, we can theoretically achieve any length, because by setting $\mu < \pi$ in Equation (2.83) and solving for δ, we find that the cylinder solution will be stable if

$$
\delta > \exp\left(\frac{2}{\sigma^2\pi^2 + 1}\right) . \tag{2.84}
$$

Hence for any fixed length, i.e., fixed σ, we can find a value of δ less than e^2 such that $\mu < \pi$ and the cylindrical bridge is stable. In the absence of an electric field, a cylindrical soap-film bridge is unattainable, and so a direct comparison is not available for this result. However, it is informative to note the stability criteria for cylindrical *liquid* bridges in the absence of an electric field, which differ from our analysis only by the addition of a volume constraint. It has long been known that cylindrical liquid bridges are stable only in the range where the ratio of the length to the diameter is less than π. This was first established theoretically and experimentally by Plateau [54], and was then considered in a different context by Lord Rayleigh a few years later with the same result [60]. According to Equation (2.84), the addition of an electric field enables for longer stable cylindrical bridges, and potentially much longer bridges with the proper balancing of parameters. It is important to note, however, that this result is potentially misleading. By increasing δ, we increase $\epsilon = \sigma(\delta - 1)$, and potentially violate the small aspect ratio needed to solve for the electric potential.

To further explore the cylinder solution and the importance of the parameter μ, we return to the phase plane and place the cylinder solution and its perturbation in the context of the spiral meander. The cylinder solution occurs when $\lambda = \lambda_{cyl} = \ln^2 \delta$. When λ is close to but less than this value, there are two solutions that are "close" to being cylindrical. As $\lambda \to \lambda_{cyl}$, one (or both) of these solutions becomes the cylinder solution, and for some critical value $\lambda^* > \lambda_{cyl}$, the solutions bifurcate.

An example of this bifurcation is given in Figure 2.18 (a), where the evolution of the spiral meander is shown as λ is increased from below λ_{cyl} to the bifurcation value. As for the spiral meander of Figure 2.10, this bifurcation takes place in the center of the spiral where the curve is manageable numerically, and so the rest of the spiral is neither visible nor of importance here. The bifurcation diagram for these two solutions is presented in Figure 2.18 (b), where the value $u(0)$ is plotted against λ and a fold bifurcation is evident.

Keep in mind what is happening in the phase plane. When $\lambda < \lambda_{cyl}$, the critical point $(u^*_{(2)}, 0)$ is to the right of the line $u = 1$ and one solution trajectory

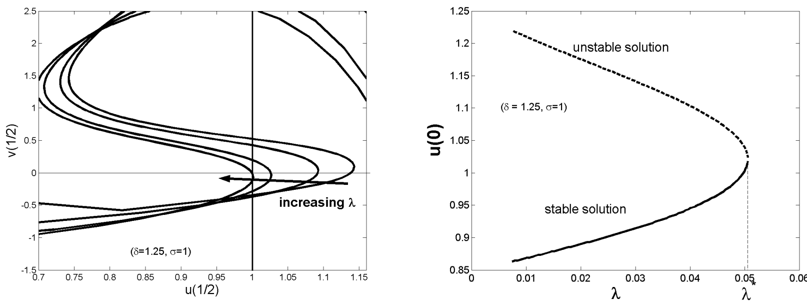

(a) (b)

Figure 2.18: (a) - The effect of increasing λ in the meander plot. (b) - Bifurcation diagram corresponding to solutions of (a). The stable branch corresponds to the solution u^L and the unstable branch corresponds to u^R. The bifurcation point λ^* appears as the value at which the fold occurs.

starts on each side of the critical point $(u^*_{(2)}, 0)$. Hence one solution satisfies $u(0) < 1$, and one satisfies $u(0) > 1$. In terms of the phase plane, the former sits to the left of the line $u = 1$ and the latter sits to the right of $u = 1$. Hence we refer to the former as u^L and the latter as u^R. When $\lambda = \lambda_{cyl}$, the critical point is on the line $u = 1$, and so the critical point itself represents a solution; namely, the cylindrical solution. One of the solutions u^L or u^R has become this solution. As we continue to increase λ, the critical point continues to move left, and the two solutions bifurcate. To put it in terms of a simple analogy, as $\lambda \to \lambda_{cyl}$, there is a "race" to the critical point between u^L and u^R where the "winner" becomes the cylinder solution. Then, taking $\lambda \to \lambda^* \geq \lambda_{cyl}$, u^L and u^R meet up on the "loser's" side of $u = 1$ and vanish in a fold bifurcation.

The details of this bifurcation, i.e., whether u^L or u^R "wins", and where the perturbation from the cylinder fits in, depends entirely on the value of μ. Upon inspection of Equation (2.66), if $\mu < \pi$ and $\lambda < \lambda_{cyl}$ so that $\nu < 0$ in the expansion

$$\lambda = \lambda_{cyl} + \nu; \quad u \sim 1 + \nu u_1 + \cdots$$

then $u(0) < 1$ because $u_1(0) > 0$. In this case, u^L represents the perturbation from the cylinder. Likewise, if $\pi < \mu < 3\pi$ and $\lambda < \lambda_{cyl}$, the cylinder perturbation will satisfy $u(0) > 1$, and so in this case u^R is the perturbation from the cylinder.

We have already seen that the cylinder solution is stable if $\mu < \pi$. To examine stability of all other solutions, we solve the initial value problem of Equation (2.80) numerically, plot the solution $h(z)$ over the interval $[-1/2, 1/2]$, and inspect for conjugate points. We find that regardless of the value of μ, u^L is always a stable solution and u^R always unstable. This implies that the perturbation from the cylinder satisfies the same stability criteria as the cylinder: it is stable if $\mu < \pi$ and unstable if $\mu > \pi$.

Increasing λ to λ_{cyl} is equivalent to taking $\nu \to 0$ in the expansion, which will of course cause the perturbation from the cylinder to become the cylinder, and so between u^L and u^R, the "winner" of the race to the critical point is the solution which represents the perturbation from the cylinder.

The value of this analysis is that it enables us to determine where the bifurcation will occur and thus the general shape of the membrane when stability is lost. When $\mu < \pi$, u^L gets to the critical point first, and so will meet up with u^R on the right side of $u = 1$. Since u^L continues to be the stable solution for $\lambda > \lambda_{cyl}$, the conclusion is that when $\mu < \pi$, a stable "bulge" of the cylinder is achievable.

On the other hand, when $\mu > \pi$, u^R gets to the critical point first and the bifurcation occurs on the left side of $u = 1$, and so in this case a stable "bulge" of the cylinder is not achievable. This is logical, because the cylinder itself is not stable for $\mu > \pi$, and the energy is greater in a "bulge" of the cylinder.

If $\mu = \pi$, we found in the previous section that there are two symmetric solutions for $\lambda < \lambda_{cyl}$, but no solution when $\lambda > \lambda_{cyl}$. In this case, u^L and u^R each

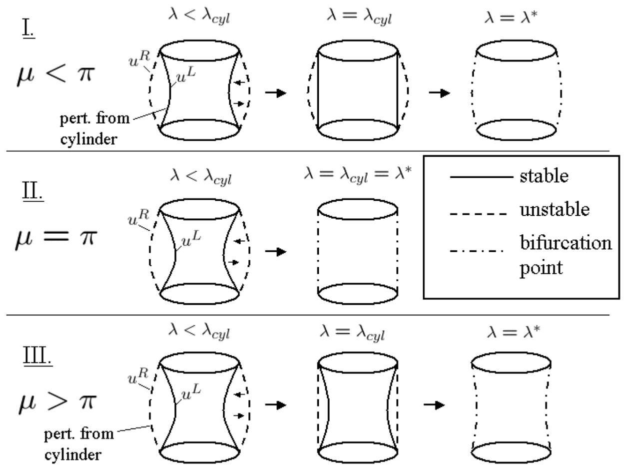

Figure 2.19: Stability of cylinder solution and dependence on the parameter μ.

represent perturbations from the cylinder, and in the racing analogy, there is a tie – that is, in the special case of the stability boundary $\mu = \pi$, the solutions both hit the critical point right when $\lambda = \lambda_{cyl}$, and there is no solution for $\lambda > \lambda_{cyl}$ because the bifurcation occurs right at λ_{cyl}.

To visualize this, consider Figure 2.19. Here, we depict a profile of the membrane (outer cylinder excluded) for 3 different cases: μ less than, equal to, and greater than π, respectively. In each case, we begin with $\lambda < \lambda_{cyl}$, increase λ to λ_{cyl}, and increase again until the bifurcation point. In all cases, the inner solution, what we have referred to as u^L, is the stable solution and moves outward, while the outer solution, u^R, is unstable and moves inward.

To consider the situation in a slightly different context and to provide some physical insight, consider the following. Suppose we have a fixed outer cylinder (i.e. fixed δ), and have fixed the voltage at the cylinder voltage (i.e., $\lambda = \ln^2 \delta$). What happens as we increase the length of the device? Increasing the length decreases $\sigma = \frac{a}{L}$, and thus increases μ. If we do this so that μ begins less than π and increases beyond π, then this situation is illustrated by following the sequence of pictures in Figure 2.19 for $\lambda = \lambda_{cyl}$ (i.e., follow the second column of pictures down). Notice that the cylinder begins as the stable solution when $\mu < \pi$, but as we increase the length, we hit a bifurcation point, $\mu = \pi$, where the outer solution crosses over to be inside the cylinder, and exchanges stability with the cylinder. In this context, then, as σ is decreased, a transcritical bifurcation occurs at the point when $\mu = \pi$. Physically, we have found that the cylindrical bridge will remain while changing the length without altering the voltage so long as the length is short enough so that $\mu < \pi$. Once the critical $\mu = \pi$ length is reached, the cylinder is no longer stable and the membrane pinches in.

We now turn our attention to the perturbations from the catenoid. Recall that with zero voltage, there are two possible catenoid solutions – a stable and an unstable solution. As we showed in Section 2.4.1, with small voltage, we have a perturbation from each of these catenoids. It is easily verified by a numerical solution of the ODE (2.80) that the perturbation of the stable catenoid is a stable solution, while the perturbation of the unstable catenoid is unstable. To see where these solutions fit into the general solution set, consider Figure 2.20. In this, we return to the full spiral meander described earlier, and mark the special solutions of the perturbations from the catenoid and the cylinder. For the cylinder perturbations, we indicate the solutions u^L and u^R described above.

As was just discussed, either u^L, u^R, or both can represent the perturbation from the cylinder, but u^L is always the stable solution. This same solution also represents the perturbation from the stable catenoid. There is a transition as the parameter λ is increased. For $\lambda << 1$, this solution will be given by the perturbation of the stable catenoid. As λ gets close to the cylinder voltage, though, the small voltage asymptotic analysis loses validity, and this solution transitions to the u^L cylinder solution.

In terms of this spiral meander, decreasing σ causes the center part of the meander between the two catenoid perturbations to move to the right, causing

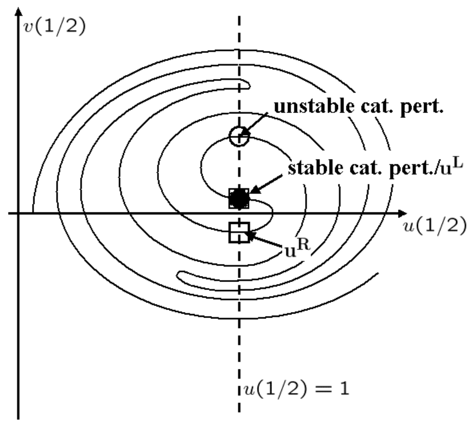

Figure 2.20: Special solutions in the spiral meander.

these two solutions to bifurcate. This bifurcation is seen numerically in Figures 2.22(a) and 2.22(b). In Figure 2.22(a), the evolution of this part of the meander curve is displayed. In Figure 2.22(b), the fold bifurcation is shown by plotting $u(0)$ versus σ for these two solutions. In this example, the bifurcation occurs for $\sigma \approx 0.725$. According to the analysis of Section 2.4.1 and in view of Equation (2.63), the bifurcation for the given parameter values should occur for $\sigma \approx 0.722$. Thus, we find good agreement between the analytical and numerical values for the critical σ for this example. Figure 2.21 provides a more thorough comparison of the analytical and numerical σ^*. As would be expected, the analytical approximation is in close agreement with the full numerical value for small λ, and loses validity as λ is increased.

2.5.1 Critical length vs. critical voltage

We have seen that for fixed λ and δ there is a critical value, σ^*, at which instability sets in, while for fixed σ and δ instability sets in at a critical value λ^*. In this section, we explore this issue in greater detail. In each case, the same stable solution, which we have denoted u^L, disappears, but the method of instability is quite different. Physically, σ^* represents reaching a critical length. When this length is

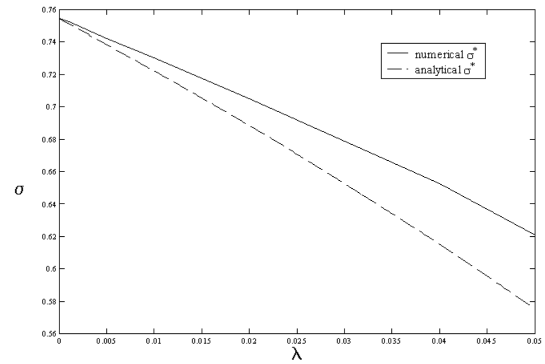

Figure 2.21: Comparison of the analytically and numerically obtained values of σ^* as a function of λ. Here, $\delta = 1.2$.

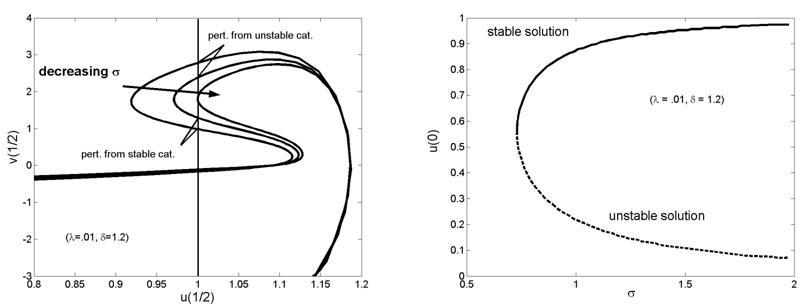

(a) (b)

Figure 2.22: (a) - The effect of decreasing σ in the meander plot. (b) - Bifurcation diagram corresponding to solutions of (a).

reached, the membrane "pinches off" in the middle and forms two separated surfaces. On the other hand, λ^* denotes the well-known "pull-in" voltage of MEMS/NEMS [51]. When this critical value is reached, the electrostatic force dominates the elastic force in the system and the membrane collides with the electrode. In this problem, we expect the instability that occurs at λ^* to be such that the membrane deflects outward until it hits the outer cylinder. Hence, the dynamics that occur at the onset of instability are very different in the case of σ^* versus λ^*. While we do not presently consider dynamics, we will explore the location of these critical values and the relationship between them.

When $\lambda = 0$, $\sigma* = \sigma_{cr} \approx 0.7544$ is the critical length for a catenoid in the absence of a field. In Section 2.4.1, we obtained an asymptotic approximation for σ^* when $\lambda << 1$,

$$\sigma^* = \left(\sigma_{cr}^2 + \frac{I_2 \lambda}{I_3}\right)^{1/2} , \tag{2.85}$$

where

$$I_2(\delta) < 0, \quad I_3 \approx 3.495 \ .$$

Hence, for $\lambda << 1$, $\sigma^* \sim \lambda^{1/2}$. A natural question is: How far can we take this stabilization effect? In other words, what is the greatest length (smallest σ) at which we can have a stable bridge? Before we answer this, it will be informative to consider λ^*.

Suppose that δ is fixed. We wish to determine the behavior of λ^* as a function of σ. We have already seen that in the case of the cylindrical solution, the bifurcation between the two solutions denoted u^L and u^R occurs at $\lambda = \lambda_{cyl} = \ln^2 \delta$ when $\mu = \pi$. Hence in the special case $\mu = \pi$, we have that $\lambda^* = \ln^2 \delta$. Recall that $\mu^2 = (2 - \ln \delta)/(\sigma^2 \ln \delta)$. If we define $\hat{\sigma}$ by

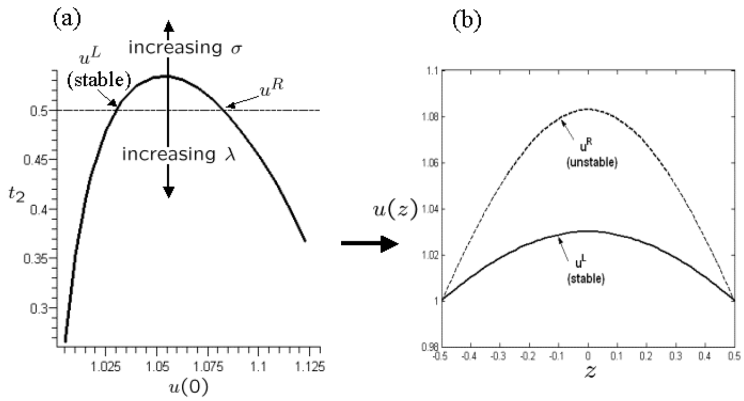

Figure 2.23: (a) - Plot of $t_2(u_0)$ for $\sigma = 2$, $\lambda = 0.05$ and $\delta = 1.2$. (b) - The resulting solution curves u^L and u^R.

$$\hat{\sigma}^2 = \frac{2 - \ln\delta}{\pi^2 \ln\delta} \ , \tag{2.86}$$

then in the $\sigma - \lambda$ plane, we know that λ^* will cross the point $\sigma = \hat{\sigma}$, $\lambda = \ln^2\delta$. This point is the minimum value of λ^*, for as we have seen, in either case $\mu < \pi$ or $\mu > \pi$, the bifurcation between u^L and u^R occurs for $\lambda > \lambda_{cyl}$. To determine the behavior of λ^*, we consider separately the cases $\sigma > \hat{\sigma}$ and $\sigma < \hat{\sigma}$, or, equivalently, the cases $\mu < \pi$ and $\mu > \pi$ respectively.

First, we consider the behavior of λ^* as σ gets large. For $\sigma > \hat{\sigma}$, $\mu < \pi$, and the bifurcation between u^L and u^R occurs to the right of the line $u = 1$. In other words, a stable bulge of the cylinder is seen. To understand the details of the bifurcation, we return to the phase plane and consider the time of flight from the u-axis to the line $u = 1$. Following the notation of Figure 2.8, we denote this by $t_2(u_0)$, $u_0 = u(0)$ where $u(0) > 1$. Recall that trajectories outside the homoclinic orbit approach vertical asymptotes and that solutions will only be found in the region $u_0 < u_0^*$, where u_0^*, given as the solution of Equation (2.32), is the trajectory bounded by $u = 1$.

A sample curve for t_2 is given in Figure 2.23(a), where we observe the two solutions u^L and u^R as the points where $t_2 = 1/2$. The corresponding solutions are then plotted in Figure 2.23(b). We may write

$$t_2(u_0) = \sigma \int_1^{u_0} \frac{du}{\sqrt{\frac{u^2}{(u_0+\lambda\Gamma)^2} - 1}}, \quad \Gamma := \frac{1}{\ln(\delta/u)} - \frac{1}{\ln(\delta/u_0)} \ . \tag{2.87}$$

Clearly, $\frac{\partial t_2}{\partial \sigma} > 0$. Also,

$$\frac{\partial t_2}{\partial \lambda} = \sigma \int_1^{u_0} \left(\frac{u^2}{(u_0 + \lambda\Gamma)^2} - 1 \right)^{-3/2} \frac{u^2 \Gamma}{(u_0 + \lambda\Gamma)^3} \, du \ . \tag{2.88}$$

Theorem 1 *If $u_0 \in (1, u_0^*)$, where u_0^* denotes the trajectory which asymptotically approaches the line $u = 1$, then $\frac{\partial t_2}{\partial \lambda} < 0$.*

Proof: First, note that from the analysis of Section 2.3.1, u_0^* satisfies

$$u_0^* = \frac{\lambda}{\ln(\delta/u_0^*)} - \frac{\lambda}{\ln \delta} \ . \tag{2.89}$$

Thus,

$$1 < u < u_0 \Rightarrow \ln(\delta/u) > \ln(\delta/u_0) > 0 \Rightarrow \Gamma < 0 \ . \tag{2.90}$$

Let $h(u) = u_0 + \lambda\Gamma$. We will show that $h(u) > 0$ for $1 < u < u_0 < u_0^*$. Since $\Gamma = 0$ when $u = u_0$, it follows that $h(u_0) = u_0 > 0$. Also,

$$h'(u) = \frac{\lambda}{u \ln^2(\delta/u)} \ ,$$

which cannot equal zero in the region $u \in (1, u_0)$. Thus, if we can show that $h(1) > 0$ $\forall \lambda$ and $\forall u_0 \in (1, u_0^*)$, it will follow that $h(u) > 0$. To this end, let

$$g(u_0) = h(1) = u_0 - \frac{\lambda}{\ln(\delta/u_0)} + \frac{\lambda}{\ln \delta} \ .$$

$g(1) = u_0$ and $g(u_0^*) = 0$ by the definition of u_0^*. Also, $g'(u_0) = 0$ if $u_0 \ln^2(\delta/u_0) = \lambda$, which only occurs at the critical points in the phase plane. Further, $g'(1)$ is positive if $\lambda < \ln^2 \delta$ and negative if $\lambda = \ln^2 \delta$.

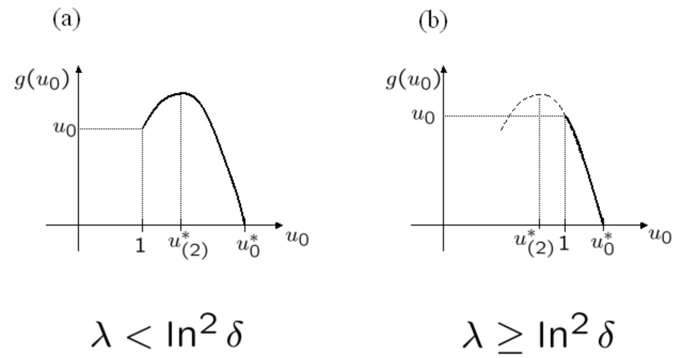

Figure 2.24: The shape of $g(u_0)$. Illustration to aid in the proof that $\frac{\partial t_2}{\partial \lambda} < 0$.

- If $\lambda < \ln^2 \delta$, then the right critical point $u^*_{(2)} \in (1, u^*_0)$. Here $g'(1) > 0$, and $g(u_0)$ must have the shape as indicated in Figure 2.24 (a).

- If $\lambda \geq \ln^2 \delta$, $g'(1) \leq 0$. However, $u^*_{(2)} \leq 1$, so g' cannot equal zero in the region $u_0 \in (1, u^*_0)$. Hence, $g(u_0)$ will have the shape indicated in Figure 2.24 (b).

In either case, $g(u_0) > 0$ for $u_0 \in (1, u^*_0)$, which implies that $h(u) > 0$. We have shown that $\Gamma < 0$ and $u_0 + \lambda\Gamma > 0$ in the region of integration in Equation (2.88), thus implying a negative integrand. The Theorem is proven. □

We see then that an increase in λ causes the two solutions to bifurcate as expected, while increasing σ causes the opposite to occur: t_2 increases, so that the curve moves upward. Again, there is a balancing effect between length and voltage. The shorter the bridge, the more voltage may be applied while keeping a stable solution. Increasing σ will not cause a critical value to be reached, and so there is no limit to the effect. For any value of λ, we may find a value of σ for which the peak of t_2 is above the line $t_2 = 1/2$. Hence, as $\sigma \to \infty$, $\lambda^* \to \infty$. This result is somewhat interesting in the context of the phase plane. As λ is increased, a value is reached independently of σ at which the homoclinic orbit is entirely to the left of the line $u = 1$ (see Equations (2.36) – (2.37)), at which point no solutions can be found inside the homoclinic orbit. However, the stable solution u^L simply crosses over the homoclinic orbit and remains. Further, as was noted in Section 2.3, for $\lambda > 4\delta/e^2$, there are no critical points in the system, the spiral structure of the meander is completely lost, and yet still a stable solution to the problem persists. One way to think of this physically is that as $\sigma \to \infty$, the surface area of the membrane becomes infinitesimally small, and so there is nothing for the electric field to "pull" on, and thus infinite voltage is required to bring about instability.

Next, we consider the case $\mu > \pi$. Suppose that $\lambda \in (\ln^2 \delta, \lambda^*)$ and $\sigma < \hat{\sigma}$. Then $\mu > \pi$, which implies that the bifurcation at λ^* will occur to the left of the line $u = 1$. Before the bifurcation, the three monotonic solutions u^L, u^R, and the perturbation from the unstable catenoid (see Figure 2.20) are all located to the left of the critical point $u^*_{(2)}$, which satisfies $u^*_{(2)} < 1$ because $\lambda > \ln^2 \delta$. For convenience, we refer to the perturbed unstable catenoid solution as u^C. We have then one stable solution, u^L, flanked by two unstable solutions, u^R to the right and u^C to the left. Since they are all monotonic, the curve $t_1(u_0)$ will intersect the line $t_1 = 1/2$ three times. From Equation (2.23), we may write

$$t_1(u_0) = \sigma \int_{u_0}^{1} \frac{du}{\sqrt{\frac{u^2}{(u_0+\lambda\Gamma)^2} - 1}}, \quad \Gamma := \frac{1}{\ln(\delta/u)} - \frac{1}{\ln(\delta/u_0)} \,. \tag{2.91}$$

Taking a derivative with respect to λ, we have

$$\frac{\partial t_1}{\partial \lambda} = \sigma \int_{u_0}^{1} \left(\frac{u^2}{(u_0 + \lambda\Gamma)^2} - 1 \right)^{-3/2} \frac{u^2\Gamma}{(u_0 + \lambda\Gamma)^3} \, du \,. \tag{2.92}$$

Since $u_0 < u < 1$ in the region of integration, $\Gamma > 0$, and so $\frac{\partial t_1}{\partial \lambda} > 0$. Hence, by increasing λ, the curve moves in the positive t_1 direction, causing a bifurcation between u^L and u^R once λ^* is reached. Also, it is clear that $\frac{\partial t_1}{\partial \sigma} > 0$, so decreasing σ will cause the curve to move downward and bring a bifurcation between u^L and u^C at

σ^*. If, however, an increase in λ is countered by a decrease in σ, the two effects can be balanced so that the stable solution u^L remains. Physically, the situation is as follows. Increasing the voltage eventually pulls the membrane to the outer cylinder. Increasing the length causes surface tension to become too great for the bridge to sustain itself, and the membrane eventually collapses in on itself and pinches off. By increasing the voltage and the length together in the right proportions, the "pulling out" and the "pinching in" may be balanced so that the membrane remains stable.

We now ask whether there is a bound to this balancing effect. We certainly don't expect to achieve stable bridges of infinite length and infinite voltage. How far can we take this process? To answer this, we consider the plot of $u(1/2)$ versus $u(0)$, produced by iterating through different values of $u(0)$, integrating the ODE forward for $1/2$, and plotting $u(1/2)$ as a function of $u(0)$. Any intersection with the line $u(1/2) = 1$ gives a solution to the problem. Qualitatively, this will produce a curve equivalent to considering $t_1(u_0)$, but is easier to produce numerically and so is used here. Note that by construction, the meander plot will behave in the exact opposite way as $t_1(u_0)$ as λ and σ are altered, so that the curve will move up as σ is decreased and down as λ is increased. In any case, the qualitative characteristics of the bifurcation are just as evident, and we are in a position to determine the limit of the balancing effect of λ and σ.

In Figure 2.25, the meander curve $u(1/2)$ is plotted as a function of $u(0)$ for varying values of σ and λ for $\delta = 1.2$ fixed. As we follow the sequence of pictures, σ is decreased while λ is increased. This balancing of the two parameters enables the stable solution u^L to remain. However, the curve flattens out as we do this, so that in Figure 2.25(d), the middle portion of the curve has completely flattened out, and the three solutions have collided into one. At this critical (σ, λ) pair, σ^* has intersected λ^*. This is really quite remarkable. Physically, it appears that if the length and the voltage are balanced in such a way that the bridge remains

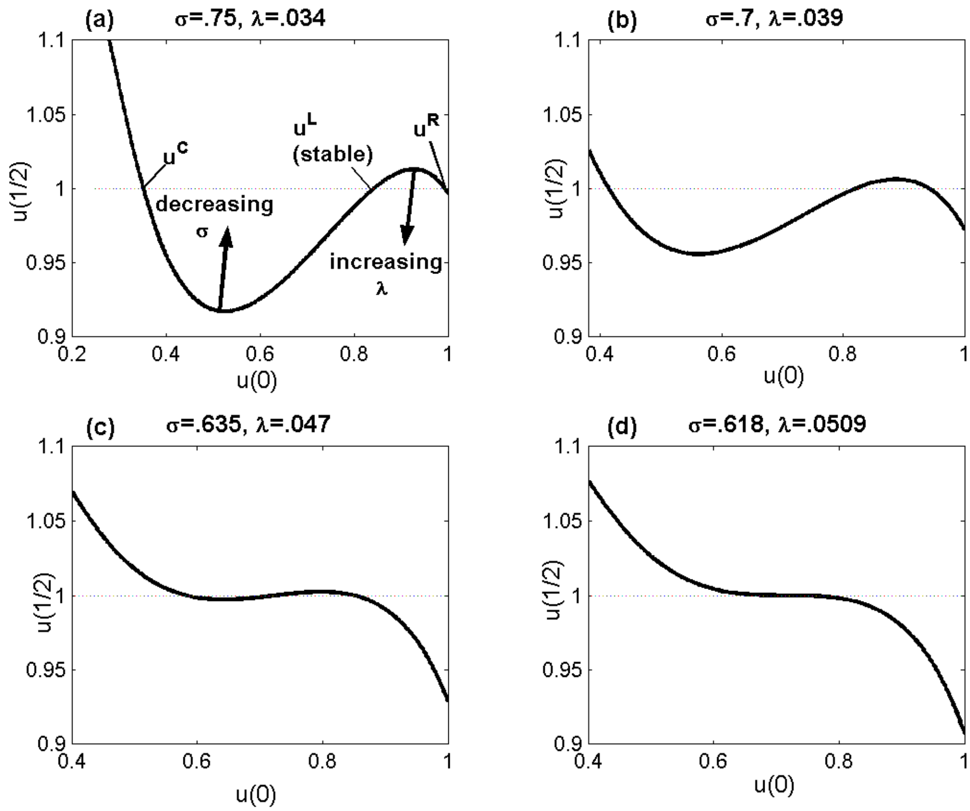

Figure 2.25: Progression of the curve $u(1/2)$ versus $u(0)$ as λ is increased and σ is decreased (and $\delta = 1.2$). The parameters are altered so that the stable solution u^L remains, but at each step, the middle portion of the curve flattens out. As is seen in (d), the three solutions coalesce and the stable solution is lost at a critical λ-σ pair.

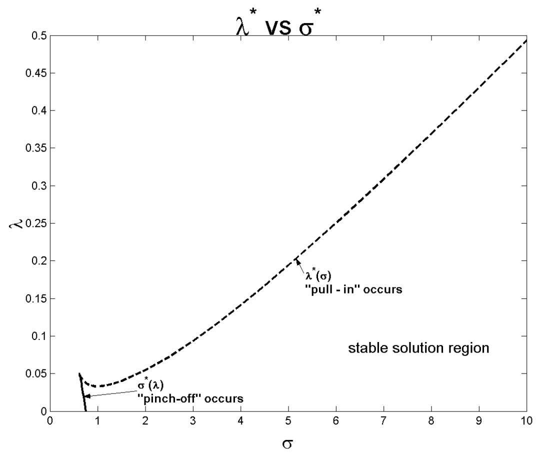

Figure 2.26: Plot of $\sigma^*(\lambda)$ vs $\lambda^*(\sigma)$. The behavior of λ^* for large σ is evident.

stable, a point is reached at which the pull-in voltage and the critical length occur simultaneously! This raises some interesting dynamics questions of what in fact the membrane will do and in which direction the instability will cause the membrane to move. We leave the answers to these questions for future work, and for the moment merely mention the end result that there is indeed a limit to the balancing of voltage and length, and it occurs at the intersection of the stability boundaries σ^* and λ^*.

The general shape of $\sigma^*(\lambda)$ and $\lambda^*(\sigma)$ is now complete. A numerically produced example is provided in Figures 2.26 and 2.27 for the value $\delta = 1.2$. Figure 2.26 shows a larger region to see more generally the structure of these two curves. Figure 2.27 is zoomed in toward the intersection of λ^* and σ^*.

It remains to see the effect of δ on these critical values and the shape of these curves. To do this, consider $\hat{\sigma}$, given in Equation (2.86). We saw that $(\hat{\sigma}, \ln^2 \delta)$ is the minimum point of $\lambda^*(\sigma)$. Observe that as $\delta \to 1$, this minimum point approaches $(\infty, 0)$. This relates the fact that as the field is placed closer and closer to the membrane, stability is lost at shorter bridges and less voltage.

On the other hand, as $\delta \to e^2$, the minimum point approaches $(0, 4)$. As we found, σ^* will intersect λ^* for $\sigma < \hat{\sigma}$, $\lambda > \ln^2 \delta$. Thus, as δ approaches e^2, we are able

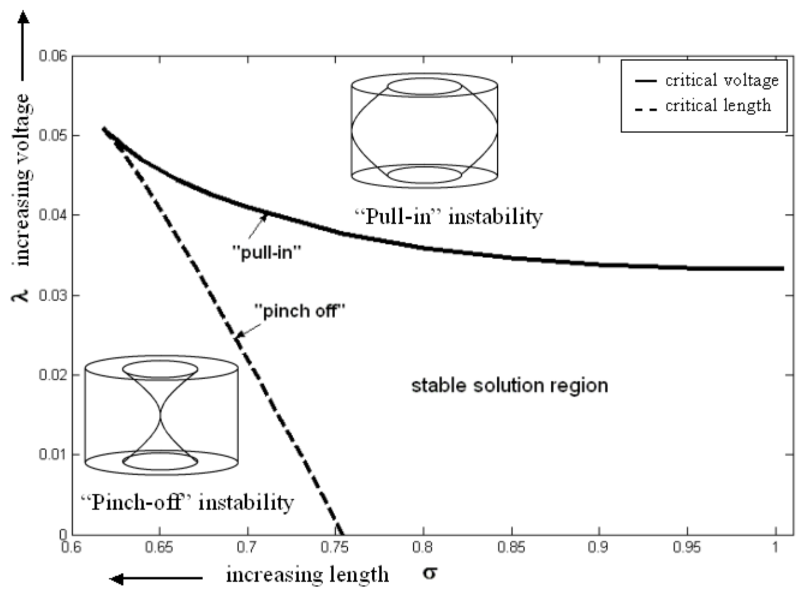

Figure 2.27: Plot of $\sigma^*(\lambda)$ vs $\lambda^*(\sigma)$, zoomed in on the region where σ^* and λ^* intersect. Stable solutions exist inside the two curves. The type of instability that occurs at each boundary is illustrated.

to obtain stable bridges for σ arbitrarily close to 0, which is equivalent to infinite length! However, we must keep in mind that as we increase δ, the aspect ratio approximation $(\frac{b-a}{L})^2 << 1$, used to solve for the electric potential, loses validity. Stability as $\sigma \to 0$, then, is unlikely to be produced physically. It remains to be seen experimentally just how long of a bridge may actually be obtained by manipulating these relationships.

2.6 Bifurcation diagrams

We conclude this chapter with a numerical analysis of the solution structure. We reiterate some of the conclusions that we have already reached through numerically produced bifurcation diagrams. We also consider a different approach to classifying stability. This approach will illuminate some interesting characteristics, and also demonstrate the existence of a stable solution which has thus far escaped our attention.

2.6.1 Branch tracing technique

In this section we will illustrate some characteristics of the solution structure via bifurcation diagrams. We begin by considering only symmetric solutions which satisfy $u'(0) = 0$. We wish to produce bifurcation diagrams as we alter the parameters λ and σ. Such diagrams were given in Section 2.5, but only for a small portion of the full solution structure. Here, we utilize a branch tracing numerical technique to produce these diagrams. This technique is outlined in [30]. We briefly describe the technique here. To begin, we cast our boundary value problem as an initial value problem:

$$\begin{aligned} 1 + \sigma^2 u'^2 - \sigma^2 u u'' &= \frac{\lambda(1+\sigma^2 u'^2)^{3/2}}{u \ln^2(\delta/u)} \\ u(0) = \alpha, \quad u'(0) &= 0 \ . \end{aligned} \tag{2.93}$$

A solution is given if $u(1/2) = 1$. We will shoot on α and λ to find solutions, and produce a curve in the λ-α plane. We define the function $G(\lambda, \alpha) = u(1/2) - 1$. Hence our solution curve is defined by $G = 0$. The idea is to introduce a new parameter s representing arc length of the curve $G = 0$. We then assume that λ and α are both functions of s.

Suppose that we have a known solution at the point (λ_0, α_0). We compute the tangent to the curve G at this point, and take a small step Δs in the tangent direction. Our guess for the next point on the curve is

$$\begin{aligned} \lambda &= \lambda_0 + \dot{\lambda}\Delta s \\ \alpha &= \alpha_0 + \dot{\alpha}\Delta s \ , \end{aligned} \tag{2.94}$$

where dots denote differentiation with respect to s. To find the point where $G = 0$ we add the condition

$$N(\lambda, \alpha) = \dot{\alpha}(\alpha - \alpha_0) + \dot{\lambda}(\lambda - \lambda_0) - \Delta s = 0 \ , \tag{2.95}$$

which is the equation for the normal line. Visually, the idea is to find the next point by moving in the tangent direction, and making corrections in the normal direction. The technique is illustrated in Figure 2.28. Numerically, we use a Newton's method to find roots of $G(\lambda, \alpha) = 0$, $N(\lambda, \alpha) = 0$, by inverting the system

$$\begin{pmatrix} G_\lambda & G_\alpha \\ \dot{\lambda} & \dot{\alpha} \end{pmatrix} \begin{pmatrix} \Delta\lambda \\ \Delta\alpha \end{pmatrix} = - \begin{pmatrix} G \\ N \end{pmatrix} . \tag{2.96}$$

Figure 2.29 shows a bifurcation diagram produced with this branch tracing technique for $\sigma = 0.8$ (solid line) and $\sigma = \sigma_{cr} = 0.7544$ (dashed line). In both cases, $\delta = 1.2$. Branch A corresponds to bulges of the cylinder, Branch B corresponds to perturbations of the stable catenoid (u^L in our prior terminology), Branch C perturbations of the unstable catenoid, and Branch F corresponds to non-monotonic

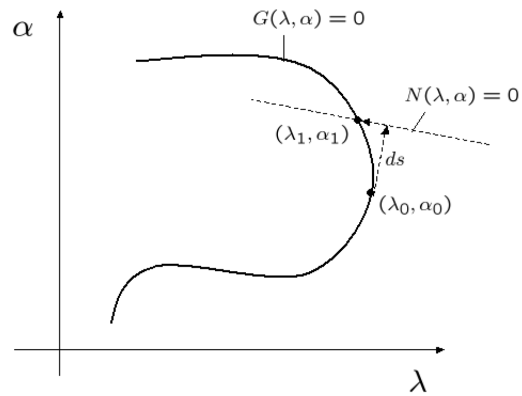

Figure 2.28: Schematic of the branch tracing numerical technique.

solutions. More non-monotonic solutions are present, and would appear as separate branches with small "hooks" at the end.

We make several observations about this diagram. First, we see the relationship between the two catenoid solutions. These solutions bifurcate where Branches B and C fold, but this occurs in the unphysical domain of negative λ when $\sigma = 0.8$. However, as we decrease σ, the fold moves to the right, so that at $\sigma = \sigma_{cr}$, the bifurcation occurs right at $\lambda = 0$. Hence, we recover the already known result of the location of σ_{cr}.

We also find the critical value of λ at which Branch B (corresponding to the stable solutions) vanishes. This occurs at the fold between Branches A and B. For λ beyond this value, Branch C continues. We then observe the hook at the end of this branch (where D and E meet). As λ is increased, it appears that another solution appears (Branch E), and then vanishes in a fold bifurcation with Branch D. More on this solution momentarily. This also occurs with the non-monotonic solution.

Along with characterizing solution structure, we may also use these diagrams to infer stability. We know that Branch B is stable, and standard bifurcation results

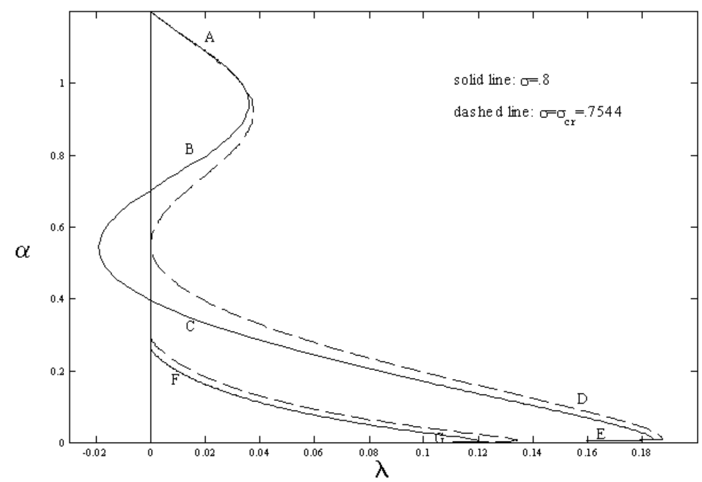

Figure 2.29: Bifurcation diagram in the λ versus α plane for fixed δ and two different values of σ.

suggest that Branch A is unstable. However, we have no further information regarding the rest of the branches. Intuitively, we would guess that all other branches are unstable. In the following section, we describe a method to determine stability straight from the shape of the diagram. We first describe the basic method, and then apply it to our problem.

2.6.2 Stability via Maddocks approach

In this section we explore a particular approach to classifying stability. This approach is due to Maddocks [37]. In this approach, stability is read directly from the shape of the proper bifurcation diagram. In general, it is known that turning points and branch points in bifurcation diagrams correspond to a change or exchange of stability. However, for an arbitrary diagram, no information is given regarding the details of the stability. For instance, having no prior knowledge, one cannot say whether any particular branch of a bifurcation diagram is stable or unstable.

The theorems presented in [37] provide an effective way to determine stability.

Given a functional $F(U, \lambda)$, one plots extremals of the functional in the λ, $-F_\lambda$ plane. In these coordinates, which are referred to as the "preferred coordinates", stability is classified in terms of the way in which simple folds occur in the diagram. Thus, for example, if there occurs in these coordinates a simple fold opening to the left, one may immediately conclude that the upper branch cannot correspond to local minima of the energy functional, regardless of any knowledge of the lower branch. It is not automatically conclusive that the lower branch does correspond to a stable energy minimizer; however, if the stability of one branch is known, the stability of all other connected branches may be ascertained by the direction of the folds.

We begin with an example to illustrate the utility of the method. The problem we consider is the following

$$\begin{aligned} u_{rr} + \frac{1}{r} u_r &= \frac{\lambda}{(1+u)^2} \\ u'(0) = 0, \quad u(1) &= 0 \; . \end{aligned} \tag{2.97}$$

This system governs the shape of an electrostatically deflected circular elastic membrane. As in our problem, λ characterizes the strength of the electric field. This problem is described and analyzed in detail in [52]. We focus on one result regarding this problem.

Figure 2.30 displays a plot of $-u(0)$, the magnitude of the deflection at the center of the disc, as a function of λ. Several things may be seen in this plot. It is evident that there is a maximum value of λ beyond which equilibrium solutions cease to exist. Also, though it is not evident in the plot, the curve folds back on itself infinitely many times as $-u(0)$ gets closer to 1. Thus there are infinite branches of solutions. The lowest branch connects to the origin. This point represents the undeflected solution when there is no voltage and is a stable solution. We can conclude that the lowest branch is stable, and can also conclude that the next branch is unstable by standard exchange of stability results. However, beyond this

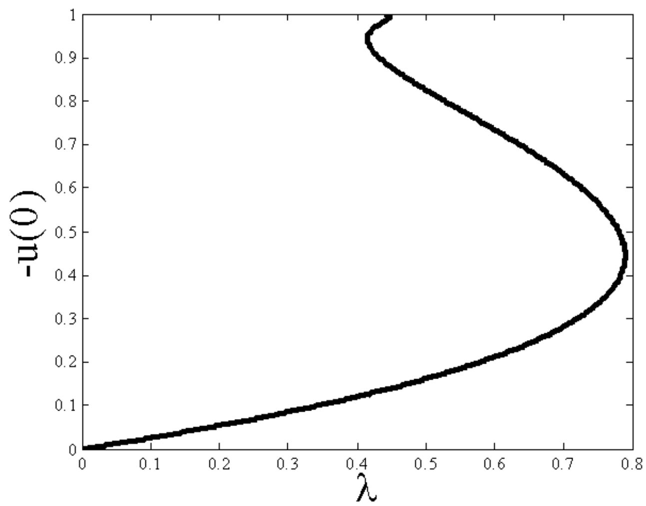

Figure 2.30: Bifurcation diagram for the electrostatically deflected disc example.

the diagram offers no information as to the stability of any other branches. It turns out that they are all unstable, but it is not trivial to demonstrate this.

Figure 2.31 displays the same solution structure, but plotted in the "preferred coordinates". For this system, the preferred coordinate for the bifurcation parameter λ is given by

$$-F_\lambda = \int_0^1 \frac{r}{1+u}\, dr \; . \tag{2.98}$$

The same basic solution structure is apparent and the same information may be garnered as before. The difference with this representation is that here the infinite branches appear as an infinite spiral. By the theorems of Maddocks, we are able to infer automatically that all branches beyond the first are unstable. In other words, the instability of all branches beyond the first is automatically seen by the direction in which the folds occur. By the same reasoning as before, the first branch may be classified as being stable, and thus stability is known for all solutions.

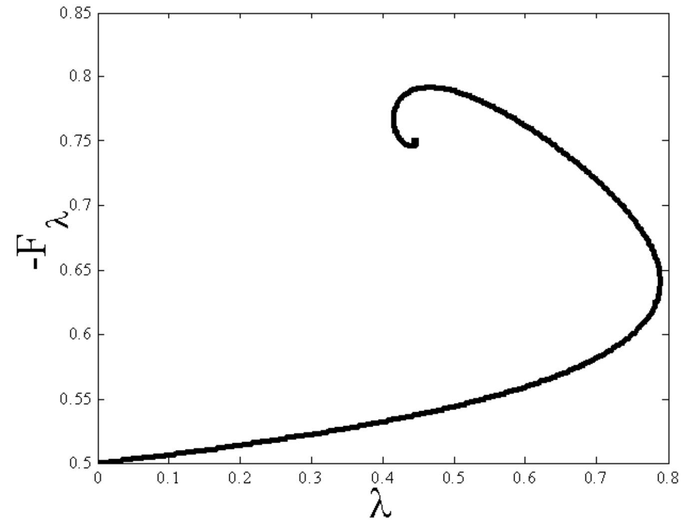

Figure 2.31: Bifurcation diagram for the disc example plotted in the "preferred coordinates".

2.6.3 Maddocks' approach applied to outer cylinder catenoid problem

In this section we apply the ideas of Maddocks' Theorem to the problem at hand. Figure 2.32 displays the same bifurcation diagram as in Figure 2.29 (for $\sigma = 0.8$), but in the "preferred coordinates" of $-F_\lambda$ versus λ. For the outer cylinder catenoid, the functional is

$$F[u] = \int_{-1/2}^{1/2} u\sqrt{1+\sigma^2 u_z^2} - \frac{\lambda}{\ln(\delta/u)}\, dz\ . \tag{2.99}$$

Choosing λ as our bifurcation parameter, we have

$$-F_\lambda = \int_{-1/2}^{1/2} \frac{1}{\ln(\delta/u)}\, dz\ . \tag{2.100}$$

It is difficult to see in the graph, but note that there is a down to up fold between Branches C and D. Thus, following the rules of stability as laid out by Maddocks, we reach a startling conclusion: stability of Branch B implies stability of Branch E!

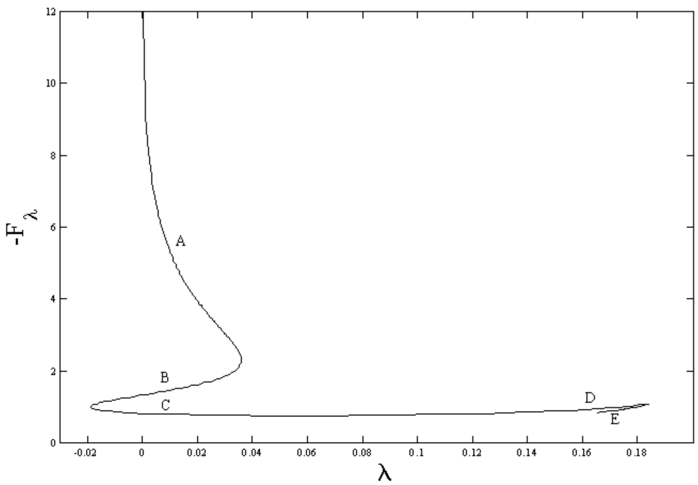

Figure 2.32: Bifurcation diagram for outer cylinder in the "preferred coordinates".

Before, we had predicted that Branch B was the only stable branch. However, we find the strange feature that Branch E is also in fact stable.

This is even more bizarre when we consider the type of solutions on Branch E. Figure 2.33 shows an example of a membrane profile for a solution on Branch E. It is certainly curious that solutions of this form should be stable. Indeed, this result is separately verifiable using the second variation approach and checking for conjugate points. We should, however, keep several things in mind. For one, note that stability in the sense we are using only refers to a *local* energy minimizer. Also, note that there is a significant gap in λ between the end of Branch B and the start of Branch E. For λ approximately between 0.03 and 0.16, there are no stable solutions present. Therefore, it is unlikely that Branch E could be reached physically. It remains, however, an interesting mathematical anomaly that such a solution should be stable, and one that we would be unlikely to have found without the preceding numerics.

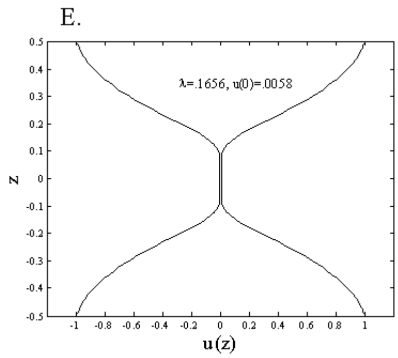

Figure 2.33: Solution profile for Branch E – this solution is stable in the sense that it is a local energy minimizer.

Finally, we consider a bifurcation diagram for the full, non-symmetric formulation. We proceed in exactly the same way, except that our initial conditions are $u(-1/2) = 1$, $u'(-1/2) = \beta$, and we produce a diagram in the λ-β plane. In this case, our shooting coordinate β represents the contact angle with the boundary.

Figure 2.34 shows the bifurcation diagram for the inner part of the spiral meander for $\delta = 1.2$ and $\sigma = 0.8$. Thus, we are plotting under the same parameter values as in Figure 2.29. Figure 2.35 displays the same bifurcation diagram in the "preferred coordinate" system. We find present in both diagrams a "hook" on the end of Branch E, representing the same stable solution found in the symmetric formulation. Branch C contains the only other stable solutions. We also see the occurrence of non-symmetric solutions in pairs – Branches F and G are exactly the same in this diagram as Branches H and I.

Figure 2.36 shows the solution profile for points on each of the different Branches A – I in Figure 2.34. Observe the shape and concavity of solution A. This branch appears to be limiting to a non-smooth pointed solution. An interesting area to explore would be whether this is the shape that appears dynamically when the "pull in" instability sets in at the critical voltage.

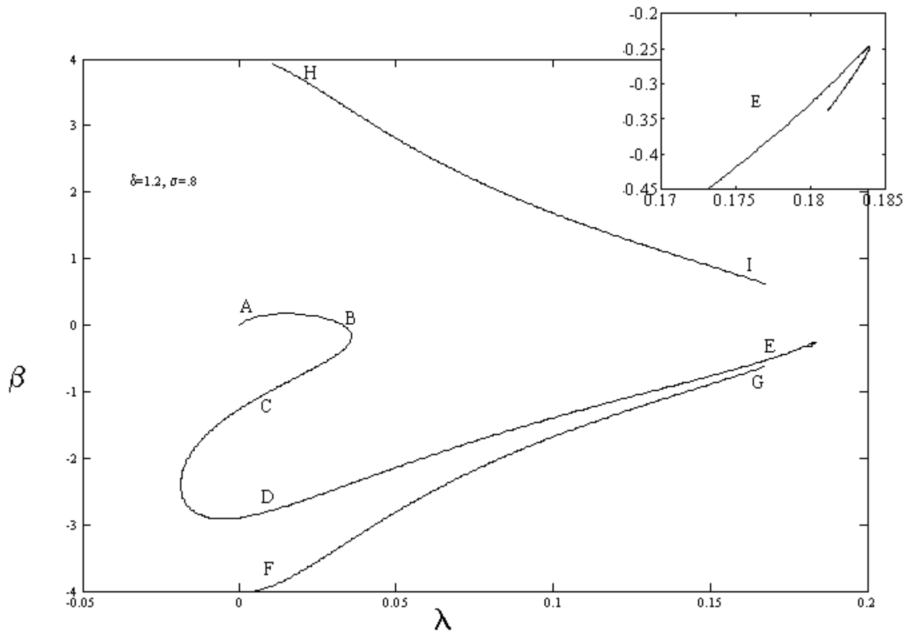

Figure 2.34: Bifurcation diagram for the non-symmetric formulation, plotted in the variables λ versus $\beta = u'(-1/2)$. In the insert, we have zoomed in on the hook at the end of Branch E.

The solution plotted from Branch B is the cylinder solution, which is unstable for these parameter values ($\mu < \pi$). Branches C and D represent the perturbed stable (C) and unstable (D) catenoids. Note also that the non-symmetric solution branches are reflections of each other about the line $\beta = 0$. Following Branches F and H to Branches G and I, respectively, we see that these non-symmetric solutions seem to be converging to the symmetric solution on Branch E. However, it appears that none of the branches actually intersect. In fact, closer inspection of the meander curves in this region verifies that are no bifurcations present at this point – the branches simply end.

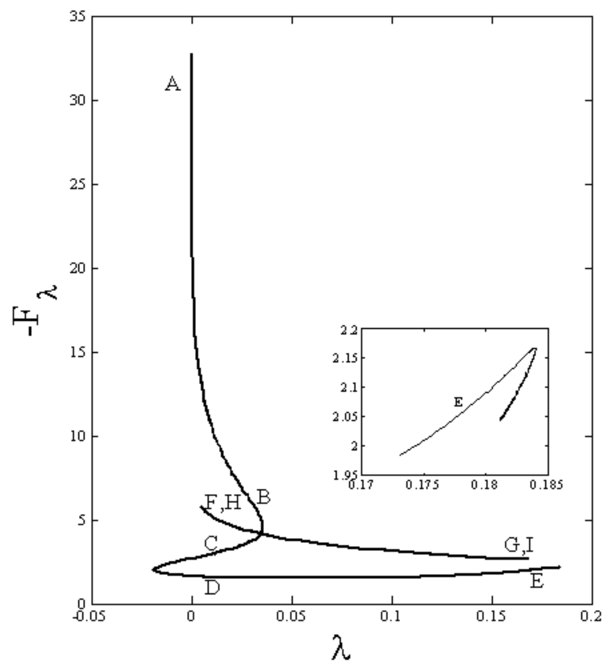

Figure 2.35: Bifurcation diagram in the preferred coordinates for the non-symmetric formulation, plotted in λ versus $\beta = u'(-1/2)$. In the insert, we have zoomed in on the hook at the end of Branch E.

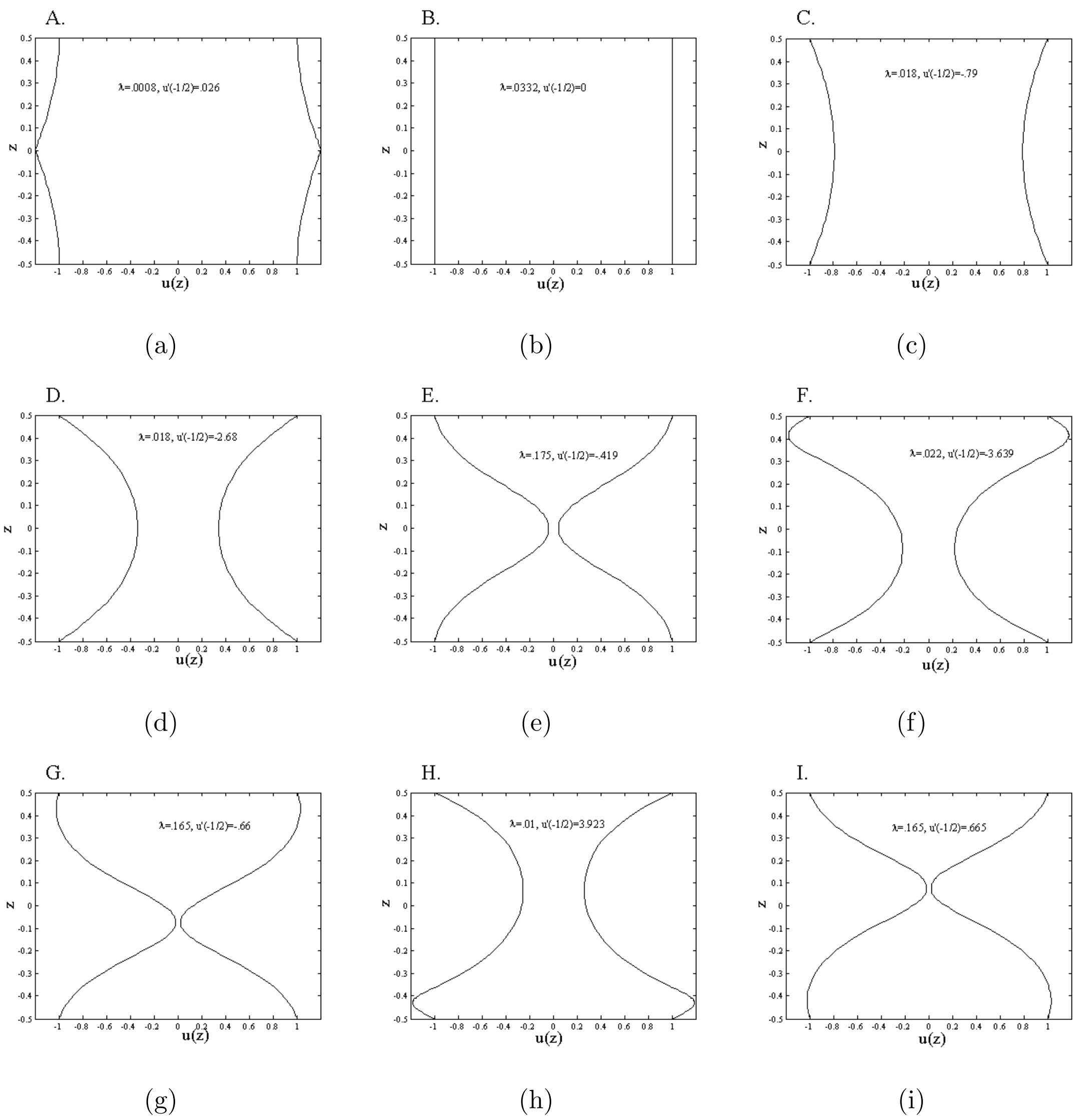

Figure 2.36: Solution profiles from the different branches of Figure 2.34.

2.7 Discussion

In this chapter, we explored equilibrium solutions of a catenoid bridge under the influence of an axially symmetric applied electric field. We began by formulating the mathematical model, arriving at the governing differential equation through minimization of an energy functional. From there, our objective was to analyze the resulting boundary value problem. We investigated the general solution set by using standard techniques from the theory of dynamical systems. We identified a homoclinic orbit in the phase plane and developed general solution criteria. This uncovered a rich solution structure, illustrated by the spiral structure of the meander curve in Figure 2.10.

Our second approach to understanding the boundary value problem was to use perturbation methods to study various limiting situations. This allowed us to find approximate solutions and also to determine the relationship between key parameters in the problem. Finally, we explored the problem numerically by plotting bifurcation diagrams. Analysis in the "preferred coordinates" led to the discovery of a bizarre stable solution.

One important technological question is whether or not the electric field allows for significant manipulation of the surface. One clear result attained here is that the field may be used to stabilize structures that would otherwise be unstable. We first saw this in the case of the perturbed catenoids, where the bifurcation between the stable and unstable catenoids occurred at a greater length than in the case of zero voltage. A similar result was obtained for the case of the cylinder. We further explored this by considering the relationship between critical length and critical voltage. Physically, the stabilization occurs because the electric field is applied to counteract the surface tension force in the system. We have shown that these forces can be balanced in interesting ways, leading to structured surfaces unobtainable without an electric field.

An important future step with this problem would be to perform an experimental analysis. For one, this would be useful in verifying the asymptotically derived approximation of the critical length σ^*. Also, one of the most interesting results of our analysis is seen in Figure 2.27, which illustrates the idea of balancing surface tension and electrostatic forces, but also reveals the intriguing limit to this balancing effect. There are peculiar dynamics questions related to the intersection of λ^* and σ^*, and an experimental study could be used to uncover the feasibility of these results and perhaps lead to a greater understanding of the mathematical curiosities obtained in this chapter. It is the authors' intent to perform an experimental study with this setup; unfortunately, at the time of writing a trustworthy experimental setup has yet to be achieved.

Chapter 3

SOAP-FILM BRIDGE IN AN ELECTRIC FIELD – INNER CYLINDER

3.1 Introduction

In this chapter, we explore the problem of a soap-film bridge placed in an axially symmetric electric field, but for a different geometry than in Chapter 2. In the present chapter we place a perfectly conducting cylindrical electrode *inside* the membrane – that is, on the radial axis – versus the placement of the electrode outside the membrane in Chapter 2. Aside from this, the setup will be exactly the same as in the previous chapter. We apply a potential difference between the cylinder and the membrane, and analyze the equilibrium shape of the membrane as a function of voltage and key length parameters. We focus on characterizing the main effect of the electric field and the interplay between electrostatic and elastic forces. As we will see, the difference in the current setup, which we refer to as the inner cylinder setup, versus the outer cylinder setup of the previous chapter, drastically alters the problem, both mathematically in terms of the structure and evolution of the solution set, and physically in terms of the effect and possible advantages of the added electric field.

We explore this system both experimentally and theoretically. Theoretically, we explore the equilibrium solution set and investigate the interplay between surface

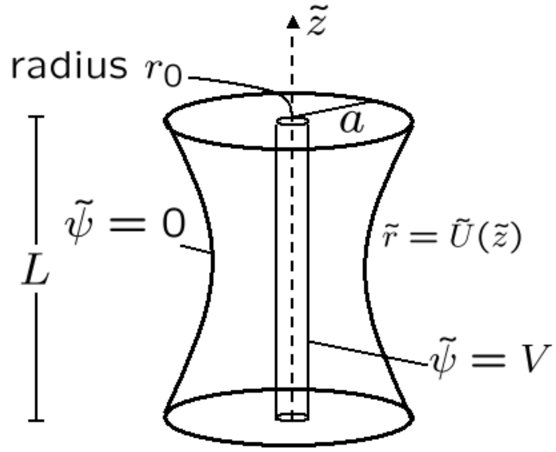

Figure 3.1: The setup for the inner cylinder.

tension and electrostatic forces. The theory is developed in Section 3.2. Experimentally, we attempt to quantify this interplay and test the predictability of the theory. Experimental results are given in Section 3.3.

3.2 Theory

In this section we perform a theoretical analysis of the equilibrium shape of the membrane. We begin by formulating a model through variational techniques. A governing boundary value problem is obtained, which we analyze first through perturbation techniques and then in a general setting.

3.2.1 The model

To begin, we derive the governing equation for the shape of the soap-film bridge. The system we study consists of two parallel rings of radius a a distance L apart with a thin conducting membrane (the soap-film) forming a bridge across the rings. A uniform perfectly conducting cylinder of radius $r_0 < a$ lies inside the membrane, and a potential difference is applied between the membrane and the cylinder. This geometry is sketched in Figure 3.1.

As in the case of the outer cylinder, the shape is governed by electrostatic and elastic forces. The derivation will follow very similar to that performed in Chapter 2, and so we will be short on the detail. Denoting the electrostatic potential by $\tilde{\psi}$ and working in cylindrical coordinates, $\tilde{\psi}(\tilde{r}, \theta, \tilde{z})$ satisfies

$$\Delta \tilde{\psi} = 0 \tag{3.1}$$

$$\tilde{\psi}(r_0, \theta, \tilde{z}) = V \tag{3.2}$$

$$\tilde{\psi}(\tilde{U}(\tilde{z}), \theta, \tilde{z}) = 0 \ , \tag{3.3}$$

where $\tilde{r} = \tilde{U}(\tilde{z})$ defines the membrane surface. Axial symmetry implies that $\tilde{U}$ depends only on $\tilde{z}$. Next, we introduce the non-dimensional variables

$$z = \frac{\tilde{z}}{L}, \quad r = \frac{\tilde{r}}{r_0}, \quad \psi = \frac{\tilde{\psi}}{V}, \quad U = \frac{\tilde{U}}{a} \ . \tag{3.4}$$

Making these substitutions in Equations (3.1) – (3.3), we obtain

$$\frac{\partial^2 \psi}{\partial r^2} + \frac{1}{r}\frac{\partial \psi}{\partial r} + \epsilon^2 \frac{\partial^2 \psi}{\partial z^2} = 0 \tag{3.5}$$

$$\psi = 1 \quad \text{at} \quad r = 1 \tag{3.6}$$

$$\psi = 0 \quad \text{at } r = U(z)/\delta_1 \ . \tag{3.7}$$

Here, $\epsilon = r_0/L$ is a dimensionless aspect ratio comparing the radius of the inner cylinder to the length of the device. We assume $\epsilon^2 << 1$. Also, $\delta_1 = r_0/a$ compares the two radial lengths in the problem. Solving Equations (3.5) – (3.7) after letting $\epsilon \to 0$, and upon using the divergence theorem, we may write the electrostatic field energy in dimensionless form as

$$\pi\epsilon_0 V^2 L \int_{-1/2}^{1/2} \left(\ln \frac{\delta_1}{U(z)}\right)^{-1} dz \ . \tag{3.8}$$

As we would expect, the elastic energy is exactly the same as in the outer cylinder case, and is given by

$$2\pi T L a \int_{-1/2}^{1/2} U(z)\sqrt{1+\sigma^2 U'(z)^2}\ dz \ , \tag{3.9}$$

where $\sigma = \frac{a}{L}$ is the ratio of the ring radius to the length is the same parameter encountered in Chapter 2, and T is the tension. The dimensionless energy functional is

$$\mathcal{E}[u] = \int_{-1/2}^{1/2} U\sqrt{1+\sigma^2 U'^2} + \frac{\lambda}{\ln(\delta_1/U)}\ dz \ , \tag{3.10}$$

where

$$\lambda = \frac{\epsilon_0 V^2}{2Ta} \tag{3.11}$$

is the same dimensionless variable as in Chapter 2, characterizing the relative strengths of electrostatic and mechanical forces in the problem. Taking a first variational derivative, we obtain

$$\frac{1+\sigma^2 U'^2 - \sigma^2 U U''}{(1+\sigma^2 U'^2)^{3/2}} = -\frac{\lambda}{U \ln^2(\delta_1/U)} \quad . \tag{3.12}$$

To complete the system, we impose the boundary condition that requires that the membrane be connected to the rings, namely

$$U(-1/2) = U(1/2) = 1 \quad . \tag{3.13}$$

Equations (3.12) – (3.13) constitute our model for the equilibrium shape of the deflected membrane. It is informative to compare these with the model we obtained for the outer cylinder, Equations (2.14) – (2.15). The only difference between the two systems, aside from the definition of the parameter δ, is that in the inner cylinder problem we find a minus sign on the right hand side of the differential equation. Recall that in each case, the left hand side is the mean curvature operator and the right hand contains the effect of the electric field. The difference in the minus sign accounts for the geometry, and the idea that the electric field is "pulling" the membrane in opposite directions in the two setups. In the outer cylinder setup the field is pulling the membrane outwards, whereas in the present setup the membrane is being pulled in.

3.2.2 Perturbation analysis – small voltage

In the case of small voltage, we assume that $\lambda << 1$ and that U can be expanded as

$$U \sim U_0 + \lambda U_1 + \lambda^2 U_2 + \ldots \tag{3.14}$$

As in Chapter 2, we require that $\epsilon^2 << \lambda$ in order for the current asymptotic expansion to be compatible with the energy formulation. Inserting the expansion (3.14) into the ODE, the leading order solution is the catenoid of zero voltage encountered in Chapter 2,

$$U_0(z) = \frac{\cosh(c_2 z)}{c_2 \sigma} \ , \tag{3.15}$$

where c_2 is a constant satisfying

$$\sigma = \frac{\cosh(c_2/2)}{c_2} \ . \tag{3.16}$$

As before, there are two catenoid solutions (one stable and one unstable) for $\sigma > \sigma_{cr} \approx 0.7545$, and no solutions beyond σ_{cr}. At $O(\lambda)$, we have

$$U_1'' - 2c_2 \tanh(c_2 z) U_1' + c_2^2 U_1 = \frac{(1+\sigma^2 U_0^2)^{3/2}}{\sigma^2 U_0^2 \ln^2(\delta_1/U_0)} \tag{3.17}$$

along with boundary conditions $U_1(-1/2) = U_1(1/2) = 0$. Proceeding in the same manner as in Chapter 2, we analyze Equation (3.17) by first considering the homogeneous solution, which is

$$U_1^h(z) = A \sinh(c_2 z) + B(c_2 z \sinh(c_2 z) - \cosh(c_2 z)) \ , \tag{3.18}$$

where A and B are constants. The boundary conditions can only be met at the critical value σ_{cr}. In this case, the criteria for there to be a solution to Equation (3.17) is that

$$\int_{-1/2}^{1/2} \frac{(1+\sigma^2 U_0'^2)^{3/2}}{U_0^2 \ln(\delta_1/U_0)^2} \cdot U_1^h \, dz = 0 \ , \tag{3.19}$$

where U_1^h is the homogeneous solution. However, U_1^h carries only one sign in the interval $[-1/2, 1/2]$, and so the integral cannot vanish and there is no solution when $\sigma = \sigma_{cr}$. As we now show, the two catenoid solutions bifurcate at a value of $\sigma > \sigma_{cr}$. To see this, we take

$$\sigma^2 = \sigma_{cr}^2 + \gamma\lambda \ , \tag{3.20}$$

where $\gamma > 0$ is to be determined, and modify our expansion as

$$U \sim U_0 + \lambda^{1/2} U_1 + \lambda U_2 + \dots \tag{3.21}$$

Plugging this expansion into Equation (3.12), we find again that $U_0 = \cosh(c_2 z)/(\sigma_{cr} c_2)$. Here, U_0 is at the bifurcation catenoid of zero voltage when $\sigma = \sigma_{cr}$. For convenience, we define

$$L[U] := U'' - 2c_2 \tanh(c_2 z) U' + c_2^2 U \ . \tag{3.22}$$

In terms of this operator, the $O(\lambda^{1/2})$ problem is

$$\begin{aligned} L[U_1] &= 0 \\ U_1(-1/2) &= U_1(1/2) = 0 \ . \end{aligned} \tag{3.23}$$

This problem has solution given by

$$U_1 = B \cdot (c_2 z \sinh(c_2 z) - \cosh(c_2 z)) \ .$$

The constant B is undetermined, as the boundary conditions are automatically satisfied. To determine B, we go to the $O(\lambda)$ problem, which may be written

$$L[U_2] = \frac{(1+\sigma_{cr}^2 U_0'^2)^{3/2}}{\sigma_{cr}^2 U_0^2 \ln(\delta_1/U_0)^2} - \frac{U_1 U_1''}{U_0} + \frac{U_1'^2}{U_0} + \gamma \left(\frac{U_0'^2 - U_0 U_0''}{\sigma_{cr}^2 U_0} \right) \ . \tag{3.24}$$

Denote the right hand side of Equation (3.24) by $G(B, \gamma)$. In this case, the orthogonality condition

$$\int_{-1/2}^{1/2} U_2^h G(B, \gamma) \, dz = 0 \tag{3.25}$$

gives us a relationship between B and γ, where again, U_2^h solves $L[U_2^h] = 0$. Now, introduce the function $\hat{U} = c_2 z \sinh(c_2 z) - \cosh(c_2 z)$ so that $u_1 = B\hat{u}$. The relationship Equation (3.25) may be expressed as

$$B^2 I_1 + I_2 = -\gamma I_3 \ , \tag{3.26}$$

where the values $I_k, \ k = 1, 2, 3$ are explicitly defined by

$$I_1 = \int_{-1/2}^{1/2} \frac{\hat{U}\hat{U}'^2 - \hat{U}^2\hat{U}''}{U_0}\, dz, \quad I_2 = \int_{-1/2}^{1/2} \frac{\hat{U}(1+\sigma_{cr}^2 U_0'^2)^{3/2}}{\sigma_{cr}^2 U_0^2 \ln^2(\delta_1/U_0)}\, dz,$$
$$I_3 = \int_{-1/2}^{1/2} \frac{\hat{U}(U_0'^2 - U_0 U_0'')}{\sigma_{cr}^2 U_0}\, dz\ . \tag{3.27}$$

Note that $I_1 \approx -10.248$ and $I_3 \approx 3.459$ are fixed values, while I_2 depends on δ_1, but will always be negative. Solving Equation (3.26) for B yields two possible solutions for U_1 which, when combined with U_0, represent the perturbations from the stable and unstable catenoids. This is only possible, however, if the term within the square root is positive when solving for B. So, Equation (3.26) enables us to approximate the critical length at which the bifurcation between the two perturbed catenoids occurs. From Equation (3.26) and in view of the signs of the integrals I_k in Equation (3.27), the bifurcation between the two solutions occurs when $\gamma = \frac{-I_2}{I_3}$, and so the critical value of σ is

$$\sigma^{**} = \left(\sigma_{cr}^2 - \frac{I_2 \lambda}{I_3}\right)^{1/2}\ . \tag{3.28}$$

In terms of notation, σ^{**} denotes the critical length ratio when the voltage is on, whereas σ_{cr} is the critical length ratio of zero voltage. Note that $\sigma^{**} > \sigma_{cr}$, meaning that stability will be lost at a shorter length with the addition of the electric field. This is in direct contrast to what we observed in Chapter 2, where we found the critical value, σ^*, to be less than σ_{cr}.

The difference is that in the present setup, the Coulomb force of the electric field is pulling the membrane inward, in effect combining with surface tension to cause instability at a shorter length. The difference in geometry with the two setups is fully apparent when considering these values of σ and the effect of the electric field on the critical length.

Returning to the expansion (3.14), we have that for arbitrary $\sigma > \sigma^{**}$, the homogeneous problem of Equation (3.17) has no solution, and so the solution U_1 may be obtained using variation of parameters. Actually, there are two solutions, one for each of the two zero voltage catenoids. Further, we find that as σ approaches σ^{**}, these solutions correspond with those of the modified expansion Equation (3.21), and the two asymptotic schemes are compatible.

3.2.3 Phase plane analysis

To analyze the general solution set, we consider the structure of the phase plane, and define a time of flight integral for trajectories. Equation (3.12) may be written as the following first order system

$$\begin{aligned} U' &= V \\ V' &= \frac{1+\sigma^2 V^2}{\sigma^2 U} + \frac{\lambda(1+\sigma^2V^2)^{3/2}}{\sigma^2 U^2 \ln^2(\delta_1/U)} \ . \end{aligned} \tag{3.29}$$

Note that $U > \delta_1$, which corresponds to the physical boundary that the membrane cannot cross over the inner electrode. Since $\lambda > 0$, there are no critical points, and trajectories monotonically travel out to infinity. Compare this to the phase plane in the outer cylinder case, and we again notice the drastic difference between the two geometries. All of the complexity that followed from the structure of the critical points and the presence of the homoclinic orbit is absent for this geometry. Due to the monotonicity of the trajectories, we immediately reach several conclusions regarding the possible types of solution.

- All solutions will satisfy $U(0) < 1$. Hence, the cylindrical solutions and "bulges" of the cylinder we saw in Chapter 2 are not possible in this geometry.

- All solutions will be monotonic on the half interval $0 < z < 1/2$. This also implies that all solutions will be symmetrical about the midplane $z = 0$, and so non-symmetrical solutions are excluded.

The above conclusions further illustrate the physical difference between the two geometries. With the inner cylinder setup, the electric field can only "pull" the membrane inwards, so that cylindrical solutions and much of the complexity found with the outer cylinder setup is removed.

Despite the apparent simplicity of the phase plane, the solution structure, as we shall show, is not trivial. To begin, we use the symmetry to define a solution in the phase plane as a trajectory that begins on the U-axis and hits the vertical line $U = 1$ after a time of flight of $1/2$.

Applying the Beltrami identity [77] to the energy functional of Equation (3.10), we obtain

$$\frac{U}{\sqrt{1+\sigma^2 U'^2}} - \frac{\lambda}{\ln(U/\delta_1)} = C \; . \tag{3.30}$$

The constant C represents a conserved quantity in the system, and may be determined by setting $z = 0$ and defining $U_0 := U(0)$. This implies that

$$C = U_0 - \frac{\lambda}{\ln(U_0/\delta_1)} \; . \tag{3.31}$$

We may then solve Equation (3.30) for $U'(z)$ and separate variables to obtain the following integral that represents the time it takes the trajectory starting at $(U_0, 0)$ to travel to the vertical line $U = 1$

$$\tau(U_0) = \int_{U_0}^{1} \frac{dU}{f(U; U_0)} \; , \tag{3.32}$$

where

$$f(U,U_0) := \frac{1}{\sigma}\left\{\left(\frac{U}{C+\frac{\lambda}{\ln(U/\delta_1)}}\right)^2 - 1\right\}^{1/2} . \tag{3.33}$$

A solution is found by locating the values U_0 for which $\tau(U_0) = 1/2$. However, we must be careful with this, because as we shall show, not all trajectories reach the line $U = 1$, and so τ is not well defined for all U_0. We first show that trajectories are bounded or unbounded depending on the sign of the conserved quantity C in Equation (3.31).

If $C < 0$, we rewrite Equation (3.30) as

$$\frac{U}{\sqrt{1+\sigma^2 U'^2}} = \frac{\lambda}{\ln(U/\delta_1)} + C . \tag{3.34}$$

Since the left hand side of Equation (3.34) is strictly positive, we set the right hand side greater than zero, and solve for U, obtaining

$$U < \delta_1 e^{-\lambda/C} . \tag{3.35}$$

Equation (3.35) gives a bound in the U-direction for the trajectory that starts at $(U_0, 0)$. Since the trajectory travels monotonically in each half plane, this implies the presence of a vertical asymptote for any trajectory for which $C < 0$. We are only able to obtain this upper bound if $C < 0$. If $C > 0$, U is unbounded. To see this, we assume positive C, set the left hand side of Equation (3.30) greater than zero, and obtain

$$\lambda\sqrt{1+\sigma^2 V^2} < U \ln(U/\delta_1) . \tag{3.36}$$

If U were bounded, V would have to be bounded as well, which contradicts the monotonic nature of the phase plane. Similar arguments apply to show that the trajectory for which $C = 0$ is also unbounded. The value of U_0 for which $C = 0$ is the solution of

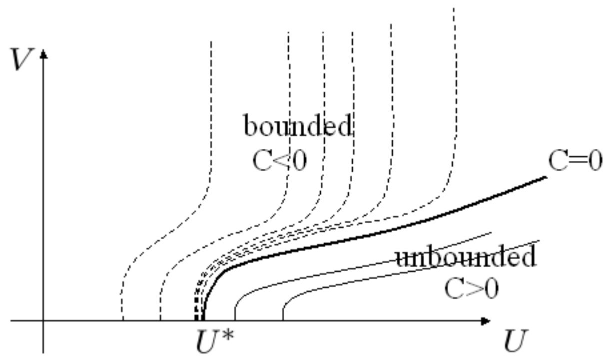

Figure 3.2: The structure of the phase plane for the inner cylinder. The bold trajectory corresponding to U^* divides the bounded and unbounded trajectories.

$$U^* \ln(U^*/\delta_1) = \lambda \,. \tag{3.37}$$

Increasing λ increases this value of U^*. Also, the quantity C increases as we increase U_0. Hence, we may divide the phase plane as follows:

- Trajectories with starting point $(U_0, 0)$ with $U_0 < U^*$ will each approach their own unique vertical asymptote.
- Trajectories starting at $(U_0, 0)$ with $U_0 \geq U^*$ are unbounded.

Due to this boundary present at the trajectory with $C = 0$, the phase plane has the structure depicted in Figure 3.2. This is evident when considering the bounds for the trajectories. As U_0 gets close to U^*, $C \to 0$, and so the bound given by Equation (3.35) and the vertical asymptotes approach infinity. As we now show, the bound given by Equation (3.35) is a tight bound.

Theorem 2 *If $C < 0$, the trajectory starting at $(U_0, 0)$ at $z = 0$ will asymptotically approach the line $U = \delta_1 e^{-\lambda/C}$.*

Proof: Denote $U_b := \delta_1 e^{-\lambda/C}$, and let $\bar{U_0}$ be the point on the U-axis for the trajectory with asymptote U_b. We will show that $U_0 = \bar{U_0}$.

Letting $U = U_b$ in Equation (3.30), we obtain the following relationship

$$1 + \sigma^2 v^2 = \frac{U_b^2}{H^2}, \quad H := \bar{U_0} - \frac{\lambda}{\ln(\bar{U_0}/\delta_1)} + \frac{\lambda}{\ln(U_b/\delta_1)} \,. \tag{3.38}$$

Since the trajectory has U_b as an asymptote, we will have $\frac{dV}{dU} \to \infty$ as $U \to U_b$. From Equations (3.29),

$$\frac{dV}{dU} = \frac{V'}{U'} = \frac{\lambda(1+\sigma^2 V^2)^{3/2}}{\sigma^2 U^2 V \ln(\delta_1/U)^2} + \frac{1+\sigma^2 V^2}{\sigma^2 U V} \,, \tag{3.39}$$

which, upon letting $U = U_b$ and using Equation (3.38), implies

$$\left.\frac{dV}{dU}\right|_{U=U_b} = \frac{\lambda U_b + H \ln(U_b/\delta_1)^2}{\sigma^2 v H^3 \ln(U_b/\delta_1)^2} \,. \tag{3.40}$$

In order for Equation (3.40) to blow up, we must have $H = 0$, since $v = 0$ corresponds to the case of infinite slope on the U-axis. Hence, $\bar{U_0}$ must satisfy

$$\bar{U_0} - \frac{\lambda}{\ln(\bar{U_0}/\delta_1)} = -\frac{\lambda}{\ln(U_b/\delta_1)} \,. \tag{3.41}$$

But, $U_b = \delta_1 e^{-\lambda/C}$ which implies that

$$\frac{-\lambda}{\ln(U_b/\delta_1)} = C = U_0 - \frac{\lambda}{\ln(U_0/\delta_1)}$$

and so Equation (3.41) becomes

$$\bar{U_0} - \frac{\lambda}{\ln(\bar{U_0}/\delta_1)} = U_0 - \frac{\lambda}{\ln(U_0/\delta_1)} \,. \tag{3.42}$$

Hence $\bar{U_0} = U_0$ by injectivity and the proof is completed. □

As an implication of this, the starting point for the trajectory which has $U = 1$ as its asymptote, denoted by U_0^*, is the solution to

$$U_0^* - \frac{\lambda}{\ln(U_0^*/\delta_1)} = \frac{\lambda}{\ln \delta_1} \ . \tag{3.43}$$

This point is of particular interest because any trajectory starting to the left of U_0^* has an asymptote less than one, meaning the trajectory never reaches the line $U = 1$ and cannot possibly be a solution to the boundary value problem.

To further understand the nature of the trajectories, we now show that in all bounded trajectories, there exists a finite time singularity.

Theorem 3 *Any trajectory satisfying $C < 0$ will blow up in finite time. That is, for any starting point on the trajectory, there exists $z_b < \infty$ such that $V(z_b)$ is infinite.*

Proof: As all trajectories cross the U-axis, we take the trajectory to be at $(U_0, 0)$ when $z = 0$ and with bound U_b, so that $U \leq U_b \ \forall z$. Referring to Equations (3.29), we have that

$$V' > c_1(1 + \sigma^2 V^2) + c_2(1 + \sigma^2 V^2)^{3/2} \ , \tag{3.44}$$

where

$$c_1 := \frac{1}{\sigma^2 U_b}, \quad c_2 := \frac{\lambda}{\sigma^2 U_b^2 \ln(U_b/\delta_1)^2} \ . \tag{3.45}$$

Let $c := \min(c_1, c_2)$. Then

$$V' > c\left(1 + \sigma^2 V^2 + (1 + \sigma^2 V^2)^{3/2}\right) > 0 \ . \tag{3.46}$$

Consider the system

$$W' = c\left(1 + \sigma^2 W^2 + (1 + \sigma^2 W^2)^{3/2}\right), \ \ W(0) = 0 \ . \tag{3.47}$$

Integrating, we find that W will satisfy

$$-\frac{\sqrt{1 + \sigma^2 W^2}}{\sigma^2 W} + \frac{1}{\sigma^2 W} + \arctan(\sigma W)/\sigma = cz \ . \tag{3.48}$$

If we let $cz \to (1-\pi/2)/\sigma$ in Equation (3.48), $W \to \infty$. In other words, W has a singularity at $z = (1-\pi/2)/(\sigma c)$. Since $V(0) = 0$, and $V(z) > W(z)\ \forall z$, it follows that V will have a finite time singularity as well, and will blow up for $z \leq (1-\pi/2)/(\sigma c)$. This completes the proof. $\square$

Corollary 4 *The trajectory starting at $(U_0, 0)$ when $z = 0$ where U_0 is such that $C < 0$ will blow up at time*

$$z = t_b := \int_{U_0}^{U_b} \frac{dU}{f(U;U_0)}\ , \tag{3.49}$$

where $U_b = \delta_1 e^{-\lambda/C}$ is the asymptotic bound of Theorem 2, and $f(U;U_0)$ is defined in Equation (3.33).

Proof: The integral in Equation (3.49) represents the time the trajectory will take to travel from $U = U_0$ to $U = U_b$. U_b defines the asymptote for the trajectory, so the trajectory will reach U_b at $V = \infty$. Since there is a finite time singularity, the trajectory reaches $V = \infty$ and hence reaches U_b at the blow up time. $\square$

Returning to the time of flight integral $\tau(U_0)$ given in Equation (3.32), we may find all solutions to the BVP by considering $\tau(U_0)$ for $U_0^* < U_0 < 1$. Clearly, $\tau(1) = 0$. In general, we find that τ has one critical point, and has the shape seen in Figure 3.3. Hence, there are at most 2 solutions. Denote the solution corresponding to the smaller value of U_0 as U_L and the other as U_R. For small λ, these two solutions correspond to the perturbations from the stable (U_R) and unstable (U_L) catenoids. As was observed in the case of small λ, these two solutions bifurcate at a critical value of σ approximated in Equation (3.28). This bifurcation will occur for general λ as well, which may be observed by the fact that the only dependence of $\tau(U_0)$ on σ is as a scalar multiplier. It is clear that $\frac{\partial \tau}{\partial \sigma} > 0$, so that as σ is decreased, τ will decrease until a bifurcation point is reached.

The dependence of τ on λ is similar.

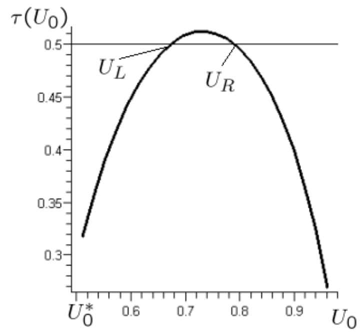

Figure 3.3: Sample plot of $\tau(U_0)$, demonstrating the two solution structure. Here, $\lambda = 0.7$, $\sigma = 1.13$, and $\delta_1 = 0.23$

Theorem 5 *For fixed σ, δ_1, there is a critical voltage λ^{**} for which no solution exists for $\lambda > \lambda^{**}$*

Proof: We begin by rewriting the time of flight integral as

$$\tau = \sigma \int_{U_0}^{1} \left\{ \left(\frac{U}{U_0 + \lambda\Gamma} \right)^2 - 1 \right\}^{-1/2} dU \ , \tag{3.50}$$

where

$$\Gamma := \frac{1}{\ln(U/\delta_1)} - \frac{1}{\ln(U_0/\delta_1)} \ . \tag{3.51}$$

Since $U \geq U_0$ in the integral τ, it follows that $\Gamma < 0$. We take a derivative with respect to λ, obtaining

$$\frac{\partial \tau}{\partial \lambda} = \sigma \int_{U_0}^{1} \left\{ \left(\frac{U}{U_0 + \lambda\Gamma} \right)^2 - 1 \right\}^{-3/2} \frac{\Gamma U^2}{(U_0 + \lambda\Gamma)^3} \ dU \ . \tag{3.52}$$

Note that $U_0 > U_0^*$, which satisfies Equation (3.43). Hence

$$U_0 - \frac{\lambda}{\ln(U_0/\delta_1)} > U_0^* - \frac{\lambda}{\ln(U_0^*/\delta_1)} = \frac{\lambda}{\ln \delta_1} > \frac{\lambda}{\ln(U/\delta_1)} \ , \tag{3.53}$$

with the last inequality holding since $U < 1$. This implies that $U_0 + \lambda\Gamma > 0$ in the region of integration. It follows that $\frac{\partial\tau}{\partial\lambda} < 0$ and thus there exists λ^{**} such that $\tau(U_0) < 1/2 \; \forall U_0 \in [U_0^*, 1]$ and $\forall \lambda > \lambda^{**}$. $\square$

Physically, λ^{**} determines the critical voltage. When the voltage is turned up beyond this value, the electrostatic forces become too strong in the system, and stability is lost. It is worth comparing this instability with that of the outer cylinder. As we saw in Chapter 2, there were two different instabilities that could occur – a “pinch-off” associated with the critical length, and a “pull-in” instability associated with the critical voltage. Very different physical mechanisms were seen at the onset of each of these instabilities. Mathematically, we saw this difference by the fact that the stable solution would bifurcate and vanish differently when λ^* was reached than when σ^* was reached, and we explored the relationship of λ^* to σ^* in Section 2.5.1.

In the present inner cylinder geometry, however, reaching the critical voltage λ^{**} is equivalent to reaching the critical length at σ^{**}. Mathematically, there are only two solutions, and so the same bifurcation occurs whether it is reached by increasing λ or by decreasing σ. Physically, the instability seen at these critical values should be equivalent as well. When the critical length is reached, the membrane wants to pinch off at the midplane. It will not be able to do this due to the presence of the inner cylinder, and so instead the membrane will collide with the inner cylinder, which is the same physical result expected with “pull-in” when the critical voltage is reached. This relates the fact that the electric field is in some sense combining with surface tension forces, and so there is no balancing effect as was seen in Chapter 2.

As was mentioned, $\tau(1) = 0$. Since $\tau(U_0)$ has only one critical point, the number of solutions to the BVP depends on $\tau(U_0^*)$. This is equivalent to the time of blow up for the trajectory starting at U_0^*, and we denote it by t_b^*. One further point of interest is found by analyzing t_b^* as a function of λ and σ. If $t_b^* < 1/2$, then $\tau(U_0)$ will cross the line $\tau = 1/2$ twice, yielding two solutions. If $t_b^* > 1/2$, the curve will only cross the line $\tau = 1/2$ once, yielding only the solution U_R. From Equation (3.49) we have

$$t_b^* = \int_{U_0^*}^{1} \frac{dU}{f(U;U_0^*)} \ . \tag{3.54}$$

We deduce from Equation (3.43) that $U_0^* \to \delta_1$ as $\lambda \to 0$ and $U_0^* \to 1$ as $\lambda \to \infty$. This means that t_b^* will approach zero as λ approaches zero and infinity. In the former case, U_0^* approaches the singularity at δ_1, and in the latter case the region of integration shrinks to a point.

Hence, t_b^* goes to zero at the extreme values of λ. If $t_b^*(\lambda)$ stays below $1/2$ $\forall\lambda$, then we can always find two solutions to the BVP for $\lambda < \lambda^{**}$. However, we observe again that σ may be pulled out of the integral t_b^*, which implies that there exists σ^s so that part of $t_b^*(\lambda)$ crosses above $1/2$ when $\sigma > \sigma^s$. In this case, let λ_1 and λ_2 correspond to the values at which the curve intersects the line $t_b^* = 1/2$, with $\lambda_1 < \lambda_2$. Then

- There are two solutions for $\lambda < \lambda_1$.
- Only one solution, U_R, exists for $\lambda_1 < \lambda < \lambda_2$.
- There are again two solutions for $\lambda_2 < \lambda < \lambda^{**}$, which bifurcate at λ^{**} .

This peculiar result suggests that for certain values of σ, the solution U_L disappears as λ is increased and then returns. The value λ_1 corresponds to the point where $t_b^* = 1/2$. At this value, the trajectory which asymptotically approaches $U = 1$ represents the solution U_L, because the time of blow up is exactly $1/2$, and so this trajectory is actually reaching $U = 1$ in time of flight $1/2$. Physically, the membrane is intersecting the boundary, i.e., the rings, with infinite slope. The same is true at $\lambda = \lambda_2$. As we now show, the solution for $\lambda_1 < \lambda < \lambda_2$ is only lost from our analysis because the curve $r = U(z)$ is not well defined in this region.

3.2.4 Parametric formulation

To retrieve the "disappearing" solutions just described, we parameterize the membrane by arc length s. Letting the membrane be defined in cylindrical coordinates by $r(s)$ and $z(s)$, we may rewrite the ODE of Equation (3.12) as

$$\dot{z} - \sigma^2 r(\ddot{r}\dot{z} - \dot{r}\ddot{z}) = \frac{-\lambda}{r \ln(r/\delta_1)^2} \ . \tag{3.55}$$

The left hand side of Equation (3.55) is the mean curvature operator expressed parametrically. Multiplying Equation (3.55) by first $\dot{z}$ and then separately by $\dot{r}$, and manipulating the relation $\sigma^2\dot{r}^2 + \dot{z}^2 = 1$, we obtain the following:

$$\begin{aligned} \ddot{r} &= \frac{\lambda \dot{z}}{\sigma^2 r^2 \ln(r/\delta_1)^2} + \frac{\dot{z}^2}{\sigma^2 r} \\ \ddot{z} &= \frac{-\lambda \dot{r}}{r^2 \ln(r/\delta_1)^2} - \frac{\dot{z}\dot{r}}{r} \ . \end{aligned} \tag{3.56}$$

The initial conditions become

$$z(0) = 0, \quad r(0) = r_0, \quad \dot{r}(0) = 0, \quad \dot{z}(0) = \sqrt{1 - \sigma^2\dot{r}(0)^2} = 1 \ . \tag{3.57}$$

Using a standard shooting procedure, we are able to locate the missing solution U_L. In Figure 3.4, we plot a sequence of solution curves for $\sigma > \sigma^s$ as λ is increased to the bifurcation point λ^{**}. As λ approaches λ_1, the angle that U_L makes with the boundary increases to infinity. As we continue to increase λ beyond λ_1, U_L continues to "bulge out", so that in Figure 3.4C, the profile cannot be represented as a function. Hence its disappearance from our analysis of $r = U(z)$. Note that in this region, physically the membrane has gone through the rings at the boundary. Eventually the profile tucks back in, having infinite slope at the boundary again at λ_2. At this point U_L returns to our analysis and bifurcates with U_R at λ^{**}.

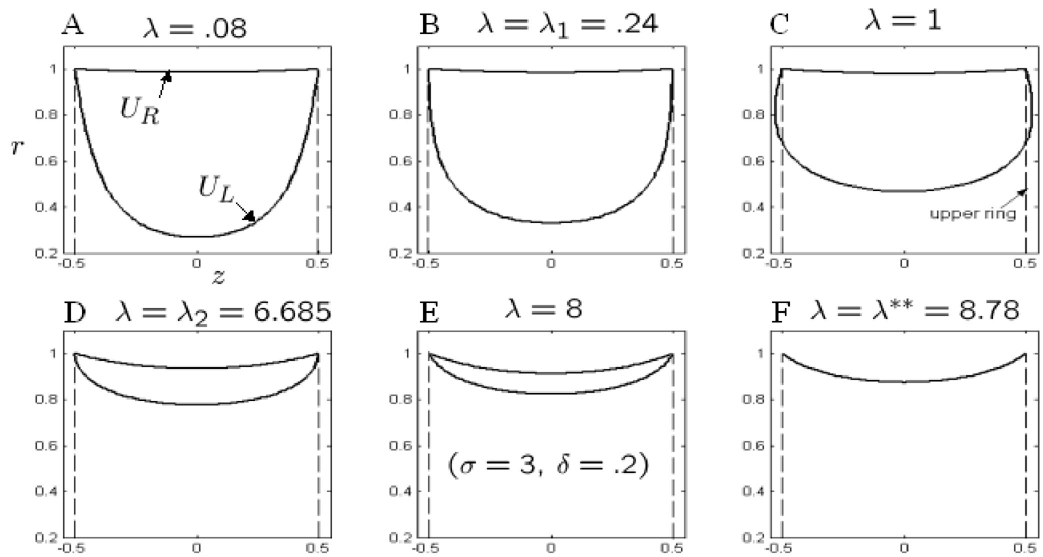

Figure 3.4: Progression of the membrane profiles as voltage is increased. (Note that the full surfaces may be envisioned by rotating the curves about the z-axis.) B and D mark the values λ_1 and λ_2 between which the solution U_L is not a function and the membrane protrudes through the rings, as seen in C. In F the critical voltage λ^{**} is reached and the two solutions become one. There is no solution beyond F.

3.2.5 Stability

As we have seen, the system has two solutions, U_L and U_R, which bifurcate when λ is increased or when σ is decreased. In relation to Section 3.2.2, U_R corresponds to the perturbation from the stable catenoid in the case of small voltage, and U_L corresponds to the perturbed unstable catenoid. We expect that in the general case, U_R should be stable and U_L unstable.

To verify this, we employ the method due to Maddocks [37] which we described in Section 2.6.2. In Figure 3.5, bifurcation diagrams are plotted for fixed δ_1 and various choices of σ. In Figure 3.5(a) is a plot of λ versus $U(0)$, i.e., the radius at the midplane. When $\lambda = 0$ the two catenoid solutions are found, and as λ is increased the outer solution U_R deflects inward and the inner solution U_L deflects outward until the bifurcation point λ^{**} is reached. Decreasing σ causes the two solutions to be closer when $\lambda = 0$ and thus the bifurcation occurs at a smaller value of λ. This is all in line with our expectations.

In Figure 3.5(b), the same solution branches are plotted in the preferred coordinates, which in this system are λ versus $-F_\lambda = -\int_{-1/2}^{1/2} \ln(\delta_1/U(z))^{-1}\, dz$. The general structure of the diagram has not changed, except for the important difference that the branches are inverted vertically; i.e., the upper branch corresponds to the lower branch of Figure 3.5(a), and vice versa. We infer via the theorems of Maddocks that the lower branch, which corresponds to the solutions U_R, is the more stable branch while the upper branch corresponding to U_L is unstable. That the lower branch does indeed correspond to local minima of the functional is established by the known stability results of zero voltage at the end of the branch.

3.3 Experimental investigation

To accompany the theoretical exploration that we have described in this chapter, in this section we present an experimental investigation of the electrostatically

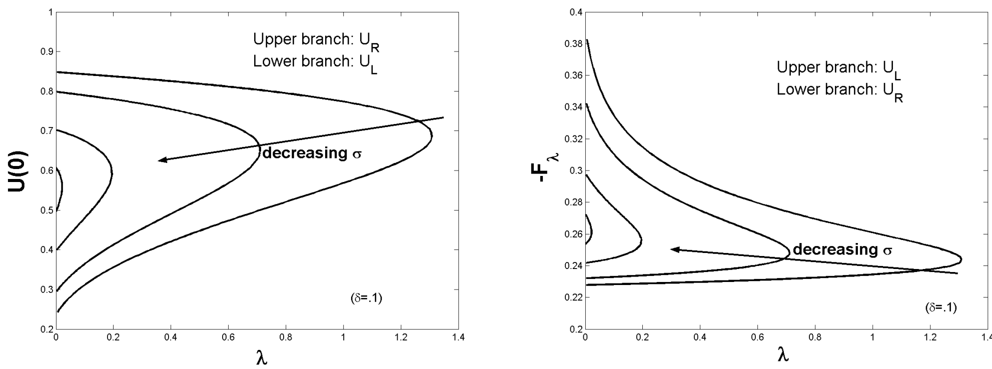

(a) $U(0)$ versus λ

(b) The "preferred coordinates"

Figure 3.5: Bifurcation diagrams for the system as σ is altered.

deflected soap-film bridge in the inner cylinder geometry. We discuss the results of the experimental analysis and compare these results with the theory.

3.3.1 Experimental apparatus

The experimental setup is depicted schematically in Figure 3.6. Two plastic tubes with an inner radius of 26.1 mm are held parallel on a common axis. The upper tube is fixed to a lab stand while the lower tube is situated on a jack to enable the length between the tubes to be altered. A copper rod with outer radius 6.25 mm is situated along the radial axis of the tubes. A soap-film membrane is suspended between the tubes, forming a catenoid. A Glasman WR Series 250 DC High Voltage Power Source (HVPS) of variable voltage is attached to the copper rod, and the lower tube is grounded in order to apply a potential difference between the rod and the membrane.

In our experiments soap-film undergoes visible deflections at voltages less than 10 kV. In Figure 3.7 we show a sample image of the membrane with the HVPS turned off (Figure 3.7(a)) compared with the profile when a potential difference of 8 kV is applied (Figure 3.7(b)).

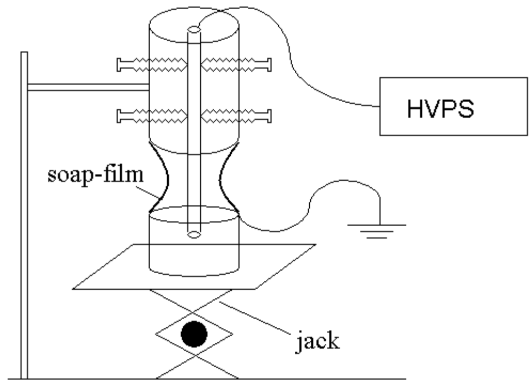

Figure 3.6: The experimental setup

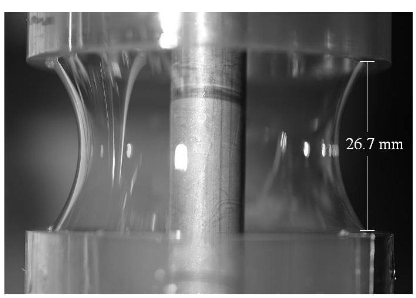

(a) 0 kV

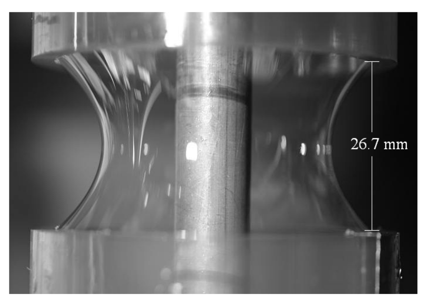

(b) 8 kV

Figure 3.7: Membrane profiles at the specified voltages.

3.3.2 Experimental difficulties

One of the obstacles in collecting data involves the uniformity of the soap-film membrane. Initial attempts at the experiment involved using a simple mixture of 5 parts water, 1 part Dawn dishwasher soap and 1 part Glycerol for the soap solution. The problem with this mixture was that when we would create a catenoid between the rings, the soap-film would visibly drain. If the catenoid were left sitting for 10 minutes, the film would drain to the point that a visible line of drainage would appear, above which just a wisp of soap-film remained. If this "wisp" of a catenoid did not just burst on its own, it would rupture once any electric field was added. Since the experiment would not always take the same amount of time to complete, there was no uniformity in the membrane so that, for instance, we could not presume surface tension to be constant throughout.

To counter this problem, we used a more sophisticated Sodium oleate soap solution recipe, originally from Rayleigh [59], modified by Robinson and Steen [61], and used in similar proportions as Robinson and Steen in our experiment. This new soap recipe was much improved. In running the experiment, we create a catenoid and then allow it to sit and drain for 10 minutes. After 10 minutes, the soap-film still remains intact and strong, and the draining is very minimal. Thus, we could presume a uniform membrane in running the experiment after 10 minutes.

Another experimental challenge concerns current. In earlier experimental attempts, we placed one set of screws in the upper tube and one set in the lower tube. While this allowed for slightly more accurate placement of the rod, after running the experiment several times the lower tube would become very moist and begin to conduct. Thus, at high voltages the HVPS would connect to ground across the lower set of plastic screws and up the moist lower tube, so that we would be unable to get the voltage beyond a certain value without introducing a current. By having two sets of screws in the upper tube, we are able to have a stable center rod, but it is much less likely for voltage to “leak”, because soap solution does not drain into the upper tubes and with this setup there is no physical connection between the lower tubes and the HVPS.

3.3.3 Membrane profile

Figure 3.8 shows a comparison between predicted and observed membrane shape as a function of voltage. The device was set at a fixed length of 26.7 mm, and images were captured with voltages of 0, 3, 6, and 8 kV. As is evident in Figure 7, we find good agreement with the theory. At this length, stability is lost at slightly greater than 8 kV. It appears then that the theory remains valid in predicting the shape throughout the range of stable equilibria.

Observe that there is a slight asymmetry present in the membrane profile, in that the distance between the membrane and the inner electrode at the midplane is not identical on the right and left sides. In Figure 7(a), when the voltage is off, we measure there to be a discrepancy of approximately 0.4 mm. However, as the voltage is turned up, this slight asymmetry becomes amplified, so that in Figure 7(d) when the voltage is 8 kV, the discrepancy has increased to approximately 1 mm. It seems that anything other than a perfect symmetry at the start will result in apparent asymmetry at high voltage, and so we find at least some asymmetry to be unavoidable.

The problem does arise, however, of whether to use the right or the left side when comparing with theory. Our method was as follows: a necessary parameter in computing the shape is surface tension. It is fairly difficult to determine the exact value of surface tension for a catenoid bridge under our experimental conditions. The use of a tensiometer, for instance, cannot account for the draining of the soap-film during which surface tension is changing. Hence, we backed out the value of surface tension as the value for which the profile matched the experiment in the case of 8 kV, and then verified this value by the subsequent matching at the other voltages.

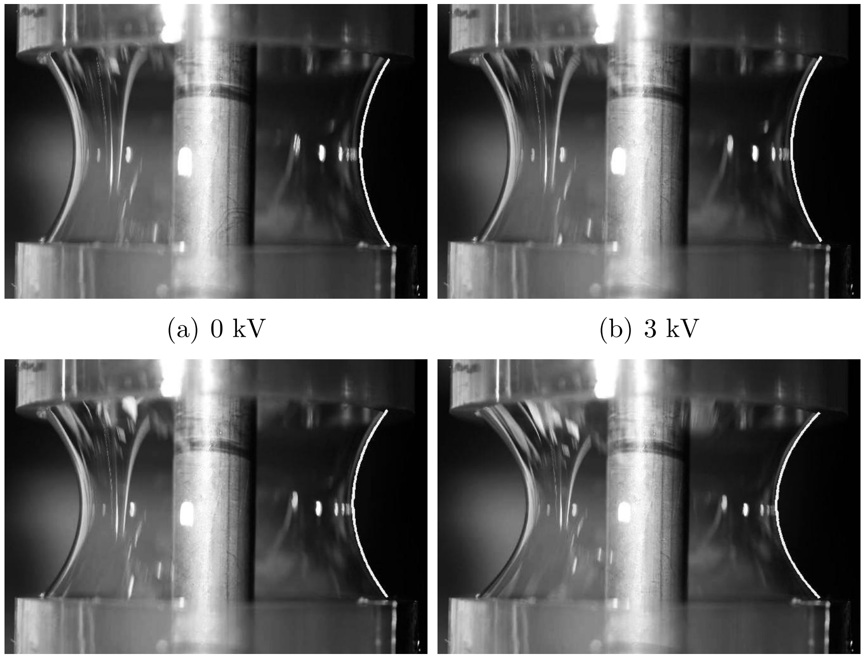

(a) 0 kV (b) 3 kV

(c) 6 kV (d) 8 kV

Figure 3.8: Membrane profiles at the specified voltages. The grey curve on the right side of each picture is the predicted shape from the theory.

In doing this and matching with the right side, the value of surface tension was 33 dyn/cm. A similar strategy on the left side produced a best fit surface tension of approximately 30 dyn/cm. We deduce that the surface tension is approximately 31.5±1.5 dyn/cm.

It is likely that the role of surface tension is more complicated than we give it credit for, and may be altered with the addition of an electric field. From our experimental comparison, it at least seems reasonable to treat it as a uniform constant. Just how large of a role changes in surface tension play is an interesting problem, and one that we leave for future work.

It should be clear that the membrane does not deflect linearly with the voltage. Analytically, this is evident from the qualitative nature of the function $\tau(U_0)$.

Table 3.1: Radius of the midplane for the different voltages. The last column gives the percent by which the radius decreased from the previous data point.

Voltage(kV)	Radius(mm)	Percent decrease
0	20.36	-
3	20.25	0.52
6	19.40	4.21
8	18.34	5.4

In viewing Figure 3.8, this is quite clear experimentally as well. The membrane deflects significantly more as the voltage is increased from 6 to 8 kV than from 0 to 3 kV. This effect is quantified in Table 3.1, in which the radius of the midplane is catalogued at each different voltage. The final column of this table contains the percent by which the radius decreases with each incremental increase in voltage, and we see that the effect becomes far more pronounced as the voltage is increased.

3.3.4 Critical length

Figure 3.9 displays a plot comparing critical length as a function of voltage obtained theoretically and experimentally. The experiment is performed by turning the voltage to a given value, and then slowly increasing the length of the device until the membrane collapses at the onset of instability. Length is measured to a tenth of a millimeter. When the membrane appears close to collapsing, we slow the rate of length increase, allowing the membrane several seconds before determining whether it is stable. The triangular points in Figure 3.9 represent the experimentally determined values. The solid line is the theoretical critical length as determined through the perturbation theory and given by Equation (3.28). As would be expected, the asymptotic theory matches well with the experimental data in the case of small voltage, and loses validity as voltage is increased. Note that for higher voltage, the asymptotic theory predicts a smaller critical length than is found experimentally. This suggests that the electrostatic force is overestimated in the asymptotic approach, and thus that the higher order terms in the expansion would serve to decrease the electrostatic effect.

The line with the circles is obtained from the phase plane analysis of Section 3.2.3 by considering the time of flight integral $\tau(U_0)$. These values take the full model into account, and are found to agree well with the experiment for all voltages tested. Accompanying this curve are error bars. The main sources of error arise in the accurate measurement of surface tension and ring radius. The plastic tubes have a thickness of approximately 4 mm. The assumption is that the soap-film always sits on the inner edge of the tubes, and so the radius used in our data was based upon this assumption. It is not entirely clear that this is always the case. Also, the tubes used were not perfect cylinders, and so radius fluctuated on the order of 1 mm based on where tube measurements were taken. For these reasons, we only assumed the radius at the boundary to be a known value within $\pm$ 1 mm. As was mentioned, surface tension was assumed to be correct to within $\pm$ 1.5 dyn/cm. The error bars around the numerically produced curve relate these discrepancies. In all cases, the observed data falls within the error bars.

It is expected that these trends should remain true if Figure 3.9 were to be continued for higher voltages. However, beyond 9 kV, the problem of voltage "leak" discussed earlier was found to be unavoidable and thus this region was untestable with our experimental setup.

3.4 Discussion

In this chapter we investigated a soap-film catenoid subjected to an axially symmetric electric field with the geometry of the cylindrical electrode inside the membrane.

Theoretically, a model to describe equilibrium solutions was formulated via variational techniques. In the asymptotic regime of small voltage, we obtained exact solutions as well as an expression to approximate critical length. This approximation

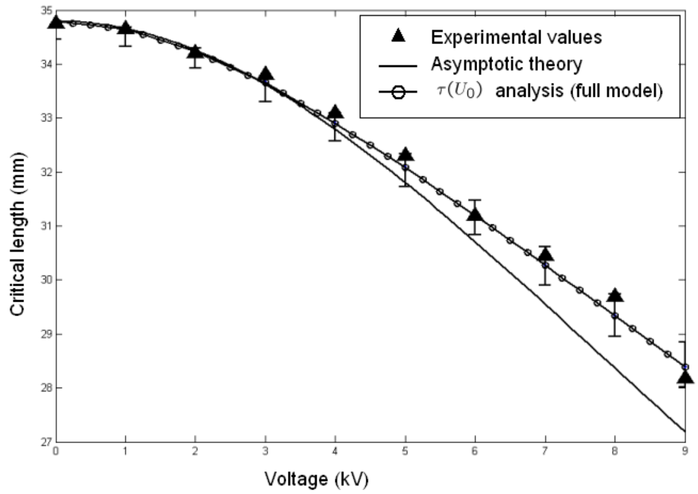

Figure 3.9: Comparison of experiment to theory for the critical length as a function of voltage. The error bars account for variations in measurements of surface tension and ring radius.

enabled us to understand the interplay of electrostatic forces and surface tension. With voltage present, the membrane collapse occurs at a shorter length than with no field. This is in direct contrast to the result of Chapter 2, and demonstrates the importance of geometry in the system. Experimental observations verified the accuracy of the asymptotic approximation of critical length in the case of small voltage, and also demonstrated its limit in predictability for higher voltages.

The general solution structure was classified by developing an analysis of trajectories in phase space. This analysis was found to agree well with experimental observations in predicting the membrane profile. The experimental analysis also demonstrated the problem of asymmetry amplification, whereby slight asymmetry in the experimental setup becomes amplified as the electric field is strengthened. This problem seems almost unavoidable in a physical setup, but is absent in the model. This suggests the possible future direction of an asymmetric formulation of the model.

Chapter 4

VARIATIONS ON SOAP-FILM BRIDGE IN AN ELECTRIC FIELD

4.1 Introduction

In the previous two chapters, we considered two different geometries for the problem of a soap-film bridge in an electric field. In this chapter we consider variations and extensions to the analysis of the previous chapters. In Section 4.2, we allow the ring radii to be unequal. This asymmetrical setup poses a difficulty in the analysis even in the absence of an electric field, and so we begin with the zero voltage case. After establishing stability and solution structure in the absence of external forces, we add an electric field. We consider both the inner and outer cylinder setups, explore the effect of the ratio of the ring radii, and compare with results obtained in Chapters 2 and 3.

An interesting extension to the analysis of Chapters 2 and 3 is to add a volume constraint. Physically, the addition of a volume constraint brings the analysis into the realm of *liquid* bridges. That is, the membrane may be thought of as the interface between a finite volume of liquid and a gas. Results become more meaningful in terms of understanding drops, columns, and liquid bridges, which has direct application in a number of industrial processes as discussed in Chapter 1. Experimentally, soap-film still provides a viable tool. A volume constrained soap-film will behave in the same manner as a bridge of finite liquid so long as gravity is negligible.

Even before applying an electric field, the volume constrained problem becomes significantly more difficult mathematically. The volume constraint is treated by adding a Lagrange multiplier representing pressure to the energy functional. The catenoid solution of zero voltage was a minimal surface, i.e., it had mean curvature equal to zero. Add the volume constraint, and the solution becomes one of *constant mean curvature*. This change makes the problem significantly more complicated. Indeed, in our cylindrical geometry, an analytical solution has not been found except in special cases.

4.2 Different ring radii

In Chapters 2 and 3, the catenoid bridge spanned two rings of the same radius. In this section, we consider a variation of this setup and allow the two rings to have different radii. In the previous chapters, both rings had radius a. We refer to this previous setup as the "a-a" problem. In this section, we take one ring to have radius a and the other to have radius b. We refer to this setup as the "a-b" problem.

A possible motivation for considering this variation could be found in terms of design optimization. Consider, for instance, the following theoretical device: suppose that the outer cylinder setup of the catenoid bridge is modified to serve as a pump apparatus. That is, suppose a fluid reservoir exists on one end of the bridge. Turning on the voltage causes the membrane to deflect outward, which creates a pressure difference and causes the bridge to draw in fluid from the reservoir. If the voltage is turned back off, the bridge will pump the fluid out the other end. A basic engineering problem that would arise naturally with such a device is to find the different length parameters that optimize the device in some way (perhaps maximize the speed of pumping). It is certainly possible that the optimal configuration occurs in an asymmetric setup with unequal radii at the input and output ends of the pump.

In order to do study this variation, we first consider the problem without an electric field. This problem has been studied before, but due to the loss of symmetry, the solution is much more difficult to analyze and the standard stability results are lost. Hence we begin by deriving these results.

4.2.1 Zero voltage solution

We begin by considering the “a-b” problem in the absence of an electric field; i.e., a membrane suspended between two rings of different radius. We maintain axial symmetry, but no longer have symmetry about the midplane between the rings. This problem has been solved before [29]. However, we take a slightly different approach which will help illuminate the form of the solution as well as facilitate certain calculations once an electric field is added.

Let the surface of revolution be given as $y = y(x)$, with $x = 0$ midway between the rings. The problem is to find the function $y(x)$ that minimizes the surface area

$$A = 2\pi \int_{-L/2}^{L/2} y\sqrt{1+y'^2}\, dx \tag{4.1}$$

subject to the boundary conditions $y(-L/2) = a$, $y(L/2) = b$, where a and b are the radii of the two rings, $a \neq b$, and L is the distance between them. Applying the Beltrami identity to the functional, it is determined that $y(x)$ is of the form

$$y(x) = c_1 \cosh(\frac{x - c_2}{c_1})\ . \tag{4.2}$$

The boundary conditions implicitly define c_1 and c_2 as the solutions to

$$c_1 \cosh(\frac{-L/2 - c_2}{c_1}) = a, \quad c_1 \cosh(\frac{L/2 - c_2}{c_1}) = b\ . \tag{4.3}$$

Equations (4.3) cannot be solved exactly and are difficult to analyze. We propose an equivalent solution which is more tractable. Returning to Equation (4.1) and taking a variational derivative, we find that $y(x)$ must satisfy

$$1 + y'^2 - yy'' = 0\ , \tag{4.4}$$

which simply states that the mean curvature must vanish everywhere. To solve this, we first make the change of variables $z = x/L$ and $u = 2y/(a+b)$. Thus, we have scaled x by the distance between the rings, and y by the average of the ring radii. The boundary value problem becomes

$$\begin{aligned} 1+&\sigma^2 u'^2 - \sigma^2 uu'' = 0 \\ u(1/2) &= \frac{2a}{a+b} := \gamma_1 \\ u(-1/2) &= \frac{2b}{a+b} := \gamma_2\ , \end{aligned} \tag{4.5}$$

where $\sigma = (a+b)/(2L)$. To proceed, we assume a solution of the form $u(z) = A\cosh(cz) + B\sinh(cz)$. Substitution into the differential equation implies

$$A^2 - B^2 = \frac{1}{\sigma^2 c^2}\ , \tag{4.6}$$

and the boundary conditions enable us to solve for A and B exactly. We find that

$$A = \frac{\gamma_1 + \gamma_2}{2\cosh(c/2)}, \quad B = \frac{\gamma_1 - \gamma_2}{2\sinh(c/2)}\ . \tag{4.7}$$

Combining Equations (4.6) and (4.7), we obtain the following relationship between c and σ

$$\sigma = \frac{2\cosh(c/2)\sinh(c/2)}{c\left\{2\gamma_1\gamma_2\left(\sinh^2(c/2) + \cosh^2(c/2)\right) - \gamma_1^2 - \gamma_2^2\right\}^{1/2}}\ . \tag{4.8}$$

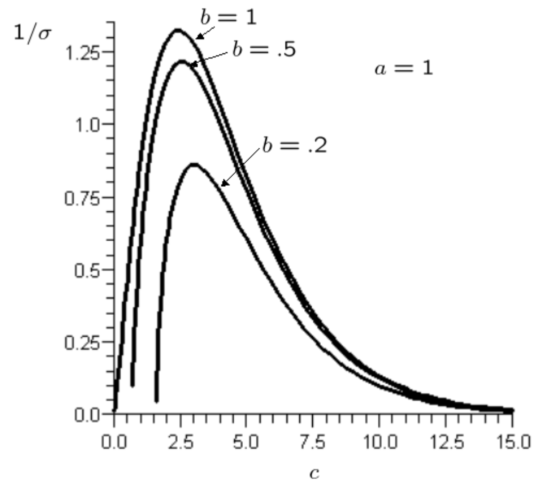

Figure 4.1: Plots of $1/\sigma$ as a function of c for $a = 1$ and different values of b.

Figure 4.1 shows a plot of $1/\sigma$ as a function of c, given by Equation (4.8) for $a = 1$ and various choices of b. When the radii are equal, the solution reduces to the catenoid $u = \cosh(cz)/(c\sigma)$ of the previous chapters, with $\sigma = \cosh(c/2)/c$. This relationship is given by the curve in Figure 4.1 with $b = 1$. As we have stated before, in this case there are two solutions for all σ greater than approximately 0.7544 (or $1/\sigma < 1.3256$ when viewing Figure 4.1). The leftmost value of c corresponds to a stable solution, the right value of c corresponds to an unstable solution, and these two solutions bifurcate at $\sigma \approx 0.7544$. The structure is the same in the general case $a \neq b$. For a given value of σ, there are two possible values of c for which we have a solution, and there is a critical value of σ below which there is no solution. Observe that this critical σ will always be greater than the critical value in the equal radius case, 0.7544. If we think of the radii as being fixed, moving towards the critical σ is achieved by increasing the length between the rings. Hence, to put this in terms of a critical length at which the membrane pinches off, we find that the critical length becomes shorter as the difference between a and b is increased. The longest stable catenoid solution that can be attained is when the radii are equal, and as $b \to 0$ while keeping $a = 1$, the critical length goes to zero, as would be expected.

We still have not investigated stability of the solutions when $a \neq b$. To do this, we consider the second variation of the functional. Stability is classified in terms of conjugate points of a Sturm-Liouville problem. For the functional at hand, we consider the solution $h(z)$ of

$$\begin{gathered} \frac{d}{dz}\left(\frac{u}{(1+\sigma^2 u'^2)^{3/2}} h'\right) + \frac{u''}{(1+\sigma^2 u'^2)^{3/2}} h = 0 \\ h(-1/2) = 0, \quad h'(-1/2) = 1 \; . \end{gathered} \tag{4.9}$$

If there are no values $c \in (-1/2, 1/2]$ such that $h(c) = 0$, then the function $u(z)$ is stable. Otherwise, it is unstable.

Theorem 6 *For any values of a and b, the peak of the curve of $1/\sigma$ in Figure 4.1 serves as a stability boundary.*

Proof: To prove this, we show that the only place where $h(z)$ has a conjugate point at $z = 1/2$ is at the peak of $1/\sigma$.

Inserting $u(z) = A\cosh(cz) + B\sinh(cz)$ into Equation (4.9), we find that h must solve

$$h'' - 2c\frac{A\sinh(cz) + B\cosh(cz)}{A\cosh(cz) + B\sinh(cz)} h' + c^2 h = 0 \; . \tag{4.10}$$

Make the change of variables $y = A\sinh(cz) + B\cosh(cz)$ and let $v(y) = h(z)$. Equation (4.10) becomes

$$\left(y^2 + (A^2 - B^2)\right) v'' - yv' + v = 0 \; . \tag{4.11}$$

This equation is found to have solution

$$v(y) = C_1 y + C_2\left(-\sqrt{y^2 + A^2 - B^2} + y \operatorname{arcsinh}\left(\frac{y}{\sqrt{A^2 - B^2}}\right)\right) \tag{4.12}$$

or,

$$h(z) = C_1(A\sinh(cz) + B\cosh(cz)) + C_2\Bigg[-(A\cosh(cz) + B\sinh(cz)) + \\ (A\sinh(cz) + B\cosh(cz))\operatorname{arcsinh}\left(\frac{A\sinh(cz) + B\cosh(cz)}{\sqrt{A^2 - B^2}}\right)\Bigg] . \quad (4.13)$$

Impose the boundary conditions that $h(-1/2) = 0$ and $h(1/2) = 0$. Note that the value of $h'(-1/2)$ is arbitrary. Inserting the boundary conditions gives a necessary condition on c for the constants C_1 and C_2. After some simplification, this condition is expressed as

$$2\sinh(c/2)\cosh(c/2)(B^2 - A^2) + \left(B^2\cosh^2(c/2) - A^2\sinh^2(c/2)\right) \cdot \\ \left[\operatorname{arcsinh}\left(\frac{B\cosh(c/2) - A\sinh(c/2)}{\sqrt{A^2 - B^2}}\right) - \operatorname{arcsinh}\left(\frac{B\cosh(c/2) + A\sinh(c/2)}{\sqrt{A^2 - B^2}}\right)\right] = 0 . \quad (4.14)$$

Define $f(c) = 1/\sigma$, where σ is given by Equation (4.8). Set $f'(c) = 0$, which may be expressed as

$$\gamma_1\gamma_2\left[2\cosh(c)\sinh(c) - c(\cosh^2(c) + 1)\right] - (\gamma_1^2 + \gamma_2^2)\left[\sinh(c) - c\cosh(c)\right] = 0 . \quad (4.15)$$

Note that in arriving at Equation (4.15), we have used the following hyperbolic function identities:

$$\sinh^2(c/2) + \cosh^2(c/2) = \cosh(c) \quad (4.16a)$$

$$2\cosh(c/2)\sinh(c/2) = \sinh(c) . \quad (4.16b)$$

We claim that the conditions given by Equations (4.14) and (4.15) are equivalent. To see this, consider the terms inside the inverse hyperbolic sines in Equation

(4.14). Observe that $(B\cosh(c/2) - A\sinh(c/2))$ is just $u'(-1/2)$, and $(B\cosh(c/2) + A\sinh(c/2))$ is $u'(1/2)$. Rewriting $u(z)$ in the equivalent form

$$u = A\cosh(cz) + B\sinh(cz) = \alpha\cosh(cz - \nu) \ , \tag{4.17}$$

where α and ν satisfy

$$\alpha^2 = A^2 - B^2, \quad \nu = \operatorname{arccosh}(A/\alpha) \ , \tag{4.18}$$

we find that

$$\begin{gathered} \frac{u'(-1/2)}{\sqrt{A^2 - B^2}} = \sinh(-c/2 - \nu), \\ \text{and} \\ \frac{u'(1/2)}{\sqrt{A^2 - B^2}} = \sinh(c/2 - \nu) \ . \end{gathered} \tag{4.19}$$

The entire term involving the inverse hyperbolic sines is thus equivalent to $-c$. Applying also the identity Equation (4.16b), Equation (4.14) becomes

$$\sinh(c)(B^2 - A^2) - c\left[B^2\cosh^2(c/2) - A^2\sinh^2(c/2)\right] \ . \tag{4.20}$$

Next, write A and B in terms of the γ_i using Equations (4.6), and make use of the following:

$$\cosh^4(c/2) - \sinh^4(c/2) = \cosh^2(c/2) + \sinh^2(c/2) = \cosh(c) \tag{4.21a}$$

$$\cosh^4(c/2) + \sinh^4(c/2) = \frac{1}{2}(\cosh^2(c) + 1) \ . \tag{4.21b}$$

Equation (4.20) becomes

$$\sinh(c)(\gamma_1^2 + \gamma_2^2) - 2\gamma_1\gamma_2\cosh(c)\sinh(c) - (\gamma_1^2 + \gamma_2^2)c\cosh(c) + \gamma_1\gamma_2(\cosh^2(c) + 1)c = 0 \ , \tag{4.22}$$

which is identical to Equation (4.15). Therefore, the value of c corresponding to the peak of the curve $1/\sigma$ also corresponds to the appearance of a conjugate point, for all values of a and b. As it is the *only* point where a conjugate point can appear at $z = 1/2$, we conclude that the peak of the curve is a stability boundary and hence that one branch will be stable and the other unstable. The theorem is proved. $\square$

When $a = b$, we know that the left branch is the stable branch. To show this in the general case $a \neq b$, we note that as $1/\sigma$ goes to zero, $c \to \infty$ on the right branch, as can be seen in Figure 4.1. To check the stability of the right branch, we take the solution $h(z)$ given in Equation 4.13 and impose the conditions

$$h(-1/2) = 0, \quad h'(-1/2) = 1 \ .$$

With this solution, we compute $h(1/2)$ and then take the limit as $c \to \infty$. The value $h(1/2)$ is a complicated expression which we omit here. However, the limit is easily computed, and we find that

$$\lim_{c \to \infty} h(1/2) = -\frac{\gamma_1}{\gamma_2} < 0 \ . \tag{4.23}$$

This demonstrates that for any a and b, the very end of the right branch is unstable. By the above arguments, we conclude that in the case of arbitrary radii, the left branch is stable and the right branch is unstable. This confirms that the stability results in the arbitrary radii case are the same as when the radii are equal. While stability is easy to prove in the equal radius case, we have seen that it is significantly more challenging in the general case.

One implication of this analysis is that for all values of a and b, there are lengths which permit stable solutions. The curve $f(c) = 1/\sigma$ flattens out as the discrepancy between a and b becomes greater, i.e., as $b \to 0$ in Figure 4.1. This means that the distance between the rings necessary for a stable solution approaches zero as the radius of the smaller ring goes to zero, which is not physically surprising.

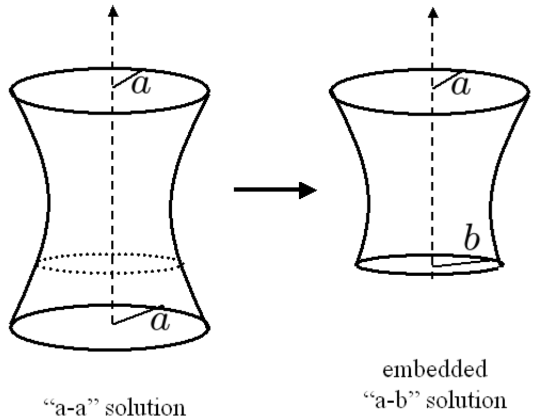

Figure 4.2: Schematic for the notion of embedded solutions.

One way to think about solutions to the “a-b” problem is to consider them as embeddings in a solution to an “a-a” problem. Given any portion of an “a-a” solution, it is easy to see that we may find infinite embedded “a-b” solutions by choosing any point between the two rings of radius a, and placing a ring having the appropriate radius at that point. This is depicted in Figure 4.2.

Note that stability is not directly transferable when thinking of these embedded solutions. If the solution to the “a-a” problem is stable, any embedded solution will be stable as well. However, it is possible to take an unstable solution to the “a-a” problem and find an embedded solution which is stable. This may be understood in terms of conjugate points. Suppose we have a solution to an “a-a” problem that is unstable. This means that $h(z)$ has a conjugate point somewhere in the domain of z; i.e., there exists c_0 such that $h(c_0) = 0$. Taking an embedding of this solution is equivalent to shrinking the domain. Hence, if we take an embedding such that c_0 is no longer in the domain, we remove the conjugate point, and thus the solution to the “a-b” problem is stable.

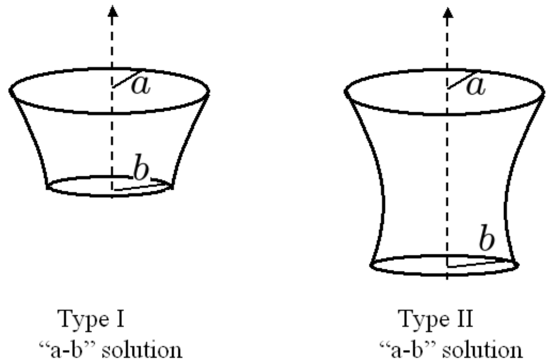

Figure 4.3: Type I versus Type II solutions to the "a-b" problem.

Note that all of the results we have derived so far concern a bridge in the absence of external forces. We make one more observation regarding the "a-b" problem, and then consider the addition of an electric field. Solutions to the "a-b" problem may be classified as one of two types. If the minimum radius occurs at the end ring, we refer to the solution as being of Type I. If the minimum radius occurs in the interior of the domain, we refer to this as Type II. This is sketched in Figure 4.3. By considering embedded solutions, it is clear that both types of solution are achievable. Suppose we have fixed a, b. Which solution type will we see? The difference in the two types may be expressed in terms of the sign of $u'(-1/2)$, i.e., the slope at the boundary of the smaller ring. If $u'(-1/2) > 0$, we will have Type I, while $u'(-1/2) < 0$ will correspond to Type II. Using the solution $u(z) = A\cosh(cz) + B\sinh(cz)$, we find that $u'(-1/2) = 0$ corresponds to $c = \operatorname{arccosh}(a/b)$. Denote this value of c by $\hat{c}$. If $c < \hat{c}$, the solution is of Type I and if $c > \hat{c}$ the solution is of Type II. Note also that when $c = \hat{c}$, the "a-b" solution is embedded directly in the middle of an "a-a" solution of twice the length.

We claim that the unstable solution is always of Type II. To prove this, we consider $f'(\hat{c})$. We will show that $f'(\hat{c})$ is always positive, meaning that $\hat{c}$ is always on the stable side of the branch of f. We have

$$f'(\hat{c}) = \frac{\left(2\gamma_1\gamma_2\cosh(\hat{c}) - \gamma_1^2 - \gamma_2^2\right)^{1/2}}{\sinh(\hat{c})} + \frac{\hat{c}\sinh(\hat{c})\gamma_1\gamma_2}{\left(2\gamma_1\gamma_2\cosh(\hat{c}) - \gamma_1^2 - \gamma_2^2\right)^{1/2}\sinh(\hat{c})} - \frac{\hat{c}\left(2\gamma_1\gamma_2\cosh(\hat{c}) - \gamma_1^2 - \gamma_2^2\right)^{1/2}\cosh(\hat{c})}{\sinh^2(\hat{c})} \ . \quad (4.24)$$

Using the relation $\cosh(\hat{c}) = \gamma_1/\gamma_2$, we make the simplification

$$\frac{\left(2\gamma_1\gamma_2\cosh(\hat{c}) - \gamma_1^2 - \gamma_2^2\right)^{1/2}}{\sinh(\hat{c})} = \gamma_2 \ . \quad (4.25)$$

Equation (4.24) reduces to

$$\gamma_2 + \frac{\hat{c}\gamma_1}{\sinh(\hat{c})} - \frac{\hat{c}\gamma_2\cosh(\hat{c})}{\sinh(\hat{c})} = \gamma_2 > 0 \ , \quad (4.26)$$

and we have proven the claim. As a side note, recall that $\sigma = (a+b)/(2L)$. By setting $1/\sigma = f(\hat{c})$ and solving for L, we obtain the critical length

$$L^* = b \,\mathrm{arccosh}(a/b) \ . \quad (4.27)$$

When $L < L^*$, the stable solution is of Type I. At $L = L^*$ there is a transition so that the stable solution is of Type II when $L > L^*$.

4.2.2 Small voltage - asymptotic analysis

Having established the structure of solutions in the absence of external forces, we add an electric field. We consider both the inner cylinder and outer cylinder configurations. These configurations are displayed in Figure 4.2.2.

The model is derived the same way as in Chapters 2 and 3. The only difference is in the scaling and the boundary conditions. We choose the z-axis so that $z = 0$

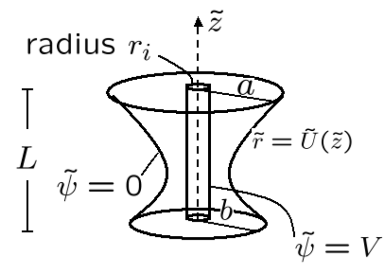

(a) Inner cylinder setup

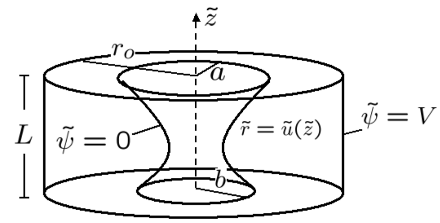

(b) Outer cylinder setup

Figure 4.4: Setup of the "a-b" problem with added electric field.

corresponds to the point midway between the rings. We then scale as follows. For the inner cylinder, we let

$$z = \frac{\tilde{z}}{L}, \quad r = \frac{\tilde{r}}{r_i}, \quad U = \frac{2\tilde{u}}{a+b}, \quad \psi = \frac{\tilde{\psi}}{V} \ . \tag{4.28}$$

For the outer cylinder, we let

$$z = \frac{\tilde{z}}{L}, \quad r = \frac{\tilde{r}}{r_o - \frac{a+b}{2}}, \quad u = \frac{2\tilde{u}}{a+b}, \quad \psi = \frac{\tilde{\psi}}{V} \ . \tag{4.29}$$

As before, in solving the potential equation for the electric field, we use a small aspect ratio so that the potential $\tilde{\psi}$ is radial to first order. The assumption in the inner cylinder case is that r_i/L is a small parameter. This is the same assumption as in Chapter 3. For the outer cylinder, the assumption is that

$$\frac{r_o - \frac{a+b}{2}}{L} << 1 \ . \tag{4.30}$$

Thus, we assume that the average of the gap size between the rings and the outer cylinder is small compared to the length. If $a = b$, this is equivalent to the small aspect ratio used in Chapter 2. Following the same procedure of deriving an energy functional and taking a variational derivative, we arrive at the following governing equations. For the inner cylinder:

$$\frac{1+\sigma^2 U'^2-\sigma^2 UU''}{(1+\sigma^2 U'^2)^{3/2}} = -\frac{\lambda}{U\ln^2(\delta_1/U)} \;, \tag{4.31}$$

where

$$\sigma = \frac{a+b}{2L}, \quad \delta_1 = \frac{2r_i}{a+b}, \quad \lambda = \frac{\epsilon_0 V^2}{(a+b)T} \;. \tag{4.32}$$

For the outer cylinder:

$$\frac{1+\sigma^2 u'^2-\sigma^2 uu''}{(1+\sigma^2 u'^2)^{3/2}} = \frac{\lambda}{u\ln^2(\delta_2/u)} \;, \tag{4.33}$$

where σ and λ are the same as in the inner cylinder setup, and

$$\delta_2 = \frac{2r_o}{a+b} \;. \tag{4.34}$$

As before, the parameter λ compares the relative strengths of electrostatic and elastic forces, and may be thought of as a control parameter for the voltage. In both the inner and outer cylinder setups, the boundary conditions are equivalent, i.e.,

$$U(-1/2) = u(-1/2) = \frac{2b}{a+b} =: \gamma_2, \quad U(1/2) = u(1/2) = \frac{2a}{a+b} =: \gamma_1 \;. \tag{4.35}$$

From a mathematical standpoint, these governing equations are identical to the governing equations we analyzed in Chapters 2 and 3. The only difference is in the boundary conditions, which are no longer symmetric.

Our first step in analyzing these systems is to perform an asymptotic analysis in the case of small voltage. We begin with the inner cylinder. Suppose $\lambda << 1$ and that $U(z)$ may be expanded as

$$U \sim U_0 + \lambda U_1 + \lambda^2 U_2 + \ldots \tag{4.36}$$

Note that in the analysis that follows, λ should be assumed to be bigger than the small aspect ratio parameter used to solve for the electric potential. This is the same necessary assumption we encountered in the asymptotic analyses of Chapters 2 and 3. Inserting the expansion (4.36) into Equation (4.31), U_0 must satisfy Equations (4.5), and is given by

$$U_0 = A\cosh(cz) + B\sinh(cz) \; , \tag{4.37}$$

where A and B are given by Equations (4.7) and c satisfies Equation (4.8). That is, the first order solution is simply the catenoid solution with no field. As we have found, there are always two first order solutions which bifurcate at a critical value of σ. At $O(\lambda)$, we have

$$\begin{aligned} &U_1'' - 2\frac{U_0'}{U_0}U_1' + \frac{U_0''}{U_0}U_1 = \frac{(1+\sigma^2 U_0'^2)^{3/2}}{\sigma^2 U_0^2 \ln^2(\delta_1/U_0)} \\ &U_1(\pm 1/2) = 0 \; . \end{aligned} \tag{4.38}$$

The homogeneous equation is identical to Equation (4.10). That is, the operator for the first order perturbation is the same as the operator for the conjugate points problem derived from the second variation of the functional without the electric field. Hence, from our analysis of Equation (4.10), the homogeneous problem will only have a solution at the bifurcation point corresponding to the peak of the curve $1/\sigma = f(c)$ defined in Equation (4.8). Denote this critical value σ_{cr}.

Similar to our analysis in Chapters 2 and 3, we can use solvability criterion to approximate the critical value of σ at which the bifurcation between the two solutions occurs. The analysis proceeds similarly to that of the "a-a" analysis in the previous chapters, and so we will be sparse with details. We let $\sigma^2 = \sigma_{cr}^2 + \nu\lambda$ and alter the expansion as

$$U \sim U_0 + \lambda^{1/2}U_1 + \lambda U_2 + \ldots \tag{4.39}$$

U_0 is the catenoid solution corresponding to the bifurcation point σ_{cr}. U_1 solves the homogeneous version of Equation (4.38), and is given by

$$U_1(z) = C_2 \cdot \left(K(z) - \frac{K(1/2)}{J(1/2)} J(z) \right) \ , \tag{4.40}$$

where

$$\begin{aligned} J(z) &= A \sinh(cz) + B \cosh(cz) \\ K(z) &= -(A \cosh(cz) + B \sinh(cz)) + (A \sinh(cz) + B \cosh(cz)) \cdot \\ &\qquad \operatorname{arcsinh}\left(\frac{A \sinh(cz) + B \cosh(cz)}{\sqrt{A^2 - B^2}} \right) \end{aligned} \tag{4.41}$$

and the constant C_2 is to be determined. Define $\hat{U}$ such that $U_1 = C_2 \hat{U}$. Then, at $O(\lambda)$, the solvability condition for U_2 may be expressed as

$$\int_{-1/2}^{1/2} G(C_2, \nu) \cdot U_2^h \, dz = 0 \ , \tag{4.42}$$

where

$$G(C_2, \nu) = \frac{(1 + \sigma_{cr}^2 U_0'^2)^{3/2}}{\sigma_{cr}^2 U_0^2 \ln(\delta_1/U_0)^2} - \frac{U_1 U_1''}{U_0} + \frac{U_1'^2}{U_0} + \nu \left(\frac{U_0'^2 - U_0 U_0''}{\sigma_{cr}^2 U_0} \right) \ . \tag{4.43}$$

For a, b, δ_1, and λ fixed, everything in Equation (4.42) is determined except for C_2 and ν. This relation may be written as

$$C_2^2 I_1 + I_2 = -\nu I_3 \ , \tag{4.44}$$

where

$$I_1 = \int_{-1/2}^{1/2} \frac{\hat{U}\hat{U}'^2 - \hat{U}^2\hat{U}''}{U_0}\, dz, \quad I_2 = \int_{-1/2}^{1/2} \frac{\hat{U}(1+\sigma_{cr}^2 U_0'^2)^{3/2}}{\sigma_{cr}^2 U_0^2 \ln^2(\delta_1/U_0)}\, dz,$$
$$I_3 = \int_{-1/2}^{1/2} \frac{\hat{U}(U_0'^2 - U_0 U_0'')}{\sigma_{cr}^2 U_0}\, dz\ . \tag{4.45}$$

Note that these integrals depend on the values of a, b and r_i, but that $I_1 < 0$, $I_2 < 0$, $I_3 > 0$. The critical value of σ with voltage on, which we denote σ_{in}^*, corresponds to the value of ν beyond which C_2 becomes complex valued. This occurs at $\nu = -I_2/I_3$, and hence

$$\sigma_{in}^* = \left(\sigma_{cr}^2 - \frac{I_2\lambda}{I_3}\right)^{1/2} . \tag{4.46}$$

By similar logic, the critical σ in the outer cylinder setup, denoted σ_{out}^*, is found to be

$$\sigma_{out}^* = \left(\sigma_{cr}^2 + \frac{I_2\lambda}{I_3}\right)^{1/2} , \tag{4.47}$$

where the I_i are given by Equations (4.45) except with δ_1 replaced by δ_2. Notice that $\sigma_{in}^* > \sigma_{cr} > \sigma_{out}^*$. As before, σ_{cr} represents the critical length at which stability is lost in the absence of a field. This value is of course dependent on the values of a and b. However, if we think of a and b as being fixed, this can be interpreted to mean that bifurcation will occur at a shorter length for the inner cylinder setup and a greater length for the outer cylinder setup. This is the same general result as was found in the equal ring radii analysis.

What is the effect of the discrepancy between the ring radii on the critical length? We saw in Figure 4.1 that the critical length with no applied field decreases as the ratio a/b increases, where $a > b$.

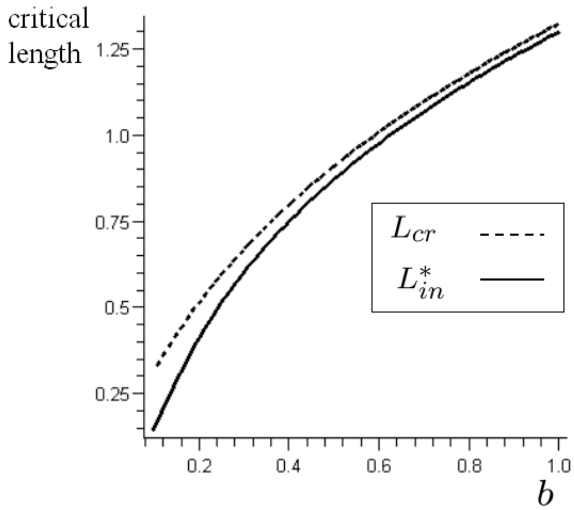

Figure 4.5: Critical length as a function of b for the inner cylinder setup.

In Figure 4.5, we plot the critical length L_{in}^* as determined from σ_{in}^* in Equation (4.46) as a function of b as well as the critical length of no voltage, σ_{cr}. We have fixed $a = 1$, $r_i = 0.05$, and $\epsilon_0 V^2/T = 0.2$. This last choice may be physically interpreted as a fixed voltage. As is indicated by Equation (4.46), the critical length is shorter with the voltage on, and so the dashed line corresponding to critical length of no voltage is above the solid line. Note, however, that the distance between the lines does not appear uniform. Figure 4.6 shows the difference between critical length with the field on and critical length without a field, again as a function of b. We see that as the ratio between a/b increases, the difference between the critical lengths increases. This means that the destabilizing effect of the electric field increases as the ring ratio increases, and in a nonlinear fashion.

Figure 4.7 shows critical length with and without the field as a function of b for the outer cylinder setup. Again, a is fixed at 1, and here $r_o = 1.2$ and $\epsilon_0 V^2/T = 0.02$. As expected, the critical length is greater with the field on for all values of b. Figure 4.8 plots the difference between the critical lengths. Notice that

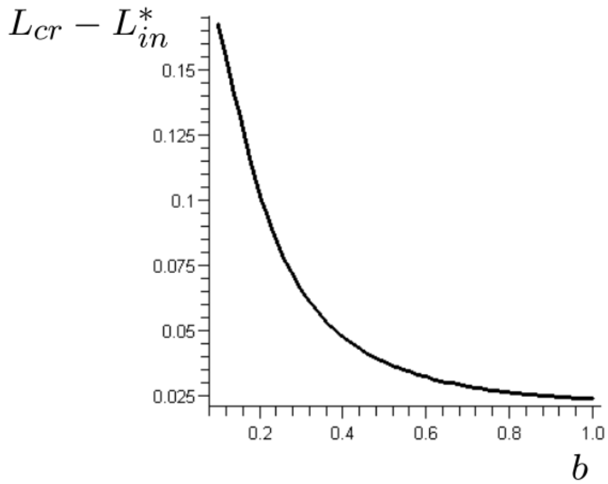

Figure 4.6: The difference in critical lengths with and without the electric field for the inner cylinder setup.

there is a minimum value around $b = 0.7$. At this ratio between the rings, the effect of the electric field as a stabilizer is minimized. Intuitively, one might think that the stabilizing effect would be minimized either at the equal ring radii end point or at the other end when the radii disparity is greatest. It is somewhat interesting that this minimum should occur for an interior value of b. Moreover, we find that the value of b at which the minimum occurs is not fixed, but rather is dependent on the voltage and the value r_o.

Another point of interest regarding Figure 4.7 is that L^*_{out} appears to curl back up at the left end. This is peculiar – it suggests that as we shrink one of the rings beyond a certain point, the field is suddenly able to stabilize the bridge at much greater lengths than could be achieved without the field. We cannot reach this conclusion too hastily though. There are several factors at play. As $b \to 0$, the integral $I_2 \to -\infty$, and does so at a faster rate than $\sigma^2_{cr} \to \infty$. Hence the relationship

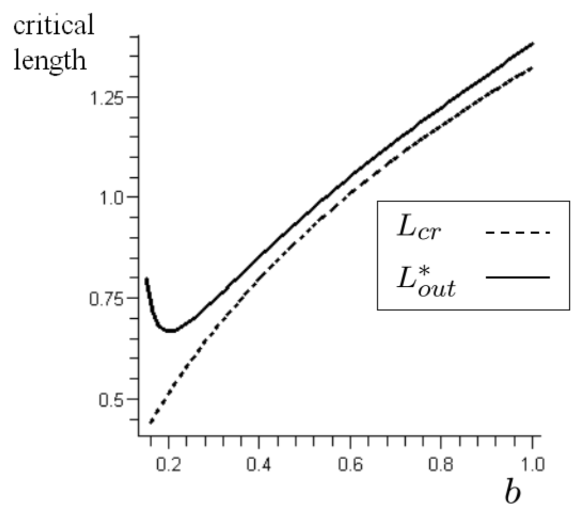

Figure 4.7: Critical length as a function of b for the outer cylinder setup.

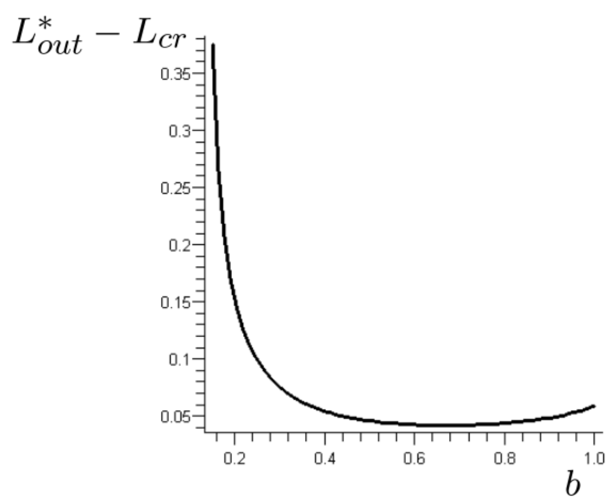

Figure 4.8: The difference in critical lengths with and without the electric field for the outer cylinder setup.

Table 4.1: A comparison of σ_{in}^* as derived from the asymptotic analysis and the numerically computed value from the full model.

b	σ_{in}^* (asymptotics)	σ_{in}^* (numerics)	**error** (num-asymp.)/num
1	0.7558	0.7558	0
0.8	0.7628	0.7626	0.000262
0.6	0.7925	0.7923	0.000252
0.4	0.8777	0.8773	0.000456
0.2	1.1784	1.1778	0.000509
0.1	1.8613	1.84	0.0112
0.075	2.4851	2.495	-0.00397

$$\sigma_{out}^* = \left(\sigma_{cr}^2 + \frac{I_2\lambda}{I_3}\right)^{1/2}$$

only yields a meaningful value of σ_{out}^* if λ is very small; otherwise the term inside the square root becomes negative. This is why the plots of L_{out}^* do not go all the way to $b = 0$. Recall that the equations for the σ^* are approximations derived from an asymptotic scheme under the assumption $\lambda << 1$. It is possible that this approximation loses validity even for small λ in the region of small b. Physically, when b is close to zero, the critical length with no field is very small, so that the two rings are practically touching. Thus, an added field as depicted in Figure 4.2.2(b) is essentially applied over a disc. Fringing fields are sure to be an issue; also, the small aspect ratio assumed to solve the potential problem loses validity. It is therefore unlikely that this phenomenon could be seen physically.

To take this one step further, Tables 4.1 and 4.2 compare the predicted critical length from Equations (4.46) and (4.47) with numerically derived values from the full models. There are several things to note regarding these tables. For the inner cylinder, the asymptotic approximation is very good for b close to a, and drops off slowly as b gets smaller, yet the error is still quite small for $b = 0.1$. Strangely, at $b = 0.1$ this trend ceases and the asymptotic approximation is closer to the numerical value at $b = 0.075$.

Table 4.2: A comparison of σ^*_{out} as derived from the asymptotic analysis and the numerically computed value from the full model.

b	σ^*_{out} (asymptotics)	σ^*_{out} (numerics)	**error** (num-asymp.)/num
1	0.7221	0.7302	0.0111
0.8	0.7366	0.7436	0.00941
0.6	0.7649	0.7757	0.0139
0.4	0.8350	0.8587	0.0276
0.2	1.0101	1.1345	0.1077
0.1	**0.4178**	**1.6575**	**0.7479**

Considering the outer cylinder, it is peculiar that the approximation when the rings are equal is worse than when they are unequal and b is close to 1. Also, notice the last row in the outer cylinder table. The predicted value of 0.4178 from the asymptotics reflects the strange behavior discussed above for small b and the critical length suddenly increasing. However, the numerical calculation does not display this behavior and this point has the largest error by far, suggesting that the predicted increase in critical length for b small by the asymptotic theory is invalid, and is most likely an artifact of the computation of the integrals I_i.

4.2.3 Bifurcation diagrams

We conclude our study of the "a-b" problem with a look at bifurcation diagrams. The diagrams were produced numerically in the same fashion as in Chapter 2. Figure 4.9 shows solutions for the inner cylinder setup. Here, we are plotting $U'(-1/2)$ versus $\epsilon_0 V^2/T$ for $b = 1$, $b = 0.8$, and $b = 0.6$ (a is fixed at 1). The indepenent axis may be interpreted as representing voltage; we do not plot against λ because the variable b depends on λ. Notice that the solution structure is not altered by varying b. As in Chapter 3, there are always two solutions which bifurcate at a critical voltage, i.e., at the fold in the diagram. The most noticeable effect of changing b is to this critical voltage, which decreases dramatically as the ratio of the ring sizes increases. Physically, this suggests that we could expect to achieve

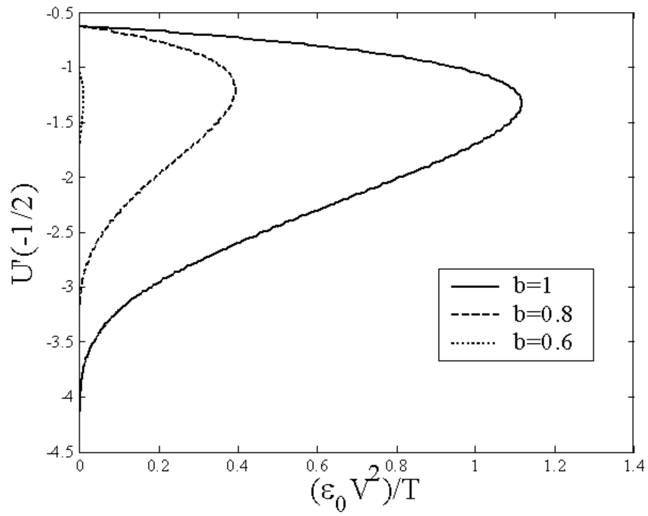

Figure 4.9: Bifurcation diagrams for the inner cylinder setup and varying values of b. Here, $a = 1$, $r_i = 0.2$, and $L = 1$.

the highest voltage at a stable state with equal ring radius.

Next, we turn our attention to the more complex diagrams in the outer cylinder setup. Figure 4.10 shows a partial diagram in the λ, β plane for $b = 0.4$, where $\beta := u'(-1/2)$. (In the following analysis we are primarily concerned with the structure of the diagrams, so the dependence of λ on b is irrelevant.) The solution types at the marked points are given in Figure 4.11. The diagram in the "preferred coordinates" $-F_\lambda = \int_{-1/2}^{1/2} (\ln(\delta/u))^{-1}\, dz$ versus λ appears in Figure 4.12. Note that in this section we are using the convention that the letters in the diagrams mark the nearest solution points on the curve.

Observe that the solutions on the branch containing points A and B are stable. This branch is divided by the line $\beta = 0$, i.e., when the contact angle at the lower ring is zero. Solution A lies above this line and is a Type I solution (see Figure 4.3), whereas solution B is of Type II. We see that both solution Types are stable at these values of b and L, and that the solution transitions from Type II to Type I as the voltage is increased.

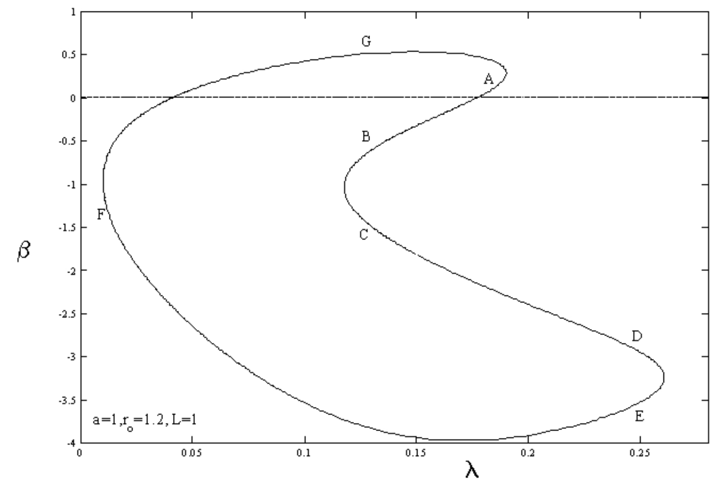

Figure 4.10: Bifurcation diagram in the outer cylinder setup for $b = 0.4$.

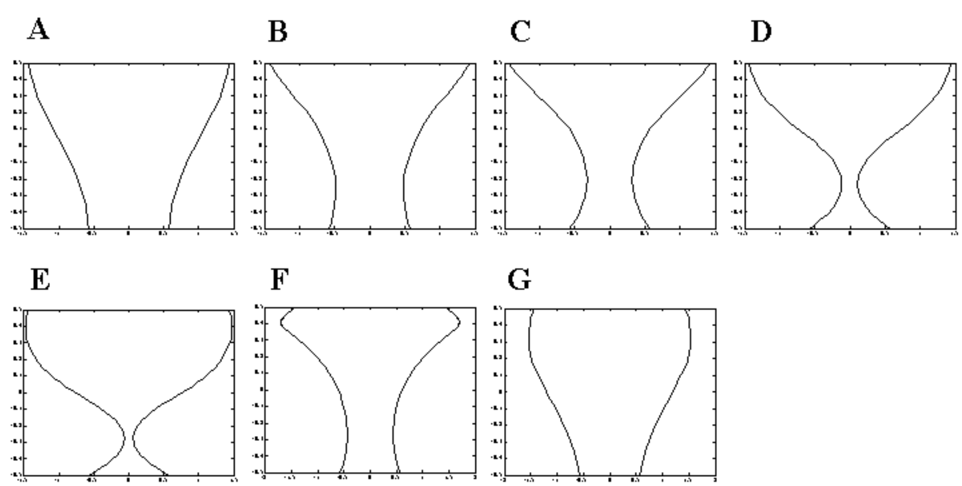

Figure 4.11: Membrane profiles at the marked points of Figure 4.10

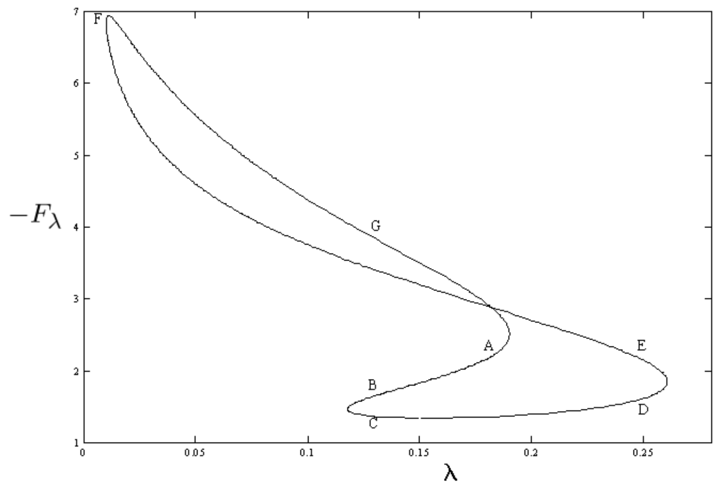

Figure 4.12: Bifurcation diagram in the outer cylinder setup for $b = 0.4$ in the preferred coordinates.

Following the rules of Maddocks in Figure 4.12, we find that all other solutions are unstable. In particular, note that C represents the perturbed unstable catenoid, while B is the perturbed stable catenoid.

Solutions E and F have two turning points, whereas all other solutions have only one or zero. In the language of Chapter 2, we would say that E and F are higher mode solutions. It is interesting, therefore, that the branches of higher mode solutions directly connect to the lower mode solutions, and there is a smooth transition among all solutions shown.

Finally, note that the entire diagram lies to the right of $\lambda = 0$. For the given length $L = 1$ and for $b = 0.4$, there is no solution in the absence of a field. In fact, a stable solution does not appear until $\lambda \approx 0.12$.

Figure 4.13 shows the same diagram as Figure 4.10, but with $b = 0.6$. The same basic structure is present except that the branches with solutions F and G are now disconnected. The main difference that has occurred in altering b is that for $b = 0.6$, a solution is present when $\lambda = 0$, i.e., a stable solution exists in the absence

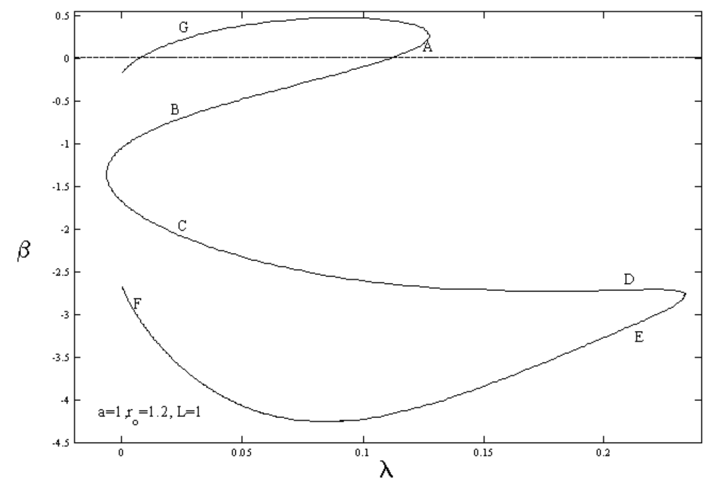

Figure 4.13: Bifurcation diagram in the outer cylinder setup for $b = 0.6$.

of a field. This is evident since the fold between B and C now occurs at a negative value of λ.

Figure 4.14 shows the diagram for $b = 0.8$. We see that another bifurcation has occurred in the structure. At this value of b, the branches with solutions D and E are no longer connected. There is no longer a smooth transition between higher mode solutions and lower mode solutions. Interestingly, the connection between D and E is replaced by "hooks" at the end of the branches. The hook at the end of D is stable, the same bizarre stable solution we found in Chapter 2 in that location.

Finally, in Figure 4.15 is the diagram in the equal radius case $b = 1$. The structure here is the same as when $b = 0.8$, although the connection between points B and C has dropped off dramatically in the negative β direction. Note that solution A is no longer present. The fold at the right end of the stable branch with solution B now lies fully below the line $\beta = 0$. Hence in increasing λ there is no transition from Type II to Type I before stability is lost. Of course, with $b = 1$ the ring radii are equal, so Type I solutions should not exist.

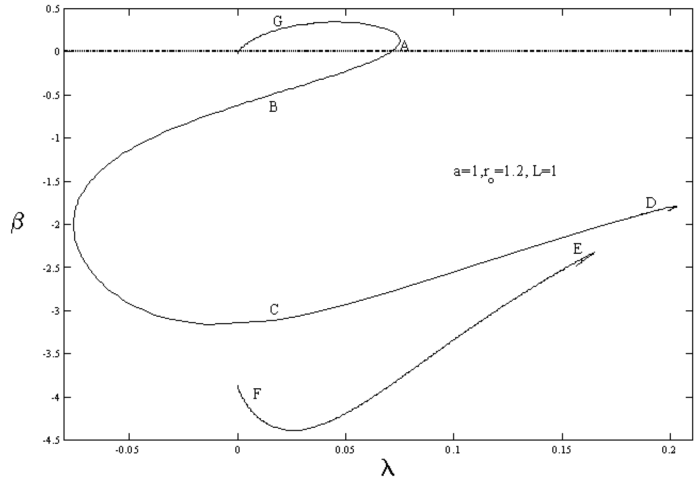

Figure 4.14: Bifurcation diagram in the outer cylinder setup for $b = 0.8$.

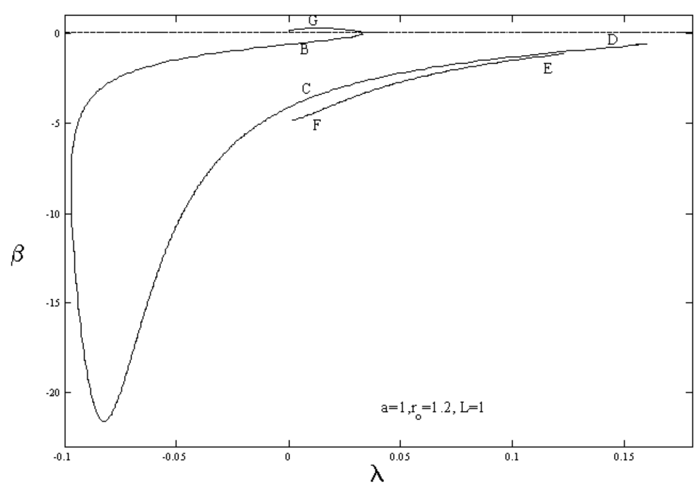

Figure 4.15: Bifurcation diagram in the outer cylinder setup for $b = 1$.

4.3 Volume constraint

In this section we explore the addition of a volume constraint to the problem of a catenoid bridge in an electric field. The analysis presented here is not exhaustive. Our goal is to outline the mathematical difference of adding a volume constraint, to take a few steps in the direction of understanding the volume constrained liquid bridge in an electric field, and to discuss potential future steps.

4.3.1 Stability classification – extension of Vogel's result

We begin by proving a means of classifying stability for volume constrained problems arising from functionals. This result is given in Theorem 4.1, Vogel [74], for the functional corresponding to the specific problem of a liquid drop trapped between parallel planes. We extend this result to general volume constrained functionals, and then apply it to our liquid bridge cylinder in an electric field. Our goal is to compare Vogel's findings regarding the stability of a cylindrical bridge to the same setup but with an added electric field. In [74], Vogel analyzes the case of a fixed contact angle, which is in contrast to the fixed contact line setup that we have considered thus far in this thesis. Note that in comparing to Vogel's result, in this section we switch to a fixed contact angle setup.

Suppose that we wish to find the function $y(x)$ that minimizes the functional

$$E[y] = \int_0^h F(x, y, y')\, dx \tag{4.48}$$

subject to the constraint

$$\int_0^h y^2\, dx = V\ . \tag{4.49}$$

Using the Lagrange multiplier ν, we form the modified functional

$$J[y] = \int_0^h F + \nu y^2\, dx\ . \tag{4.50}$$

A first variation gives the Euler-Lagrange equation

$$F_y - \frac{d}{dx} F_{y'} = -2\nu y \ . \tag{4.51}$$

Along with this we impose boundary conditions at $x = 0$ and $x = h$. For the present discussion, we will use the boundary conditions $y'(0) = \alpha_1$, $y'(h) = \alpha_2$. However, the result will hold whether y is prescribed at both ends, y' is prescribed at both ends, or if y is prescribed at one end and y' at the other.

Given the functional

$$K[y] = \int_0^h G(x, y, y') \, dx \ ,$$

the stability of a solution to the corresponding Euler-Lagrange equation may be expressed as the condition that the quadratic form

$$B(\psi) = \int_0^h (R\psi'^2 + S\psi^2) \, dx \tag{4.52}$$

be positive definite on the space of functions orthogonal to y, where

$$R = \frac{1}{2} G_{y'y'}, \quad S = \frac{1}{2}\left(G_{yy} - \frac{d}{dx} G_{yy'} \right) \ . \tag{4.53}$$

This requirement may further be restated in terms of eigenvalues of a Sturm-Liouville problem. Namely, one considers the eigenvalues of

$$\begin{aligned} &L(\psi) = -(R\psi')' + S\psi = \mu\psi \\ &\psi'(0) = 0, \quad \psi'(h) = 0 \ . \end{aligned} \tag{4.54}$$

As this is a Sturm-Liouville problem, the sequence of eigenvalues μ_k is strictly increasing. If all eigenvalues μ_k are positive, the function $y(x)$ is stable. The interesting case to consider, as is described by Vogel, is when the first eigenvalue is negative and the second is positive. The following theorem is a generalization of Theorem 4.1 in [74]:

Theorem 7 *Suppose $y(x)$ solves Equation (4.51), satisfies the given boundary conditions, and also satisfies the constraint Equation (4.49). Then y is a stable solution, i.e., minimizes the functional $J[y]$, if the following hold:*

> **(a)** *The eigenvalues of the Sturm-Liouville problem Equations (4.54) satisfy*
>
> $$\mu_0 < 0 < \mu_1 < \ldots$$
>
> **(b)** *$y(x) = y(x;\epsilon_0)$ may be embedded in a smoothly parameterized family of solutions $y(x;\epsilon)$, such that*
>
> $$\nu'(\epsilon_0)V'(\epsilon_0) > 0 \ ,$$
>
> *where $V(\epsilon) = \int_0^h y^2(x;\epsilon)$ and $\nu(\epsilon)$ is the Lagrange multiplier.*

In order to prove the theorem, we first need the following result, proved in Vogel for general functionals.

In the case where the first two eigenvalues satisfy $\mu_0 < 0 < \mu_1$, let $\phi(x)$ be the function such that $L(\phi) = y$, with $\phi'(0) = \phi'(h) = 0$. Then the stability condition that $B(\psi)$ be positive definite on $y^\perp$ is equivalent to the condition

$$\int_0^h \phi y \, dx < 0 \ . \tag{4.55}$$

Proof of Theorem: Given the above classification, to prove the theorem we will show that the inequality (4.55) may equivalently be expressed as condition **(b)**. To do this, we take a derivate with respect to ϵ across Equation (4.51), obtaining after some simplification

$$-\left(F_{y'y'}\frac{dy'}{d\epsilon}\right)' + \left(F_{yy} - \frac{d}{dx}F_{y'y} + 2\nu\right)\frac{dy}{d\epsilon} = -2y\frac{d\nu}{d\epsilon} \ . \tag{4.56}$$

For the functional $J[y]$, we have

$$R = \frac{1}{2}F_{y'y'}, \quad S = \frac{1}{2}\left(F_{yy} - 2\nu - \frac{d}{dx}F_{yy'}\right) \ . \tag{4.57}$$

Thus, Equation (4.56) may equivalently be written as

$$-\left(R\frac{dy'}{d\epsilon}\right)' + S\frac{dy}{d\epsilon} = -y\frac{d\nu}{d\epsilon} \ . \tag{4.58}$$

If we define

$$\phi = \frac{-\frac{dy}{d\epsilon}}{\frac{d\nu}{d\epsilon}} \ , \tag{4.59}$$

then, noting that ν is independent of x, Equation (4.58) may be written

$$-(R\phi')' + S\phi = y \ , \tag{4.60}$$

or, $L(\phi) = y$. Therefore, the requirement Equation (4.55) is equivalent to

$$\int_0^h \frac{y\frac{dy}{d\epsilon}}{\frac{d\nu}{d\epsilon}} \ dx > 0 \ , \tag{4.61}$$

which reduces to

$$\frac{d\nu}{d\epsilon}\int y\frac{dy}{d\epsilon} \ dx > 0 \ , \tag{4.62}$$

Now, recalling that

$$V(\epsilon) = \int_0^h y^2 \ dx \ ,$$

we can write (4.62) as

$$\nu'(\epsilon)V'(\epsilon) > 0 \tag{4.63}$$

and the proof is complete. $\square$

Further, it may be shown that if either $\mu_1 < 0$ or $\nu'(\epsilon_0)V'(\epsilon_0) < 0$ then $y(x;\epsilon_0)$ is unstable. For details see [74].

After proving the above theorem in the trapped drop case, Vogel uses it to classify stability of cylindrical drops. He finds that a cylindrical drop of radius a is stable if $a > \frac{L}{\pi}$, where L is the distance between the parallel plates. It is worth pointing out that this result applies to bridges with a fixed contact angle as opposed to a fixed contact line. For this reason, the result differs from the classic stability result of Plateau and Rayleigh that the drop will be stable for $a > \frac{L}{2\pi}$.

We now apply Theorem 7 to test stability of cylindrical bridges in the presence of an electric field. Consider the inner cylinder geometry of Chapter 3 with an added volume constraint and a fixed contact angle. Since we are not fixing the contact line, the bridge does not span rings but instead spans parallel plates. This setup is depicted in Figure 4.16.

If we fix the contact angle at $\pi/2$ so that we allow for cylindrical bridges, it is best envisioned by a soap-film bridge spanning two parallel plates. This is the same problem Vogel considered except we have the addition of an applied potential difference between the membrane and the inner cylinder. Our goal is to determine how the field affects the stability of the cylindrical bridge.

To proceed, we scale everything the same way as in Chapter 3. That is, we take

$$z = \frac{\tilde{z}}{L}, \quad \psi = \frac{\tilde{\psi}}{\hat{V}}, \quad r = \frac{\tilde{r}}{r_i}, \quad U = \frac{\tilde{U}}{a} \ ,$$

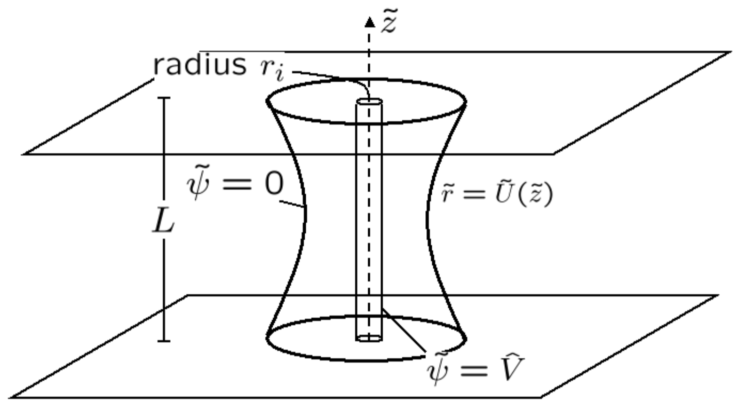

Figure 4.16: Volume constrained inner cylinder setup.

where $a = L/\pi$. Note that we have scaled U by the radius of the cylinder at the stability boundary in the absence of an electric field. Having scaled the same way, the potential problem is solved as before, and we reach the same energy functional,

$$\mathcal{E}[u] = \int_{-1/2}^{1/2} U\sqrt{1+\sigma^2 U'^2} + \frac{\lambda}{\ln(\delta/U)}\, dz \;, \tag{4.64}$$

where, as before, λ characterizes the strength of the field, $\sigma = a/L = 1/\pi$, and $\delta = r_i/a = \pi r_i/L$.

We wish to minimize the functional subject to the volume constraint, expressed in dimensionless form as

$$\int_{-1/2}^{1/2} U^2\, dz = V := \frac{\tilde{V}}{\pi a^2 L} \;, \tag{4.65}$$

where $\tilde{V}$ is the dimensional volume. Adding the Lagrange multiplier P, we form the modified functional

$$\mathcal{J}[u] = \int_{-1/2}^{1/2} U\sqrt{1+\sigma^2 U'^2} + \frac{\lambda}{\ln(\delta/U)} + PU^2 \, dz \; . \tag{4.66}$$

Applying Euler-Lagrange to this functional, we obtain

$$P = \frac{1}{2}\left\{\frac{\sigma^2 U''}{(1+\sigma^2 U'^2)^{3/2}} - \frac{1}{U(1+\sigma^2 U'^2)^{1/2}} - \frac{\lambda}{U^2 \ln^2(\delta/U)}\right\} \; . \tag{4.67}$$

This is the same differential equation from Chapter 3 with the addition of the term $2PU$. For the present purposes it is most convenient to solve for P.

Consider cylindrical solutions $U = c$. In the parlance of Theorem 7, c is the parameter for the family of cylindrical solutions. We wish to determine for which values of c the cylindrical solution is stable.

Substituting $U = c$ into the appropriate forms for R and S from Equations (4.53), the Sturm-Liouville problem to solve is

$$\begin{aligned} L(\psi) &= \left(\frac{\sigma^2 c}{2}\psi'\right)' - \frac{1}{2}\left(\frac{2\lambda(1+\ln(c/\delta)}{c^2\ln^3(c/\delta)} - \frac{1}{c}\right)\psi = \mu\psi \\ \psi'(-1/2) &= \psi'(1/2) = 0 \; . \end{aligned} \tag{4.68}$$

The eigenvalues are $\mu_k = k^2 c/2 - f(c) - 1/(2c)$, where

$$f(c) = \frac{\lambda(1+\ln(c/\delta))}{c^2\ln^3(c/\delta)} \; .$$

Note that $\tilde{U} > r_i$, i.e., the liquid bridge cylinder must be at least as large as the inner electrode. This implies that c must be greater than δ. Consider stability condition **(b)** of Theorem 7. Since the volume $V(c) = c^2$, $V'(c) > 0$. From Equation (4.67), we find

$$P'(c) = \frac{\lambda(\ln(c/\delta)+1)}{c^3\ln^3(c/\delta)} + \frac{1}{2c^2} > 0 \quad \forall c > \delta \; . \tag{4.69}$$

Thus condition **(b)** holds for all cylinders. We now consider the signs of the first two eigenvalues. To facilitate this, we first make some observations regarding $f(c)$. Observe that

- $f(c) > 0$ for all $c > \delta$
- as $c \to \delta$, $f \to -\infty$
- as $c \to \infty$, $f \to 0$.

We have $\mu_0 = -f(c) - 1/(2c)$, which will be less than zero for all $c > \delta$. Also,

$$\mu_1 = \frac{c}{2} - f(c) - \frac{1}{2c} \ . \tag{4.70}$$

We note that as $c \to \delta$, $\mu_1 \to -\infty$, and that as $c \to \infty$, $\mu_1 \to \infty$. This merely confirms that very narrow bridges are unstable and very wide bridges are stable. Thus, there should be a stability boundary for some finite c. Recall that we scaled $\tilde{U}$ by $a = L/\pi$, the stability boundary with no field present. Hence $c = 1$ corresponds to this stability boundary. Inserting $c = 1$, we have $\mu_1 = -f(1) < 0$. This implies that adding the field has served to destabilize the cylinder.

The stability boundary with the field present is found by setting $\mu_1 = 0$, from which we determine that the critical value, which we denote c^*, is the solution of

$$c^2 - \frac{2\lambda(1 + \ln(c/\delta))}{c^2 \ln^3(c/\delta)} = 1 \ . \tag{4.71}$$

Any bridge with radius greater than c^* will be stable, while bridges with smaller radius are unstable. From the above argument, we can be certain that for any value of $\lambda > 0$, c^* will be greater than 1. To see the effect of λ and δ on the stability, consider Figure 4.17, which is a plot of the stability boundary c^* as a function of λ for different values of δ. As would be expected, c^* increases with increasing λ, meaning that increasing the voltage causes the minimum radius for a stable bridge

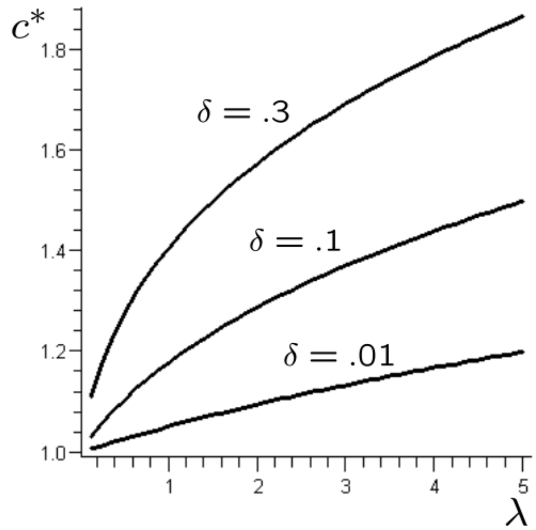

Figure 4.17: The stability boundary c^* as a function of λ for various values of δ.

to increase. Recall that $\delta = \pi r_i / L$, so that a decrease in δ can be interpreted as increasing the length or decreasing the radius of the electrode. A decrease in δ seems to dampen the effect of the voltage.

The situation is more complex and interesting in the case of the outer cylinder. With the outer cylinder, we are restricted in how large of a cylindrical bridge we can possibly make – the bridge cannot be larger than the outer electrode itself. As we saw in Chapter 2, we would expect to be able to use the field as a stabilizer, and achieve stable bridges that are narrower than Vogel's result L/π in the absence of a field. On the other hand, as the radius of the bridge approaches the radius of the outer cylinder, we expect the field to destabilize. Hence, intuition suggests that there should be a finite region for the radius for which the cylindrical bridge is stable.

The derivation necessary to use Theorem 7 is very similar to our derivation for the inner cylinder given above, and so we skip the details. As before, we consider the stability of the family of solutions $u = c$. We find that the first two eigenvalues are

$$\begin{aligned} \mu_0 &= g(c) - \frac{1}{2c} \\ \mu_1 &= g(c) - \frac{1}{2c} + \frac{c}{2} \,, \end{aligned} \tag{4.72}$$

where

$$g(c) := \frac{\lambda\,(\ln(\delta/c) - 1)}{c^2 \ln(\delta/c)^3} \,. \tag{4.73}$$

Here, λ is the same parameter as before, characterizing field strength, and $\delta = r_o/a = r_o\pi/L$, where r_o is the radius of the cylindrical electrode. The physically relevant domain here is thus $c \in (0, \delta)$. If $P(c)$ is the Lagrange multiplier, we find

$$P'(c) = -\frac{1}{c}\mu_0 \,. \tag{4.74}$$

$P'(c)$ is only positive if μ_0 is negative, and so the cylinder $u = c$ is only stable if $\mu_0 < 0$ and $\mu_1 > 0$. Thus, if we let

$$y = \mu_0 \mu_1$$

then any value of c for which $y < 0$ implies a stable cylinder. Note that in the derivation, we scaled $\tilde{u}$ by the stability boundary with no field $a = L/\pi$, the same as with the inner cylinder. Thus, $c = 1$ corresponds to the zero field stability boundary. If $c \to 0$ this of course represents an infinitely thin bridge, while $c \to \delta$ when the bridge is the same radius as the outer electrode. Note that δ must be greater than one.

In Figure 4.18, we plot the curve $y = \mu_0\mu_1$ for $\delta = 1.2$ fixed and increasing values of λ. In (a) $\lambda = 0.0001$, so that the electric field is very small. In this case, there is a small stable region near $c = 1$, with all other values of c unstable. Physically, this implies that the cylinder is stable only in a narrow region with the

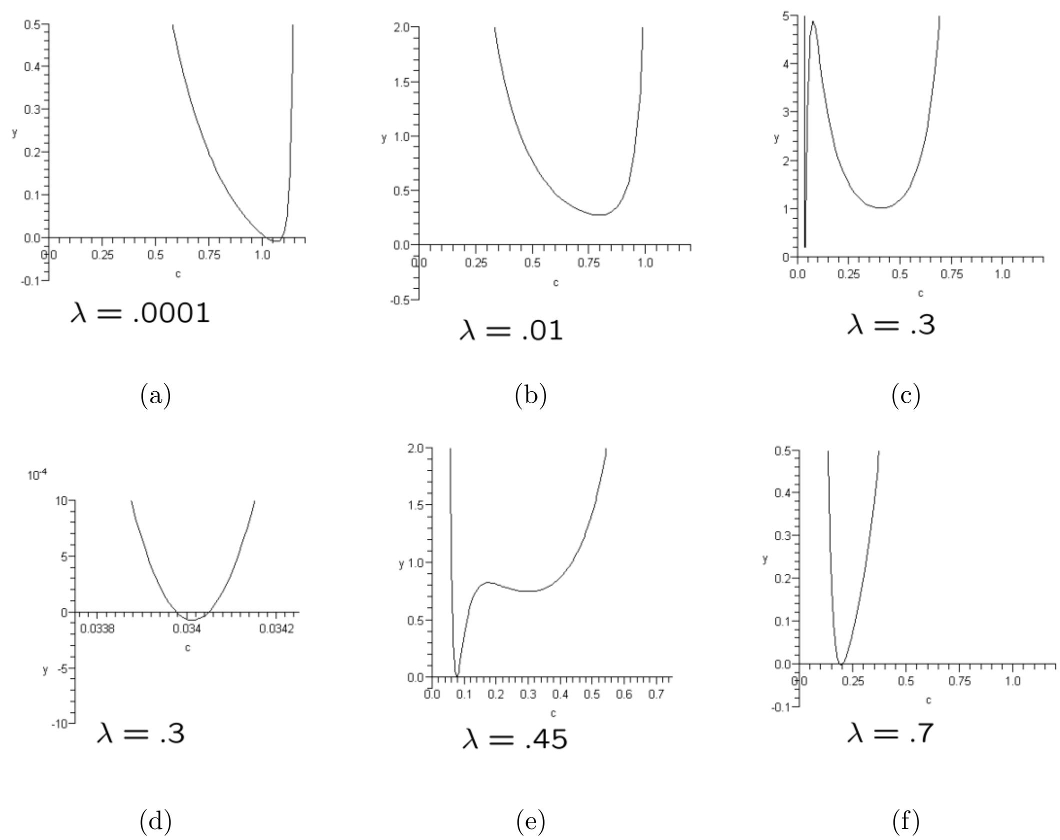

Figure 4.18: The curve $y = \mu_0\mu_1$ as a function of c for $\delta = 1.2$ and increasing values of λ. Anywhere that $y < 0$ represents a stable cylinder solution.

radius greater than Vogel's stability limit and less than the outer electrode. With an increase in λ, this small stable region is lost. This is evident in (b), in which it appears that there are no stable bridges at these parameter values. However, something peculiar occurs in (c) at $\lambda = 0.3$ – two more folds appear in the curve near the left edge. In (d) we have zoomed in on this thin region, revealing that in fact the curve dips below zero over a *very* small region, $0.03397 < c < 0.034048$. In fact, closer inspection reveals that such a region is present in (a) and (b) as well, but is too thin to appear in the plots.

Mathematically, this behavior can be understood by examining the functions μ_0 and μ_1. Observe that as $c \to 0$, both μ_0 and μ_1 approach infinity. However, since μ_1 is always greater than μ_0, there is a small region near $c = 0$ where $\mu_1 > 0$ and $\mu_0 < 0$. This region is so narrow in some instances that it is not visible when plotting – hence its absence from (a) and (b). Physically, this is rather bizarre. Returning to (a), we have not only the small stable region near $c = 1$, but also an incredibly small stable region near $c = 0$!

As we continue to increase λ, the curve gets smoothed out (as is evident in (e)), and the three critical points become one. Thus, at $\lambda = 0.7$ there remains a narrow stable region, but it occurs for a larger value of c and is slightly wider – here the cylinder is stable for $0.187 < c < 0.201$.

In Figure 4.19 we explore the effect of δ on the stability. Physically, increasing the value of δ is equivalent to increasing the radius of the outer electrode. In (a), we note that there is a stable region near $c = 1$ at $\lambda = 0.01$ with $\delta = 2$, whereas there was no such region with $\delta = 1.2$. This is reasonable – the field is in effect farther away, and so we have a larger stable region just beyond $c = 1$. If we were to increase λ with $\delta = 2$, we would find a very similar pattern as occurred at $\delta = 1.2$, just at higher voltages. Things become interesting once we let $\delta \geq e$. Observe that the only root of the function $g(c)$ is at $c = \delta/e$. This implies that $c = 1$ will always

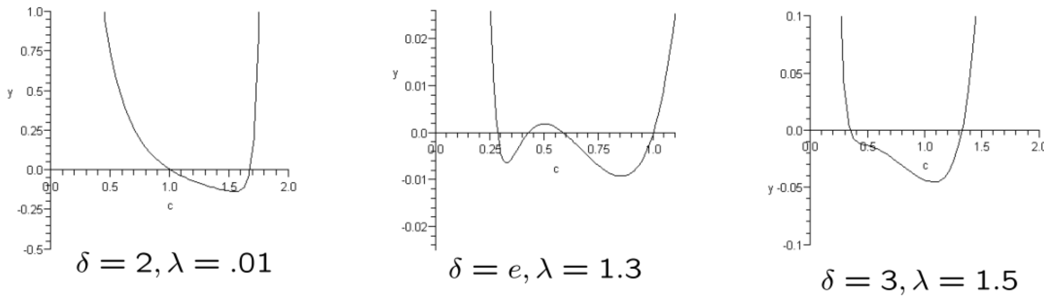

(a) (b) (c)

Figure 4.19: The curve $y = \mu_0\mu_1$ at the indicated values of λ and δ.

be unstable when $\delta < e$. If we take $\delta \geq e$, the basic structure is the same, but we are able to obtain some interesting regions of stability. In (b), $\delta = e$ and $\lambda = 1.3$. Here, the cylinder is stable for $0.28 < c < 0.42$ and for $0.59 < c < 1$, yet unstable for $0.42 < c < 0.59$. Strangely, the field is balanced in such a way that a small unstable region sits between two stable regions! Finally, in (c) we demonstrate that large stable regions surrounding $c = 1$ are possible.

One final remark: In deriving the problem, a small aspect ratio is assumed to solve for the electric potential, as is done in Chapter 2. In particular, the assumption may be expressed as

$$\frac{(\delta - 1)^2}{\pi^2} << 1 \ . \tag{4.75}$$

We begin to violate this by taking δ near or greater than e, and so we must be cautious in the physical interpretation of Figure 4.19(b) and (c).

4.4 Discussion

In this chapter we have explored two variations of the problem of a catenoid bridge in an electric field – we considered having unequal ring radii and then the addition of a volume constraint. In the case of the former, we first developed tools to analyze the system in the absence of a field, an analysis which was far less trivial than with equal ring radii. Then, in the presence of an electric field, we explored the effect of the ratio of ring radii on previous results from Chapters 2 and 3. In particular, we found that the destabilization effect for the inner cylinder setup increases as the ring ratio increases, while the stabilization effect in the outer cylinder setup was minimized at an interior value of b. We also uncovered some interesting bifurcations in the solution structure as the ratio of ring radii is altered.

There are more areas that could be explored with the “a-b” problem. A more qualitative analysis could be applied to help understand the changes in the bifurcation diagrams of Section 4.2.3. As was mentioned at the start of the chapter, the purpose of using different ring radii could be to find an optimal design. This question is much better approached when considered in terms of a specific application, and so we did not address optimization in our analysis. Our primary objective was to see how unequal ring radii could alter the solution structure and general effect of the electric field.

With the addition of a volume constraint, the problem becomes significantly more complex. In this chapter we developed a means of characterizing stability via a generalization of Vogel’s theorem, and then considered cylindrical volume constrained bridges in this context. In our analysis, we really incorporated another variation to the system in the previous chapters, in that our boundary conditions were changed in order to compare with Vogel’s stability result. Our analysis here was brief, but it was clear that even in the simple case of a cylindrical bridge, the addition of the electric field can have a significant and counterintuitive effect on stability.

There are many directions one could go in continuing this exploration. The ODE governing the volume constrained system is the same as in Chapters 2 and 3, but with an added term containing a Lagrange multiplier. Hence, a useful avenue would be to attempt to modify the analysis of the previous chapters to account for the extra term. The difficulty is that the Lagrange multiplier is not necessarily a fixed parameter in the problem, which would complicate an asymptotic or phase plane analysis. Numerically, it would be interesting to explore the volume constrained system with bifurcation diagrams. The branch tracing techniques we have utilized could easily be applied, and an alternative choice for "preferred coordinates" arises by plotting the Lagrange multiplier against the volume.

Chapter 5

COLLAPSING BUBBLE SYSTEMS AND THE INFLUENCE OF AN ELECTRIC FIELD

5.1 Introduction

In this chapter we explore a different system where electrostatic and elastic forces interact. In particular, we consider the collapse of a soap-bubble in the presence of an electric field. A bubble in connection with a tube will collapse, i.e., deflate, with air flow through the tube driven by the pressure difference across the surface of the bubble. We analyze this scenario in Section 5.2, and then modify the system with an added electrostatic pressure in Sections 5.4 and 5.5. In Section 5.6 we extend to a two bubble system, where two bubbles compete for a fixed volume of air.

This presents a different type of system than we have considered in the previous chapters. Here, our goal is to capture dynamics of a changing system, whereas in the previous chapters we analyzed static equilibrium solutions. One motivation for studying this problem is that it provides a simple enough model to develop qualitative analysis of a dynamical system with a field driven mean curvature surface. In the previous chapters, had dynamics been our focus we would have needed a numerical approach. For the present chapter, dynamics is a must by the nature of the system, but will be far more tractable.

Despite this difference, the main components of the system are the same as for the catenoid in the electric field: we have an elastic membrane whose shape is governed by the minimization of free surface energy and an added electrostatic force acting on the membrane. In our models, we take a quasistatic approach to determine interface shape. That is, at each instant of time, the shape of the membrane is found as the solution of the equation governing static equilibrium. As was the case for the shape of the bridge in the previous chapters, the shape of the collapsing bubble is determined by a combination of surface tension and electrostatic forces.

5.2 Basic problem – simple model

Before we explore the effects of electric fields, we consider various models to describe the dynamics of a collapsing bubble in the absence of external forces. The general problem is as follows: a soap-film bubble is formed on the end of a tube. Given an initial size of the bubble, tube radius, and tube length, we wish to find the size of the bubble as a function of time as the bubble collapses, i.e., as the air in the bubble flows out through the tube.

We model the dynamics of the collapsing bubble by setting the change of volume of the bubble equal to the flux of air through the tube. To determine the flux of air, we solve the one-dimensional Navier-Stokes equations for flow through a cylinder, resulting in a Poiseuille flow. Taking a flux integral of the flow, we arrive at the equation

$$\frac{dV}{dt} = -\frac{\pi a^4 \Delta p}{8\mu l}\,, \tag{5.1}$$

where V is the volume of the bubble, a is the radius of the tube, Δp is the pressure difference across the bubble, μ is the viscosity of the air, and l is the length of the tube.

As a first modeling attempt, we treat the bubble as a perfect sphere. This approach was suggested by Grosse [26]. Letting $R(t)$ denote the radius of the sphere at time t, we have from the Young-Laplace relation applied to the surface of the bubble

$$\Delta p = \frac{4\gamma}{R} \; , \tag{5.2}$$

where γ is the surface tension of the bubble, and the extra factor of 2 in the numerator accounts for the two layers of the soap-film. Inserting Δp into Equation (5.1), we have the following differential equation for $R(t)$

$$\frac{d}{dt}\left(\frac{4\pi R^3}{3}\right) = -\frac{\pi a^4 \gamma}{2l\mu R} \; . \tag{5.3}$$

Solving Equation (5.3), the radius satisfies

$$R(t) = (R_0^4 - Kt)^{1/4} \; , \tag{5.4}$$

where R_0 is the radius at time $t = 0$ and

$$K = \frac{a^4 \gamma}{2\mu l}$$

is a fixed constant. Note that the bubble fully collapses in finite time $t = \frac{R_0^4}{K}$.

5.3 Improved bubble collapse model

The problem with the previous theory lies in the assumption that the bubble is a full sphere, which does not take into account the connection of the bubble with the collapsing tube. When the volume of the bubble is large compared to the radius of the collapsing tube, this approximation is valid. However, it becomes increasingly worse during the collapse.

More accurately, a bubble sitting on the end of a capillary tube will form a *part* of a sphere. This is easily verified – the bubble will assume the shape that minimizes the surface energy, which is proportional to surface area, subject to a

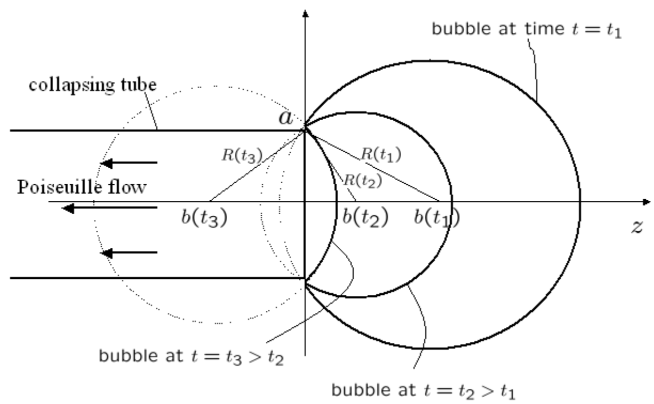

Figure 5.1: Improved partial sphere collapse model, following the point b as a function of time.

volume constraint. It is easily shown that a part of a sphere is the desired energy minimizer, and the boundary conditions and the volume determine the details.

Consider Figure 5.1. In this setup, a is the radius of the collapsing tube, and the bubble is aligned along the z-axis, with the center of the sphere located at $z = b$. Hence the radius of the bubble is given by $R = \sqrt{a^2 + b^2}$. The collapse is still driven by the pressure difference which is again inversely proportional to the radius of the sphere. With this setup, the dynamics are most easily formulated in terms of the location of the center of the sphere. That is, we formulate an ODE for $b(t)$ rather than $R(t)$. Note that the bubble is uniquely determined by b, which is not the case with the radius. Also observe that $b = 0$ corresponds to a hemispherical bubble, and $b < 0$ corresponds to a spherical cap, such that the bubble forms a planar disc at the end of the collapsing tube as $b \to -\infty$.

The collapse is still governed by Equation (5.1). The shape of the bubble is given as a surface of revolution by the function $u(z) = \sqrt{R^2 - (z - b)^2}$, and so the volume is given by

$$\pi \int_0^{b+R} u^2 \, dz = \pi \left(\frac{2}{3}(b^2 + a^2)^{3/2} + \frac{2}{3} b^3 + a^2 b \right) . \tag{5.5}$$

Inserting this into Equation (5.1), we obtain the following differential equation

$$\frac{d}{dt} \left(\frac{2}{3}(b^2 + a^2)^{3/2} + \frac{2}{3} b^3 + a^2 b \right) = - \frac{a^4 \gamma}{2 \mu l (b^2 + a^2)^{1/2}} . \tag{5.6}$$

In order to see how the collapse has been altered, it is informative to non-dimensionalize and solve Equation (5.6) asymptotically. We add to Equation (5.6) the initial condition $b(0) = \sqrt{R_0^2 - a^2}$, where $R_0 = R(0)$ is the initial radius. The regime we consider here is when the initial radius is large compared to the radius of the collapsing tube. Thus, we let $\epsilon = a/R_0$, and assume $\epsilon << 1$. In this regime, we expect the collapse to be similar to the simplified $R(t)$ theory.

To non-dimensionalize, we introduce

$$B = \frac{b}{a}, \quad \tau = \frac{\epsilon^\alpha \gamma t}{2 \mu l} ,$$

where α is to be determined. Rescaling Equation (5.6), we have the following IVP:

$$\begin{aligned} \frac{d}{d\tau} \left(\frac{2}{3}(B^2 + 1)^{3/2} + \frac{2}{3} B^3 + B \right) &= - \frac{\epsilon^{-\alpha}}{(B^2 + 1)^{1/2}} \\ B(0) = \sqrt{\frac{1}{\epsilon^2} - 1} &\sim \frac{1}{\epsilon} - \frac{1}{2}\epsilon + O(\epsilon^3) . \end{aligned} \tag{5.7}$$

Next, we expand $B(\tau)$ as

$$B \sim \frac{1}{\epsilon} B_0 + \epsilon B_1 + \dots \tag{5.8}$$

Inserting this expansion into the IVP (5.7), we find that in order to have a non-trivial solution for B_0, we must choose $\alpha = 4$. With this choice, we obtain

$$B_0(\tau) = (1 - \tau)^{1/4} \tag{5.9}$$

as the leading order solution. At $O(\epsilon^2)$, we have

$$\frac{d}{d\tau}(4B_0^2 B_1 + 2B_0) = \frac{B_1}{B_0^2} + \frac{1}{2B_0^3} \; . \tag{5.10}$$

Inserting B_0 from Equation (5.9) and solving Equation (5.10) subject to initial condition $B_1(0) = -1/2$, we find

$$B_1(\tau) = \frac{-1}{2(1-\tau)^{3/4}} \; . \tag{5.11}$$

Notice that $B_0(\tau)$ has the same form as the solution obtained in the previous $R(t)$ theory given in Equation (5.4). To first order then, $B(\tau)$ goes to zero in finite time and the collapse is similar to the previous theory. However, when we include the second term B_1, we get finite time blow-up of $B(\tau)$. This correction term takes into account the collapsing tube, and enables for $b(t) \to -\infty$ and thus for $R(t)$ to decrease down to the radius of the collapsing tube, and then increase to infinity as the bubble flattens out.

In Figure 5.2, we plot $R(t)$ as given in Equation (5.4) as well as $R(t) = \sqrt{b(t)^2 + a^2}$ where $b(t)$ is obtained from the first two terms of the asymptotic expansion. Also included in this plot is the radius $R(t)$ determined by numerically solving Equation (5.6) for $b(t)$. Observe that all three curves overlap exactly until the end of the collapse. In the inset in Figure 5.2 we have zoomed in at the final fraction of a second of the collapse. Here we are able to see the difference between the $R(t)$ and $b(t)$ theories. For the $b(t)$ theory, the asymptotic solution seems to coincide exactly with the full numerical solution. Note that the ordering in the asymptotic expansion poses a problem at the end of the collapse, as $B_1(\tau) \to -\infty$ as $\tau \to 1$. It is somewhat curious that the asymptotic solution matches perfectly with the numerical solution despite this potential problem.

We leave the asymptotic analysis here, as our purpose was to demonstrate when a noticable difference might occur between the $R(t)$ theory and the $b(t)$ theory.

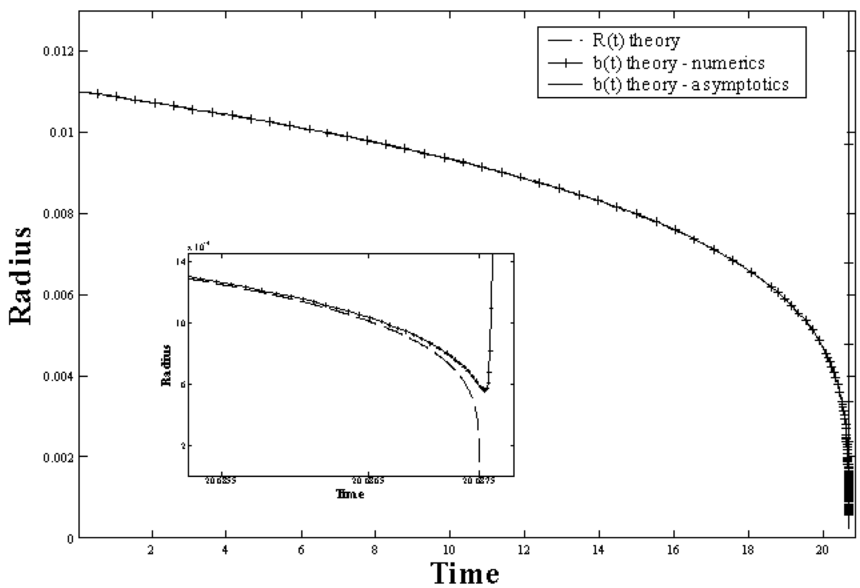

Figure 5.2: Comparison of the collapse by the $R(t)$ theory and the $b(t)$ theory both numerically and asymptotically. The inset is zoomed in at the very end of the collapse.

We conclude that the main value in predicting a single bubble collapse with the $b(t)$ theory should come at the end of the collapse when the size of the bubble is on the same order as the collapsing tube. In the next subsection, we verify this through a series of experiments.

5.3.1 Experimental comparison

We now consider several experiments to test the validity of the theory. We demonstrate in which regimes the $b(t)$ theory is essentially equivalent to the $R(t)$ theory, in which regimes it provides a better description, and also determine the limits in using such a model to predict bubble collapse.

Small radius collapse

In the first experiment, a bubble is formed on the lower end of a vertically positioned capillary tube. Both the tube and bubble are placed in a laboratory box to isolate the bubble from external air currents. The bubble is allowed to collapse, and the collapse is filmed with a high speed camera at 60 frames per second. For this experiment, we used the following values:

- collapse tube radius $5.645 \cdot 10^{-4}$ m
- collapse tube length .1 m
- viscosity of air $1.82 \cdot 10^{-5}$ Pa s
- soap-film surface tension $2.5 \cdot 10^{-2}$ N/m
- initial bubble radius $1.1 \cdot 10^{-2}$ m

Figure 5.3 shows a comparison between the radius as a function of time predicted by the different theories, matched against the experimental data. In producing Figure 5.3, the radius at each time step was determined using a least squares fit. The curve for the $b(t)$ theory is obtained by solving Equation (5.15) for $b(t)$ with a standard

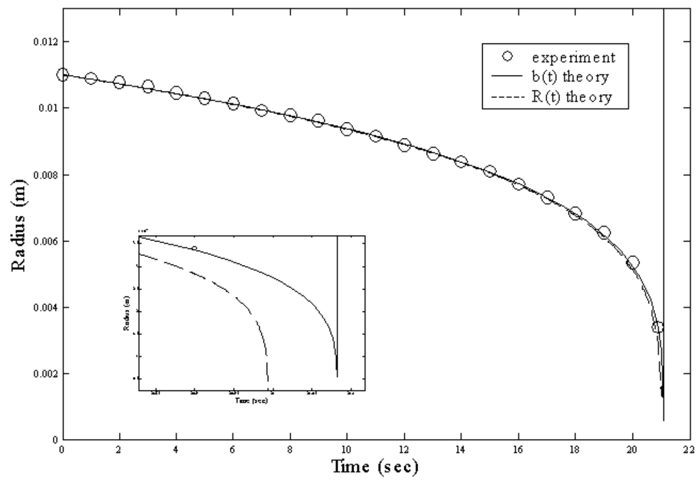

Figure 5.3: Comparison of theory and experiment for the collapse of a bubble through a capillary tube. In the inset, we have zoomed in on the very end of the collapse.

ode solver in Matlab, and then using the relation $R(t)^2 = b(t)^2 + a^2$ to back out the radius. The $R(t)$ theory is plotted from Equation (5.4).

Observe that both the $b(t)$ and the $R(t)$ theories match very well with the experimental data. The only place where any discernible difference between the two theories occurs is at the very end of the collapse. As we have stated, the radius goes to zero in the $R(t)$ theory, whereas the radius goes to infinity in the $b(t)$ theory as the bubble flattens out into a disc spanning the collapsing tube. Since the radius of the tube is so small in this setup, there is only a discrepancy in the final fraction of a second of the collapse. Experimentally, the increase in radius predicted by the $b(t)$ theory was not observed at the speed with which the collapse was filmed. This suggests that in the regime of a small radius tube, there is essentially no difference between the two theories and the simpler full-sphere approximation appears to be justified.

Large radius constrained collapse

In order to see the effect of the bubble's connection with the collapsing tube, a larger tube is needed. In our second experiment, we form a bubble on the end of a tube of radius 10.55 mm and length 305 mm. To ensure that the quasistatic approach is valid, we slow the air flow and constrain the collapse. To do this, on the opposite end of the large tube we attach a much smaller tube of radius 1.5 mm and length 184 mm.

In modeling this collapse, we must modify the flux equation to account for the setup of two tubes in series. To do this, consider the general flow depicted in Figure 5.4. A tube of radius a_1 and length L_1 connects to a tube of radius a_2 and length L_2. Given known pressures at the ends, p_1 and p_2, we wish to know the flux through the tubes. Suppose the pressure p_{mid} at the junction where the radius changes is known. We take the flow through the large tube and the small tube to be Poiseuille, driven by the pressure differences $p_1 - p_{mid}$ and $p_{mid} - p_2$, respectively. Then we may write the flux through each portion, denoted Q_i, as

$$\begin{aligned} Q_1 &= \frac{-\pi a_1^4 (p_1 - p_{mid})}{8\mu L_1} \\ Q_2 &= \frac{\pi a_2^4 (p_{mid} - p_2)}{8\mu L_2} \ . \end{aligned} \tag{5.12}$$

We require that the flux through each tube be equal, and so we set $Q_1 = Q_2$ and eliminate p_{mid} from the equations. We obtain

$$Q = \frac{-\pi \omega_1}{8\mu} \left(p_1 - \frac{\omega_1 p_1 + \omega_2 p_2}{\omega_1 + \omega_2} \right) \ , \tag{5.13}$$

where $\omega_i = a_i^4 / L_i$.

Using this modified flow theory, we return to the collapsing bubble experiment. Figure 5.5 shows snapshots at various times during the collapse, which was filmed at 125 fps. The grey circles overlayed on the images are least squares fit

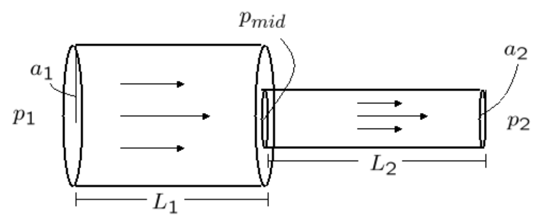

Figure 5.4: Flow through two tubes in series, driven by known pressures p_1 and p_2.

circles. Observe that all times, the spherical approximation is accurate. In Figure 5.5(c), the bubble has reached the hemispherical state and the point with the smallest best fit circle. Beyong this time the radius increases as the bubble flattens out.

In modeling the collapse, we note that the bubble is connected to the larger radius tube, so that p_1 is the pressure inside the bubble and p_2 the ambient pressure. The Young-Laplace law gives an expression for $p_1 - p_2$, which we may solve for p_1. Then, setting the rate of change of volume of the bubble equal to the flux through the tubes, we obtain

$$\frac{d}{dt}\Bigg(V(b(t))\Bigg) = \frac{-\pi\omega_1}{8\mu}\left(\frac{4\sigma}{(b^2+a_1^2)^{1/2}} + p_2 - \frac{\omega_1(\frac{4\sigma}{(b^2+a_1^2)^{1/2}} + p_2) + \omega_2 p_2}{\omega_1+\omega_2}\right) , \quad (5.14)$$

where

$$V\left(b(t)\right) = \pi\left(\frac{2}{3}(b^2+a_1^2)^{3/2} + \frac{2}{3}b^3 + a_1^2 b\right) . \quad (5.15)$$

The choice of the pressure p_2 is arbitrary, so we choose it to be zero. Figure 5.6 is a comparison of theory and experiment, plotting radius of the partial sphere as a function of time. The curve for the theory is obtained by solving Equation (5.15) for $b(t)$, and then using the relation $R(t)^2 = b(t)^2 + a_1^2$. Also included in this plot is

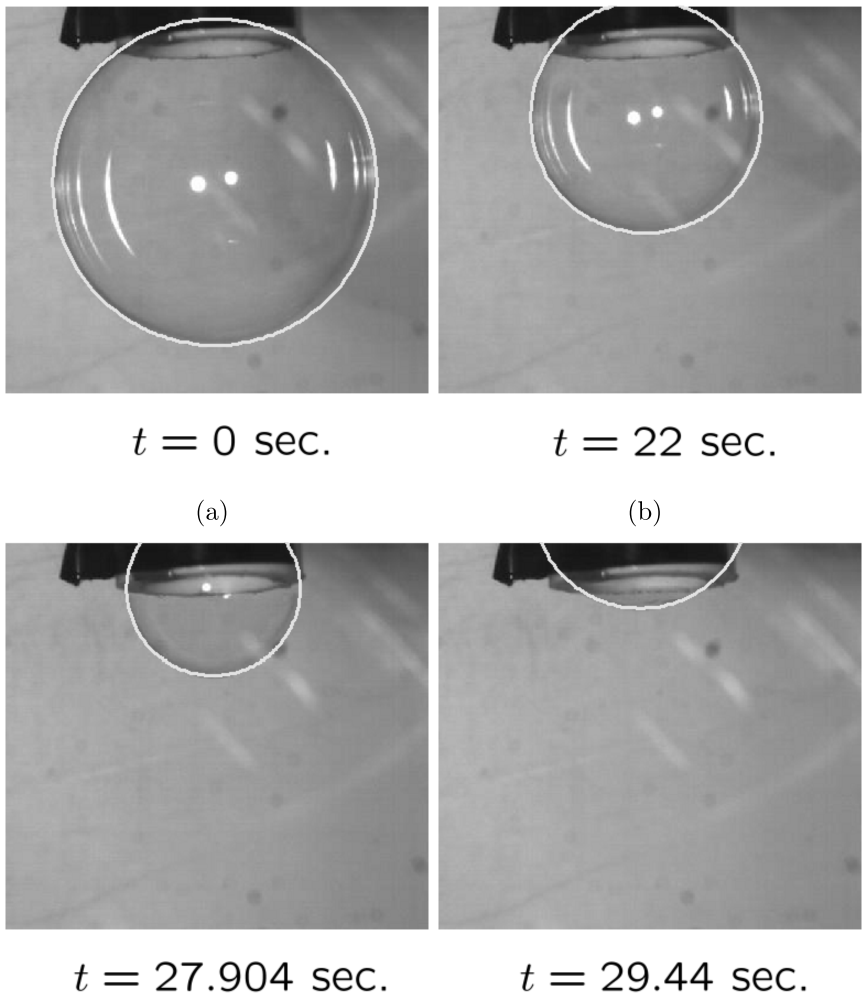

(a) (b) (c) (d)

Figure 5.5: The collapse of a bubble through a constrained tube of large radius, with least squares fit circles overlayed.

the collapse given by the $R(t)$ theory using the modified flow. For the $R(t)$ theory for the tubes in series, the solution is found to be

$$R(t) = \left(R(0)^4 - \frac{\sigma}{2\mu}(\omega_1 - \frac{\omega_1}{\omega_1 + \omega_2})t \right)^{1/4} . \tag{5.16}$$

Comparing this to Equation (5.4), we note that the collapse through two tubes in series is quantitatively equivalent to the collapse through a single tube. To be precise, the collapse through two tubes of different radii is mathematically identical to the collapse through a single tube of radius $\omega_1^{1/4}(1-\omega_1)^{1/4}$ and length $\omega_1+\omega_2$. For the $b(t)$ theory, on the other hand, the two tube collapse is fundamentally different from any collapse through a single tube. In the $R(t)$ theory, the tubes in series may be handled by properly averaging out the properties of each tube. This does not work in the $b(t)$ theory due to the fixed radius at the collapsing tube.

We see in Figure 5.6 that for the beginning of the collapse, both the $b(t)$ and the $R(t)$ theory agree with experimental observation. When the radius gets small, however, the $R(t)$ theory falls off with the radius going to zero. The radius as derived from the $b(t)$ theory, however, continues to match well with the experiment through the transition of minimum radius all the way to the end of the collected data as the bubble flattens out and the radius gets large.

There is a small discrepancy between the data and the $b(t)$ theory toward the end of the collapse, however. We conjecture that this is due to the way the bubble connects to the collapsing tube. For large volumes the bubble intersects the tube on the outer edge. This is evident in Figure 5.5(a) and (b). As the volume decreases, the bubble rolls over to the inside edge of the tube, where it clearly sits in Figure 5.5(d). It appears that the bubble rolls over to the inside edge of the tube during the transition through the hemispherical state. We observe from Figure 5.6 that the only apparent discrepancy between the $b(t)$ theory and the experimental data occurs around this point of the collapse. This is likely a result of the bubble

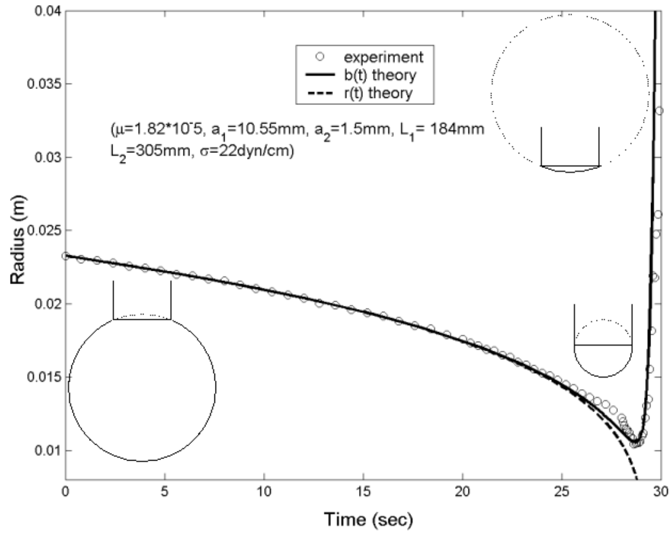

Figure 5.6: Comparison of theory and experiment for the large tube constrained collapse.

"rolling over" to the inside edge of the tube. Our model treats the tube as being infinitesimally thin, and so cannot capture this behavior. It would be an interesting future problem to analyze exactly when and how the bubble changes its connection to the tube.

Large radius unconstrained collapse

To briefly illustrate the limit of the model, consider Figure 5.7. This experiment follows the collapse of a bubble for the exact same setup as in the previous experiment, except that here the large tube is unconstrained. That is, the large tube does not feed into a smaller tube; the collapse is only through the large tube on which the bubble is formed. As would be expected, the collapse occurs on a much shorter time scale. The entire collapse occurs in just over a tenth of a second, as compared with the constrained collapse which took nearly 30 seconds. The unconstrained collapse of Figure 5.7 was filmed at 500 fps.

Initially, the bubble appears spherical, and for the very beginning of the collapse, the $b(t)$ theory is reasonably valid. However, as the collapse proceeds, the

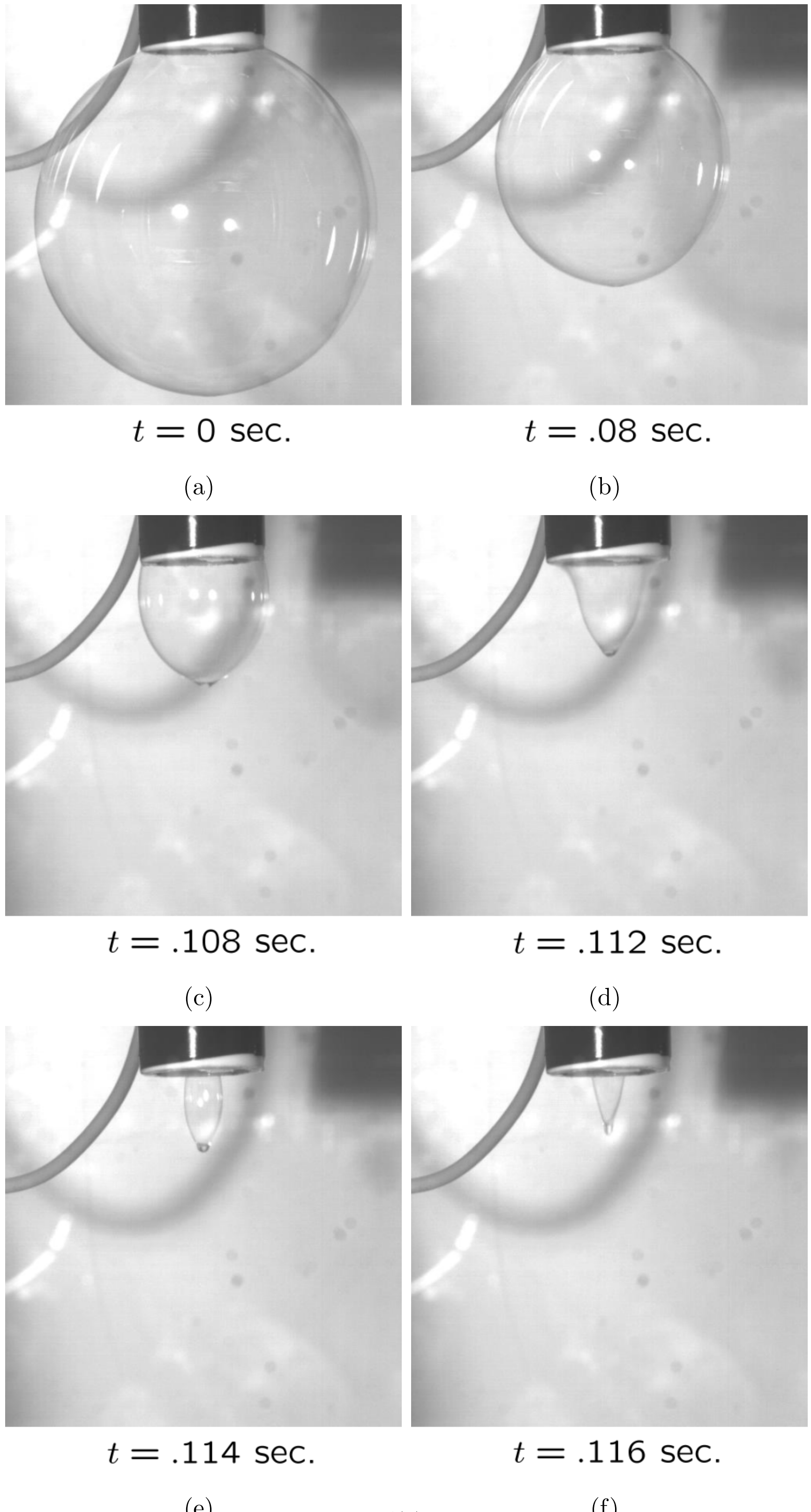

Figure 5.7: The collapse of a bubble through an unconstrained tube of large radius.

bubble is deformed. In Figure 5.7(b), we see that the bubble has become elongated and appears similar to a prolate spheroid. In Figure 5.7(c), it has become further elongated. Also, notice that a drop of soap solution has accumulated on the bottom of the bubble. This is likely a result of the fact that the same number of soap-film molecules that made the large initial bubble have been very quickly compacted as the bubble shrinks. This added weight pulling the bubble down almost certainly has a significant effect on the collapse. In Figure 5.7(d) the part of the bubble closest to the tube has pinched in, so that it almost appears to pinch off and form a satellite bubble in Figure 5.7(e).

Clearly, some important effects are missing in the theory in describing a collapse through an unconstrained large radius tube. To begin with, the quasistatic approach of using the Young-Laplace law and assuming the bubble will minimize surface area at each instant in time is certainly not valid. It is likely that this needs to be augmented with the inertia of the soap-film itself. The molecular redistribution of the soap particles seems more difficult to include, but is likely playing an important role as well.

5.4 Collapse of a charged bubble

5.4.1 $R(t)$ theory

Having analyzed the collapse of a bubble, we now consider the effect of electrostatic forces. The general form of the problem is the same as in the previous sections: our equation will come from the relation that the change in volume of the bubble with respect to time will equal the flux of air through the collapsing tube. As we have seen before, the flux is driven by, and more precisely proportional to, the pressure difference between the two ends of the tube. Before, we used the Young-Laplace relation for the pressure difference. Here, we must augment the Young-Laplace relation to include the electrostatic pressure due to the field.

To begin, in this section we explore the collapse of a charged bubble. We assume the same setup as in the uncharged case, but take the bubble to maintain a total electric charge Q. We also take the bubble to be electrically isolated so that during the collapse, the charge remains constant.

As a first approach, we assume that the bubble is a full sphere with radius $R(t)$. Taking a uniform charge density σ, we have

$$\sigma = \frac{Q}{4\pi R^2} \ .$$

If we consider a differential patch of the sphere, the electric field $\mathbf{E}$ should satisfy

$$dE = \frac{\sigma}{2\epsilon_0} \ ,$$

which is the field intensity on the surface of a conductor. Now, using the relations $dF = qdE$ and $q = \sigma dA$, where F is the magnitude of the electrostatic force, q is a differential charge element, and dA is the area of a differential patch, we may write the electrostatic pressure p_E as

$$p_E = \frac{dF}{dA} = \frac{Q^2}{32\pi^2\epsilon_0 R^4} \ . \tag{5.17}$$

We then modify the Young-Laplace relation as

$$\Delta p = \frac{4\gamma}{R} - p_E \ . \tag{5.18}$$

The differential equation for the radius in Equation (5.3) becomes

$$\frac{d}{dt}\left(\frac{4\pi R^3}{3}\right) = -\frac{\pi a^4 \gamma}{8l\mu}\left(\frac{4\gamma}{R} - \frac{Q^2}{32\pi^2\epsilon_0 R^4}\right) \ . \tag{5.19}$$

Equation (5.19) may be written

$$\frac{dR}{dt} = -\frac{a^4\gamma}{32l\mu}\left(\frac{4\gamma}{R^3} - \frac{Q^2}{32\pi^2\epsilon_0 R^6}\right) \ . \tag{5.20}$$

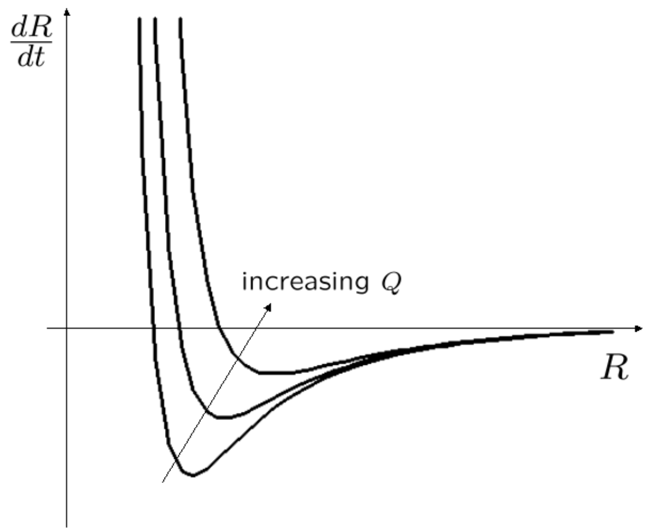

Figure 5.8: The form of dR/dt for a charged collapsing bubble.

Figure 5.8 shows the form of dR/dt as a function of R for various choices of Q. Observe that $\frac{dR}{dt} = 0$ for

$$R = \left(\frac{Q^2}{128\pi^2 \gamma \epsilon_0} \right)^{1/3} . \tag{5.21}$$

At this radius, the outward electrostatic pressure perfectly balances the pressure from the surface tension on the bubble, and the bubble's volume no longer changes. Denote this equilibrium radius as R_{eq}. Note that if at time zero, $R < R_{eq}$, the bubble should theoretically pull air in through the tube to reach this value, while if $R > R_{eq}$ initially, the bubble should collapse until it reaches this value. We note also that R_{eq} increases like $Q^{2/3}$.

There are several problems with the above analysis. For one, it suffers from the same problem as the $R(t)$ theory in the absence of electric charge. Namely, treating the bubble as a full sphere is an approximation which is only valid in the regime of a large bubble. Adapting the above approach to the $b(t)$ theory is not difficult, but there is a bigger problem concerning the shape of the bubble. Place a fixed charge on a bubble, and intuition suggests that the system should tend to the state where the charge is uniformly distributed around the the surface, causing the outward force to be equal at all points on the sphere. Hence, the bubble should remain spherical. In actuality, it is more complicated than this. As we mentioned in Chapter 1, the spherical shape is only stable given small enough charge or large enough radius. To be precise, the sphere becomes unstable when the charge satisfies

$$Q > 8\pi\sqrt{2\epsilon_0 R^3\gamma}\ . \tag{5.22}$$

In view of Equation (5.21), we see that the stability boundary corresponds to the radius at which the bubble should stop collapsing. For bubbles smaller than this radius, the assumption of a spherical bubble is invalid, and even a $b(t)$ model is inherently flawed.

Perhaps the biggest problem with the charged bubble collapse is that it is tremendously difficult to implement experimentally. We have made multiple attempts to experimentally investigate a collapsing bubble with a fixed electrical charge. Our primary goal was to see whether the non-zero equilibium radius given in Equation (5.21) could be attained physically. All efforts toward this end have invariably failed. One of the big experimental obstacles is simply charging the bubble. That is, how do you put a charge on a bubble in such a way that you can control the exact amount of charge? Beyond this, the other significant problem is *keeping* the charge on the bubble. We found that upon letting the bubble collapse, the charge would never remain constant. As we could never achieve a fully isolated system, the charge always managed to "leak off" as the bubble got small.

5.4.2 Collapse of a bubble on a plate

In light of the experimental difficulties just described, in this section we develop a theory for a related system of a collapsing charged bubble, but which should

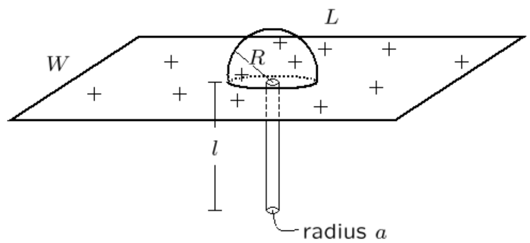

Figure 5.9: The setup for a collapsing bubble on a charged plate.

be much easier to implement experimentally. The setup we consider is depicted in Figure 5.9. A hemispherical bubble with radius R is formed on a plate of length L and width W over a collapsing tube of length l and radius a. The plate is given total charge Q. We assume that a portion of the charge distributes evenly over the surface of the bubble while the rest of the charge is distributed on the free surface of the plate outside the bubble. Depending on the material properties, the charge may have preference for either plate or bubble. Letting Q_B be the charge on the bubble, we assume

$$Q_B = \alpha \frac{A_B}{A_T} Q = \frac{\alpha 2\pi R^2}{LW + \pi R^2} Q \ , \tag{5.23}$$

where A_B is the area of the bubble and A_T is the total free surface area. The constant α determines the preference of the charge for the bubble or the plate. If we had $\alpha = 1$, this would imply a perfectly uniform distribution of the charge. The electrostatic pressure on the bubble is given by

$$p_E = \frac{Q_B^2}{2\epsilon_0 A_B^2} = \frac{\alpha^2 Q^2}{2\epsilon_0 (LW + \pi R^2)^2} \ . \tag{5.24}$$

Augmenting the Young-Laplace relation with this pressure and equating the rate of change of volume to the flux out of the tube, we have the following ODE for the radius $R(t)$:

$$\frac{d}{dt}\left(\frac{2}{3}\pi R^3\right) = -\frac{\pi a^4}{8\mu l}\left(\frac{4\gamma}{R} - \frac{\alpha^2 Q^2}{2\epsilon_0 (LW + \pi R^2)^2}\right) . \tag{5.25}$$

In our model of Section 5.4.1, it was determined that the system reached a stable equilibrium at a non-zero radius. The primary difference in the present model is that the charge on the bubble is not fixed. As the bubble shrinks the charge is able to redistibute between the plate and the bubble. Is there a non-zero equilibrium in this system? If so, we would need $\frac{dR}{dt} = 0$, or

$$(LW + \pi R^2) = cR, \quad c := \frac{\alpha^2 Q^2}{8\gamma\epsilon_0} . \tag{5.26}$$

Any solution to Equation (5.26) is an equilibrium radius for the system. A graphical analysis demonstrates that

1. $LW > \dfrac{3c^{2/3}}{4}(4\pi)^{-1/3} \Rightarrow 0$ equilibrium points, $\frac{dR}{dt}$ is always negative.

2. $LW < \dfrac{3c^{2/3}}{4}(4\pi)^{-1/3} \Rightarrow 2$ equilibrium points, $0 < R_1 < R_2$, with R_1 unstable and R_2 stable.

3. $LW = \dfrac{3c^{2/3}}{4}(4\pi)^{-1/3} \Rightarrow 1$ semistable equilibrium point.

The fate of the system thus depends on the size of the plate relative to the amount of total charge. If the charge is small enough or the plate large enough (Case 1), the bubble will collapse all the way. But, with large enough charge or a small enough plate (Case 2), the situation is similar to Section 5.4.1 – the electrostatic pressure balances the pressure from surface tension at a non-zero radius. The difference here is that a second unstable equilibrium also exists. Thus, in Case 2, if the system starts with $R = R_1 - \epsilon$, the bubble fully collapses, while if initially $R = R_1 + \epsilon$, the bubble increases to the stable equilibrium at R_2.

This revised theory should be easier to implement experimentally, although we do not present any experimental results here. A potential use of this theory involves α, the constant of proportionality representing the preference of the electrical charge to distribute over the plate or the bubble. This constant should be a material property, and a collapsing bubble experiment could theoretically be used to determine the value of this constant.

5.5 Collapse of a bubble in a uniform electric field

In this section, we consider the problem of a bubble collapsing in a uniform electric field. The big difference here is that even for a small electric field, the bubble will no longer remain spherical. Following the work of Taylor [69], we will approximate the bubble as a spheroid and solve the potential equation for the field in ellipsoidal coordinates.

We orient the problem as follows. Let the center of the bubble be at the origin when there is no applied field, and let the exit tube be oriented along the x-axis. Apply a uniform electric field in the x direction:

$$\vec{E} = E_0 \hat{x} \ .$$

A bubble in a uniform field is elongated at the poles, and may be approximated by a prolate spheroid. Thus, we take the shape of the bubble to be

$$\frac{x^2}{a^2} + \frac{y^2 + z^2}{b^2} = 1, \quad a > b \ . \tag{5.27}$$

Working in ellipsoidal coordinates, we may solve the potential equation and then calculate the electrostatic pressure p_E on the bubble. Denoting the potential by ϕ and the bubble surface Γ, we find that

$$p_E = \frac{\epsilon_0}{2}\left(\left.\frac{\partial \phi}{\partial n}\right|_\Gamma\right)^2 = -\frac{\epsilon_0 E_0^2 b^2 \frac{\xi + a^2}{a^2 - b^2}}{2\xi\left(\frac{1-e^2}{2e^3}\left(\log\frac{1+e}{1-e} - 2e\right)\right)^2} \ , \tag{5.28}$$

where ξ is the ellipsoidal coordinate corresponding to constant surfaces that are ellipsoids. Details may be found in [33]. Here, $\xi = -b^2$ corresponds to the poles on the x-axis, and $\xi = -a^2$ corresponds to the equator, or the $y - z$ plane. Also,

$$e = \sqrt{1 - \frac{b^2}{a^2}}$$

is the ellipticity of the spheroid.

The augmented Young-Laplace relation is

$$\Delta p = 2\gamma(r_1^{-1} + r_2^{-1}) + p_E \ , \tag{5.29}$$

where γ is the surface tension of the soap film and the r_i are the principal radii of curvature for the ellipsoid. For a prolate spheroid, these are given by

$$r_1 = a^2 b^2 \left(\frac{x^2}{a^4} + \frac{z^2}{b^4} \right)^{3/2} , \quad r_2 = b^2 \left(\frac{x^2}{a^4} + \frac{z^2}{b^4} \right)^{1/2} . \tag{5.30}$$

In the collapse equation

$$\frac{d}{dt} \, \text{Volume} = \text{flux} = -K\Delta p \ ,$$

we cannot apply the general relation for Δp, as it is given as a function of position on the spheroid, whereas the volume is not a pointwise quantity. Instead, we apply the pressure difference equation at a particular point to obtain an ODE depending only on $a(t)$ and $b(t)$ – values that determine the shape and volume of the bubble. More precisely, the flow of air through the collapsing tube is driven by the pressure difference across the tube. Thus, we apply the pressure difference equation at the point where the bubble meets the tube, i.e., at the pole $\xi = -b^2$. Plugging $\xi = -b^2$ into Equation (5.28), letting $x = a$, $z = 0$ in Equations (5.30), and noting that the volume of a prolate spheroid is $4\pi ab^2/3$, we obtain the following equation for the collapse of the bubble

$$\frac{d}{dt}\left(\frac{4}{3}\pi ab^2\right) = -K\left(2\gamma\left(\frac{2a}{b^2}\right) - f(e)\right), \quad K = \frac{\pi A^4}{8\mu l} \ . \tag{5.31}$$

Here, A is the radius and l the length of the collapse tube, and μ air viscosity. Also,

$$f(e) = \frac{\epsilon_0 E_0^2}{2\left(\frac{1-e^2}{2e^3}(\log\frac{1+e}{1-e} - 2e)\right)^2} \tag{5.32}$$

is the electrostatic pressure as a function of the eccentricity.

Equation (5.31) is to be solved for the unknown shape parameters $a(t)$ and $b(t)$. However, even with initial values, the system is underdetermined, because we have stated no relation between the two dependent variables a and b. One possibility to rectify this is to make the assumption that the eccentricity remains constant during the collapse. In this case, b may be written in terms of a, the function $f(e)$ becomes a constant, and the ODE reduces to one that may be solved for $a(t)$. Refer to this as Method 1.

As an alternative approach, we can couple the ODE with an equation describing the shape of the bubble at any fixed time in order to relate a and b. To do this, we assume that the pressure at the equator is equal to the pressure at the poles. Hence, we equate the pressure difference at these two points, and eliminate Δp to obtain one equation for the shape parameters a and b. We obtain

$$2\gamma\left(\frac{2a}{b^2} - \frac{b}{a^2} - \frac{1}{b}\right) = f(e) \ . \tag{5.33}$$

This provides a relationship between a and b for any given time, and so combining this equation with the ODE (5.31) completes the system. However, Equation (5.33) is not easily solved for a or b, so to simplify matters we employ the change of variables suggested by Taylor [69]. We introduce r and α such that

$$\frac{4}{3}\pi r^3 = \frac{4}{3}\pi ab^2, \quad \alpha = 1 - e^2 \ . \tag{5.34}$$

Thus, r is the radius of the sphere with equivalent volume as the spheroid, and α gives the relative shape of the ellipsoid. In terms of these variables, we have $a = r\alpha^{-1/3}$, $b = r\alpha^{1/6}$. With this change of variables, the shape Equation (5.33) may be solved for r as a function of α, and we may obtain an ODE only in terms of $\alpha(t)$.

With one further assumption, in fact, we can reach an exact solution. If we assume that the bubble remains nearly spherical, i.e., $e << 1$ we can expand $f(e)$ as

$$f(e) \sim \frac{45\epsilon_0 E_0^2}{10 - 8e^2} = \frac{45\epsilon_0 E_0^2}{2 + 8\alpha} .$$

With this simplification, we find that

$$r = \frac{4\gamma}{45\epsilon_0 E_0^2}\left(2\alpha^{-2/3} - 5\alpha^{5/6} - \alpha^{-1/6} + 8\alpha^{1/3} - 4\alpha^{11/6}\right) := M(\alpha) . \tag{5.35}$$

We then obtain the following ODE for $\alpha(t)$

$$\frac{4}{3}\pi\frac{d}{dt}\left(M^3(\alpha(t))\right) = -\frac{2K\gamma}{M(\alpha)}\cdot\frac{\alpha+1}{\alpha^{1/6}} . \tag{5.36}$$

Equation (5.36) may be integrated, yielding an analytic implicit solution. Refer to this as Method 2. If we do not assume small eccentricity, we can still write Equation (5.33) as $r = N(\alpha)$ and obtain a differential equation solely in terms of $\alpha(t)$. In this case, however, the ODE will not yield an analytic solution. Refer to this as Method 3.

Note that we have formulated the collapse in terms of the relative shape of the bubble, which on its own gives us no information about the size of the bubble. In solving the ODE, we provide an initial condition as follows: the initial volume of the bubble is taken to be known, which implies that we know the value $r(0)$. Thus, we may solve the equation $M(\alpha) = r(0)$ to find the initial value of α. Then, at any

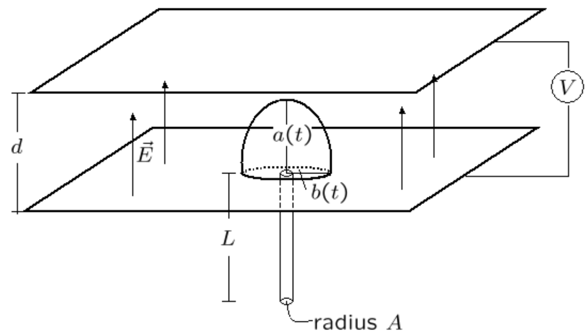

Figure 5.10: Experimental setup for collapsing bubble in a uniform field.

point during the collapse, knowing α gives r which in turn determines the exact shape with a and b.

5.5.1 Collapse of a bubble in a uniform electric field – experimental analysis

In this section we report experimental results on a collapsing bubble in a uniform field, and check the validity of the above theory. The experimental apparatus is depicted in Figure 5.10. Instead of a full bubble, a half of a bubble is formed on a plate. A second plate is placed parallel at a distance $d = 46.4$ mm to the first, and a potential difference V is applied between the plates, creating a uniform field $\vec{E}$ of strength V/d. Soap-film maintains a contact angle of $\pi/2$ with the plate, and so we treat the bubble as always forming half of a spheroid. The only change in the theory then is to account for the factor of 2 missing in the volume. The bubbles are given an initial volume of 40 cubic centimeters. The collapsing tube has radius $A = 2.15$ mm and length 36 cm. The surface tension $\gamma = 0.025$ N/m was determined by a least squares fit on collapse data in the absence of a field.

Figure 5.11 shows a sequence of pictures from a collapsing bubble experiment. For this experiment, the potential difference was 7.3 kV. Initially, the bubble is

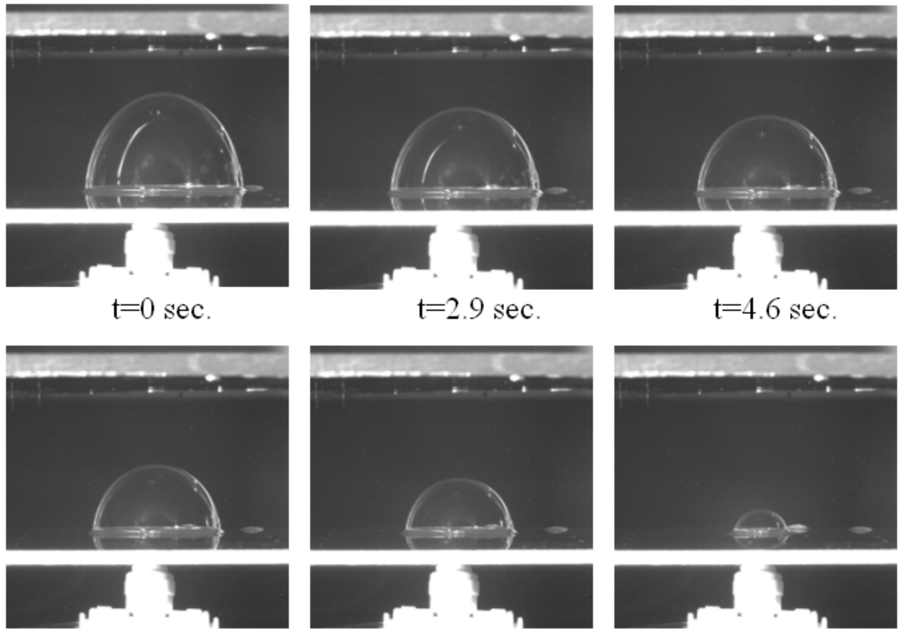

Figure 5.11: Sequence of pictures during the collapse with a uniform field from a potential difference of 7.3 kV.

clearly deflected toward the upper plate. Note that 7.3 kV is just under the critical pull-in voltage at which the bubble loses stability. The full collapse occurs in just under 10 seconds.

Figure 5.12 shows a comparison of theoretical Methods 1 – 3 with the experiment of Figure 5.11. The data was collected by determining a and b from the sequence of pictures and then calculating the apparent radius r from Equation (5.34). Both Methods 2 and 3 are reasonably accurate in predicting apparent size during the collapse. Clearly, Method 1 is not at all accurate. Recall that the assumption in Method 1 was that the eccentricity remains constant. It is clear from inspection of Figure 5.11 that it does not.

Methods 2 and 3 are essentially equivalent, except that Method 3 should be more accurate in that no assumptions are made on the eccentricity. To further test

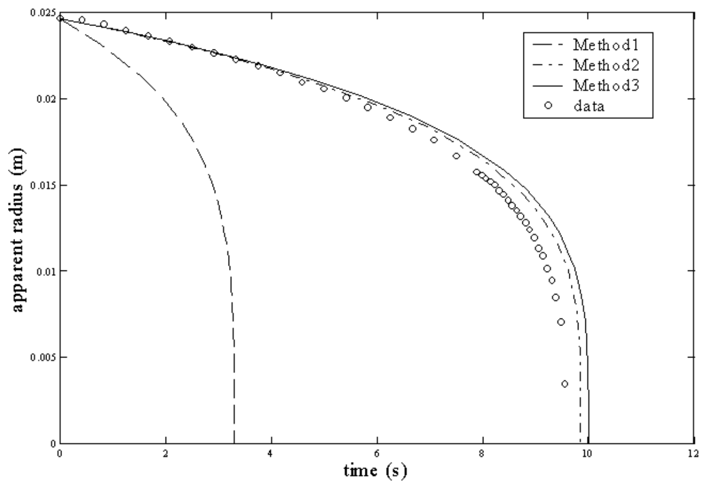

Figure 5.12: Comparison of Methods 1, 2 and 3 with experimental data for collapse at 7.3kV.

the validity of Method 3, consider Figure 5.13. The apparent radius is plotted as a function of time, with data and Method 3 predictions presented at 0, 4, and 7.3 kV. Observe that as the voltage is increased (i.e., field strengthened), the total collapse time increases. This is as predicted by the theory. However, with increased voltage the theory seems to lose accuracy. While the theory matches well at 4 kV, it is far less accurate at 7.3 kV.

It seems that our model for a collapsing bubble in a uniform field does a reasonable job of predicting the time of collapse and relative size as a function of time. However, the theory is far less reliable in predicting the exact shape of the bubble during the collapse. This is evident upon closer inspection of Figure 5.11. Our quasistatic approach implies that at any snapshot in time, the bubble should be a prolate spheroid. While this is clearly true at the start of the collapse, toward the end of the collapse the shape actually switches so that at the end, the height a is less than the radius at the plate b.

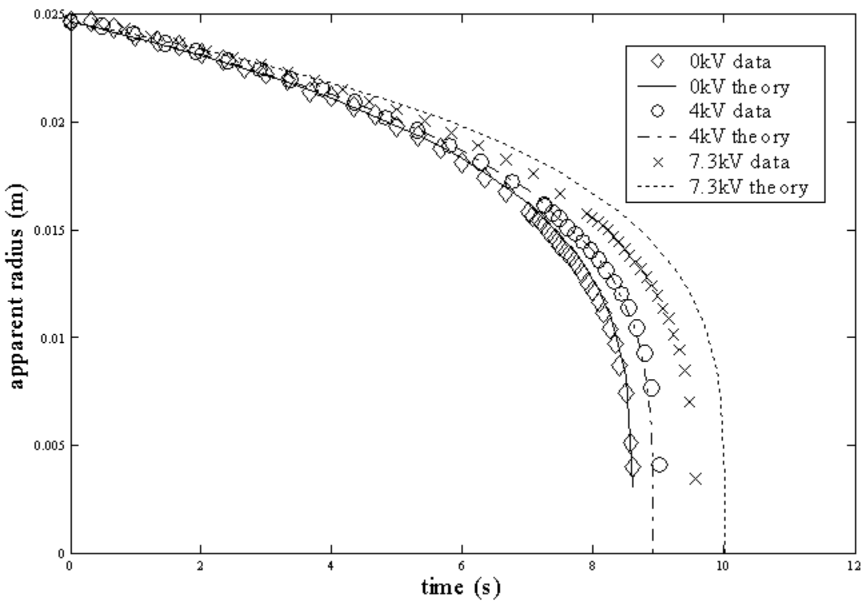

Figure 5.13: Comparison of Method 3 to experimental data at voltages 0, 4, and 7.3 kV.

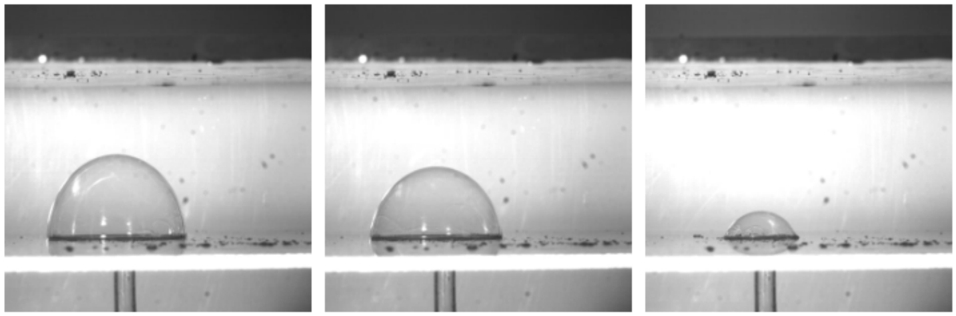

Figure 5.14: Sequence of pictures from a quickly collapsing bubble through a short collapsing tube.

In terms of the theory, this transition is not at all predicted. In the theory, $\alpha = b^2/a^2$ is always less than 1, and α approaches 1 as r approaches 0, meaning that theoretically the bubble approaches a spherical shape as the volume approaches zero.

One final point: in all of our models, we have taken a quasistatic approach. In the above experiments, we may have been right at the edge of the regime where quastistatic is appropriate. Figure 5.14 shows an example where the quasistatic approach is certainly not valid. This is a sequence of pictures from the same experimental setup, except that the length of the collapsing tube is much shorter so that the collapse occurs much more quickly. Notice that toward the end of the collapse, the bubble is no longer connecting with the plate at a right angle, and is surely not approximated by half of a spheroid. Clearly, the quasistatic approach is only valid in regimes of a relatively slow collapse.

5.6 Two bubble systems

In this section we extend the analysis of collapsing bubbles to multiple bubble systems. The difference physically is that instead of a single bubble deflating into the ambient, we have multiple bubbles competing for a fixed volume of air, so that if one bubble begins to deflate another must inflate.

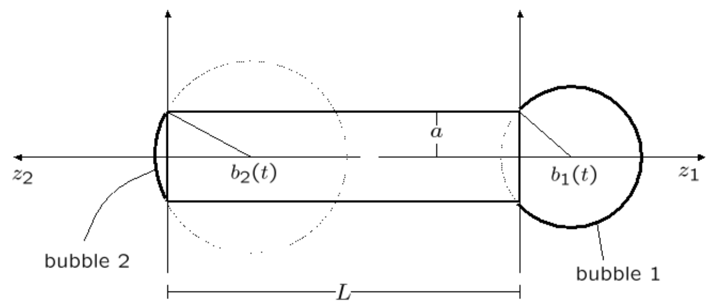

Figure 5.15: Setup for the two bubble system.

In particular, in this section we explore the system depicted in Figure 5.15. Two bubbles are connected by a tube of radius a and length l. The system has a fixed volume, and so the dynamics are dictated by the competition for a finite amount of air. We allow the bubbles to have arbitrary surface tensions as well as surface charges, which need not be equal on each bubble. Through a largely geometrical approach, we will characterize the behavior of the system, and investigate the dependence on the relative surface tensions and surface charges on the bubbles.

As in the case of a single bubble, the dynamics are best cast in terms of the middle point of the spheres of each bubble, denoted b_1 and b_2. The Poiseuille flow through the connecting tube is driven by the pressure difference between each bubble, which is determined by the Young-Laplace relation, modified to account for an added electrostatic pressure due to the surface charges. Letting V_i be the volume and p_i the pressure of the ith bubble, the system is governed by

$$\begin{aligned}\frac{dV_1}{dt} &= -\frac{\pi a^4}{8\mu L}(p_1 - p_2)\\ \frac{dV_2}{dt} &= -\frac{\pi a^4}{8\mu L}(p_2 - p_1)\\ V_1 + V_2 &= V\ .\end{aligned} \tag{5.37}$$

Note that the volume constraint follows naturally as a conservation law from the

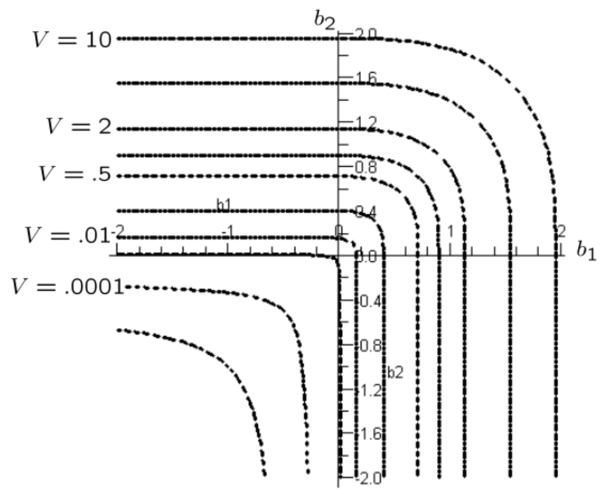

Figure 5.16: Contours for various values of volume V.

differential equations. For the current setup, we will have

$$
\begin{aligned}
V_i &= \pi\left(\frac{2}{3}(b_i^2+a^2)^{3/2}+\frac{2}{3}b_i^3+a^2b_i\right)\\
p_i &= \frac{4\gamma_i}{(b_i^2+a^2)^{1/2}}-\frac{Q_i^2}{8\pi^2\epsilon_0\left(b_i^2+a^2+b_i(b_i^2+a^2)^{1/2}\right)^2}\ .
\end{aligned}
\tag{5.38}
$$

Here, γ_i is the surface tension and Q_i the surface charge of the ith bubble.

To analyze this system, we turn to the phase plane and consider the nature of trajectories and equilibria in the b_1-b_2 plane. Due to the volume constraint, trajectories lie upon the lines

$$
\left(\frac{2}{3}(b_1^2+a^2)^{3/2}+\frac{2}{3}b_1^3+a^2b_1\right)+\left(\frac{2}{3}(b_2^2+a^2)^{3/2}+\frac{2}{3}b_2^3+a^2b_2\right)=c\ , \tag{5.39}
$$

where c is a constant. A few contours are plotted in Figure 5.16. Note that the shape is independent of the values of the γ_i or Q_i.

We begin our analysis by proving some characteristics of the structure and stability of equilibria in the general case. We then consider specific examples and discuss their physical relevance. For simplicity of presentation, we define

$$\hat{\gamma}_i = 4\gamma_i, \quad \hat{Q}_i = \frac{Q_i^2}{8\pi^2\epsilon_0} \ .$$

This convention will be convenient in exploring equilibria, but is also useful in that it enables us to consider the surface charge more generally as simply an outward force exerted on the surface of the bubble.

The variables whose effect we wish to explore are surface tension and surface charge. The other variables in the problem have a quantitative effect on the dynamics, but it is only the surface tension and surface charge which may change the qualitative structure of the system. Thus, we view the system as follows:

$$\begin{aligned} \frac{dV_1}{dt} &= \kappa F(b_1, b_2; \hat{\gamma}_1, \hat{\gamma}_2, \hat{Q}_1, \hat{Q}_2) \\ \frac{dV_2}{dt} &= -\kappa F(b_1, b_2; \hat{\gamma}_1, \hat{\gamma}_2, \hat{Q}_1, \hat{Q}_2) \ , \end{aligned} \tag{5.40}$$

where $\kappa = \pi a^4/8\mu l$. In order to characterize the structure and stability of equilibria, define

$$H(x; \hat{\gamma}, \hat{Q}) = \frac{\hat{\gamma}}{(x^2 + a^2)^{1/2}} - \frac{\hat{Q}}{\left(x^2 + a^2 + x(x^2 + a^2)^{1/2}\right)^2} \tag{5.41}$$

so that $F(b_1, b_2; \hat{\gamma}_1, \hat{\gamma}_2, \hat{Q}_1, \hat{Q}_2) = H(b_2; \hat{\gamma}_2, \hat{Q}_2) - H(b_1; \hat{\gamma}_1, \hat{Q}_1)$. Equilibrium solutions of Equation (5.40) and their stability may be understood by considering the function H. A sample plot of H is given in Figure 5.17. The salient features of this function are that

- $H \to 0$ from above as $x \to \infty$
- $H \to -4\hat{Q}/a^4 < 0$ as $x \to -\infty$

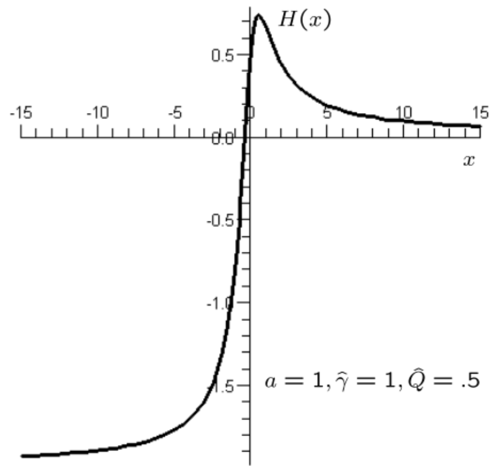

Figure 5.17: The form of the function $H(x)$.

- H has one local extremum, a local max occurring at a point in the first quadrant

Equilibria of the two bubble system Equation (5.40) occur at the points (b_1, b_2) for which $H(b_1; \hat{\gamma}_1, \hat{Q}_1) = H(b_2; \hat{\gamma}_2, \hat{Q}_2)$. We claim that these equilibria, when plotted in the b_1-b_2 plane, will always have a four branch structure. This structure is depicted in Figure 5.18, with the details determined by comparing the peaks of $H(x; \hat{\gamma}_1, \hat{Q}_1)$ and $H(x; \hat{\gamma}_2, \hat{Q}_2)$. It is sufficient to demonstrate this structure in the case where $\max H(x; \hat{\gamma}_1, \hat{Q}_1) > \max H(x; \hat{\gamma}_2, \hat{Q}_2)$, i.e., case (a) in Figure 5.18. Similar arguments demonstrate the structure in Cases (b) and (c).

Theorem 8 *If* $\max H(x; \hat{\gamma}_1, \hat{Q}_1) > \max H(x; \hat{\gamma}_2, \hat{Q}_2)$*, the equilibrium curve* $F = 0$ *will have the four branch structure of Figure 5.18(a).*

Proof: Consider the slope of the curve $F = 0$, given by

$$\frac{db_2}{db_1} = \frac{-F_{b_1}}{F_{b_2}} = \frac{H'(b_1; \hat{\gamma}_1, \hat{Q}_1)}{H'(b_2; \hat{\gamma}_2, \hat{Q}_2)} \,. \tag{5.42}$$

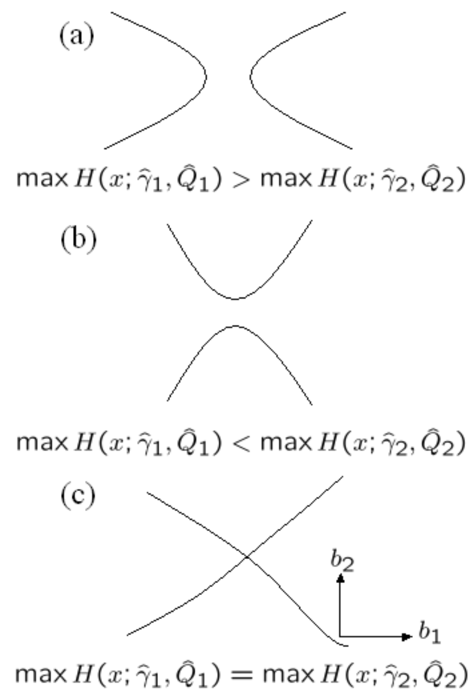

Figure 5.18: The structure of equilibria based on the function H.

Let $x = \alpha_i$ be the unique point where $H(x;\hat{\gamma}_i,\hat{Q}_i)$ takes its maximum. By our assumptions, $H(\alpha_2;\hat{\gamma}_2,\hat{Q}_2) > H(\alpha_1;\hat{\gamma}_1,\hat{Q}_1)$. Let $b_2 = \alpha_2$. Since $\max H(x;\hat{\gamma}_1,\hat{Q}_1) > \max H(x;\hat{\gamma}_2,\hat{Q}_2)$, it follows that there will be two points, $b_1 = b_{1_A}$ and $b_1 = b_{1_B}$, $b_{1_A} < b_{1_B}$, for which $F(b_1,\alpha_2) = 0$. In other words, the equilibrium curve has a vertical tangent at the points (b_{1_A},α_2) and (b_{1_B},α_2). Further, there are no equilibrium points for $b_{1_A} < b_1 < b_{1_B}$.

By similar reasoning, there are no points b_2 such that $F(\alpha_1,b_2) = 0$. Hence there are no points on the equilibrium curve with a horizontal tangent. By the nature of $H'(x)$, it follows that

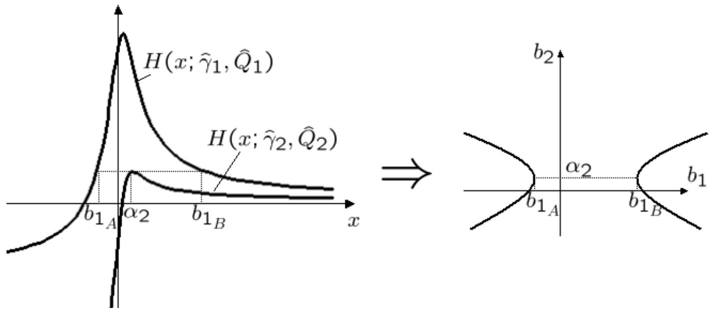

Figure 5.19: Geometrical depiction of the branch structure in Case A.

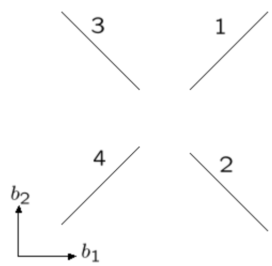

Figure 5.20: Branch labeling convention used in this section.

$$
\begin{aligned}
\frac{db_2}{db_1} &> 0 \quad \text{for } b_1 > b_{1_A}, b_2 > \alpha_2 \\
\frac{db_2}{db_1} &< 0 \quad for b_1 > b_{1_A}, b_2 < \alpha_2 \\
\frac{db_2}{db_1} &< 0 \quad for b_1 < b_{1_B}, b_2 > \alpha_2 \\
\frac{db_2}{db_1} &> 0 \quad for b_1 < b_{1_B}, b_2 < \alpha_2 \ .
\end{aligned}
\tag{5.43}
$$

This is depicted geometrically in Figure 5.19. We have proven the four branch structure for Case (a) in Figure 5.18. □

Having established the four branch structure for arbitrary parameters, we now consider stability of the equilibria. Let $(b_1, b_2) = (\eta_1, \eta_2)$ be a point of equilibrium, so that $F(\eta_1, \eta_2) = 0$. We take a perturbation of size ϵ and consider

$$\left.\frac{dV_1}{dt}\right|_{(\eta_1,\eta_2+\epsilon)} = \kappa F(\eta_1,\eta_2+\epsilon) \sim \kappa(F(\eta_1,\eta_2) + \epsilon F_{b_2}(\eta_1,\eta_2)) = \kappa F_{b_2}(\eta_1,\eta_2)\ . \quad (5.44)$$

Stability is determined by the sign of $\frac{dV_1}{dt}$, and so all we need to know is the sign of $F_{b_2}(\eta_1,\eta_2) = H'(\eta_2;\hat{\gamma}_2,\hat{Q}_2)$. Label the branches as in Figure 5.20. (This branch labeling will be used for the remainder of this chapter.) In light of the above analysis, it is easily determined that F_{b_2} is negative on Branches 1 and 3, and positive on Branches 2 and 4.

Branch 1 is always located in the first quadrant. If we perturb off this branch in the positive b_2 direction, $\frac{dV_1}{dt}$ is negative, meaning that b_1 will decrease. By the shape of the volume constraint curves, b_1 can only decrease by departing from Branch 1 and we can conclude that Branch 1 is always unstable. By similar reasoning, Branch 4 is always stable. The situation is not as simple with Branches 2 and 3, both of which may have stable and unstable portions based on how these branches intersect the volume constraint curves. In any case, stability is easily determined from our knowledge of the sign of F_{b_2}.

5.6.1 Two bubble system examples

Having established the structure and stability of the equilibria in general, we now consider some specific cases, and place our analysis in physical terms. For the remainder of the section, we adopt the convention of saying that a bubble "wins" a particular setup if that bubble gets large at the expense of the other bubble.

Case I: Equal surface tension, no surface charge

We begin with the simplest case, in which $\hat{\gamma}_1 = \hat{\gamma}_2 = \hat{\gamma}$, and both $\hat{Q}_i = 0$; i.e., the case of equal surface tension and no surface charge. Stability of equilibrium solutions in this case has been considered previously by Wente [78]. Wente examined surface area and thus free energy as a function of volume for equilibrium solutions, and placed these results in the framework of catastrophe theory. His analysis did

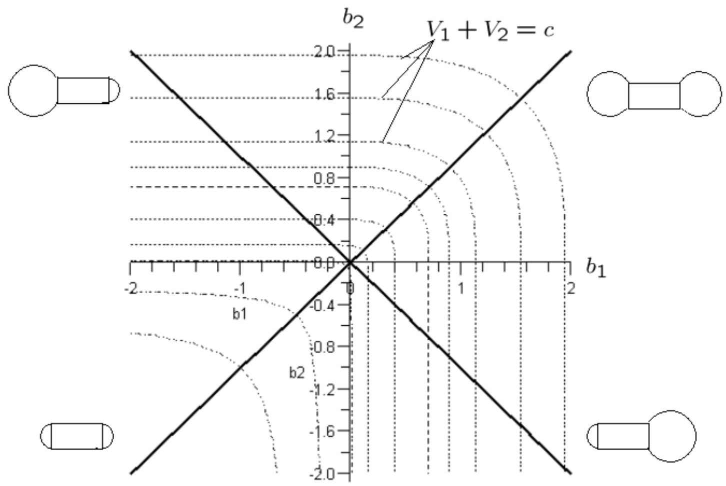

Figure 5.21: Equilibrium curves for Case I.

not involve dynamics. Some of the results we present for this case are given by Wente - we restate them here to demonstrate our geometrical approach.

The equilibrium curve is given by the lines $b_2 = \pm b_1$. Figure 5.21 displays the equilibrium curves along with the trajectory lines given by the volume constraint. Via the preceding analysis, it is clear that Branch 1 is unstable, and all others are stable.

Note that the origin $b_1 = b_2 = 0$ corresponds to the case of two hemispherical bubbles. All points on Branch 1 therefore may be thought of as equal radius large bubbles, and points on Branch 4 are equal radius small bubbles. Branches 2 and 3 correspond to one large and one small bubble. We find that if the volume is smaller than the critical two hemisphere volume, the equal radius solution is stable. If the volume is larger than the two hemisphere volume, the equal radius solution becomes unstable, and the system will tend to either Branch 2 or 3. Hence, when increasing volume there is a pitchfork bifurcation at the two hemisphere volume. This is described in [78].

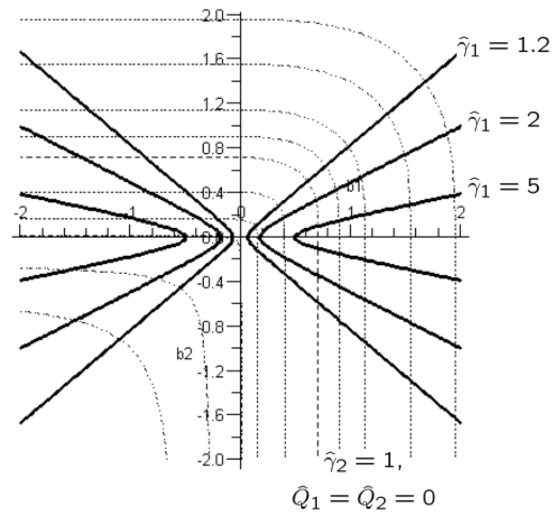

Figure 5.22: Sample equilibrium curves for Case II.

If b_2 is initially greater than b_1, the system will tend to the state where b_2 is large and b_1 is small. Physically, the bubble that starts larger always "wins".

Case II: Unequal surface tension, no surface charge

We next consider the case where the $\hat{\gamma}_i$ are unequal and the $\hat{Q}_i = 0$. Geometrically, the straight line equilibrium curves of Case I pinch off to form hyperbolas. Several sample plots are given in Figure 5.22 for $\hat{\gamma}_2$ kept fixed at one and increasing values of $\hat{\gamma}_1$. The greater the discrepancy between the surface tensions, the narrower the hyperbola and the farther apart the foci.

Again, we find that Branch 1 is unstable while all others are stable. Note that the equal radius configuration is no longer an equilibrium state, for any volume. For large volumes, the equal radius equilibrium is shifted to smaller b_2. Since $\hat{\gamma}_1 > \hat{\gamma}_2$, Bubble 1 is essentially pushing harder than Bubble 2, and so equilibrium occurs for $b_2 < b_1$. Interestingly, for small volumes, the equal radius configuration has been shifted to larger b_2.

We also observe that a bubble that is initially smaller can now "win" and get large. This is understandable by the fact that the bubbles are no longer "pushing" equally. Note that the greater the discrepancy between the surface tensions, the more pronounced the effect.

An interesting phenomenon occurs at the critical volume corresponding to the vertex of the hyperbola on the right side. This vertex occurs at the point $b_2 = 0$, $b_1 = a\sqrt{1 - \hat{\gamma}_1^2/\hat{\gamma}_2^2}$. Inserting this into Equation (5.38), we find that this critical volume, denoted V_c, is given by

$$V_c := \pi a^3 \left(\frac{2\hat{\gamma}_1^3}{3\hat{\gamma}_2^3} + \frac{2}{3}(\hat{\gamma}_1^2/\hat{\gamma}_2^2 - 1)^{3/2} + (\hat{\gamma}_1^2/\hat{\gamma}_2^2 - 1)^{1/2} + \frac{2}{3} \right) . \tag{5.45}$$

If $V < V_c$, there is only one equilibrium, i.e., the point on the left side of the hyperbola, corresponding to either Branch 3 or 4. This equilibrium is stable. If $V > V_c$, Branches 1, 2, and 3 all have possible equilibria. Again, there is a sort of pitchfork bifurcation, but in a peculiar way. Consider Figure 5.23, in which trajectories are shown for the volume slightly greater than and slightly less than the critical volume. First, suppose that $V = V_c - \epsilon$ and that the bubbles begin initially with b_2 very small. In other words, begin the system at point A in Figure 5.23 and follow trajectory II. Even though $b_1 > b_2$, and potentially Bubble 1 could be much larger than Bubble 2, the system will follow the trajectory around the corner to Branch 3, and so will end up at point C with Bubble 2 large and Bubble 1 small. However, if we again start the system at point A but with $V = V_c + \epsilon$, then in this case the system will not make it around the corner. The trajectory intersects Branch 2, and so the system will stop at point B with b_2 very close to 0 and $b_1 > 0$ and potentially very large depending on the discrepancy in surface tensions. Thus, the same starting configuration reaches drastically different equilibria with only an infinitesimal change in volume. The dynamics of this situation are illustrated in Figure 5.24, which shows numerically produced $b_i(t)$ in each situation. Note that there is a drastic difference in time scales. In Case I, the system reaches equilibrium

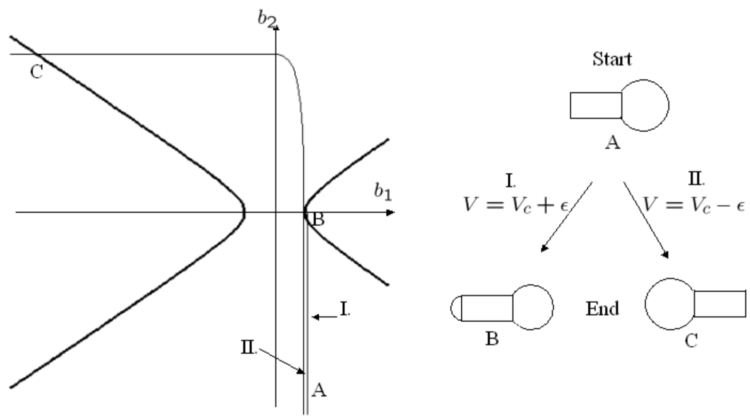

Figure 5.23: Depiction of the bifurcation that occurs at $V = V_c$. On the left are trajectories starting at $V = V_c + \epsilon$ and $V = V_c - \epsilon$. The cartoon on the right demonstrates the starting and ending configurations in each case.

almost two orders of magnitude quicker than in Case II.

Case III: Equal surface tension, equal non-zero surface charge

Here we consider the case where $\hat{\gamma}_1 = \hat{\gamma}_2 = \hat{\gamma}$ and $\hat{Q}_1 = \hat{Q}_2 = \hat{Q} > 0$. Equilibrium curves are given in Figure 5.25 for increasing values of $\hat{Q}_i$.

Note that geometrically, the only difference with the added charge is that Branches 2 and 3 have been bent in the positive b_2 and b_1 directions, respectively. Branches 1 and 4 are unchanged, reflecting the symmetry that remains in this setup. We find again that Branch 1 is unstable while all others are stable. To understand Branches 2 and 3, consider that we have added an outward force that is inversely proportional to the area of the bubble, and that this force dominates as $b_i \to -\infty$. Essentially, the system does not allow either of the bubbles to get too small.

To take the point further, we write the equilibrium curve as

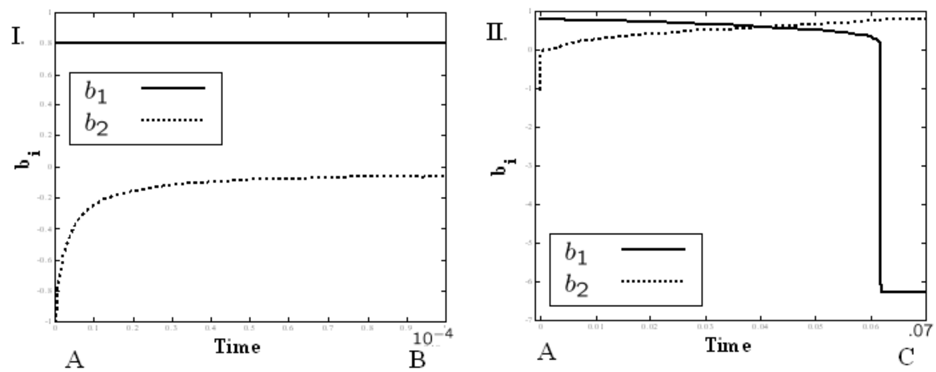

Figure 5.24: Numerical solutions of the $b_i(t)$ corresponding to Figure 5.23. In Case I, equilibrium is reached in approximately 0.0005 sec., whereas it takes 0.07 sec. in Case II.

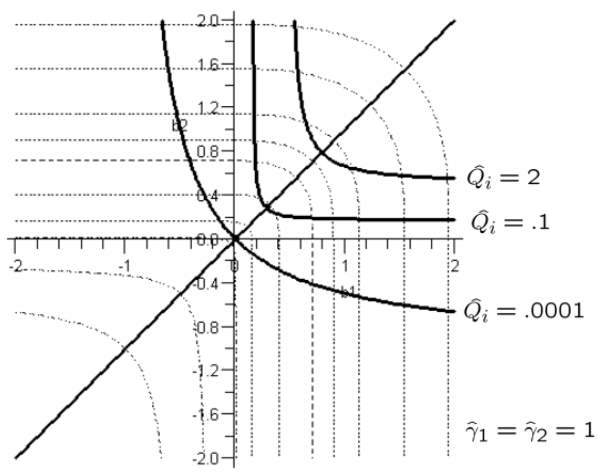

Figure 5.25: Sample equilibrium curves for Case III.

$$H(b_1; \hat{\gamma}, \hat{Q}) - H(b_2; \hat{\gamma}, \hat{Q}) = 0 \ .$$

As was stated earlier, $H(x) \to 0$ as $x \to \infty$. Thus, if we take b_1 to infinity, b_2 must satisfy $H(b_2; \hat{\gamma}, \hat{Q}) = 0$, and so b_2 will tend to the horizontal asymptote corresponding to the unique root of H. This means that Branches 2 and 3 are not just bent but in fact have asymptotes. Physically, for a fixed charge, there is a smallest value that the b_i will take, regardless of how large the volume gets.

Also notice that the critical volume at which stability changes is increased. Each bubble is "pushing" equally in this case. Thus, just as in Case I, when the total volume is small the equal radius solution is stable. In Case I, once the hemispherical state is reached surface tension takes over and the equal radius solution becomes unstable. Adding surface charge adds a force counter to surface tension and so the equal radius configuration remains stable beyond the hemispherical state. But, as volume increases the electrostatic force decays faster than surface tension. This is easy to see from the modified Young-Laplace equation: the surface tension term goes like one over the radius while the electrostatic term goes like one over the radius to the fourth. The pitchfork bifurcation still occurs, just at a larger volume.

Case IV: Equal surface tension, one bubble charged

We now consider the case where the $\hat{\gamma}_i$ are equal, $\hat{Q}_1 > 0$, and $\hat{Q}_2 = 0$. Equilibrium curves for varying values of $\hat{Q}_1$ are given in Figure 5.26.

In this case, the bubbles are not pushing equally, and the equal radius configuration is not an equilibrium state for any volume. However, as the volume goes to infinity the electrostatic force becomes negligible, and so the equilibrium curve will tend to the equal radius state in this limit. This is observable in Figure 5.26. Note that if we take $b_2 \to \pm\infty$, the equilibrium curve must satisfy $H(b_1; \hat{\gamma}, \hat{Q}_1) = 0$. This implies a unique vertical asymptote at $b_1 = C$, such that $H(C; \hat{\gamma}, \hat{Q}_1) = 0$. Branches 3 and 4 will always stay to the right of $b_1 = C$, meaning that there are no

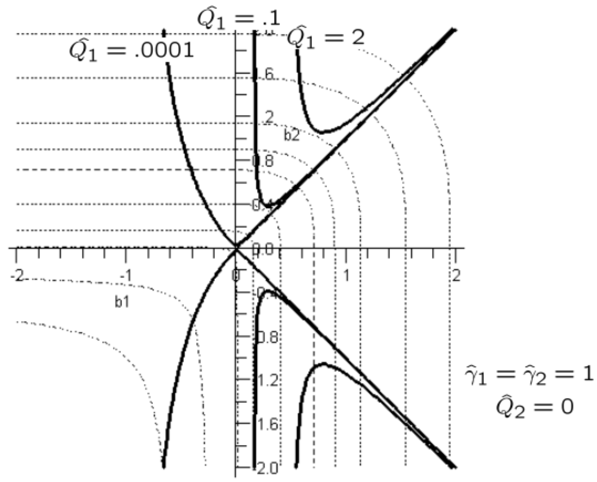

Figure 5.26: Sample equilibrium curves for Case IV.

equilibrium points for $b_1 \leq C$. Physically, this means that there is a critical volume below which there are no equilibrium solutions.

In this system, there are actually three critical volumes, labeled V_1, V_2, and V_3 in Figure 5.27. V_1 is the volume for which the volume constraint curve intersects $b_1 = C$ at $b_2 = -\infty$. V_2 is the volume which intersects the turning point between Branches 2 and 4. V_3 is the smallest volume which intersects the upper Branches 1 and 3.

When the volume $V < V_1$, there are no equilibrium solutions, and all trajectories tend to $b_2 = -\infty$, which corresponds to the state where Bubble 2 is a planar disc. This is due to the overwhelming electrostatic force on Bubble 1 when the area is small. Once $V = V_1$, the planar disc case corresponds to equilibrium. As the volume is increased from V_1 to V_2, the value of b_2 quickly increases as we walk up the asymptote. At V_2, b_2 reaches its maximum, so that if we continue to increase the volume, b_1 will continue to increase while b_2 decreases. This relationship is demonstrated in Figure 5.27(b), which shows a qualitative plot of b_2 versus volume.

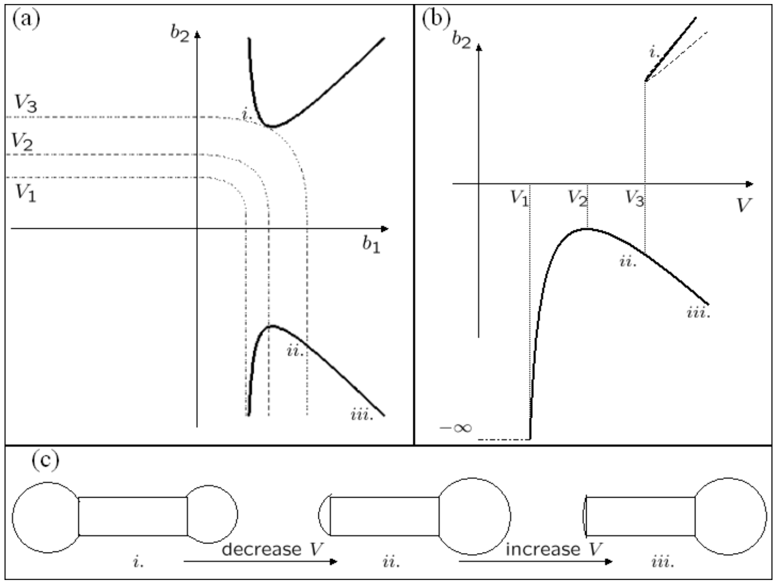

Figure 5.27: (a) - The critical volumes in Case IV. (b) - b_2 as a function of volume, corresponding to the marked points in (a). (c) - Cartoon depiction of the hysteresis shown in (b).

At the third critical volume, V_3, we have a pitchfork bifurcation and two more equilibrium solutions are introduced. Due to the separated state of Branches 1 and 3 from 2 and 4, we again have the phenomenon we observed in Case II, where infinitesimal changes in volume cause the same initial configuration to reach very different ending states. Namely, compare the result of beginning with b_1 negative and $V = V_3 - \epsilon$ versus $V = V_3 + \epsilon$. The point that we bring to attention presently is the hysteresis present in the system. If we begin at point i in Figure 5.27 so that $V > V_3$, and decrease the volume below V_3, the system will jump to point ii. From point ii, we are unable to get back to point i, though. Increasing the volume from point ii will simply move the system along Branch 2 to point iii. This hysteresis is depicted in Figure 5.27(c).

Case V: Unequal surface tension, one bubble charged

Finally, we consider a combination of the above effects, with unequal surface tension as well as added surface charge. There are multiple combinations that could

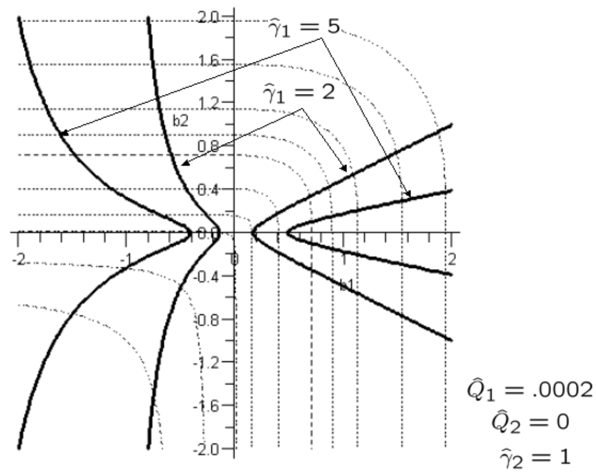

Figure 5.28: Sample equilibrium curves for Case V.

be considered; here we take the case where $\hat{\gamma}_1 > \hat{\gamma}_2$, $\hat{Q}_1 > 0$, and $\hat{Q}_2 = 0$. Equilibrium curves for varying values of $\hat{\gamma}_1$ are given in Figure 5.28. The difference in surface tension qualitatively means that Bubble 1 is pushing harder. However, we counter this by adding a surface charge to Bubble 1 only, thereby adding an outward force on Bubble 1.

Geometrically, the difference in surface tension pushes the curves to be hyperbolas, as in Case II, while the added charge skews the curve to the positive b_1 direction. As in Case IV, there is a value $b_1 = C$ for which Branches 3 and 4 have vertical asymptotes. Hence, we again have a critical volume below which there are no equilibrium solutions. The effects of hysteresis and sensitivity to infinitesimal changes in volume discussed previously are present in this case as well.

We make one final observation which is illustrated in Figure 5.29. Follow the path from i to iii. It begins on Branch 2 with $V > V_2$ and Bubble 1 large. As volume is decreased below V_2, the system jumps to point ii on Branch 3, with Bubble 2 large and Bubble 1 now small. Decrease the volume further and, somewhat

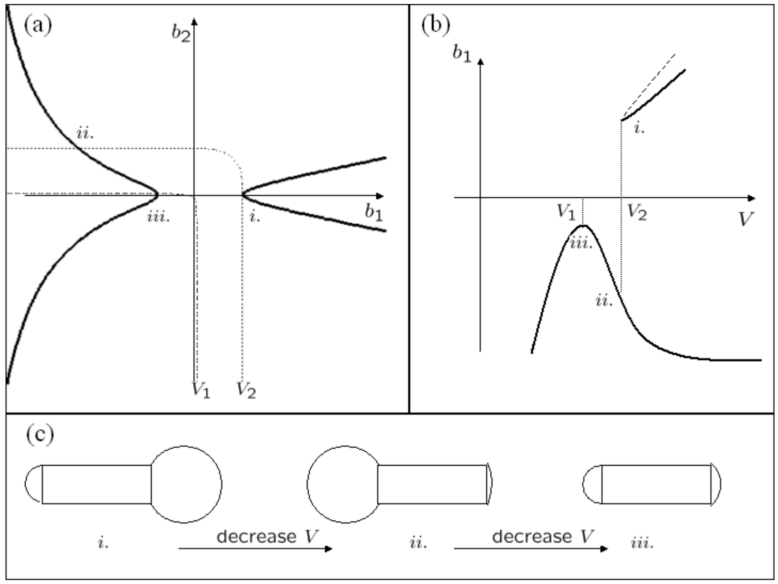

Figure 5.29: Following the path from i to iii is equivalent to decreasing the volume. At first Bubble 1 deflates, but then inflates as the system moves from ii to iii. For this scenario, (a) shows equilibrium curves, (b) shows b_1 as a function of volume, and (c) is a cartoon depiction of the bubbles.

counterintuitively, Bubble 1 increases and Bubble 2 decreases as we move to point iii. If we continue to decrease the volume from point iii, Bubble 2 again decreases.

5.7 Discussion

In this chapter we have explored various systems of collapsing bubbles, and the effect of an applied surface charge or a uniform electric field. The models we developed were straightforward. We captured collapse dynamics from a quasistatic approach, with the shape of the bubble being determined at any instant by the Young-Laplace relation, modified for the electric field as necessary. The advantage of this approach was that it led to tractable models. In most cases, we could solve the equations exactly; even when we could not, the models still proved useful. In this fashion, we could make qualitative statements regarding the general form of the collapse and the influence of the field.

The downside was that in certain situations, some necessary physics was clearly missing from the models. For one, a Poiseuille description of the air flow is only valid when the flow is laminar. Experiments in which it was not demonstrated the limit of the models. Also, some questionable simplifications were taken with regard to the electric field. Most noticeably was the assumption that a bubble will keep the same charge as it deflates but also that it will remain spherical. More complex experimental analysis might demonstrate the reasonableness of these assumptions.

Despite these potential problems, our goal was to investigate the interplay of surface tension and electrostatic forces in this dynamic system. In this respect our models were successful. We determined that the distortion due to an electric field slows down the collapse, which was validated by experiment. The interplay was most dramatic in the two bubble system, in which we found that the dynamics could be drastically altered by different combinations of surface tension, surface charge, and total volume.

Further steps related to this chapter could include extending to three bubble systems or a generalization to an N bubble system. Even adding a third bubble creates a significant complication. Much of the analysis presented in Section 5.6 will not work, as trajectories in phase space are restricted to surfaces rather than curves in a three bubble system. It will be interesting to see whether theoretical progress can be made beyond a two bubble system.

Beyond this, a useful future step could include a more complex collapse model, in particular one that is able to account for quicker collapse regimes. This is likely quite challenging even in the absence of an external field. For instance, can the shape change dynamics in the large tube unconstrained collapse of Figure 5.7 be accurately predicted? It is likely that any attempt at such a prediction would have to be numerical.

Chapter 6

CONCLUSION

In this thesis, we have analyzed two particular Field Driven Mean Curvature (FDMC) surfaces. Physically, these are surfaces or interfaces whose shape is governed by a combination of surface tension and electrostatic forces. From a general standpoint, FDMC surfaces are of interest in a range of applications. This is because surface tension and electrostatic forces are dominant in the micro and nano world, and govern the behavior of many systems in areas such as MEMS/NEMS, self-assembly, nanolithography, and microfluidics. Combining these forces and exploiting the tendencies of each in small scale systems is of great potential value. This idea is hardly new, yet with micro and nano technology in a sense still in its infancy, there is much to be explored. The geometry of boundary conditions and how electrostatic forces are applied has a dramatic impact on behavior, and so studying these systems in a generic geometry is unrealistic. In this thesis, we considered two particular systems.

The first system we explored consists of a catenoid shaped membrane subjected to an applied axially symmetric electric field. In a sense, this system sits at an intersection of two distinct fields. One is the theory of electrostatic actuation, in which electric potential differences induce actuation of an elastic membrane. This is of key importance in MEMS/NEMS technology, and as such many models have been developed to analyze this type of system. The other area is the theory of liquid and soap-film bridges. Liquid bridges are of fundamental importance in many fluid mechanical systems, are found in a host of applications, and have been explored for hundreds of years. The feature of our system which served to unite these two disparate areas was the geometry. The geometries we explored in relation to the catenoid system provided a new twist for both areas and opened up new questions in the theories of electrostatic actuation and liquid bridges.

With regard to electrostatic actuation, our geometry raised *mathematical* questions. The catenoid system we explored is fundamentally the same as in previous systems of electrostatic actuation, but in an unexplored configuration where many of the previous tools of analysis do not apply. Hence, our system raised the questions: "How does the mathematics change? What kind of analysis is viable in this geometry?"

The mathematical complexity was immediately apparent by inspection of the governing equations for the shape of the membrane, which involved the non-linear mean curvature operator as well as inverse logarithmic functions arising from the presence of the electric field. In analyzing these equations, we employed various methods. Perturbation theory applied in special cases of small voltage and nearly cylindrical bridges. Dynamical techniques and analysis of the phase plane provided information of the structure of the general solution set. Branch tracing numerical methods provided further information about the solution structure, and also uncovered new solutions. Mathematically, we determined that the field could have a drastic effect on general solution structure. For instance, in the inner cylinder setup, at most two solutions existed, whereas high multiplicity of solutions could be obtained in the outer cylinder setup.

With regard to the theory of liquid bridges, our geometry again presented a system previously unexplored. Here, though, *physical* questions were of the most relevance. One of the big issues explored with liquid bridges is stability, in particular bridge length at which instability sets in. Questions of stability for liquid bridges have been analyzed in many different situations. Different external effects and varying configurations have been considered, including the addition of electric fields. However, our geometry had not been previously explored. Hence, the pertinent questions related to liquid bridge theory were of a physical nature: "How does the physics change in this geometry? How does the electric field affect bridge stability?"

The clearest answer to these questions came in our study of the critical length parameter σ. We determined that the electric field serves to destabilize the bridge in the inner cylinder setup, in the sense that stability is lost at a shorter length than with zero voltage. Analytic approximations of the critical length were obtained through an asymptotic analysis, and verified through experiment. In the outer cylinder setup, on the other hand, we obtained the result that the field could be used to counteract surface tension and stabilize the bridge. Mathematically, this was achieved by analyzing time of flight curves and tweaking parameters to maintain the stable solution. Physically, we understood this in the sense that the proper combination of length and voltage led to a balance of surface tension and electrostatic forces.

Having gained an understanding of the outer cylinder setup in Chapter 2 and the inner cylinder setup in Chapter 3, in Chapter 4 we considered several variations to the system. We first explored the effect of unequal radii at the boundary rings. This alteration complicated the system in that it removed the inherent symmetry about the midplane, and it was necessary to explore the structure of solutions in the absence of a field as a starting point. Upon adding the field, we modified the asymptotic approach taken in the prior chapters, and obtained new approximations for the critical stability boundary length. The general relation was the same, namely that the electric field could be used to stabilize in the outer cylinder setup and destabilize in the inner cylinder setup. Interestingly, we found that the magnitude of the stabilization/destabilization effect was not constant but rather a function of the ratio of ring radii, and a non-monotonic function in the case of the outer cylinder.

We then performed a numerical analysis by plotting bifurcation diagrams. In the inner cylinder setup, it was determined that decreasing the radius of one ring led to a significant and non-linear decrease of critical voltage. In the outer cylinder setup, we found complex changes in the diagrams caused by altering the ratio of ring radii, both in the general structure and stability of diagrams as well as in the connection of different solution branches.

A potential motivation for studying the “a-b” problem, or a non-symmetric configuration in general, is in design criteria. The situation is broadly stated as an inverse problem: “I want a membrane to do X; what parameters should I use?” Our analysis in this thesis has primarily dealt with the forward problem: “Here are the parameters; what will the membrane do?” However, understanding the forward problem is typically an important step to take before approaching the backward problem. For one, the forward problem provides information on what types of inverse problems are reasonable to pose. Hence, while issues of design criteria and parameter optimization may not have been directly explored, our analysis suggests where to find the answer to any such question. For example, suppose a device is desired at which “pull-in” instability is needed at a *specific* voltage. Though we never explored this question directly, our analysis in Chapter 4 indicates that the solution likely may be found in unequal ring radii, and the bifurcation diagrams produced in Chapter 4 provide the means to obtain the desired design parameters.

In the second part of Chapter 4, we added a volume constraint to the system. While this addition does not greatly change the governing differential equation, it does pose a significant mathematical complication. In our analysis, we extended a particular theorem used to classify stability, and then utilized the theorem in studying the stability of volume constrained cylindrical liquid bridges in an electric field. We found again the destabilization effect in the inner cylinder setup, but a strangely complex effect in the outer cylinder setup, highly dependent on the balancing of parameters. The volume constrained problem is an interesting one, and we suggested several avenues for its continued analysis.

Aside from further development of the volume constrained problem, an interesting direction for future work with the catenoid system is to consider non-axisymmetric solutions. In all of our analysis, we maintained the assumption of axial symmetry; the solutions were always surfaces of revolution. This is consistent with the cylindrical formulation of the problem, yet the question arises of whether there are parameter regimes for which asymmetric solutions are possible. The need for this type of exploration is also evident in view of our experimental analysis, in which we found that asymmetry in the initial setup becomes amplified as the field is strengthened.

In Chapter 5, we investigated collapsing bubble systems. The primary appeal of these systems was that they offered dynamic FDMC surfaces that could be explored analytically. Minus the dynamics, determining the structure of equilibria and interface shape was much easier than for the catenoid systems of the previous chapters. However, unlike the catenoid system, the collapsing bubble system was by nature dynamic, which complicated the analysis and offered an element not yet explored.

We considered multiple collapsing bubble configurations, with and without electric fields, both theoretically and experimentally. First, several models were developed for the collapse of a single bubble. We gained a sense of the accuracy of the models through experimental comparison. The experiments suggested that the qualitative features of the system were captured by the models, and enabled us to develop an understanding of the interplay of electrostatic forces with mean curvature surfaces in a dynamic setting. At the same time, the experiments demonstrated that more complex models are necessary in certain regimes and to capture more accurate quantitative behavior.

We then added a second bubble to the system, and investigated the interaction of two bubbles sharing a total fixed volume. We explored this problem for arbitrary values of surface tension and electric charge, determining the structure of equilibria and stability, before looking at specific examples. A main result obtained from this analysis was that altering the parameters relative to each other can lead to drastically different dynamics. This idea might prove to be of interest in applications such as the droplet-droplet switches discussed in Chapter 1, systems which exploit bistability and surface tension driven dynamics. We found that combining surface tension variation and electrostatic forces enhances the controllability of these systems, and also allows one to move the locations of equilibria. The idea of *controllability* is very appealing in these types of systems, and our analysis suggests that this can be attained through the proper combinations of parameters.

One of the major conclusions of this thesis is that the interaction of electrostatic forces with mean curvature surfaces can lead to unexpected and counterintuitive results. In Chapter 2, for instance, it is physically intuitive that the electrostatic forces could be used to balance surface tension and stabilize longer bridges. In exploring this effect deeper, though, we found that the limit to this balancing effect occurs at a specific point at which critical voltage and critical length are both reached simultaneously. Dynamically, this poses a dilemma, in that two different instabilities should occur simultaneously at this specific point. Also in Chapter 2, we found through producing bifurcation diagrams a bizarre branch of solutions, made more bizarre by the verification that they represented stable solutions. In Chapter 4, we found an equally curious stability result, when it was determined that incredibly small stability regions could exist for very thin volume constrained cylindrical bridges. With regard to two bubble collapsing systems, we encountered several situations where infinitesimal changes in volume caused nearly equivalent initial setups to have very different dynamics and ending configurations.

We found all of these results to be unexpected and counterintuitive, and could offer no physical explanations for their existence. Physically, in fact, it is difficult to say whether these results are actually realizable or if they merely exist as mathematical anomalies unattainable in the lab due to either some aspect of missing physics or experimental "imperfections". In fact, it would be unwise to make any claims about these bizarre phenomena without careful experimental investigation. From a mathematical point of view, at least, it is clear that these systems have the potential to produce strange and unexpected results.

Finally, we point out that the systems explored in this thesis were not chosen in the spirit of investigating any particular application or device. It is unlikely, though possible, that someone might directly apply our analysis to a particular engineering or industrial system. What may potentially be taken from our analysis is not necessarily *what* we have explored, but *how* we have explored these systems. What may be gained from this thesis is the methods with which we have approached understanding these particular FDMC surfaces, tools which might be adequately adapted to related systems. From a mathematical standpoint, we took a multifaceted approach to analyzing complex systems. In both the catenoid in an electric field and the collapsing bubble systems, we employed a variety of techniques, including asymptotic methods, calculus of variations, dynamical techniques, geometrical analysis, phase plane analysis, numerical integration, arc-length continuation methods, and experimental investigation. Each of these areas provided a separate piece of the puzzle. Together, the different approaches collectively enabled us to reach a full understanding of the systems. Along with how we explored these systems, a primary objective was to further the physical understanding of FDMC surfaces. From a physical standpoint, our analysis provides a step in understanding how electric fields interact with mean curvature surfaces.

REFERENCES

[1] M.A. Abbas, J. Latham, *The instability of evaporating charged drops*, J. Fluid Mech. **30** No. 4 (1967), pp. 663-670.

[2] American Institute of Physics (2006, November 14). Cheaper Color Printing By Harnessing Ben Franklin's Electrostatic Forces. *ScienceDaily*. Retrieved February 26, 2008, from `http://www.sciencedaily.com/releases/2006/11/061113180530.htm`

[3] S. Andersson, S.T. Hyde, K. Larsson, S. Lidin, *Minimal-surfaces and structures - from inorganic and metal crystals to cell-membranes and bio-polymers*, Chem. Rev. **88** No. 1 (1988), pp. 221-242.

[4] P.A. Ark, W. Parry, *Application of high-frequency electrostatic fields in agriculture*, Quarterly Rev. of Biology **15** No. 2 (1940), pp. 172-191.

[5] O.A. Basaran, L.E. Scriven, *Axisymmetric shapes and stability of isolated charged drops*, Phys. Fluids A **1** No. 5 (1989), pp. 795-798.

[6] O.A. Basaran, L.E. Scriven, *Axisymmetric shapes and stability of charged drops in an external electric field*, Phys. Fluids A **1** No. 5 (1989), pp. 799-809.

[7] O.A. Basaran, L.E. Scriven, *Axisymmetric shapes and stability of pendant and sessile drops in an electric field*, J. Colloid Interface Sci. **140** No. 1 (1990), pp. 10-30.

[8] P.W. Bates, G.W. Wei, S. Zhao, *Minimal molecular surfaces and their applications*, J. Comput. Chem. **29** No. 3 (2008), pp. 380-391.

[9] A.S. Bhandar, P.H. Steen, *Liquid-bridge mediated droplet switch: A tristable capillary system*, Phys. Fluids **17** (2005), 127107.

[10] M. Blank, P.R. Mussellwhite, *The permeabilities of adsorbed monolayers to water*, J. Colloid Interface Sci. **27** No. 2 (1968), pp. 188-192.

[11] C.V. Boys, *Soap-Bubbles, Their Colours and the Forces Which Mould Them*, Dover, New York, 1959.

[12] C.L. Burcham, D.A. Saville, *The electrohydrodynamic stability of a liquid bridge: microgravity experiments on a bridge suspended in a dielectric gas*, J. Fluid Mech. **405** (2000), pp. 37-56.

[13] V. Caselles, R. Kimmel, G. Sapiro, C. Sbert, *Minimal surfaces based object segmentation*, IEEE Trans. Pattern Anal. and Machine Intelligence **19** No. 4 (1997), pp. 394-398.

[14] Y.-J. Chen, N.D. Robinson, J.M. Herndon, P.H. Steen, *Liquid bridge stabilization: theory guides a codimension-two experiment*, Comput. Methods Appl. Mech. Eng. **170** (1999), pp. 209-221.

[15] Y.-J. Chen, P.H. Steen, *Dynamics of inviscid capillary breakup: collapse and pinchoff of a film bridge*, J. Fluid Mech. **341** (1997), pp. 245-267.

[16] P. Concus, R. Finn, J. McCuan, *Liquid bridges, edge blobs, and Scherk-type capillary surfaces*, Indiana Univ. Math. J. **50** (2001), pp. 411-441.

[17] S.A. Cryer, P.H. Steen, *Collapse of the soap-film bridge: quasistatic description*, J. Colloid Interface Sci. **154** No. 1 (1992), pp. 276-288.

[18] A. Doyle, D.R. Moffett, B. Vonnegut, *Behavior of evaporating electrically charged droplets*, J. Colloid Sci. **19** No. 2 (1964), pp. 136-143.

[19] M.A. Erle, R.D. Gillette, D.C. Dyson, *Stability of interfaces of revolution with constant mean curvature. The case of catenoid*, Chem. Eng. J. **1** (1970), pp. 97-109.

[20] J. Eggers, J.R. Lister, H.A. Stone, *Coalescence of liquid drops*, J. Fluid Mech. **401** (1999), pp. 293-310.

[21] R. Finn, *Capillary surface interfaces*, Notices of the AMS **46** No. 7 (1999), pp. 770-781.

[22] G. Flores, G. Mercado, J.A. Pelesko, *Dynamics and Touchdown in Electrostatic MEMS*, in Proceedings of Design Engineering Technical Conferences, ASME, Chicago, IL, 2003.

[23] I.M. Gelfand and S.V. Fomin, *Calculus of Variations*, Dover, Mineola, New York, 1963.

[24] H. Gonzalez, F.M.J. McCluskey, A. Castellanos, A. Barrero, *Stabilization of dielectric liquid bridges by electric fields in the absence of gravity*, J. Fluid Mech. **206** (1989), pp. 545-561.

[25] D.J. Griffiths, *Introduction to Electrodynamics*, Prentice Hall, New Jersey, 1981.

[26] A.V. Grosse, *Efflux time of soap bubbles and liquid spheres*, Science **156** No. 3779 (1967), pp. 1220-1222.

[27] A.H. Hirsa, C.A. Lopez, M.A. Laytin, *Low-dissipation capillary switches at small scales*, App. Phy. Lett. **86** (2005) 014106.

[28] D.F. Horne, *Optical Production Technology*, Adam Hilger, Bristol, UK, 1979.

[29] C. Isenberg, *The Science of Soap Films and Soap Bubbles*, Dover, New York, 1992.

[30] H.B. Keller, *Numerical Solution of Bifurcation and Nonlinear Eigenvalue Problems,* in Applications of Bifurcation Theory, ed. P.H. Rabinowitz, Academic Press, New York, 1977.

[31] E. Kim, G.M. Whitesides, *Use of minimal free energy and self-assembly to form shapes*, Chem. Mater. **7** (1995), pp. 1257-1264.

[32] A. Klingner, J. Buehrle, F. Mugele, *Capillary bridges in electric fields*, Langmuir 20 (2004), pp. 6770-6777.

[33] L.D. Landau, E.M. Lifshitz, *Electrodynamics of Continuous Media*, Pergamon Press, Oxford, 1960.

[34] P. Lenz, R. Lipowsky, *Morphological transitions of wetting layers on structured surfaces*, Phys. Rev. Lett. **80** No. 9 (1998), pp. 1920-1923.

[35] C.A. Lopez, C.-C. Lee, A.H. Hirsa, *Electrochemically activated adaptive liquid lens*, App. Phys. Lett. **87** (2005), 134102.

[36] B.J. Lowry, P.H. Steen, *Capillary surfaces: stability from families of equilibria with application to the liquid bridge*, JSTOR Proc: Math. and Phys Sci. **449** No. 1937 (1995), pp. 411-439.

[37] J.H. Maddocks, *Stability and Folds*, ARMA **99** (1987), pp. 301-328.

[38] H.R. Manouchehri, K.H. Rao, K.S.E. Forssberg, *Review of electrical separation methods - Part 2: practical considerations*, Minerals and Metallurgical Processing **17** No. 3 (2000), pp. 139-166.

[39] J. Meseguer, J.M. Perales, and J. Alexander, *A perturbation analysis of the stability of long liquid bridges between almost circular supporting disks*, Phys. Fluids **13** No. 9 (2001), pp. 2724-2727.

[40] J.B. Meusnier, *Mémoire sur la courbure des surfaces*, Mém. des savans étrangers **10** (1785), pp. 477-510.

[41] N.P. Money, *More gs than the space shuttle: ballistospore discharge*, Mycologia **90** No. 4. (1998), pp. 547-558.

[42] F. Muller, R. Stannarius, *Collapse of catenoid-shaped smectic films*, Europhys. Lett. **76** No. 6 (2006), pp. 1102-1108.

[43] H.C. Nathanson, W.E. Newell, R.A. Wickstrom, J.R. Davis Jr., *The resonant gate transistor*, IEEE Trans. on Electron Devices **14** No. 3 (1967), pp. 117-133.

[44] D.M. Pai, B.E. Springett, *Physics of electrophotography*, Rev. of Modern Phys. **65** No. 1 (1993), pp. 163-211.

[45] P. Paik, V.K. Pamula, R.B. Fair, *Rapid droplet mixers for digital microfluidic systems*, Lab Chip **3** (2003), pp. 253-259.

[46] S. Paruchuri, M.P. Brenner, *Splitting a liquid jet*, Phys. Rev. Lett. **98** (2007), 134502.

[47] N.A. Pelekasis, K. Economou, J.A. Tsamopoulos, *Linear oscillations and stability of a liquid bridge in an axial electric field*, Phys. Fluids **13** No. 12 (2001), pp. 3564-3581.

[48] N.A. Pelekasis, J.A. Tsamopoulos, G.D. Manolis, *Equilibrium shapes and stability of charged and conducting drops*, Phys. Fluids A **2** No. 8 (1990), pp. 1328-1340.

[49] J.A. Pelesko, *Electrostatic field approximations and implications for MEMS devices*, in Proceedings of ESA, 2001.

[50] J.A. Pelesko, *Self Assembly - The Science of Things That Put Themselves Together*, Chapman Hall/CRC, Florida, 2007.

[51] J.A. Pelesko and D. Bernstein, *Modeling MEMS and NEMS,* Chapman Hall and CRC Press, 2002.

[52] J.A. Pelesko and X.Y. Chen, *Electrostatic deflections of circular elastic membranes*, J. of Electrostatics 57 (2003), pp. 1-12.

[53] J.A. Pelesko and G. Goldsztein, *Modeling constrained capacitive systems,* J. Comput. Theoretical Nanoscience **1** (2005), pp. 1-5.

[54] J. Plateau, *Statique Expérimentale et Théoretique des Liquides,* Gautier-Villars, Paris, 1873.

[55] G. Rämme, *Surface tension from deflating a soap bubble*, Phys. Educ. **32** No. 3 (1997), pp. 191-194.

[56] A. Ramos, A. Castellanos, *Bifurcation diagrams of axisymmetric liquid bridges of arbitrary volume in electric fields and gravitational axial fields*, J. Fluid Mech. **249** (1993), pp. 207-225.

[57] A. Ramos, H. Gonzalez, A. Castellanos, *Experiments on dielectric liquid bridges subjected to axial electric fields*, Phys. Fluids **6** No. 9 (1994), pp. 3206-3208.

[58] Lord Rayleigh, Phil. Mag. **14** (1882), pp. 184-186.

[59] Lord Rayleigh, *Nature* **44** (1891), p. 49.

[60] Lord Rayleigh, *On the capillary phenomena of jets*, Scientific Papers, **1**, Cambridge Univ. Press, Cambridge, 1899, pp. 377-401.

[61] N. Robinson, P.H. Steen, *Observations of singularity formation during the capillary collapse and bubble pinch-off of a soap film bridge*, J. Colloid Interface Sci. **241** (2001), pp. 448-458.

[62] M. Russo, P.H. Steen, *Instability of rotund capillary bridges to general disturbances: experiment and theory*, J. Colloid Interface Sci. **113** (1986), pp. 154-163.

[63] E. Schäffer, T. Thurn-Albrecht, T.P. Russell, U. Steiner, *Electrically induced structure formation and pattern transfer*, Nature **403** (2000) pp. 874-877.

[64] L.A. Slobozhanin, J.I.D. Alexander, *The stability of two connected drops suspended from the edges of circular holes*, J. Fluid Mech. **563** (2006), pp. 319-355.

[65] L. Slobozhanin, J. Alexander, and A. Resnick, *Bifurcation of the equilibrium states of a weightless liquid bridge,* Phys. Fluids **9** (1997), pp. 1893-1905.

[66] S.P. Song, B.Q. Li, *A hybrid boundary/finite element method for simulating viscous flows and shapes of droplets in electric fields*, Int. J. Comput. Fluid Dyn. **15** No. 4 (2001), pp. 293-308.

[67] S. Strogatz, *Nonlinear Dynamics and Chaos*, Perseus Books, Cambridge, MA, 1994.

[68] R.A. Syms, E.M. Yeatman, V.M. Bright, G.M. Whitesides, *J. MEMS* **12** No. 4 (2003), pp. 387-417.

[69] G.I. Taylor, *Disintegration of water drops in an electric field*, Proc. R. Soc. London Ser. A **280** No. 1382 (1964), pp. 383-397.

[70] G.I. Taylor, *The coalescence of closely spaced drops when they are at different electric potentials*, Proc. Roy. Soc. A **306** (1968), pp. 423-434.

[71] E.A. Theisen, M.J. Vogel, C.A. Lopez, A.H. Hirsa, P.H. Steen, *Capillary dynamics of coupled spherical-cap droplets*, J. Fluid Mech. **580** (2007), pp. 495-505.

[72] W.S.N. Trimmer, *Microrobots and micromechanical systems*, Sensors and Actuators **19** No. 3 (1989), pp. 267-287.

[73] C. Truesdell, *Jean-Baptiste-Marie Charles Meusnier de la Place (1754-1793): an historical note*, Meccanica **31** (1996), pp. 607-610.

[74] T. Vogel, *Stability of a liquid drop trapped between two parallel planes,* SIAM J. Appl. Math. **47** (1987), pp. 516-525.

[75] T. Vogel, *Stability of a liquid drop trapped between two parallel planes II: General contact angles,* SIAM J. Appl. Math. **49** (1989), pp. 1009-1028.

[76] D. Volkov, D.T. Papageorgiou, P.G. Petropoulos, *Accurate and efficient boundary integral methods for electrified liquid bridge problems*, SIAM J. Sci. Comput. **26** No. 6 (2005), pp. 2102-2132.

[77] R. Weinstock, *Calculus of Variations, with Applications to Physics and Engineering*, Dover, New York, 1974.

[78] H.C. Wente, *A surprising bubble catastrophe*, Pacific J. Math **189** No. 2 (1999), pp. 339-375.

[79] C.T.R. Wilson, G.I. Taylor, *The bursting of soap-bubbles in a uniform electric field*, Proc. Cambridge Phil. Soc. **22** (1925), pp. 728-730.

[80] M. Wu, T. Cubaud, C.-M Ho, *Scaling law in liquid drop coalescence driven by surface tension*, Phys. Fluids **16** No. 7 (2004), L51-L54.

[81] L. Zhou, *On stability of a catenoidal liquid bridge*, Pacific J. of Math. **178** No. 1 (1997), pp. 185-197.